# APPLIED COMPUTATIONAL ELECTROMAGNETICS SOCIETY JOURNAL

April 2015
Vol. 30 No. 4
ISSN 1054-4887

**The ACES Journal is abstracted in INSPEC, in Engineering Index, DTIC, Science Citation Index Expanded, the Research Alert, and to Current Contents/Engineering, Computing & Technology.**

The illustrations on the front cover have been obtained from the research groups at the Department of Electrical Engineering, The University of Mississippi.

## EMERITUS EDITORIAL ASSISTANTS



## APRIL 2015 REVIEWERS

# THE APPLIED COMPUTATIONAL ELECTROMAGNETICS SOCIETY

## JOURNAL

Vol. 30 No. 4 April 2015


## TABLE OF CONTENTS

# Coulombian Model for 3D Analytical Calculation of the Torque Exerted on Cuboidal Permanent Magnets with Arbitrary Oriented Polarizations

**Hicham Allag [1,2], Jean-Paul Yonnet [1], Houssem R. E. H. Bouchekara [2], Mohamed E. H. Latreche [2], and Christophe Rubeck [1]**

[1] Laboratoire de Génie Electrique de Grenoble, UMR 5269 CNRS/INPG/UJF
Institut Polytechnique de Grenoble, Saint Martin d'Hères, 38402, France
allag_hic@yahoo.fr, jean-paul.yonnet@g2elab.grenoble-inp.fr,
christophe.rubeck@g2elab.grenoble-inp.fr

[2] Constantine Electrical Engineering Laboratory, LEC, Department of Electrical Engineering
University of Constantine 1, 25000 Constantine, Algeria
bouchekara.houssem@gmail.com, latreche_med@yahoo.fr

***Abstract*** ─ This paper proposes improved analytical expressions of the torque on cuboidal permanent magnets. Expressions are valid for any relative magnet position and for any polarization direction. The analytical calculation is made by replacing polarizations by distributions of magnetic charges on the magnet poles (coulombian approach). The torque exerted on the second magnet is calculated by Lorentz force formulas for any arbitrary position. The three components of the torque are written with functions based on logarithm and arc-tangent. Results have been verified and validated by comparison with finite-element calculation. Further, the torque can be obtained with respect to any reference point. Although these equations seem rather complicated, they enable an extremely fast and accurate calculation of the torque exerted between two permanent magnets.

***Index Terms*** ─ Analytical calculation, coulombian approach, force, permanent magnet, torque.

## I. INTRODUCTION

Analytical expressions are very powerful, giving a very fast method to calculate magnetic interactions. It is why the analytical expressions of all the interactions, energy, forces, and torques between two cuboidal magnets are very important results. Many problems can be solved by the addition of element interactions.

Up to now, for the torque components, the calculations were first realized for a system of two magnets with parallel polarization direction by Allag [1] and Janssen [2]. For the perpendicular case the results have been recently published [3].

In this paper, we develop the calculation for systems with two magnets with inclined polarization direction. The torque expressions are valid for any given point in the space, not only around the center of the moving magnet. The expressions of the torque components are obtained using the Lorentz force method [4]. A comparison with numerical results using the commercial software Flux3D validates our analytical calculation of the torque exerted between two permanent magnets.

## II. MATHEMATICAL MODEL

We study the interaction between two parallelepiped magnets, as presented in Fig. 1. The polarizations J and J' are supposed to be rigid and uniform in each magnet. The difference is that J' are arbitrary oriented in the YZ plane. The model can be replaced by distributions of magnetic charges on the poles, generally called coulombian approach. For simplifying calculation, the polarization J' will be decomposed into parallel

*Submitted On: September 3, 2013*
*Accepted On: November 30, 2014*

component J'// and perpendicular one J'⊥ (Fig. 2).

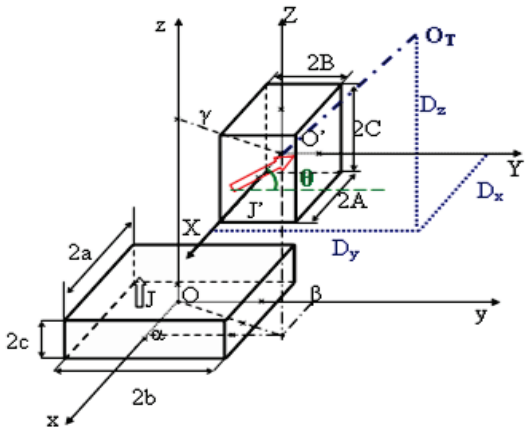


Fig. 1. System with two magnets.

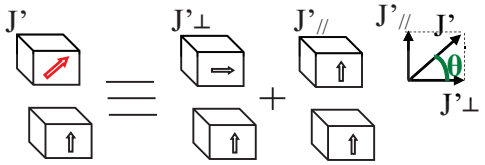


Fig. 2. Polarization decomposition.

### A. Parallel polarizations

The first 3-D fully analytical expressions of the energy and force were presented at the 1984 INTERMAG Conference, Hamburg, Germany [5]. The forces were analytically calculated for two cuboidal magnets with parallel polarization directions (Fig. 3).

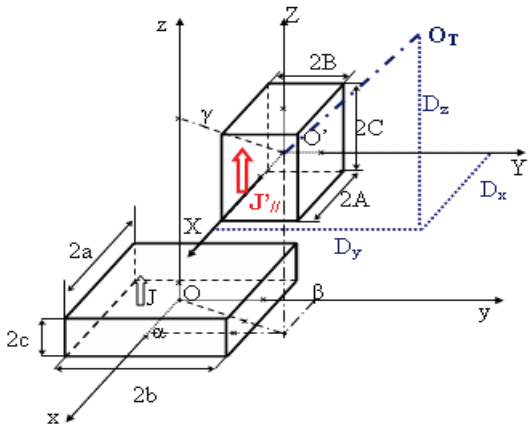


Fig. 3. Parallel polarizations.

The energy expressions are:

$$E_{//} = \frac{J.J_{//}'}{4\pi\mu_0}\sum_{p=0}^{1}\sum_{q=0}^{1}(-1)^{p+q}\int_{-C}^{C}dY\int_{-A}^{A}dX\int_{-b}^{b}dy\int_{-a}^{a}\frac{1}{r}dx, \quad (1)$$

with

$$r=\sqrt{(\alpha+X-x)^2+(\beta+Y-y)^2+(\gamma+(-1)^l C-(-1)^p c)^2}\,. \quad (2)$$

The obtained expressions of the interaction energy are:

$$E_{//} = \frac{J\cdot J_{//}'}{4\pi\mu_0}\sum_{i=0}^{1}\sum_{j=0}^{1}\sum_{k=0}^{1}\sum_{l=0}^{1}\sum_{p=0}^{1}\sum_{q=0}^{1}(-1)^{i+j+k+l+p+q}.\psi(U_{ij},V_{kl},W_{pq},r), \quad (3)$$

with

$$\psi_{//}(U,V,W,r)=\frac{U\left(V^2-W^2\right)}{2}\ln\left(r-U\right)+\frac{V\left(U^2-W^2\right)}{2}\ln\left(r-V\right)+UVW\cdot tg^{-1}\left(\frac{UV}{rW}\right)+\frac{r}{6}\left(U^2+V^2-2W^2\right). \quad (4)$$

The secondary variables are:

$$U_{ij}=\alpha+(-1)^i A-(-1)^i a,$$
$$V_{kl}=\beta+(-1)^l B-(-1)^k b, \quad (5)$$

where:

$$W_{pq}=\gamma+(-1)^q C-(-1)^p c,$$

and

$$r=\sqrt{U_{ij}^2+V_{kl}^2+W_{pq}^2}\,.$$

From the interaction energy, the force components can be obtained by $\vec{F}=-grad\ E$. Consequently, the force components are:

$$F_{//} = \frac{J\cdot J_{//}'}{4\pi\mu_0}\sum_{i=0}^{1}\sum_{j=0}^{1}\sum_{k=0}^{1}\sum_{l=0}^{1}\sum_{p=0}^{1}\sum_{q=0}^{1}(-1)^{i+j+k+l+p+q}.\varphi(U_{ij},V_{kl},W_{pq},r), \quad (6)$$

with

$$\varphi_{//X}(U,V,W,r)=\frac{\left(V^2-W^2\right)}{2}\ln\left(r-U\right)+UV\ln(r-V)+VW\cdot tg^{-1}\left(\frac{UV}{W\cdot r}\right)+\frac{1}{2}U\cdot r,$$
$$\varphi_{//Y}(U,V,W,r)=\frac{\left(U^2-W^2\right)}{2}\ln\left(r-V\right)+UV\ln(r-U)+UW\cdot tg^{-1}\left(\frac{UV}{W\cdot r}\right)+\frac{1}{2}V\cdot r,$$
$$\varphi_{//Z}(U,V,W,r)=-UW\ln\left(r-U\right)-VW\ln(r-V)+UW\cdot tg^{-1}\left(\frac{UV}{W\cdot r}\right)-W\cdot r\,. \quad (7)$$

For the torque calculation, the first magnet is supposed to be fixed and the second magnet is free to move in any direction. The torque is calculated for a movement around the point $O_T$. The $O_T$ position is defined by its coordinates ($D_x$, $D_y$, $D_z$) in the reference axes of the second magnet OXYZ. View from O, the centre of the fixed permanent magnet, the $O_T$ position is defined by ($D_x$+α, $D_y$,+β, $D_z$+γ).

The torque exerted in the second magnet at $O_T$ is calculated by Lorentz formulas [2, 3, 4]:

$$\vec{\Gamma}_{//} = \frac{J.J_{//}'}{4\pi\mu_0}\iint_S\begin{pmatrix} r'_Y B_z - r'_Z B_y \\ r'_Z B_x - r'_X B_z \\ r'_X B_y - r'_Y B_x \end{pmatrix}dS = \frac{J.J_{//}'}{4\pi\mu_0}\iint_{ZX}\begin{pmatrix} r'_Y B_z - r'_Z B_y \\ r'_Z B_x - r'_X B_z \\ r'_X B_y - r'_Y B_x \end{pmatrix}dXdY, \quad (8)$$

with

$$\vec{r}'=r'_X\vec{i}+r'_Y\vec{j}+r'_Z\vec{k}=(X-D_X)\vec{i}+(Y-D_Y)\vec{j}+(Z-D_Z)\vec{k}\,. \quad (9)$$

The torque can be also written as:

$$\vec{\Gamma}_{//} = \frac{J.J_{//}'}{4\pi\mu_0}\iint_{Z\,X}\begin{pmatrix}(Y-D_Y)\dfrac{\partial}{\partial z}\iint_{y\,x}\dfrac{1}{r}dxdy-(Z-D_Z)\dfrac{\partial}{\partial y}\iint_{y\,x}\dfrac{1}{r}dxdy\\(Z-D_Z)\dfrac{\partial}{\partial x}\iint_{y\,x}\dfrac{1}{r}dxdy-(X-D_X)\dfrac{\partial}{\partial z}\iint_{y\,x}\dfrac{1}{r}dxdy\\(X-D_x)\dfrac{\partial}{\partial y}\iint_{y\,x}\dfrac{1}{r}dxdy-(Y-D_y)\dfrac{\partial}{\partial x}\iint_{y\,x}\dfrac{1}{r}dxdy\end{pmatrix}dXdY. \quad (10)$$

The distance ***r*** is always the same (see equation (2)), and $D_X$, $D_Y$ and $D_Y$ are the projections of the distance between the centre of the moving magnet and the point of torque calculation $O_T$.

After the analytical integrations, the torque is given by:

$$\Gamma_{//} = \frac{J\cdot J_{//}'}{4\pi\mu_0}\sum_{i=0}^{1}\sum_{j=0}^{1}\sum_{k=0}^{1}\sum_{l=0}^{1}\sum_{p=0}^{1}\sum_{q=0}^{1}(-1)^{i+j+k+l+p+q}.\tau_{//}(U_{ij},V_{kl},W_{pq},r). \quad (11)$$

And the functions τ are respectively:

For $\Gamma_{//x}$:

$$\tau_{//X} = \left(\frac{(U^2-W^2)}{2}\ln(r-V)+UV\ln(r-U)+UW\cdot tg^{-1}\left(\frac{UV}{W\cdot r}\right)+\frac{1}{2}V\cdot r\right)\cdot\left(C(-1)^q-\frac{W}{2}\right)$$
$$-\left(-UW\ln(r-U)-VW\ln(r-V)+UV\cdot tg^{-1}\left(\frac{UV}{W\cdot r}\right)-W\cdot r\right)\cdot\left(B(-1)^l-\frac{V}{2}\right),$$

For $\Gamma_{//y}$:

$$\tau_{//Y} = \left(-UW\ln(r-U)-VW\ln(r-V)+UV\cdot tg^{-1}\left(\frac{UV}{W\cdot r}\right)-W\cdot r\right)\cdot\left(A(-1)^j-\frac{U}{2}\right)$$
$$-\left(\frac{(V^2-W^2)}{2}\ln(r-U)+UV\ln(r-V)+VW\cdot tg^{-1}\left(\frac{UV}{W\cdot r}\right)+\frac{1}{2}U\cdot r\right)\cdot\left(C(-1)^q-\frac{W}{2}\right),$$

For $\Gamma_{//z}$:

$$\tau_{//Z} = \left(\frac{(V^2-W^2)}{2}\ln(r-U)+UV\ln(r-V)+VW\cdot tg^{-1}\left(\frac{UV}{W\cdot r}\right)+\frac{1}{2}U\cdot r\right)\cdot\left(B(-1)^l-\frac{V}{2}\right)$$
$$-\left(\frac{(U^2-W^2)}{2}\ln(r-V)+UV\ln(r-U)+UW\cdot tg^{-1}\left(\frac{UV}{W\cdot r}\right)+\frac{1}{2}V\cdot r\right)\cdot\left(A(-1)^j-\frac{U}{2}\right). \quad (12)$$

It is easy to identify the link between the expressions of the torque (12) and the force components $\phi_{//X}$, $\phi_{//Y}$, $\phi_{//Z}$ from (7). Therefore we can write:

$$\tau_{//X} = \phi_{//Y}\cdot\left(C(-1)^q-\frac{W}{2}\right)-\phi_{//Z}\cdot\left(B(-1)^l-\frac{V}{2}\right),$$
$$\tau_{//Y} = \phi_{//Z}\cdot\left(A(-1)^j-\frac{U}{2}\right)-\phi_{//X}\left(C(-1)^q-\frac{W}{2}\right),$$
$$\tau_{//Z} = \phi_{//X}\cdot\left(B(-1)^l-\frac{V}{2}\right)-\phi_{//Y}\left(A(-1)^j-\frac{U}{2}\right). \quad (13)$$

**B. Perpendicular polarizations**

For the perpendicular polarizations case, the chosen system is presented in Fig. 4, in which the polarization of a second magnet is collinear with the Y axis.

The analytical expressions of the interaction energy and the forces components for this system were previously developed [6, 7]. The difference is in the Z integration:

$$E_\perp = \frac{JJ_\perp'}{4\pi\mu_0}\sum_{l=0}^{1}\sum_{p=0}^{1}\int_{-C}^{C}dZ\int_{-A}^{A}dX\int_{-b}^{b}dy\int_{-a}^{a}\frac{1}{r}dx. \quad (14)$$

The distance ***r*** is given by:

$$r = \sqrt{(\alpha+X-x)^2+(\beta+(-1)^l B-y)^2+(\gamma+Z-(-1)^p c)^2}. \quad (15)$$

After analytical integration, the energy is given by:

$$E_\perp = \frac{JJ_\perp'}{4\pi\mu_0}\sum_{i=0}^{1}\sum_{j=0}^{1}\sum_{k=0}^{1}\sum_{l=0}^{1}\sum_{p=0}^{1}\sum_{q=0}^{1}(-1)^{i+j+k+l+p+q}.\psi_\perp(U_{ij},V_{kl},W_{pq},r). \quad (16)$$

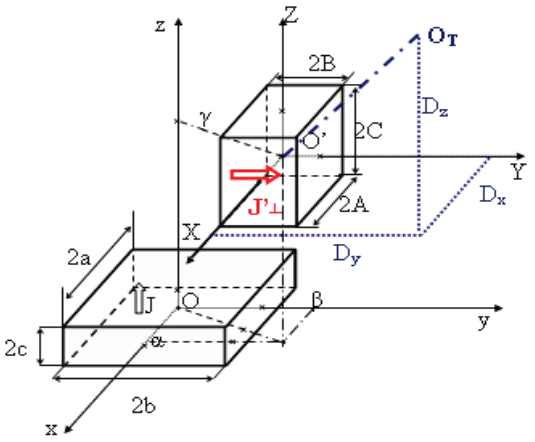


Fig. 4. System with perpendicular polarizations.

The $\psi_\perp$ function depends on the geometrical parameters (U, V, W, r):

$$\psi_\perp = \frac{V(V^2-3U^2)}{6}\ln(W+r)+\frac{W(W^2-3U^2)}{6}\ln(V+r)+UVW\cdot\ln(-U+r)$$
$$+\frac{U}{6}\left(3V^2\mathrm{tg}^{-1}\left(\frac{UW}{V\cdot r}\right)+3W^2\mathrm{tg}^{-1}\left(\frac{UV}{W\cdot r}\right)+U^2\mathrm{tg}^{-1}\left(\frac{VW}{U\cdot r}\right)\right)+\frac{V\cdot W\cdot r}{3} \quad (17)$$

The variables *U*, *V*, *W* are given by (5).

The force components can be calculated from the gradient of energy:

$$F_\perp = \frac{JJ_\perp'}{4\pi\mu_0}\sum_{i=0}^{1}\sum_{j=0}^{1}\sum_{k=0}^{1}\sum_{l=0}^{1}\sum_{p=0}^{1}\sum_{q=0}^{1}(-1)^{i+j+k+l+p+q}.\phi_\perp(U_{ij},V_{kl},W_{pq},r) \quad (18)$$

For $F_x$, the function $\phi_{\perp x}$ is given by:

$$\phi_{\perp x} = -VW\ln(r-U)+VU\ln(r+W)+WU\ln(r+V)$$
$$-\frac{U^2}{2}\mathrm{tg}^{-1}\left(\frac{VW}{U\cdot r}\right)-\frac{V^2}{2}\mathrm{tg}^{-1}\left(\frac{UW}{V\cdot r}\right)-\frac{W^2}{2}\mathrm{tg}^{-1}\left(\frac{UV}{W\cdot r}\right).$$

For $F_y$ and $F_z$:

$$\phi_{\perp y} = \frac{(U^2-V^2)}{2}\ln(r+W)-UW\ln(r-U)-UV\cdot\mathrm{tg}^{-1}\left(\frac{UW}{V\cdot r}\right)-\frac{1}{2}W\cdot r,$$
$$\phi_{\perp z} = \frac{(U^2-W^2)}{2}\ln(r+V)-UV\ln(r-U)-UW\cdot\mathrm{tg}^{-1}\left(\frac{UV}{W\cdot r}\right)-\frac{1}{2}V\cdot r. \quad (19)$$

Similarly to the parallel polarization case, the torque exerted on the second magnet at $O_T$ (Fig. 4) is expressed by:

$$\vec{\Gamma}_{\perp}=\frac{J.J'}{4\pi\mu_0}\iint_S\begin{pmatrix}r'_Y B_z-r'_Z B_y\\ r'_Z B_x-r'_X B_z\\ r'_X B_y-r'_Y B_x\end{pmatrix}dS=\frac{J.J'}{4\pi\mu_0}\iint_{Z\,X}\begin{pmatrix}r'_Y B_z-r'_Z B_y\\ r'_Z B_x-r'_X B_z\\ r'_X B_y-r'_Y B_x\end{pmatrix}dXdZ \quad (20)$$

with

$$\vec{r}'=r'_X\,\vec{i}+r'_Y\,\vec{j}+r'_Z\,\vec{k}=(X-D_X)\vec{i}+(Y-D_Y)\vec{j}+(Z-D_Z)\vec{k}\,. \quad (21)$$

The torque can be also written as:

$$\vec{\Gamma}_{\perp}=\frac{J.J'}{4\pi\mu_0}\iint_{Z\,X}\begin{pmatrix}(Y-D_Y)\frac{\partial}{\partial z}\iint_{y\,x}\frac{1}{r}dxdy-(Z-D_Z)\frac{\partial}{\partial y}\iint_{y\,x}\frac{1}{r}dxdy\\ (Z-D_Z)\frac{\partial}{\partial x}\iint_{y\,x}\frac{1}{r}dxdy-(X-D_X)\frac{\partial}{\partial z}\iint_{y\,x}\frac{1}{r}dxdy\\ (X-D_x)\frac{\partial}{\partial y}\iint_{y\,x}\frac{1}{r}dxdy-(Y-D_y)\frac{\partial}{\partial x}\iint_{y\,x}\frac{1}{r}dxdy\end{pmatrix}dXdZ \quad (22)$$

The final result is given by:

$$\Gamma_{\perp}=\frac{J\cdot J'}{4\pi\mu_0}\sum_{i=0}^{1}\sum_{j=0}^{1}\sum_{k=0}^{1}\sum_{l=0}^{1}\sum_{p=0}^{1}\sum_{q=0}^{1}(-1)^{i+j+k+l+p+q}.\tau_{\perp}(U_{ij},V_{kl},W_{pq},r)\,. \quad (23)$$

For the torque component $\Gamma\perp_x$, parallely oriented to the Ox axis, the $\tau\perp_x$ function is given by:

$$\tau_{\perp X}=\phi_{\perp y}\cdot\left(C(-1)^q-D_Z\right)-\phi_{\perp Z}\cdot\left(B(-1)^l-D_Y-V\right)+\begin{pmatrix}\frac{U\left(V^2+W^2\right)}{2}\ln(r-U)-\frac{W\left(U^2-V^2\right)}{2}\ln(r+W)\\ -\frac{V\left(U^2-W^2\right)}{2}\ln(r+V)\\ +UVW\left(\mathrm{tg}^{-1}\left(\frac{UW}{V\cdot r}\right)+\mathrm{tg}^{-1}\left(\frac{UV}{W\cdot r}\right)\right)+\frac{r^3}{6}\end{pmatrix}.$$

Function $\tau\perp_Y$ for the torque component $\Gamma\perp_Y$:

$$\tau_{\perp Y}=\varphi_{\perp Z}\cdot\left(A(-1)^j-D_x\right)-\varphi_{\perp X}\left(C(-1)^q-D_Z-W\right)+\begin{pmatrix}-\frac{U^3}{3}\ln(V+r)-\frac{V\left(V^2+3W^2\right)}{12}\ln(U+r)\\ +\frac{U^2V}{2}\ln(-U+r)\\ +\frac{W\left(W^2+3U^2\right)}{6}\cdot tg^{-1}\left(\frac{UV}{Wr}\right)+\frac{1}{12}VU\cdot r\end{pmatrix}, \quad (24)$$

Function $\tau\perp_Z$ for the torque component $\Gamma\perp_Z$:

$$\tau_{\perp z}=\varphi_{\perp X}\cdot\left(B(-1)^l-D_Y\right)-\varphi_{\perp Y}\cdot\left(A(-1)^j-D_X-U\right)+\begin{pmatrix}-\frac{U^3}{3}\ln(W+r)-\frac{W\left(W^2+3V^2\right)}{12}\ln(U+r)\\ +\frac{U^2W}{2}\ln(-U+r)\\ +\frac{V\left(V^2+3U^2\right)}{6}\cdot tg^{-1}\left(\frac{UW}{Vr}\right)+\frac{1}{12}WU\cdot r\end{pmatrix}.$$

The torque components in perpendicular case are also function of the force ones ($\phi\perp_X$, $\phi\perp_Y$ and $\phi\perp_Z$).

## III. TORQUE CALCULATION FOR INCLINED POLARIZATION DIRECTION

For an inclined polarization J' as presented on Fig. 1 and Fig. 2. It can be represented as:

$$J'=J'_{//}\sin(\theta)+J'_{\perp}\cos(\theta). \quad (25)$$

Therefore the total torque will be:

$$\Gamma=\Gamma_{//}\sin(\theta)+\Gamma_{\perp}\cos(\theta). \quad (26)$$

Using equations (11) and (23), final expressions of the torque are:

$$\Gamma=\begin{matrix}\frac{J\cdot J_{//}'\sin(\theta)}{4\pi\mu_0}\sum_{i=0}^{1}\sum_{j=0}^{1}\sum_{k=0}^{1}\sum_{l=0}^{1}\sum_{p=0}^{1}\sum_{q=0}^{1}(-1)^{i+j+k+l+p+q}.\tau_{//}(U_{ij},V_{kl},W_{pq},r)\\ \frac{J\cdot J_{\perp}'\cos(\theta)}{4\pi\mu_0}\sum_{i=0}^{1}\sum_{j=0}^{1}\sum_{k=0}^{1}\sum_{l=0}^{1}\sum_{p=0}^{1}\sum_{q=0}^{1}(-1)^{i+j+k+l+p+q}.\tau_{\perp}(U_{ij},V_{kl},W_{pq},r)\end{matrix} \quad (27)$$

The components of $\tau_{//}$ and $\tau_{\perp}$ are given by equations (12), (13) and (24).

Expressions of the torque components:

For $\Gamma_x$:

$$\Gamma_X=\begin{matrix}\frac{J\cdot J_{//}'\sin(\theta)}{4\pi\mu_0}\sum_{i=0}^{1}\sum_{j=0}^{1}\sum_{k=0}^{1}\sum_{l=0}^{1}\sum_{p=0}^{1}\sum_{q=0}^{1}(-1)^{i+j+k+l+p+q}.\tau_{//X}(U_{ij},V_{kl},W_{pq},r)\\ \frac{J\cdot J_{\perp}'\cos(\theta)}{4\pi\mu_0}\sum_{i=0}^{1}\sum_{j=0}^{1}\sum_{k=0}^{1}\sum_{l=0}^{1}\sum_{p=0}^{1}\sum_{q=0}^{1}(-1)^{i+j+k+l+p+q}.\tau_{\perp X}(U_{ij},V_{kl},W_{pq},r)\end{matrix} \quad (28)$$

with

$$\tau_{//X}=\phi_{//Y}\cdot\left(C(-1)^q-\frac{W}{2}\right)-\phi_{//Z}\cdot\left(B(-1)^l-\frac{V}{2}\right),$$

$$\tau_{\perp X}=\phi_{\perp y}\cdot\left(C(-1)^q-D_Z\right)-\phi_{\perp Z}\cdot\left(B(-1)^l-D_Y-V\right)+\begin{pmatrix}\frac{U\left(V^2+W^2\right)}{2}\ln(r-U)-\frac{W\left(U^2-V^2\right)}{2}\ln(r+W)\\ -\frac{V\left(U^2-W^2\right)}{2}\ln(r+V)\\ +UVW\left(\mathrm{tg}^{-1}\left(\frac{UW}{V\cdot r}\right)+\mathrm{tg}^{-1}\left(\frac{UV}{W\cdot r}\right)\right)+\frac{r^3}{6}\end{pmatrix}.$$

For $\Gamma_Y$:

$$\Gamma_y=\begin{matrix}\frac{J\cdot J_{//}'\sin(\theta)}{4\pi\mu_0}\sum_{i=0}^{1}\sum_{j=0}^{1}\sum_{k=0}^{1}\sum_{l=0}^{1}\sum_{p=0}^{1}\sum_{q=0}^{1}(-1)^{i+j+k+l+p+q}.\tau_{//y}(U_{ij},V_{kl},W_{pq},r)\\ \frac{J\cdot J_{\perp}'\cos(\theta)}{4\pi\mu_0}\sum_{i=0}^{1}\sum_{j=0}^{1}\sum_{k=0}^{1}\sum_{l=0}^{1}\sum_{p=0}^{1}\sum_{q=0}^{1}(-1)^{i+j+k+l+p+q}.\tau_{\perp y}(U_{ij},V_{kl},W_{pq},r)\end{matrix} \quad (29)$$

with

$$\tau_{//Y}=\phi_{//Z}\cdot\left(A(-1)^j-\frac{U}{2}\right)-\phi_{//X}\left(C(-1)^q-\frac{W}{2}\right),$$

$$\tau_{\perp Y}=\varphi_{\perp Z}\cdot\left(A(-1)^j-D_x\right)-\varphi_{\perp X}\left(C(-1)^q-D_Z-W\right)+\begin{pmatrix}-\frac{U^3}{3}\ln(V+r)-\frac{V\left(V^2+3W^2\right)}{12}\ln(U+r)\\ +\frac{U^2V}{2}\ln(-U+r)\\ +\frac{W\left(W^2+3U^2\right)}{6}\cdot tg^{-1}\left(\frac{UV}{Wr}\right)+\frac{1}{12}VU\cdot r\end{pmatrix},$$

and finally, for $\Gamma_Z$:

$$\Gamma_Z=\begin{matrix}\frac{J\cdot J_{//}'\sin(\theta)}{4\pi\mu_0}\sum_{i=0}^{1}\sum_{j=0}^{1}\sum_{k=0}^{1}\sum_{l=0}^{1}\sum_{p=0}^{1}\sum_{q=0}^{1}(-1)^{i+j+k+l+p+q}.\tau_{//Z}(U_{ij},V_{kl},W_{pq},r)\\ \frac{J\cdot J_{\perp}'\cos(\theta)}{4\pi\mu_0}\sum_{i=0}^{1}\sum_{j=0}^{1}\sum_{k=0}^{1}\sum_{l=0}^{1}\sum_{p=0}^{1}\sum_{q=0}^{1}(-1)^{i+j+k+l+p+q}.\tau_{\perp Z}(U_{ij},V_{kl},W_{pq},r)\end{matrix} \quad (30)$$

with

$$\tau_{//Z}=\phi_{//X}\cdot\left(B(-1)^l-\frac{V}{2}\right)-\phi_{//Y}\left(A(-1)^j-\frac{U}{2}\right),$$

$$\tau_{\perp z} = \varphi_{\perp X} \cdot \left( B(-1)^{l} - D_Y \right) - \varphi_{\perp Y} \cdot \left( A(-1)^{j} - D_X - U \right) + \left( \begin{array}{l} -\frac{U^3}{3}\ln(W+r) - \frac{W(W^2+3V^2)}{12}\ln(U+r) \\ +\frac{U^2 W}{2}\ln(-U+r) \\ +\frac{V(V^2+3U^2)}{6} \cdot tg^{-1}\left(\frac{UW}{Vr}\right) + \frac{1}{12}WU \cdot r \end{array} \right).$$

## IV. APPLICATION AND RESULTS

The following example presents the torque calculation between two magnets. These magnets are identical; two cubes of 1 cm edge. The lower magnet has a vertical polarization (oriented in Z direction). For the second magnet, its polarization is inclined in the YZ plane (Fig. 5). The intensity of polarization is 1 Tesla for the two magnets. The upper magnet moves in translation along the Ox axis above the lower fixed one. The vertical distance between them (air gap when the upper magnet is above the fixed magnet) is 0.01 m (β = 0 m and γ = 0.02 m).

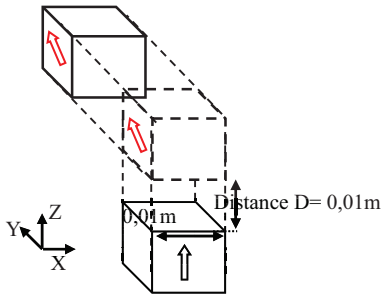


Fig. 5. Geometrical disposition of the magnets.

For the first application, the second magnet polarization is inclined (θ = 45°). The torque is calculated in the centre of the second magnet (Dx, Dy and Dz are equal to zeros). The results from analytical and numerical model using Flux3D are given in Fig. 6, proving a good accuracy of our approach.

We let the same physical and geometrical parameters as in previous example, except for the degree of inclination which is changed to θ = 30°. In this case also, the results are compared with Flux3D finite element software (Fig. 7).

In the second application, the second magnet is fixed at α = 0.0025 m, β = 0 m, γ = 0.02 m. We simulate and calculate the torque for one complete rotation of polarization (Fig. 8). The torque is computed at the centre of the magnet and its three components are presented in Fig. 9.

We can also calculate the torque components at any position of $O_T$, the next results concern the calculation of the torque at the position shown in Fig. 10, corresponding to Dx = -2 α, Dy = 0 and Dz = 0. The dimensions α, β and γ are the same as the last application (α = 0.0025 m, β = 0 m, γ = 0.02 m).The result in this case is presented as a function of a rotation angle θ on Fig. 11.

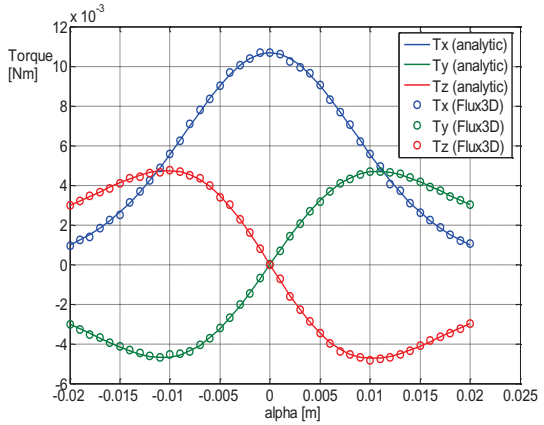


Fig. 6. Torque components for 45° inclined polarization of PM2.

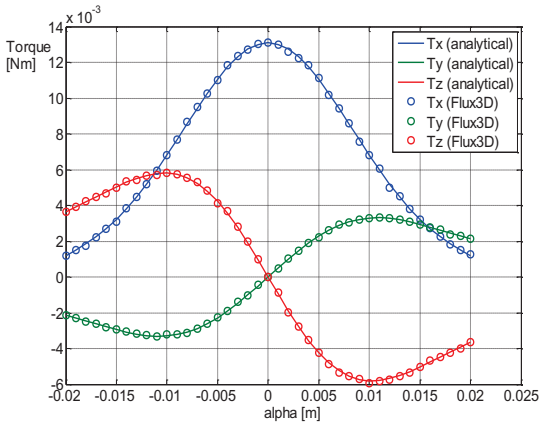


Fig. 7. Torque components for 30° inclined polarization of PM2 (second magnet).

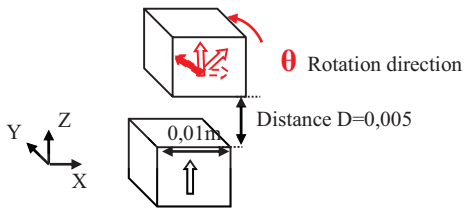


Fig. 8. Magnet position and polarization directions.

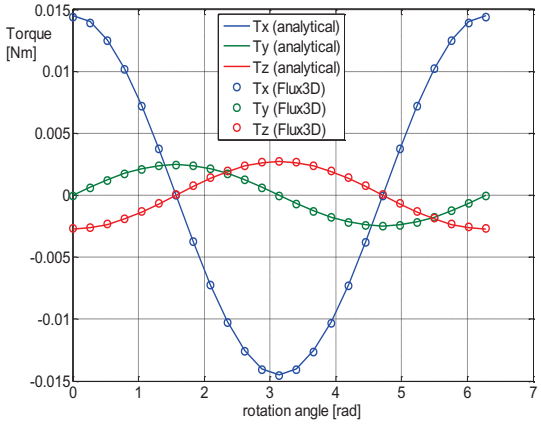


Fig. 9. Torque components calculation for one rotation of inclined polarization of PM2 (α = 0.0025 m, β = 0 m, γ = 0.02 m).

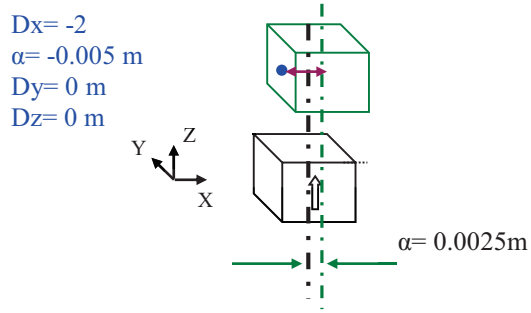


Fig. 10. Localization of the torque calculation point.

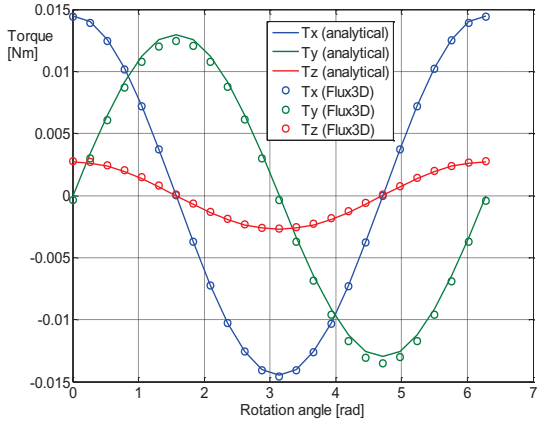


Fig. 11. Torque calculation at Dx = -0.005 m, Dy = 0 m and Dz = 0 m, as function of rotation angle θ.

## V. CONCLUSION

This paper presents a new contribution in analytical torque calculations for cuboidal permanent magnets with inclined polarizations from any position. These investigations allow the direct calculation of many systems working by the forces or the torques between magnetized cuboidal elements (magnetic bearings, Halbach arrays…). These results can also be used for many other calculations, like complex shapes of magnets which can be replaced by a combination of several parallelogram ones.

## REFERENCES

[1] H. Allag and J.-P. Yonnet, "3-D analytical calculation of the torque and force exerted between two cuboidal magnets," *IEEE Trans. Magn.*, vol. 45, no. 10, pp. 3969-3972, Oct. 2009.

[2] J. L. G. Janssen, J. J. H. Paulides, J. C. Compter, and E. A. Lomonova, "Three-dimensional analytical calculation of the torque between permanent magnets in magnetic bearings," *IEEE Trans. Magn.*, 46, 1748 (2010).

[3] H. Allag, J.-P. Yonnet, and M. E. H. Latreche, "Analytical calculation of the torque exerted between two perpendicularly magnetized magnets," *Journal of Applied Physics*, 109, 07E701 (2011).

[4] E. P. Furlani, "Formulas for the force and torque of axial couplings," *IEEE Trans. Magnetics*, vol. 29, no. 5, pp. 2295-2301, Sept. 1993.

[5] G. Akoun and J.-P. Yonnet, "3D analytical calculation of the forces exerted between two cuboidal magnets," *IEEE Trans. Magn.*, vol. MAG-20, no. 5, pp. 1962-1964, Sept. 1984.

[6] J.-P. Yonnet, H. Allag, and M. E. H. Latreche, "2D and 3D analytical calculations of magnet interactions," in *Proc. MmdE Conf.*, Bucharest, June 15-16, 2008.

[7] H. Allag and J.-P. Yonnet, "3D analytical calculation of interactions between perpendicularly magnetized magnets application to any magnetization direction," *Sensor Lett.*, vol. 7, no. 3, pp. 486-491, Aug. 2009.

# Design of Wide Stopband Narrow-Band BPFs Exhibiting Harmonic Suppression

**Sh. Amiri [1], N. Khajavi [2], and M. Khajavi [2]**

[1] Scientific Member of E.E. Department
Iranian Research Organization for Science and Technology (IROST), Tehran, Iran
amiri@irost.ir

[2] Faculty of E.E. Department of Dezful Branch
Islamic Azad University, Dezful, Iran
N_khajavi89@yahoo.com, Zefins2011@yahoo.com

***Abstract*** ─ This paper presents narrow-band bandpass filters with wide stopband for WLAN and WiMAX systems. First, open-stub and T-shaped resonators were used to design a filter ($F_1$) with the center frequency 2.4 GHz. In order to examine the architectures of the proposed resonators, their frequency responses were compared to the response of an LC model. Next, Defected Ground Structure (DGS) was utilized to achieve a wide stopband within the frequency response of $F_1$. Then, the structure of $F_1$ (without using DGS) only with some changes in the dimensions of the resonators was employed to design the narrow-band filters $F_2$ and $F_3$ with the center frequencies 3.7 GHz and 5.1 GHz, respectively. Advantages of these filters include simplicity, architectural symmetry, tenability for applications at other frequency, and proper bandwidth. The filters also provide optimal return loss and insertion loss.

***Index Terms*** ─ Defected Ground Structure (DGS), narrow-band, open-stub resonators, T-shaped resonators, upper-stopband.

## I. INTRODUCTION

High-quality compact bandpass filters are among the common elements in wireless communication systems. Wide-stopband filters are used in nonlinear elements such as power amplifiers or mixers for rejecting noise or unwanted interference in the stopband. Bandpass filters with wide stopbands may be designed for different frequencies. There are different techniques for designing narrow-band filters with wide stopbands. For example, ring resonators have been used to eliminate the second harmonic in a bandpass filter with the center frequency 2.6 GHz. This narrow-band filter, however, does not have an acceptable insertion loss [1]. DGS has been used to improve the filter parameters, including its bandwidth. Dumbbell-Shaped DGS (DS-DGS) was implemented at the ground structure [2]. A bandpass filter with the center frequency 2.4 GHz has been designed by coupling two open-loop DGS slot resonators with microstrip resonators [3]. DGS technique has also been implemented on bandpass filter structures to examine how this technique impacts the results [4]. An LC model has been developed for microstrip lines [5,6].

This paper presents narrow-band bandpass filters with wide stopbands for WLAN and WiMAX applications. Open-stub and T-shaped resonators were used to design the architecture of the filters. The frequency responses of these structures were compared to the frequency response of the LC model in order to examine the architecture of the proposed resonators. For the first filter ($F_1$) with the center frequency 2.4 GHz, DGS was applied to improve the width of the stopband. Next, it has been shown that due the simplicity and symmetry in the architecture of this filter, two other filters with the center frequencies 3.7 GHz and 5.1 GHz can be constructed only by modifying the dimensions of the resonators.

*Submitted On: February 27, 2014*
*Accepted On: September 6, 2014*

## II. DESIGNING FILTER $F_1$

Open-stub resonators and a combination of these resonators with T-shaped resonators were used in designing $F_1$, and then the stopband of this filter was extended using DGS.

### A. Designing open-stubs resonators

The conductive pattern shown in Fig. 1 was employed in designing the proposed resonator. Using open-stub resonators placed in parallel to each other (the resonators are connected through a middle stub), the basic resonator architecture shown in Fig. 2 (a) was obtained.

As seen in the frequency response of the basic resonator (Fig. 2 (b)), this architecture has a resonance frequency of 2 GHz, an insertion loss of -0.22 dB, and a return loss of -32.88 dB. The presence of a neutral harmonic at 5.46 GHz limits the stopband. In addition, the center frequency of this architecture does not match the WLAN frequency. The dimensions of the basic resonator are: L1=5.3 mm, W1=0.1 mm, L2=6.4 mm, W2=0.1 mm, L3=20.06 mm, W3=0.1 mm and G1=0.15 mm.

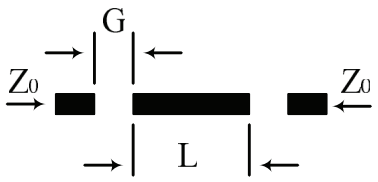


Fig. 1. The conductive pattern.

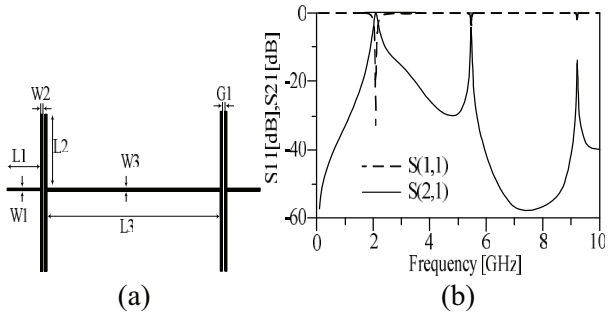


Fig. 2. (a) Basic structure of the proposed resonator, and (b) frequency response of basic structure of the proposed resonator.

### B. Analysis of proposed resonator circuit

Before going into the circuit analysis for the proposed resonator, it is quite useful to understand how this resonator functions in terms of wave reflections. The proposed resonator depicted in Fig. 2 (a) uses a capacitor-coupled bipolar stripline resonator. The gap width G1 was selected based on the required capacitance in series connection. The capacitance Cg1 was selected so that a large reactance ($X_C$) is provided within the frequency range of interest. Larger values of $X_C$ lead to narrower-band filters. Since this reactance is connected in series, large values of $X_C$ create large wave reflections. Overall reflection resulting from such a capacitor coupling depends on the spacing between the capacitors. The proposed bandpass resonator shown in Fig. 2 (a) was designed as follows. For the resonance frequency 2 GHz and the bandwidth 3 dB (167 MHz), the calculated value for $Q_L$ (equation (2)) is 11.976, and using Fig. 3 the value of $\overline{X}_{cr}$ is about 4. Equation (1) can be used to obtain the exact value of $\overline{X}_{cr}$ [7]:

$$Q_L = \frac{\overline{X}_{Cr}}{4}\sqrt{\overline{X}_{Cr}^2+4}\left(\Pi - \arctan\frac{2}{\overline{X}_{Cr}^2}\right). \quad (1)$$

For a filter with the resonance frequency $f_0$ and the bandwidth BW, $Q_L$ can be obtained using:

$$Q_L = \frac{f_o}{BW}. \quad (2)$$

Equation (3) was used to calculate $\phi_r$, the electrical length of the transmission line $L_3$:

$$\phi_r = \Pi - \arctan\left(\frac{2}{\overline{X}_{Cr}}\right). \quad (3)$$

The value obtained for the electrical length of the transmission line $L_3$ is $\varphi_r = 153.435^\circ$.

According to equation (4), condition for zero fall is fallowing:

$$2\cos\varphi_r = -\overline{X}_{cr}\sin\varphi_r. \quad (4)$$

According to the values obtained for $\overline{X}_{cr}$ and $\phi_r$, 4 draws the relationship is established. Since $\overline{X}_c \approx \overline{X}_{cr}$ is in the frequency range of interest for narrow band frequency characteristics, the value for $\overline{X}_c$ is 4. Using equation (5) and the value of $Z_0$=50 Ω, the calculated value for the reactance ($X_C$) is 200 Ω:

$$\overline{X_C} = \frac{X_C}{Z_0}. \quad (5)$$

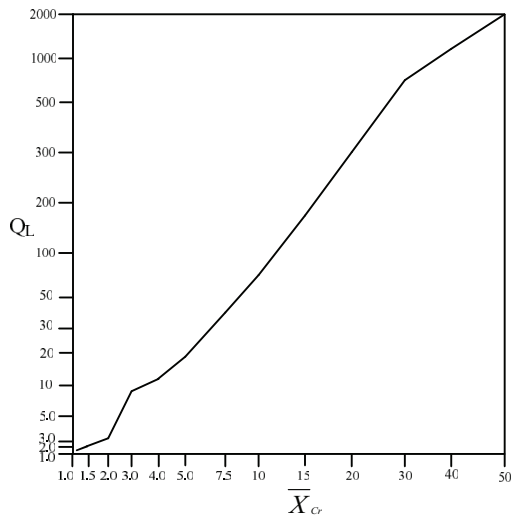


Fig. 3. $Q_L$ was evaluated as a function of $\overline{X}_{cr}$ bandpass filters [7].

### C. Designing model LC proposed resonator

The conductive pattern shown in Fig. 4 was used to obtain an equivalent circuit for the transmission line. Equivalent circuit for the transmission line of the conductive pattern is presented to further examine the basic resonator.


Fig. 4. Equivalent circuit for the transmission line of the conductive pattern.

The effective dielectric constant $\varepsilon_{ref}$ and characteristic impedance $Z_C$ are used to identify the characteristics of microstrip lines [8]. For substrate R04003 with the thickness H=0.508 mm and a microstrip line with the width W (the width of microstrip lines are presented in Fig. 2), $\varepsilon_{ref}$ can be obtained from (6) [7]:

$$\begin{aligned} \varepsilon_{ref} &= \frac{\varepsilon_r+1}{2} + \left\{1+12\left(\frac{H}{W}\right)^{-0.5} + 0.04\left(1-\frac{W}{H}\right)^2\right\} & \frac{W}{H} \le 1 \\ \varepsilon_{ref} &= \frac{\varepsilon_r+1}{2} + \frac{\varepsilon_r-1}{2}\left(1+12\frac{H}{W}\right)^{-0.5} & \frac{W}{H} \ge 1 \end{aligned}. \quad (6)$$

Equation (7) is used to calculate $C_a$ [7]. $\varepsilon_r$ is the dielectric constant of free space. $C_a$ is capacitance per unit length for an air substrate:

$$\begin{aligned} C_a &= \frac{2\pi\varepsilon_r}{Ln\left(\frac{8H}{W}+\frac{W}{4H}\right)} & \frac{W}{H} \le 1 \\ C_a &= \varepsilon_r\left(\frac{W}{H}+1.393+0.66Ln\left(\frac{W}{H}+1.444\right)\right) & \frac{W}{H} \ge 1 \end{aligned}. \quad (7)$$

L and C are derived from (8). For this purpose, one should first calculate Phase velocity $V_P$ and characteristic impedance $Z_C$ ($c \simeq 3.0\times10^8$ m/s):

$$Z_C = \frac{120\pi}{\frac{C_a}{\varepsilon_r}\sqrt{\varepsilon_{ref}}}, \quad V_P = \frac{c}{\sqrt{\varepsilon_{ref}}},$$

and

$$L = \frac{Z_C l}{V_P}, \quad C = \frac{l}{Z_C V_P}. \quad (8)$$

In this model (Fig. 5 (a)), Lt1 represents the stubs which connect the ports to the basic resonator, while Lt2 shows the stub connecting open-stub resonators. The gap between the open-stub resonators is denoted by Cg1. The grounded capacitor Cop and the inductor Lop were used to model the open-stub resonators. The LC model is shown in Fig. 5 (a).

Comparison of the frequency response of the LC circuit with the simulation results indicates a proper match between the center frequencies of both frequency responses shown in Fig. 5 (b). The values of inductance and capacitance for the LC model are: Lt1=3 nH, Lt2=8.3 nH, Lop=0.95 nH, Cop=0.5 pF and Cg1=0.37 pF. Table 1 presents the relationships between Cg1, the LC model, the gap between the two open-stub resonators, and the parameters of the frequency response of $F_1$. Cg1 decreases as G1 increases. This shows an inverse relationship between the resonator gap and its equivalent capacitance. The center frequency shifts toward higher frequencies and return and insertion losses become smaller, which is not optimum.

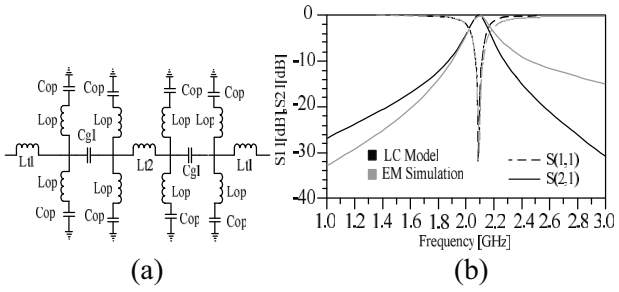


Fig. 5. (a) The LC model of the basic structure, and (b) frequency response of the LC model and EM simulation of the basic structure.

Table 1: The relationship between gap of the two open-stub resonators with LC parameters, and the parameters of the frequency response

| Filter $F_1$ | G1=0.15 mm | G1=0.17 mm | G1=0.19 mm | G1=0.21 mm | G1=0.23 mm |
|---|---|---|---|---|---|
| Cg1 | 0.37 pF | 0.33 pF | 0.31 pF | 0.29 pF | 0.27 pF |
| $F_0$ | 2 GHz | 2.11 GHz | 2.12 GHz | 2.13 GHz | 2.14 GHz |
| $S_{21}$ | -0.22 dB | -0.24 dB | -0.27 dB | -0.3 dB | -0.34 dB |
| $S_{11}$ | -32.88 dB | -30.7 dB | -29.97 dB | -28.35 dB | -27.3 dB |

### D. Designing model T-shape resonators

In the next step, T-shaped resonators were used to improve the stopband and to obtain a center frequency which is consistent with IEEE 802.11a (Fig. 6 (a)).

The arrangement of the T-shaped resonators has created a deep zero at 5.4 GHz. Frequency response of T-shape structure resonators is shown in Fig. 6 (b). The dimensions of the T-shaped resonators are: W4=0.247 mm, L4=10.266 mm, W5=1.08 mm, L5=5.74 mm, W6=0.70 mm, L6=1.98 mm and G2=0.24 mm.

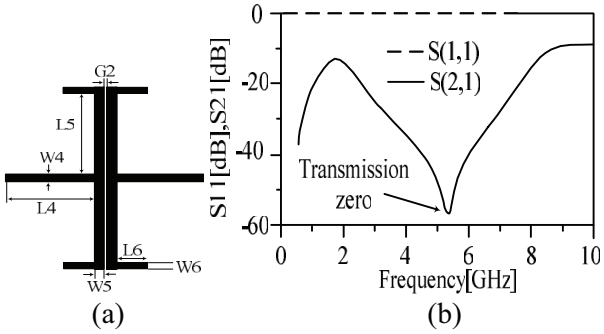


Fig. 6. (a) T-shape structure resonators, and (b) frequency response of T-shape structure resonators.

### E. Designing model LC T-shape resonators

Again, an LC model was used to examine these T-shaped resonators. In this model, the microstrip lines are modeled based on their corresponding indices using inductors and capacitors. Cg2 represents the gap between the T-shaped resonators. The open-ended sections are grounded through a capacitor and the transmission lines are modeled by inductors. The model is shown in Fig. 7 (a).

The values of the capacitance and inductance are: L4=0.85 nH, L5=1.45 nH, L6=0.5 nH, C6=0.5 pF and Cg2=0.1 pF. A comparison of the frequency response of the LC model for the T-shaped resonators and the associated EM simulation indicates a good match between the two simulations as seen in Fig. 7 (b).

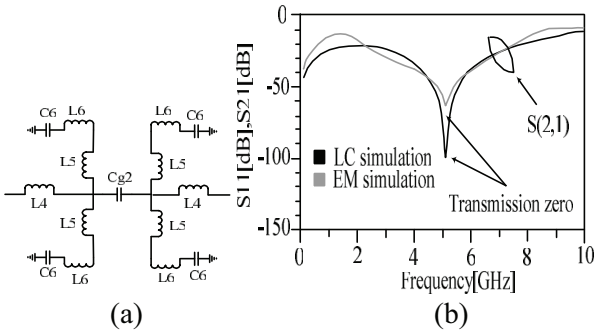


Fig. 7. (a) The LC model of the T-shape structure resonators, and (b) frequency response of the LC model and EM simulation of the T-shape structure resonators.

### F. Coupling between two resonators

The presence of a deep zero at 5.4 GHz along with a frequency response with a pole at the same frequency cancels the effect of the zero and the pole at this frequency, thereby widening the stopband. This can be seen in Fig. 8. This results in a center frequency of 2.69 GHz, an insertion loss of -4.36 dB, and a return loss of -2.5 dB, which show a considerable drop in losses compared to the frequency response obtained for open-stub resonators.

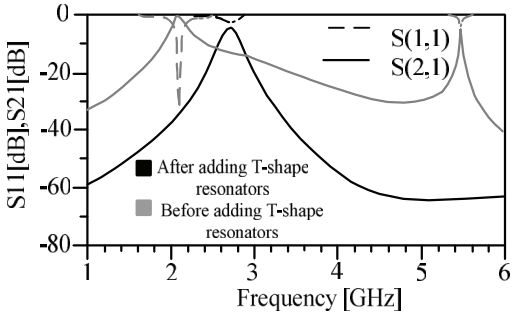


Fig. 8. Comparison of frequency basic structure before and after adding the T-shaped resonators.

In fact, the final architecture of filter $F_1$ was obtained by putting together the open-stub

resonators and the T-shaped resonators. The architecture is shown in Fig. 9 (a).

Desirable center frequency, insertion loss, return loss, and bandwidth were achieved by changing the dimensions of different parts of the open-stub and T-shaped resonators. The dimensions of the filter structure $F_1$ are: W1=0.1 mm, L1=3.06 mm, W2=0.34 mm, L2=6.50 mm, W3=0.1 mm, L3=1.35 mm, W4=0.24 mm, L4=10.26 mm, W5=1.08 mm, L5=5.74 mm, W6=0.70 mm, L6=1.98 mm, G2=0.24 mm and G1=0.18 mm. As seen in the frequency response of $F_1$ (Fig. 9 (b)), return loss and insertion loss for this filter are 32.8 dB and -0.5 dB, respectively. In addition, the bandwidth of $F_1$ is 112 MHz. Another property of $F_1$ examined here is sharpness. The value of this parameter is 0.121 GHz. This low sharpness indicates that the frequency response is close to the desirable response. Figure 10 shows a schematic of constructed filter and a comparison of its frequency response to that of the simulation model. As seen in Fig. 10, the two responses are in close agreement. All simulations in this paper were implemented using Momentum simulator in ADS.

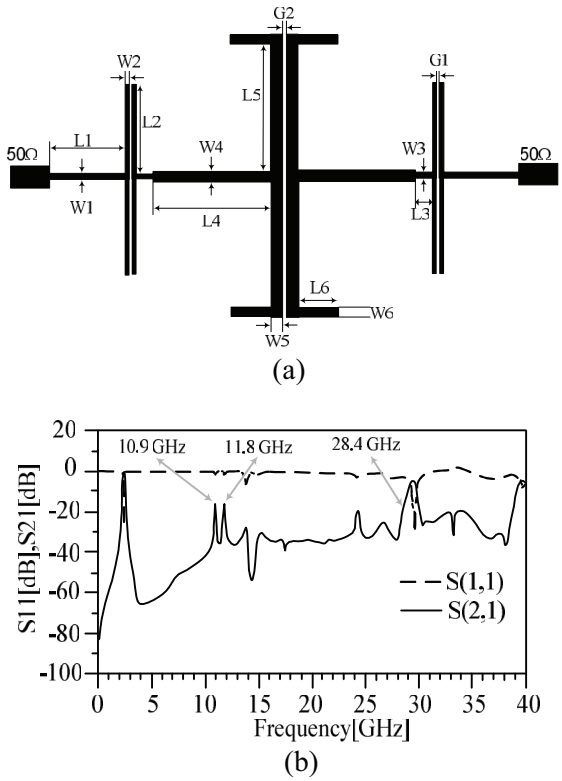


Fig. 9. (a) Structure of the filter $F_1$, and (b) frequency response of structure of the filter $F_1$.

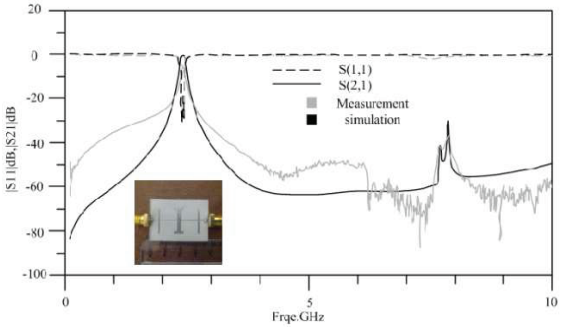


Fig. 10. Comparison of the results EM-simulation and measurement for filter $F_1$.

### G. Adding DGS to structure of the filter $F_1$

The presence of some harmonics at 10.9 GHz, 11.8 GHz, and 28.4 GHz in the frequency response of filter $F_1$ has limited the stopband. DGS was used to eliminate the neutral harmonics in the stopband and to widen this band. DGS technique was employed to create the dumbbell-shaped structure shown in Fig. 11. In Fig. 11 (a), the architecture is seen from above. Then in Fig. 11 (b), the substrate and dumbbell-shaped structure is seen from below. Figure 12 shown, compares the frequency responses of filter $F_1$ before and after applying DGS. Applying DGS shifts all the neutral harmonics in the stopband, up to the frequency 39 GHz, into the levels below -20 dB, thereby widening the stopband by 16.25 $F_0$.

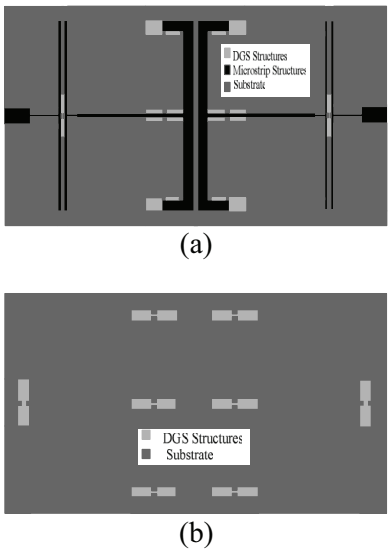


Fig. 11. (a) The architecture seen from above, and (b) the substrate and dumbbell-shaped structure seen from below.

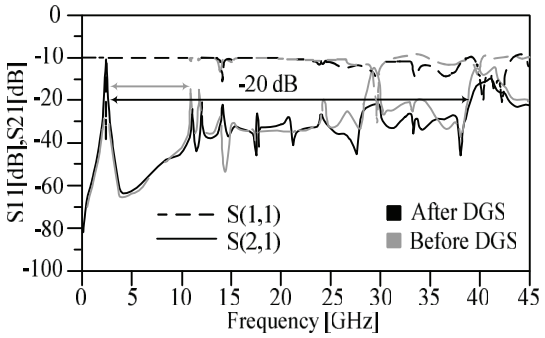


Fig. 12. Compares the frequency responses of filter $F_1$ before and after applying DGS.

According to the comparison presented in Table 2, DGS improves not only the stopband but also return loss and insertion loss.

Table 2: Comparison of the results for filter $F_1$ before and after applying DGS

| Filter $F_1$ | Center Frequency | Upper-Stop Band | Band Width | Return Loss (dB) | Insertion Loss (dB) |
|---|---|---|---|---|---|
| Before DGS | 2.42 GHz | 12 $F_0$ | 0.121 GHz | -33.35 | -0.521 |
| After DGS | 2.42 GHz | 16.25 $F_0$ | 0.121 GHz | -38.3 | -0.426 |

## III. DESINING FILTER WITH CENTER FREQUENCY 3.7 GHz AND 5.1 GHz

One objective in designing microstrip filters is to design small size architectures with high capabilities which are regarded as advantages of this type of architecture. These small and highly capable architectures can be designed by combining open-stub resonators with T-shaped resonators. Therefore, filter $F_2$ with the center frequency 3.7 GHz and filter $F_3$ with the center frequency 5.1 GHz were obtained simply by changing the dimensions of filter $F_1$. Filters $F_1$ and $F_3$ can be used in WLAN applications, while filter $F_2$ is suitable for WiMAX systems.

### A. Designing filter $F_2$

The architecture of this filter is the same as the architecture of filter $F_1$, therefore its dimensions are: W1=0.1 mm, L1=5.3 mm, W2=0.16 mm, L2=6.4 mm, W3=0.1 mm, L3=0.5 mm, W4=0.8 mm, L4=8.88 mm, W5=0.8 mm, L5=5.4 mm, W6=0.4 mm, L6=1.6 mm, G1=0.2 mm and G2=0.15 mm. The frequency response of the filter is shown in Fig. 13. As seen in this figure, filter $F_2$ has its center frequency at 3.7 GHz, a bandwidth of 214 MHz, an insertion loss of -0.42 dB and a return loss of -41.578 dB. Since $S_{21}$ is below -20 dB, for frequencies up to 11.79 GHz, the second and third harmonics are eliminated in filter $F_2$.

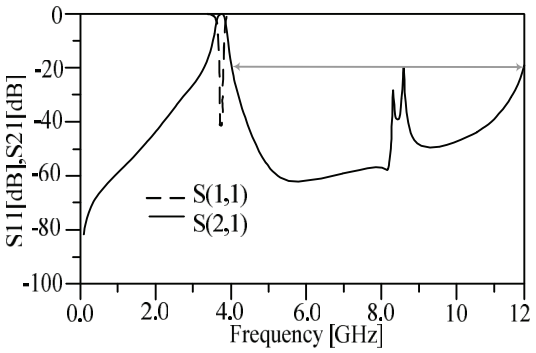


Fig. 13. Frequency response of the filter $F_2$.

### B. Designing filter $F_3$

The architecture of this filter is the same as the architecture of filter $F_1$, therefore its dimensions are: W1=0.1 mm, L1=4.69 mm, W2=0.12 mm, L2=4.48 mm, W3=0.1 mm, L3=0.76 mm, W4=0.56 mm, L4=6.16 mm, W5=0.616 mm, L5=3.66 mm, W6=0.397 mm, L6=1.12 mm, G1=0.14 mm and G2=0.105 mm.

The frequency response of this filter is shown in Fig. 14. As seen in this figure, filter $F_3$ has its center frequency at 5.1 GHz, a bandwidth of 423 MHz, an insertion loss of -0.318 dB and a return loss of -53.23 dB. Since $S_{21}$ is below -20 dB, for frequencies up to 16.27 GHz, the first and second harmonics are eliminated in filter $F_3$. Table 3 compares the results obtained for the filters designed in this paper.

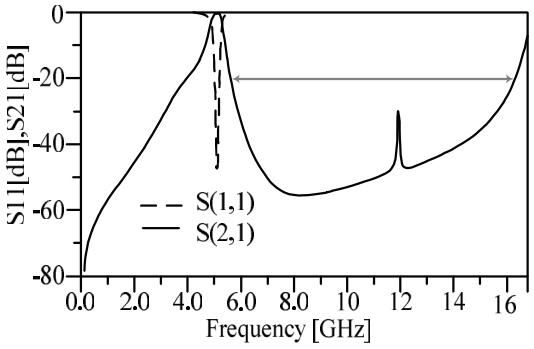


Fig. 14. Frequency response of $F_3$ filter.

Table 3: Final results for optimized architectures of the proposed microstrip single-band bandpass filters

| Filter Name | $F_1$ | $F_2$ | $F_3$ |
|---|---|---|---|
| Center Frequency (GHz) | 2.42 | 3.7 | 5.1 |
| Insertion Loss (dB) | -0.426 | -0.42 | -0.318 |
| Return Loss (dB) | -38.3 | -41.57 | -53.23 |
| Fractional Band Width (GHz) | 0.121 | 0.214 | 0.423 |
| Upper Stop Band (x $F_0$) | 16.25 | 3 | 2 |
| Size of the Filter (mm*mm) | 37.182*13.4 | 36.46*12.91 | 29.81*9 |

## IV. COUPLING COEFFICIENTS CALCULATED FOR THE THREE FILTERS

Effective coupling between the resonators was evaluated using coupling bandwidth [9]. In calculation of effective coupling for a narrowband filter we have:

$$K = \frac{W_2^2 - W_1^2}{W_2^2 + W_1^2} \approx \frac{W_2 - W_1}{W_0}, \quad (9)$$

$$W_0 = \frac{W_2 + W_1}{2}, \quad (10)$$

$$\Delta W_{12} = W_2 - W_1 = W_0 \times K. \quad (11)$$

Where K represents effective coupling, $\Delta W_{12}$ represents coupling bandwidth, and finally $W_1$ and $W_2$ are equal to resonator peak frequencies, and $W_0$ represents the center frequency. Bandwidth of an optimum filter is proportional to $\Delta W_{12}$. The data presented in Table 2 were used in these calculations. Given the center frequencies and bandwidths of the three filters, effective coupling for $F_1$, $F_2$, and $F_3$ is 0.05, 0.057, and 0.082, respectively.

## V.CONCLUSION

This paper presents narrow-band bandpass filters with wide stopband for WLAN and WiMAX applications. First, using parallel open-stub resonators connected by stubs, the frequency response of the basic resonator was obtained with the resonance frequency 2 GHz and a pole at 5.4 GHz. T-shaped resonators were placed next to open-stub resonators to cancel this pole, widen the stopband, and construct the final architecture for filter $F_1$. The T-shaped resonators create a deep zero at the same frequency, thereby cancelling the effect of this pole. To examine the architectures of the proposed resonators, the frequency responses of these architectures were compared with the frequency responses of their corresponding LC model. Then, narrow-band filters with the center frequencies 3.7 GHz and 5.1 GHz (for filter $F_2$ and filter $F_3$, respectively) were obtained simply by changing the dimensions of the resonators in the basic structure of filter $F_1$. Finally, DGS was utilized to achieve a wide stopband in the frequency response of filter $F_1$. An advantage of these filters is having a good bandwidth. In addition, these filters have optimal return loss and insertion loss.

## REFERENCES


[1] J. Fraresso and C. E. Saavedra, "Narrowband bandpass filter exhibiting harmonic suppression," *Electronics Letters*, vol. 39, no. 16, pp. 1189-1190, 2003.

[2] A. Kumar and M. V. Kartikeyan, "A design of microstrip bandpass filter with narrow bandwidth using DGS/DMS for WLAN," *2013 National Conference on Communications (NCC)*, New Delhi, India, pp. 1-4, 2013.

[3] P. Vagner and M. Kasal, "A novel bandpass filter using a combination of open-loop defected ground structure and half-wavelength microstrip resonators," *Radioengineering*, vol. 19, no. 3, pp. 392-396, 2010.

[4] M. Kufa and Z. Raida, "Comparison of planar fractal filters on defected ground substrate," *Radioengineering*, vol. 21, no. 4, pp. 1019-1024, 2012.

[5] M. Shobeyri and M. H. Vadjed Samiei, "Compact ultra-wideband bandpass filter with defected ground structure," *Progress In Electromagnetics Research Letters*, vol. 4, pp. 25-31, 2008.

[6] T. Yang, M. Tamura, and T. Itoh, "Compact hybrid resonator with series and shunt resonances used in miniaturized filters and balun filters," *IEEE Transactions on Microwave Theory and Techniques*, vol. 58, no. 2, pp. 390-402, 2010.

[7] P. A. Rizzi, "Microwave engineering: passive circuits," Book, *Prentice Hall PTR*, 1988.

[8] J. S. Hong and M. J. Lancaster, "Microstrip filters for RF/microwave applications," *Book* (Hong, et al., 2001), A Wiley-Interscience Publication, *John Wily & Sons, Inc*., 2001.

[9] A. C. Guyette, "Alternative architectures for

narrowband varactor-tuned bandpass filters," *Proceedings of the 4th European Microwave Integrated Circuits Conference*, Rome, Italy, pp. 28-29, September 2009.

**Shervin Amiri** is a Scientific Member of the Electrical Engineering Department of Iranian Research Organization for Science and Technology (IROST) in Tehran, I.R. Iran. He received the Associate Professor degree in 2013. His research interest fields are Antenna and RF subsystems in microwave and millimeter wave bands.

**Nafiseh Khajavi** received the M.Sc. degree in Electrical Engineering from Kermanshah Science and Research Branch Islamic Azad University, Kermanshah. Her research interests include microstrip filter, the analysis and design of high-frequency electronics and microwave passive circuits.

**Mahboubeh Khajavi** received the M.Sc. degree in Electrical Engineering from South of Tehran Branch Islamic Azad University. Her research interests include microstrip filter, the analysis and design of high-frequency electronics.

# Novel Phase Shifter Based on Dielectric Resonator on Liquid Crystal Substrate

**S. A. Attya [1], Nihal F. F. Areed [1,2], Mohamed Farhat O. Hameed [2], M. A. El-Razzak [1], and Salah Sabry A. Obayya [2]**

[1] Department of Electronics and Communications Engineering
Faculty of Engineering, Mansoura University, Mansoura 35516, Egypt
seham_abdo@mans.edu.eg, nahoolaf@yahoo.com, mabdelrazzak@hotmail.com

[2] Center for Photonics and Smart Materials
Zewail City of Science and Technology, Sheikh Zayed District, 6th of October City, 12566, Egypt
nfayez@zewailcity.edu.eg, mfarahat@zewailcity.edu.eg, sobayya@zewailcity.edu.eg

***Abstract*** ― In this paper, a novel design of microwave phase shifter with enhanced high level of flexible integration is proposed and analyzed using 3D finite difference time domain. The proposed design is based on the combination of dielectric resonators and nematic liquid crystal (NLC) layer of type E7. The effects of the structure geometrical parameters on the transmission angle are carried out. Based on the simulation results, optimizations of the geometries are curial for varying the phase of the transmitted signal. In addition, the use of NLC layers placed in silica pan as a substrate to the dielectric resonator offers a number of advantages over existing microwave phase shifters such as simple design, high bandwidth and phase tunability. Moreover, the suggested design has an excellent potential for being very useful in microwave encryption systems.

***Index Term*** ― Dielectric resonator filter, finite difference time domain, liquid crystal, phase shifter.

## I. INTRODUCTION

Dielectric resonator (DR) has primarily been used in microwave circuits, such as oscillators [1], filters [2], and recently as antenna [3]. The DR is normally made of high-permittivity material, with dielectric constant $\varepsilon_r > 20$. The unloaded Q-factor of the DR can be as high as 10,000 [4]. In addition, inexpensiveness, high power tolerance and high temperature stability can be achieved [5].

The DR structures are divided into two basic configurations: individual dielectric resonators that are loaded axially in metal enclosures, in which it is difficult to physically support the resonators [6-8], or individual resonators that are mounted in a planar configuration [9-12]. In the latter case, DRs are centered in position and mounted inside a filter housing using a support of low-dielectric-constant and low-loss material.

Phase shifters are one of the key elements for future reconfigurable radio frequencies (RF) devices. Widely known technologies include passive tunable dielectrics like barium-strontium-titanate (BST) [13], micro-electro-mechanical system (MEMS) [14] and semiconductor solutions are mostly based on varactor diodes [15]. Also, liquid crystal (LC) can give very promising opportunity to realize tunable RF devices. The LC material consists of anisotropic molecules, where by applying an external electrical field, the molecules of the LC type start to align along the field lines. The magnitude of the orientation is depending on the field strength. Due to the anisotropy of the molecules, this effect can be employed to tune the effective permittivity of the LC layer inside the device continuously [16].

This work represents new numerical finite difference time domain (FDTD) calculations of the transmission angle of the DR bandpass filter proposed by [17]. Simulation effects of the geometrical parameters on the transmission angle

*Submitted On: March 25, 2014*
*Accepted On: January 3, 2015*

are carried out. Based on the simulation results, optimizations of the geometries are crucial for varying the phase of the transmitted signal. A simple implementation of tunable phase shifter is proposed and based on inserting a thin layer of liquid crystal material of type E7 as a substrate in the considered DR structure. By this way, an electrical frequency dependent tunable phase shifter can be obtained. Furthermore, this work has opened up an entirely new direction for the usage of the presented phase shifter as a real time encryptor in various communication systems.

## II. DEVICE ARCHITECTURE

Figures 1 (a) and 1 (b) show 3-D view and front view of the conventional DR [17], respectively. As shown from the figure, the DR structure consists of two cylindrical dielectric discs made of ceramic type material ($Ca_5Ta_2Tio_{12}$) of $\varepsilon_r$ =38 separated by a distance $\zeta$. The two dielectric discs of radius $R$, and relative permittivity $\varepsilon_r$ act as coupled resonators such that the entire device becomes high quality bandpass filter which feed through two coaxial coupler. One of the coaxial coupler is used as an input port while the other is taken as the output port. These two ports are drilled on a metallic ground plane substrate of thickness $h$. The two dielectric discs are placed above the ground plane with an offset distance $d$ (air substrate height).

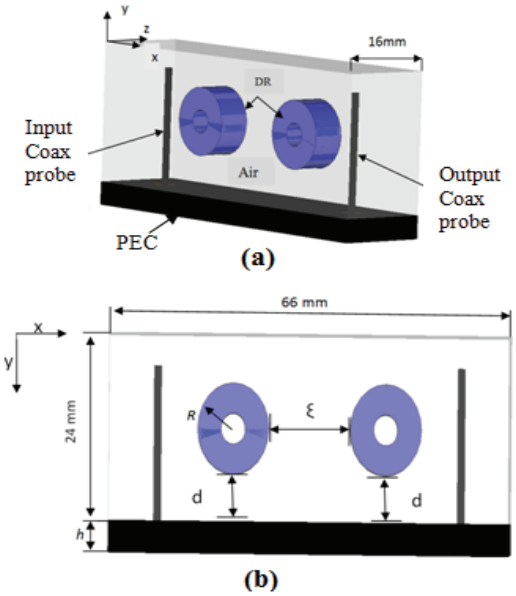


Fig. 1. DR geometry details: (a) 3D view, (b) front view.

## III. SIMULATION RESULTS

Firstly, 3D FDTD method is used to investigate the effects of the mesh size on the accuracy of the simulation results. In this study, the DR geometrical parameters are taken as $d$= 6 *mm*, $R$ = 5.85 mm, and $\zeta$ = 13.5 mm, $h$ = 3.9 mm, $\varepsilon_r$ = 38. In addition, the substrate has dimensions of 66×16 mm and the surrounding space has dimensions of 66×24×16 mm. Figure 2 (a) shows the variation of $S_{21}$ parameter with different mesh densities. It can be noted from this figure that to keep a reasonable accuracy, this structure should be discretized with a mesh cell size equal to λ/35 or less. Figure 2 (b) shows variation of magnitude of $S_{21}$ and frequency calculated by finite integration time domain (FITD) [17], and that obtained by FDTD [18-20] at different mesh densities. It is evident from the figure that there is a good agreement between the presented results and the published results by [17] where, the operating resonant frequency for the considered bandpass filter is equal to 4.525 GHz.

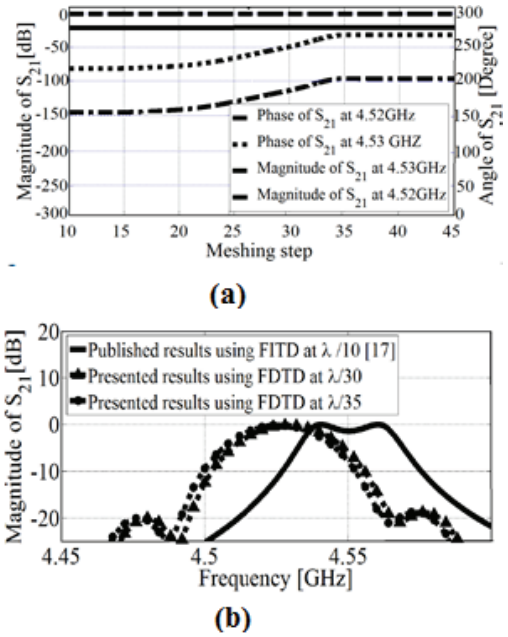


Fig. 2. Simulation of DR: (a) transmission coefficients vs. meshing step, (b) magnitude of $S_{21}$ vs. frequency.

The effect of the structure geometrical parameters that may affect the angle of the transmission signal to the output coaxial port is investigated. In this study, the initial parameters are

chosen to be $h$ = 3.9 mm, $R$ = 5.85 mm, $d$ = 6 mm, and $\zeta$ = 13.5 mm. It should be noted that, the numerical simulations reveal that to maintain bandpass performance, the ranges of $h$, $R$, $d$, and $\zeta$ are chosen to be (1:11), (5.85:5.87), (4:8), (10:17) in mm, respectively.

First, the effect of the ground plane thickness ($h$) on the transmission angle is studied while the other parameters $d$, $R$, and $\zeta$ are kept constant at their initial values. Figure 3 (a) shows the calculated $S_{21}$ angle for different values of the ground plane thickness ($h$) at two different frequencies, 4.52 GHz and 4.53 GHz. It can be noted from this figure that the phase of $S_{21}$ ($\theta$) decreases linearly as ground plane thickness increases and this linear relation can be equated as follows:

$$\Theta = -Ah+B, \quad (1)$$

where the calculated value of A is around 16.87 and the value of B is variable that depends on the resonant frequency. The correlation coefficient $r^2 \approx 1$ between the fitting data and the original data indicates that a linear approximation is a good fit to this data. The small variability in the data and the large number of data points have resulted in a small standard deviation of $5\times10^{-4}$ between an angle-estimate for a given value of $h$. It should be noted that, any positive or negative output phase can be easily obtained by changing the ground plane thickness. For example, at the operating frequency 4.52 GHz, the phase +90º and the complementary phase -90º can be easily obtained by using ground planes of thickness 1 mm and 11 mm, respectively. These obtained phase values can be used in encryption.

Next, the effect of the outer radius ($R$) of the dielectric disc on the transmission angle is studied while the other parameters $d$, $h$, and $\zeta$ are kept constant at 6 mm, 3.9 mm, and 13.5 mm, respectively. Figure 3 (b) shows the calculated angle of $S_{21}$ as a function of $R$ at two different frequencies 4.52 GHz and 4.53 GHz. It is evident from the figure that, the phase of $S_{21}$ decreases with increasing the outer radius of the dielectric disc, and this linear relation is estimated as follows:

$$\Theta = -AR+B, \quad (2)$$

where the calculated value of A is around 3465.8 and the value B is a variable that depends on the resonant frequency. The correlation coefficient $r^2 = 0.9988$ between the fitting data and the original data indicates that a linear approximation is a good fit to this data. The large variability in the data and the large number of data points have achieved a small standard deviation of 0.6868 between an angle-estimate for a given value of $R$.

It should be noted from Fig. 3 (b), that at the operating frequency 4.52 GHz, the phase +90º can be easily obtained by setting the outer radii of the two dielectric discs to 5.855 mm.

The effect of air substrate height ($d$) on the transmission angle is also investigated while the other parameters $R$, $h$, and $\zeta$ are kept constant at 5.85 mm, 3.9 mm, and 13.5 mm, respectively. The correlation coefficient $r^2$ = 0.9 between the fitting data and the original data indicates that a parabolic approximation is a good fit to this data. The small variability in the data and the large number of data points have resulted in a small standard deviation of 0.14597 between an angle-estimate for a given value of $d$. Figure 3 (c) shows the calculated angle of $S_{21}$ for different values of air substrate height ($d$) at two different frequencies, 4.52 GHz and 4.53 GHz. It can be found form the figure that, the relation between them follows a parabolic shape where the phase decreases by increasing the offset distance $d$ from 4 to 6 mm, while the phase increases with increasing offset distance from 6 to 8 mm.

The effect of the separation distance between the two dielectric discs ($\zeta$) on the transmission angle is also studied while the other parameters $R$, $h$, and $d$ are kept constant. Figure 3 (d) shows the numerical analysis of $S_{21}$ for different values of ($\zeta$) at two different frequencies, 4.52 GHz and 4.53 GHz. It is evident from this figure that, the phase values of $S_{21}$ tend to be constant with increasing the value of $\zeta$. The correlation coefficient $r^2$ = 0.994 between the fitting data and the original data indicates that a parabolic approximation is a good fit to this data. The small variability in the data and the large number of data points have produced in a small standard deviation of 0.133925 between an angle-estimate for a given value of $\zeta$.

Based on the above geometrical study, -90º

phase shifters at the operating frequency 4.52 GHz with allowable bandwidth of 1 MHz can be obtained using the considered structure shown in Fig. 1 with $R$ = 5.87 mm while the other parameters $d$, $h$ and $\zeta$ are taken as 6 mm, 10.9 mm and 13.5 mm, respectively. Further, +90° phase shift can be obtained at $R$ to be 5.8525 mm, as shown in Fig. 4 (a). Also, physical movement of the dielectric discs above the ground plane results in tunable phase shifter with allowable range -21° to 21° at the operating frequency 4.53 GHz when dielectric disc is moved above the ground plane with dielectric discs radius of 5.87 mm, as shown in Fig. 4 (b).

Figures 4 (c) and 4 (d) show the steady state z-polarized magnetic field distributions along the *xy*-plane at frequencies of 4 GHz and 4.53 GHz, respectively. It is evident from these figures that, the field along the structure is highly confined at port 1 at $f$ = 4 GHz, while at $f$ = 4.53 GHz the field propagates from port 1 to port 2. These field distributions confirm the behavior of $S_{21}$ shown earlier in Figs. 4 (a) and 4 (b). Figure 4 (e) demonstrates the steady state distributions of the *z*-polarized magnetic field along the propagation $x$ direction at the wavelength of 10.7 mm for the chosen ground plane thicknesses $h$ = 0.9 mm and 10.9 mm, respectively. It can be observed from the figure that, the transmitted signal at $h$ = 10.9 mm overrides the transmitted signal at $h$ = 0.9 mm by about $\ell = \lambda/2$, which clearly fits with the behavior of the argument of $S_{21}$ shown in Fig. 4 (a).

The designed phase shifter has some limitation such as complexity of design, implementation and physical movement which is obtained using an electrically driven actuator. The actual configuration can vary considerably from 'trombone' transmission lines adjusted by stepper motor to dielectric/capacitive loading adjusted with solenoid/piezo-electric actuators. The most common is the 'trombone' type and these are usually associated with high-precision bench top test equipment, rather than high volume use [21].

By using values in Fig. 4 (a), the proposed phase shifter can be used as asymmetric hardware key for data encryption and decryption as referenced by Nihal, *et al*. [22]. The phase of the audio data can be encoded by adding a constant phase shift 90° within the frequency band of the signal. However, complementary phase shift -90° will be added to decode the signal. The accuracy of retrieved signal is estimated through root mean squared error (RMS) calculations which equals to $3.6333\times10^{-4}$.

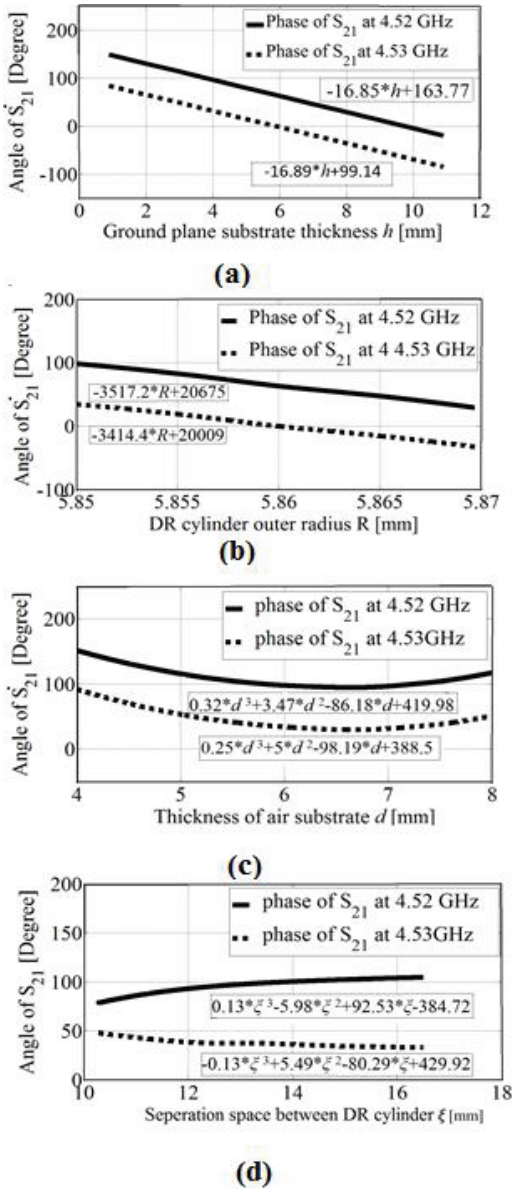


Fig. 3. Effect of geometrical parameters on the phase of $S_{21}$: (a) ground plane thickness, (b) dielectric disc outer radius, (c) thickness of air substrate, and (d) separation between two dielectric discs.

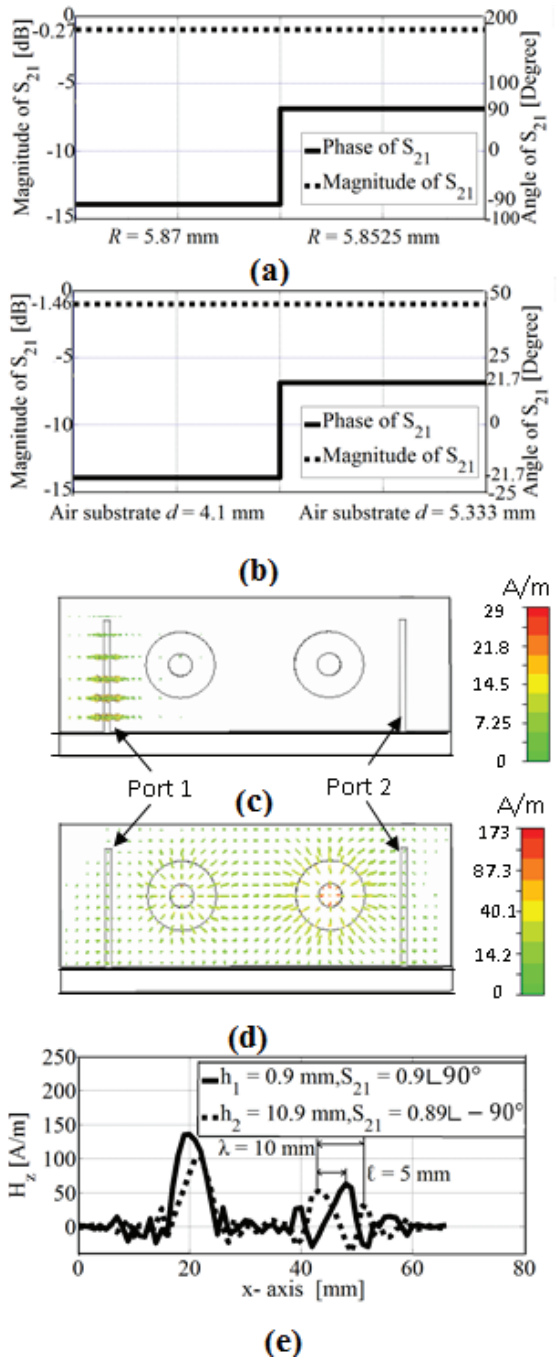


Fig. 4. (a) Simulated $S_{21}$ at 4.52 GHz, (b) simulated $S_{21}$ at 4.53 GHz, (c) 2D z-magnetic field along *xy*-plane at 4 GHz, (d) 2D z-magnetic field along *xy*-plane at 4.53 GHz, and (e) 1D z-magnetic field along *x-axis* at y = -10.3 mm and z = 8 mm.

It is observed from the analysis that the designed phase shifter has some limitation such as mechanical variations. In this study, liquid crystals layer can be used as a substrate to the considered dielectric resonator instead of air to obtain an electrical tunable phase shifter as shown in Fig. 5. The LC consists of anisotropic molecules. The rod-shaped molecules tend to align themselves along the surface. When applying an external electrical field, the molecules of the LC start to align along the field lines. The magnitude of the orientation is depending on the field strength. Due to the anisotropy of the molecules, this effect can be employed to tune the effective permittivity of the LC layer inside the device continuously [16,22-24]. The LC has two principal refractive indices, ordinary refractive index $n_o$ and extraordinary refractive index $n_e$. The first one, $n_o$, is measured for the light wave where the electric vector vibrates perpendicular to the optical axis (ordinary wave). However, the index $n_e$ is measured for the light wave where the electric vector vibrates along the optical axis (extraordinary wave). Then the birefringence ($\Delta n$) is given by:

$$\Delta n = n_e - n_o. \quad (3)$$

The nematic liquid crystal (NLC) used in the proposed structure is of type E7 with relative permittivity tensor $\underline{\varepsilon_r}$ [22-24]:

$$\varepsilon_r = \begin{pmatrix} n_o^2 \sin^2\varphi + n_e^2 \cos^2\varphi & (n_e^2 - n_o^2)\cos\varphi\sin\varphi & 0 \\ (n_e^2 - n_o^2)\cos\varphi\sin\varphi & n_o^2\cos^2\varphi + n_e^2\sin^2\varphi & 0 \\ 0 & 0 & n_o^2 \end{pmatrix}, \quad (4)$$

where φ is the molecule rotation angle.

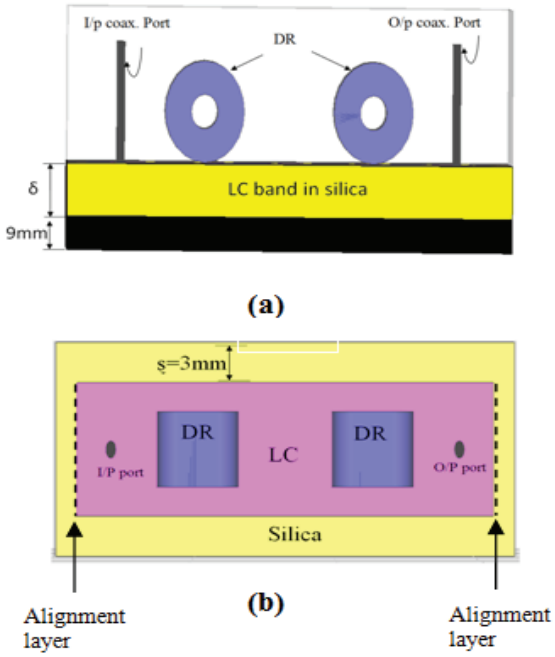


Fig. 5. Electrical tunable phase shifter structure: (a) front view, (b) top view.

Glass cavity filled with LC of type E7 is used as a substrate for the considered dielectric resonator. Two alignment layers along the *x*-axis have to be used to align the molecules along the y-axis (unbiased state), as shown in Fig. 5.

The effect of varying the thickness of the unbiased liquid crystal ($\delta$) on the phase of the transmitted wave has been studied as shown in Fig. 6 (a). As shown in this figure, liquid crystal thickness below 3 mm results in bandstop filter. If the thickness is further increased beyond 3 mm, bandpass filter will be obtained. By changing the biasing state of the LC, the applied voltage across the biasing layers along the *x*-axis rotates the LC molecules. At saturation the director is oriented perpendicular to the cell wall along *x*-axis, with rotation angle $\varphi = 90^o$. It should be noted that changing the biasing voltage will vary the phase of the transmitted signal. Hence, using liquid crystal with thickness 8 mm and changing the rotation angle ($\varphi$) of its molecules from 0º to 90º, the phase will be changed from -26º to -6º, respectively, as shown in Fig. 6 (b). Moreover, changing the positions of electrodes will vary the phase of the transmitted signal. Figures 6 (b) and 6 (c) show the numerical results of $S_{21}$ for two different electrodes positions: along y-axis and along z-axis, respectively. It should be noted from these figures, that the position of electrodes along the z-axis results in phase shifter with wide tunable range from 6º to 83º for different biasing voltage at LC with thickness 4 mm, as shown in Fig. 7 (a).

Figures 7 (b) and 7 (c) show the steady state z-polarized magnetic field distributions along the *xy* plane at frequencies of 4 GHz and 4.53 GHz, respectively. It is evident from these figures that, the field along the structure is highly confined at port 1 at $f$ = 4 GHz, while at $f$ = 4.53 GHz the field propagates from port 1 to port 2. These field distributions confirm the behavior of $S_{21}$ shown earlier in Fig. 6 (a). Figure 7 (d) demonstrates the steady state distributions of the *z*-polarized magnetic field along the propagation *x* direction at the wavelength of 9 mm for the chosen LC thicknesses $\delta$ = 4 mm with placing electrodes along *x*-axis at $\varphi = 0^o$ and $\varphi = 90^o$. It can be observed from the figure that, the transmitted signal at $\varphi = 90^o$ overrides the transmitted signal at $\varphi = 0^o$ by about $\ell = \lambda/4.5$, which clearly fits with the behavior of the argument of $S_{21}$ shown in Figs. 6 (a) and 7 (a).

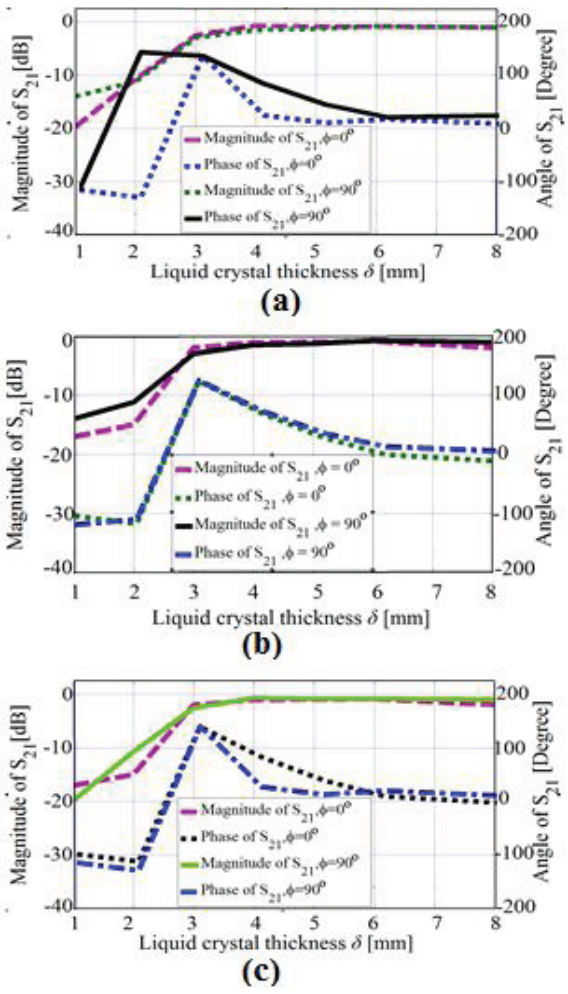


Fig. 6. Transmitted S-parameter vs. LC thickness at different electrode positions: (a) along x-axis, (b) along y-axis, and (c) along z-axis.

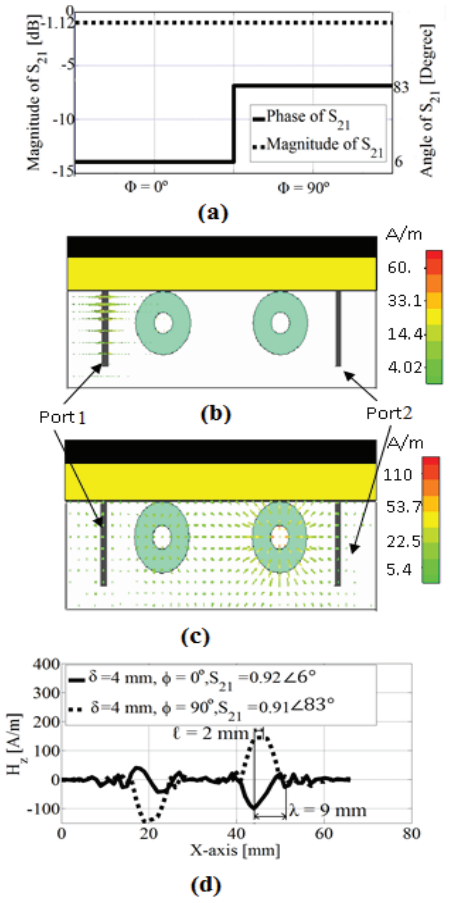


Fig. 7. (a) Electrical tunable phase shifter results for LC thickness of $\delta$ = 4 mm and the electrodes are positioned along *x*-axis, (b) 2D z-magnetic field along *xy*-plane at 4 GHz, (c) 2D z-magnetic field along *xy*-plane at 4.53 GHz, and (d) 1D z-magnetic field along *x-axis* at y = -10.3 mm and z = 8 mm.

It is evident from Fig. 8 that, the phase and magnitude of $S_{21}$ will be decreased 66.5% and 2235%, respectively by increasing the wall thickness of the silica pan by around 50% from its original value (3 mm to 4.5 mm). However, the phase and magnitude of $S_{21}$ will be decreased by 33.93% and 20.3%, respectively, by decreasing the silica pan wall thickness from 3 mm to 1.5 mm. This means that the performance of the suggested phase shifter is sensitive to the silica pan thickness. Figures 8 (c) and 8 (d) show the steady state z-polarized magnetic field distributions along the *xy*-plane at frequencies of 4 GHz and 4.53 GHz, respectively. It is evident from these figures that, the field along the structure is highly confined at port 1 at $f$ = 4 GHz, while at $f$ = 4.53 GHz the field propagates from port 1 to port 2. These field distributions are compatible with the behavior of $S_{21}$ shown earlier in Figs. 8 (a) and 8 (b). Figure 8 (e) demonstrates the steady state distributions of the *z*-polarized magnetic field along the propagation *x* direction at the wavelength of 9 mm for the chosen silica pan wall thickness $\wp$ = 1.5 mm and $\wp$ = 4.5 mm, respectively with LC thicknesses $\delta$ = 4 mm. It can be observed from the figure that, the transmitted signal at $\wp$ = 4.5 mm overrides the transmitted signal at $\wp$ = 1.5 mm by about $\ell = \lambda/6$, which clearly fits with the behavior of the argument of $S_{21}$ shown in Fig. 8 (b).

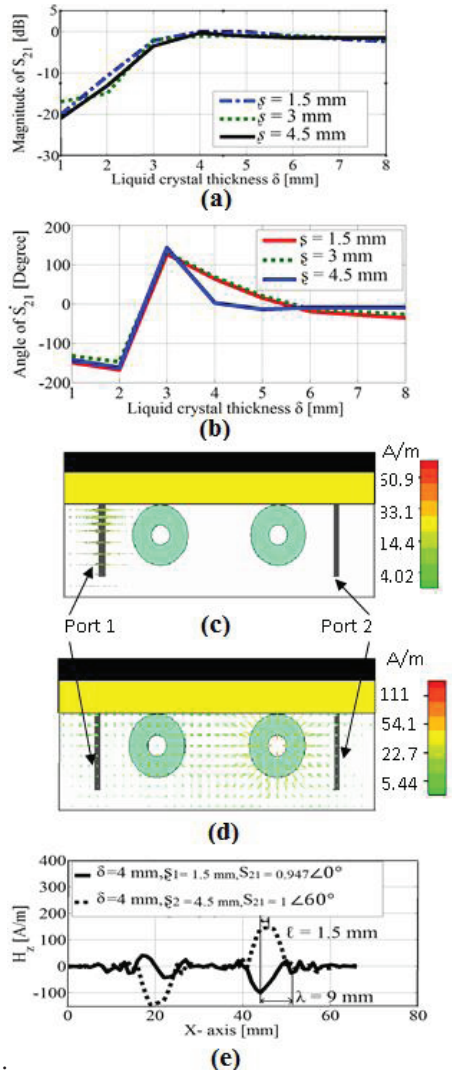


Fig. 8. Silica pan thickness variation at $\varphi$ = 0º: (a) magnitude of $S_{21}$, (b) phase of $S_{21}$, (c) 2D z-magnetic field along *xy*-plane at 4 GHz, (d) 2D z-magnetic field along *xy*-plane at 4.53 GHz, and (e) 1D z-magnetic field along *x-axis* at y = -10.3 mm and z = 8 mm.

## IV. CONCLUSION

The scope of this paper is to present a new simple design, highly compact and tunable phase shifter for different microwave applications. The proposed design is based for the first time to the best of our knowledge on the combination of dielectric resonators and nematic liquid crystal layer of type E7. Parametric study has been carried out to investigate the different geometrical parameters that affect the angle of $S_{21}$. Based on the simulation results, tunable phase shifter based on physical movement of the dielectric discs above the ground plane has been presented. However, the proposed novel design based on the use of NLC layers placed in silica pan as a substrate to the dielectric resonator overcomes the complexity of the phase shifter using physical movement. The suggested design has an excellent potential for being very useful in microwave encryption systems.

## REFERENCES


[1] L. Zhou, Y. W. Yin, J. Wang, and S. L .Wu, "Dielectric resonators with high Q-factor for tunable low phase noise oscillators," *IEEE Trans. Components, Packaging and Manufacturing Tech.*, vol. 3, pp. 1008-1015, 2013.

[2] H. Hu and K.-L. Wu, "A $TM_{11}$ dual-mode dielectric resonator filter with planar coupling configuration," *IEEE Trans. Microwave Theory Tech*., vol. 61, pp. 131-138, 2013.

[3] A. A. Kishk and W. Huang, "Size-reduction method for eielectric-resonator antennas," *IEEE Field, Waves, and Electromagnetics*, vol. 53, pp. 26-38, 2011.

[4] M. Memarian and R. Mansour, "Quad-Mode and Dual-Mode Dielectric Resonator Filters," *IEEE field, waves, and electromagnetics*, vol. 57, pp. 3418 - 3426, 2009.

[5] R. Saliminejad and M. R. Ghafourifard, "A novel and accurate method for designing dielectric resonator filter," *Progress In Electromagnetics Research B*, vol. 8, pp. 293-306, 2008.

[6] S. B. Cohn, "Microwave bandpass filters containing high-Q dielectric resonators," *IEEE Trans. Microwave Theory Tech*., vol. 16, pp. 218-227, 1968.

[7] S. J. Fiedziuszko, "Dual-mode dielectric resonator loaded DR cavity filters," *IEEE Trans. Microwave Theory Tech*., vol. 30, pp. 1311-1316, 1982.

[8] K. Wakino, T. Nishikawa, and Y. Ishikawa, "Miniaturization technologies of dielectric resonator filters for mobile communications," *IEEE Trans. Microwave Theory Tech*., vol. 42, pp. 1295-1300, 1994.

[9] R. R. Mansour, "Filter technologies for wireless base stations," *IEEE Microwave Magazine*, vol. 5, pp. 68-74, 2004.

[10] R. Vahidieck, "Design and development of high-Q microwave filters-past, present and future," *IEEE African*, vol. 2, pp. 1099-1104, 1999.

[11] C. Wang, H.-W. Yao, K. A. Zaki, and R. R. Mansour, "Mixed modes cylindrical planar dielectric resonator filters with rectangular enclosure," *IEEE Trans. Microwave Theory Tech*., vol. 43, pp. 2817-2823,1995.

[12] I. C. Hunter, J. D. Rhodes, and V. Dassonville, "Dual mode filters with conductor-loaded dielectric resonators," *IEEE Trans. Microwave Theory Tech*., vol. 47, pp. 2304-2311, 1999.

[13] G. Velu, K. Blary, L. Burgnies, A. Marteau, G. Houzet, D. Lippens, and J. Carru, "A 360° BST phase shifter with moderate bias voltage at 30 GHz," *IEEE Trans. Microwave Theory Tech*., vol. 55, no. 2, pp. 438-444, Feb. 2007.

[14] B. Pillans, S. Eshelman, A. Malczewski, J. Ehmke, and C. Goldsmith, "Ka-band RF MEMS phase shifters," *IEEE Microwave Guided Wave Letters*, vol. 9, pp. 520-522, 1999.

[15] R. Coats, J. Klein, S. Pritchett, and D. Zimmermann, "A low loss-monolithic five-bit pin diode phase shifter," *IEEE M1T-S International Microwave Symposium Digest*, vol. 2, pp. 915-918, 1990.

[16] M. F. O. Hameed and S. S. A. Obayya, "Highly nonlinear birefringent soft glass photonic crystal fiber with liquid crystal core," *IEEE Photonic Tech.*, vol. 23, pp. 1478-1480, 2011.

[17] http://www.cst.com/Content/Applications/Article/ArticlePDF.aspx?articleId=30.

[18] D Pinto and S. S. A. Obayya, "Improved complex-envelope alternating-direction-implicit finite-difference-time-domain method for photonic-bandgap cavities," *J. of Light Wave Tech*., vol. 25, no. 1, pp. 440-447, 2007.

[19] M Rajarajan, S. S. A. Obayya, B. M. A. Rahman, K. T. V. Grattan, and H. A. El-Mikali, "Characterization of low-loss waveguide bends with offset-optimisation for compact photonic

integrated circuits," *J. of Optoelectronics, IEE Proceedings*, vol. 147, no. 6, pp. 382-388, 2000.

[20]N Somasiri, B. M. A. Rahman, and S. S. A. Obayya, "Fabrication tolerance study of a compact passive polarization rotator," *J. of Light Wave Tech*., vol. 20, no. 4, pp. 751-757, 2002.

[21]N. Tucker, *Very Low Cost Electro-Mechanical Phase Shifter*, Technical Notes, 2010.

[22]N. F. F. Areed and S. S. A. Obayya, "Multiple image encryption system based on nematic liquid photonic crystal layers," *J. of Light Wave Tech*., vol. 32, no. 7, pp. 1344-1350, Jan. 2014.

[23]N. F. F. Areed and S. S. A. Obayya, "Novel all-optical liquid photonic crystal router," *J. of IEEE, Photonics Technology Letters*, vol. 25, no. 13, pp. 1254-1257, May 17, 2013.

[24]G. Ren, P. Shum, X. Yu, J. Hu, G. Wang, and Y. Gong, "Polarization dependent guiding in liquid crystal filled photonic crystal fibers," *Elsevier, Opt. Commun*., vol. 281, pp. 1598-1606, 2008.

# A Compact UWB Printed Monopole Antenna with Triple-Band Notched Characteristics

**Aref Abdollahvand [1], Abbas Pirhadi [1], Mohammad Rasoul Hosseinnezhad [2], and H. Ebrahimian [3]**

[1] Department of Electrical Engineering
Shahid Beheshti University G.C. (SBU), Tehran, +98, Iran
a.abdollahvand@mail.sbu.ac.ir

[2]A Lecture of Islamic Azad University, Meshkin Shahr Branch, +98, Iran

[3] Department of Biomedical Engineering
Islamic Azad University, Ardabil Branch, Ardabil, Iran

***Abstract*** ─ A compact triple band-notched printed monopole antenna for ultra-wideband (UWB) application is presented. By inserting two triangular-shaped notches in both sides of the ground plane of microstrip feed line, additional resonances are excited and the bandwidth is increased up to 160%. Three sharp notched frequency bands at 3.8 GHz, 5.5 GHz, and 7.5 GHz are achieved by embedding a pair of rectangular-shaped slits in the ground plane and two pairs of modified bow-shaped slits in the patch. This novel monopole antenna has ultra-wide frequency bandwidth for input impedance, compact size (24 mm × 20 mm), low cost fabrication and Omni-directional H-plane radiation pattern which makes it suitable for ultra-wideband applications. The measured results reveal that the presented triple band-notched monopole antenna is a promising candidate for UWB communication systems to avoid interference with WiMax band (3.3-3.7 GHz), some C-band (3.7-4.2 GHz), WLAN (5.15-5.825 GHz) bands and some C-band satellite communication systems (7-8 GHz).

***Index Terms*** ─ Bow-shaped slits, printed monopole antenna, rectangular-shaped slits, triangular-shaped notch.

## I. INTRODUCTION

Ultra-wideband technology has undergone many significant developments in recent years. However, there still remains many challenges in improving this technology to its full potential [1]. Several printed monopole antennas have been proposed recently [2-6], to cover the UWB frequency band 3.1 GHz to 10.6 GHz allocated by the Federal Communications Commission (FCC) for UWB applications [7]. However, this will cause interference to other existing wireless systems WiMAX (3.3-3.7 GHz), WLAN (5.15-5.825 GHz), terrestrial microwave and satellite communications in C-band (3.7-4.2 GHz). Hence, UWB antennas with band-notches are required to avoid harmful interference to other existing communications systems. Some UWB antennas with band-notch have been reported in the literature [8-12]. A recently reported antenna has been designed by making use of two split resonant rings (SRR) to obtain dual band-notch characteristic [13]. In [14], dual band-notch is achieved by using a U-slot in the ground plane and an E-slot in the radiation patch. In [15], the dual notched bands are achieved by embedding a pair of Γ-shaped stubs in the radiation patch and a modified G-slot defected ground structure in the feed line.

The dual band-notch characteristic is achieved by etching a single tri-arm resonator below the patch in [16]. The F-shape feed line is designed to achieve dual notch band characteristic in [17]. In [18], by inserting a novel parasitic strip in trapezoidal slot and a pair of L-shaped slots in metallic ground, dual band-notched characteristics

*Submitted On: July 9, 2014*
*Accepted On: November 14, 2014*

are obtained. In [19], for a notched frequency band, two L-shaped slits are embedded on the ground plane. In [20], the desired band-notch antenna is achieved by etching a narrowband triple complementary split-ring resonator into the radiating element of an existing UWB antenna. However, most of the existing antennas can generate no more than two notched bands.

In this paper, in addition to increase the bandwidth of the UWB monopole antenna, a novel triple band-notched monopole antenna is proposed. To increase the bandwidth, two triangular-shaped notches are inserted on the ground plane. Three notched frequency bands are achieved by embedding two pairs of modified bow-shaped slits in the radiation patch and a pair of rectangular-shaped slits in the ground of microstrip feed line. The simulation results using the Ansoft-HFSS show that for VSWR<2, this antenna covers 2-18 GHz frequency band with three notched band of (3.3-4.2 GHz), (5.15-5.95 GHz), and (7-8 GHz). Section 2 presents the details of the antenna structure. Full wave analysis of the proposed antennas in frequency domain is obtained by using Ansoft HFSS which is based on Finite Element Method. The VSWR and far field results obtained are presented in Section 3.

## II. ANTENNA DESIGN

The configuration of the proposed ultra-wideband antenna is depicted in Fig. 1. The basic monopole antenna structure consists of a circular patch, a microstrip feed line, and a ground plane. The design of the proposed antenna starts by choosing the dimensions of the designed antenna. This antenna is printed on an FR4 microwave substrate with a size of $W_{sub}\times L_{sub}=20\times 24$ mm$^2$, thickness of 1.6 mm, and relative dielectric constant of 4.4. In the next step in the design of the proposed antenna, the radius of the circular patch is calculated. Radius of the circular patch has a lot of effects on the antenna bandwidth. As this parameter decreases, so does the antenna bandwidth, and vice versa. This parameter is approximately $\lambda_{lower}/4$, where $\lambda_{lower}$ is the lower bandwidth frequency wavelength. $\lambda_{lower}$ depends on a number of parameters such as the monopole width as well as the thickness and dielectric constant of the substrate on which the antenna is fabricated. The patch is connected to a 50 Ω microstrip feed line of width $W_f$. The width of the microstrip feed line $W_f$ is fixed at 2 mm. The final step in the design of the proposed antenna is to choose the length of the band-notch slots. The circular radiating patch has two pairs of modified bow-shaped slits. On the other side of the substrate, a conducting ground plane with two triangular notches and a pair of rectangular-shaped slits is placed. In this design, the optimized length $L_{notch}$ is set to band-stop resonates at $0.25\lambda_{notch}$.

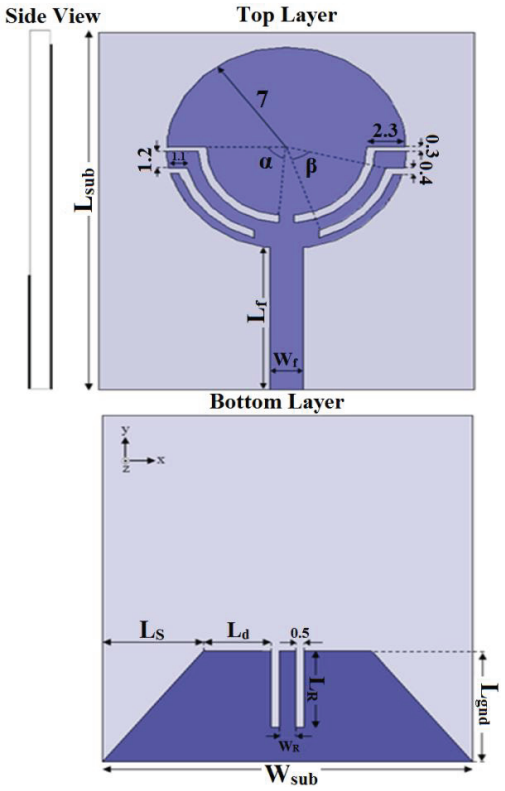


Fig. 1. Configuration and parameters of the proposed antenna (unit: mm).

By inserting two triangular-shaped notches in both sides of the microstrip feed line on the ground plane, additional resonances are excited and hence the bandwidth is increased up to 160%. The improvement in impedance matching over its entire bandwidth is attributed to the phenomenon of defected ground structure (DGS) with slits that creates additional surface current paths in the antenna. Moreover, this ground-plane structure changes the inductive and capacitive nature of the input impedance, which in turn leads to changes in bandwidth [4].

To achieve triple notches at central frequencies of 3.8 GHz, 5.5 GHz, and 7.5 GHz, two pairs of bow-shaped slits on the radiating patch and

rectangular-shaped slits in the ground plane are adopted. The antenna is symmetrical longitudinally. The optimal dimensions of the designed antenna are as follows: $L_{sub}$ = 24 mm, $W_{sub}$ = 20 mm, $L_f$ = 9 mm, α = 85$^0$, β = 60$^0$, $L_R$ = 6 mm, $W_R$ = 1 mm, $L_S$ = 6 mm, and $L_d$ = 3 mm. The width of the arms at bow-shaped slits in the radiation patch is set at 0.5 mm. The height of the feed gap between the main patch and the ground ($d$= $L_f$- $L_{gnd}$) is also an important parameter to control the impedance bandwidth [21]. The radiating patch has a distance of 1 mm to the ground plane with a length of $L_{gnd}$ = 8 mm printed on the back surface of the substrate.

## III. RESULTS AND DISCUSSIONS

The parameters of proposed antenna are studied by changing one parameter at a time and fixing the others. To fully understand the behavior of the antenna and to determine optimal parameter values, the antenna was analyzed using Ansoft's high-frequency structure simulator (HFSS™).

Figure 2 shows the effects of two triangular-shaped notches on the VSWR characteristics of the ordinary antenna. As illustrated in Fig. 2, the value of the $L_S$ is playing an important role in the wideband characteristics and in $L_S$ = 6 mm much wider impedance bandwidth is produced. $L_S$ can adjust the inductive and capacitive nature of the input impedance, and improves impedance bandwidth without any cost of size or expense. It is observed from the Fig. 2, that the designed antenna without the filter structures exhibits wideband performance from 2.2 GHz to 17.5 GHz for VSWR<2, covering the entire UWB frequency band.

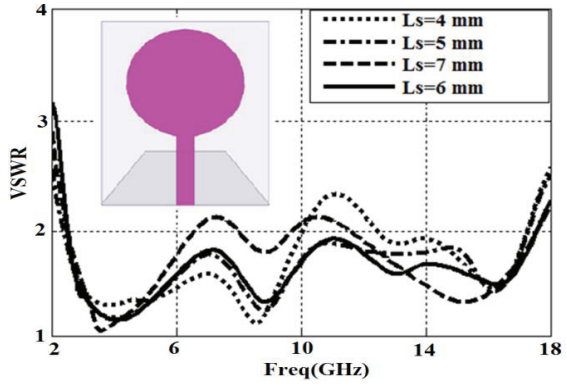


Fig. 2. Simulated VSWR characteristics of the ordinary antenna with different values of $L_S$.

Triple notched frequency bands are achieved by embedding two pairs of modified bow-shaped slits in the radiation patch and a pair of rectangular-shaped slits in the ground plane. As shown in Figs. 3 (a), 3 (b) and 3 (c), at the notch frequency, current flows are more dominant around the filter and are in opposite directions at interior and exterior edges. Hence, the resulting radiation fields are canceled out and high attenuation near the notch frequency is achieved. This means that the antenna does not radiate efficiently.

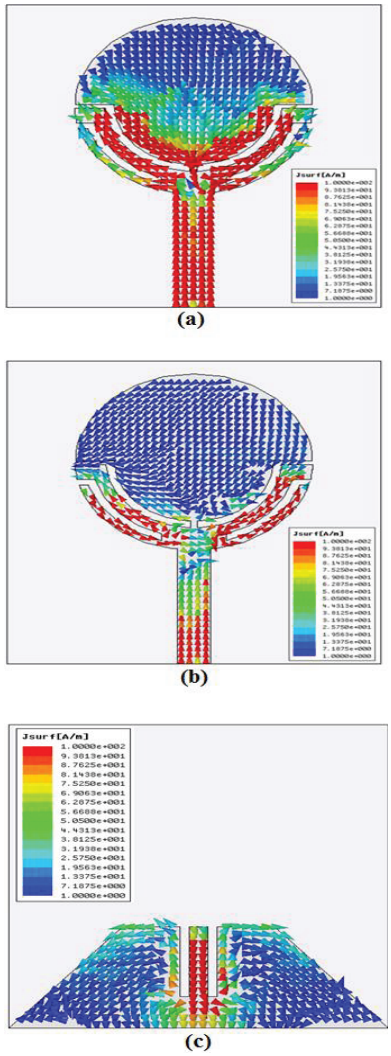


Fig. 3. Simulated surface current distributions on the radiating patch and ground plane for the proposed antenna at: (a) 3.8 GHz, (b) 5.5 GHz, and (c) 7.5 GHz.

Parametric analysis is made to further understand the antenna's behavior. The effects of

$L_S$, α, β, and $L_R$ parameters are studied in the bandwidth and notch band variations. Simulation results show that the bandwidth and notched frequencies are controllable by changing the length of these parameters. Various notched bands can be achieved by properly changing the parameters of the filter. The notch characteristics are mainly determined by α, β, and $L_R$. By adjusting the lengths of slots to about a quarter-wavelength at the center frequency of the desired notched-frequency band, the proposed UWB planar monopole antenna becomes non-responsive at that frequency band [21].

In the proposed structure, to increase the bandwidth and achieve triple notches at central frequencies of 3.8 GHz, 5.5 GHz, and 7.5 GHz, two triangular-shaped notches in both sides of the microstrip feed line on the ground plane and two pairs of bow-shaped slits on the radiating patch and rectangular-shaped slits in the ground plane are adopted. Each slots act as a resonator at their resonance or notch frequency. Resonant slot length, which is a multiple of quarter-wavelength, can be calculated approximately by $L_{total} \cong n\,\lambda_g/4$. For a desired notch frequency the wavelength is given by $\lambda_g = \lambda/\sqrt{\varepsilon_r}$, which $\lambda$ is the free space wavelength. In this design, a good start point for the length $L_{notch}$ is $\lambda_{notch}/4$, where $\lambda_{notch1}$, $\lambda_{notch2}$ and $\lambda_{notch3}$ corresponds to first band-notch frequency (3.8 GHz), second band-notch frequency (5.5 GHz), and third band-notch frequency (7.5 GHz) respectively. As shown in Figs. 4 (a) and 4 (b), the first and the second notch frequencies depend on the values of α and β, respectively. As illustrated in Fig. 4 (a), by increasing α from 60° to 88°, while maintaining other parameter values, the first notched band moves to a lower frequency. As shown in Fig. 4 (b), when β increases from 50° to 75°, the center frequency of 5.5 GHz notch band changes from 6 GHz to 4.4 GHz.

Figure 5 illustrates the simulated VSWR characteristics with various lengths $L_R$, and also shows that small changes in $L_R$ significantly affects the center frequency of 7.5 GHz notch band. As $L_R$ is increased from 3.5 to 7 mm, the center frequency of the notch band is changed from 12.7 GHz to 6.3 GHz. Hence, we conclude that notch frequencies are controllable by carefully choosing the values of α, β, and $L_R$. The results indicate that the antenna is a promising candidate for UWB communication systems to avoid interference with WiMax band (3.3-3.7 GHz), some C-band (3.7-4.2 GHz), WLAN (5.15-5.825 GHz) bands and some C-band satellite communication systems (7-8 GHz).

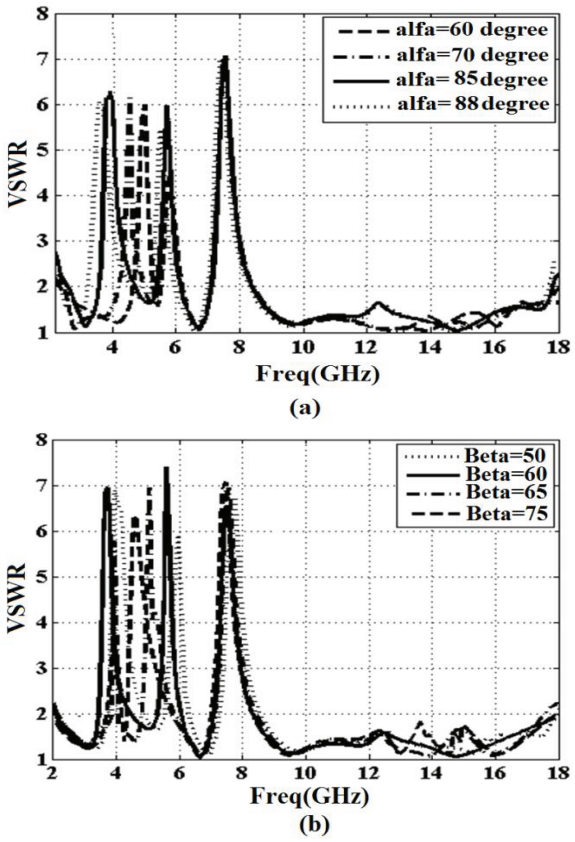


Fig. 4. Simulated band-rejection characteristics of the proposed antenna with notched bands for different values of α (a), and β (b).

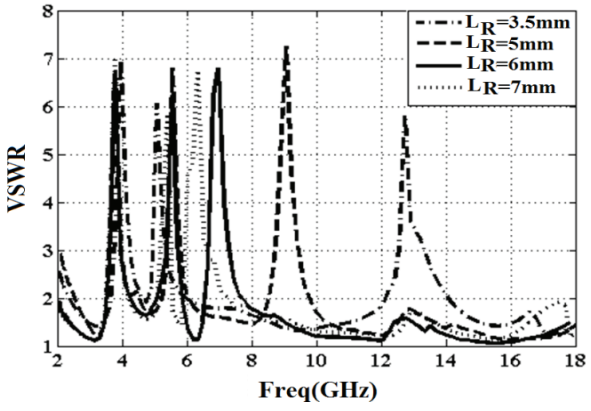


Fig. 5. Simulated band-rejection characteristics of the proposed antenna with notched bands for various $L_R$.

To verify the proposed design, a prototype of the antenna based on optimized dimensions has been fabricated, as shown in Fig. 6, which also shows the measured and simulated VSWR characteristics of the proposed antenna. Note that, there exists a discrepancy between measured data and the simulated results, which could be due to the SMA port.

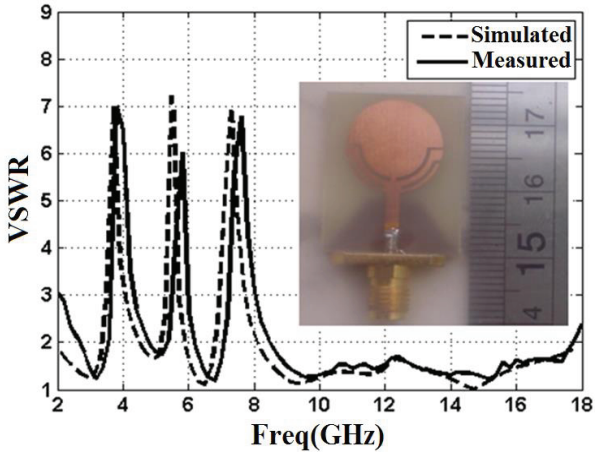


Fig. 6. Photograph of the fabricated prototype and comparison between measured and simulated VSWR for the proposed antenna.

In order to attain the VSWR characteristics for the designed antenna, the measurement and manufacturing processes need to be performed carefully. Note also that, the designed antenna with the filter structures exhibits three notch bands 3.3-4.2 GHz, 5.15-5.95 GHz and 7-8 GHz, which covers the 3.5/5.5-GHz (3.4-3.69/5.25-5.85 GHz) WiMAX bands, 5.2/5.8-GHz (5.15-5.35/5.725-5.825 GHz) WLAN bands and some C-bands, while maintaining wideband performance from 2 GHz to 18 GHz for VSWR<2, covering the entire UWB frequency band.

Figure 7 shows the measured radiation patterns of the fabricated antenna, obtained for the y-z plane (E-plane) and the x-z plane (H-plane) at 4, 7 and 10 GHz. The patterns in the H-plane are omnidirectional as expected, whereas in the E-plane, radiation patterns have a dumbbell shape. Cross-polarization levels are generally much lower than the co-polarization ones. Note that, the fabricated antenna actually radiates over a wide frequency band.

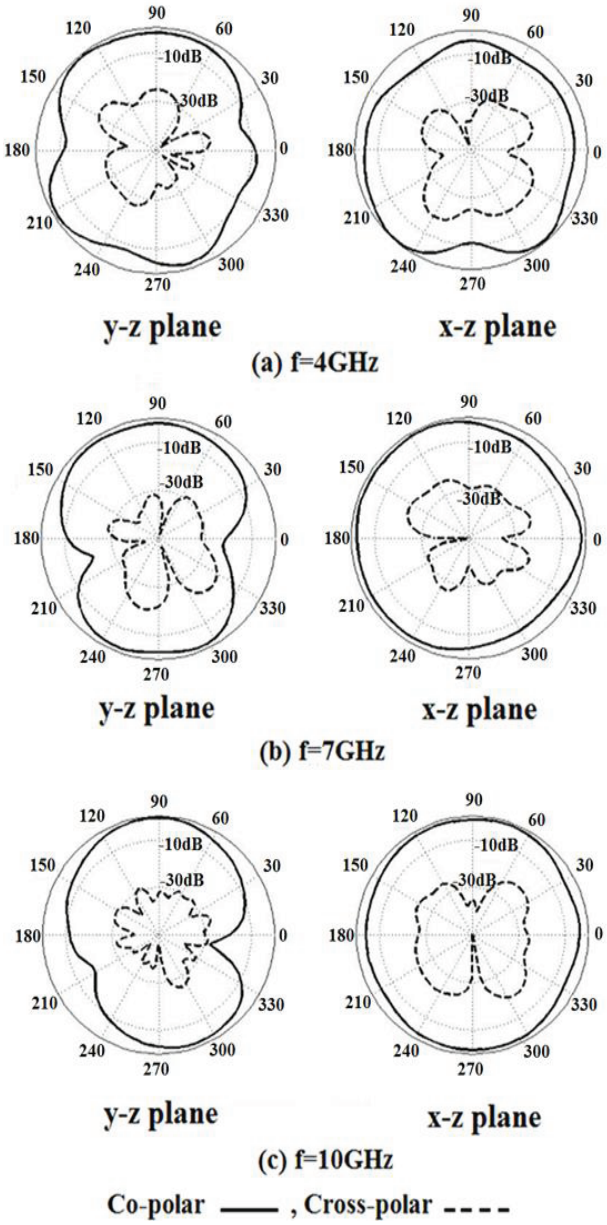


Fig. 7. Measured radiation patterns at frequencies: (a) 4 GHz, (b) 7 GHz, and (c) 10 GHz.

Figure 8 presents the measured peak antenna gain with and without filters. The figure indicates that the realized triple band notched antenna has good gain flatness, except in three notched bands. As desired, the antenna gain is decreased in the vicinity of 3.5 GHz, 5.5 GHz and 7.5 GHz. Outside the notch band, antenna gain is relatively constant (variations below 2.5 dB). Thus, the antenna exhibits stable gain across the operation band.

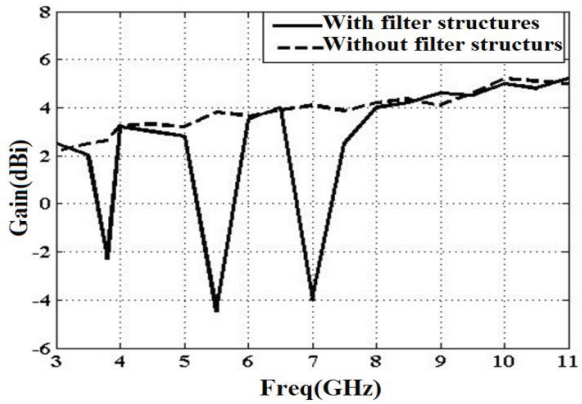


Fig. 8. Peak gain of the optimized UWB antenna with and without filter structures.

## IV. CONCLUSION

A novel compact printed monopole antenna with triple band-notched characteristics, suitable for UWB applications was presented and analyzed. We showed that by inserting two triangular-shaped notches on the ground plane with proper dimensions, a wide impedance bandwidth is achieved. Triple band-notches are achieved by embedding two pairs of bow-shaped slits in the radiation patch and a pair of rectangular-shaped slits in the ground plane. The radiation pattern of this antenna shows good omni-directional pattern throughout the UWB frequency range. The gain of the proposed antenna is almost flat in the operation frequency band with sharp notched bands.

## REFERENCES

[1] H. Schantz, *The Art and Science of Ultra Wideband Antennas*, Artech House, 2005.

[2] A. A. Eldek, "Numerical analysis of a small ultra wideband microstrip-fed tap monopole antenna," *Progress In Electromagnetics Research*, PIER 65, pp. 59-69, 2006.

[3] M. N. Moghadasi, G. R. Dadashzadeh, M. Abdollahvand, Y. Zehforoosh, and B. S. Virdee, "Planar triangular monopole antenna with multioctave bandwidth," *Microwave Opt. Technol. Lett.*, 53, pp. 10-14, 2011.

[4] M. Abdollahvand and G. R. Dadashzadeh, "Compact double-fed dual annular ring printed monopole antenna for UWB application," *Journal of Electromagnetic Waves and Applications*, vol. 23, no. 14-15, pp. 1969-1980, 2009.

[5] R. Zaker, C. Ghobadi, and J. Nourinia, "A modified microstrip-fed two-step tapered monopole antenna for UWB and WLAN applications," *Progress In Electromagnetics Research*, PIER 77, pp. 137-148, 2007.

[6] S. Yazdanifard, R. A. Sadeghzadeh, and M. Ojaroudi, "Ultra-wideband small square monopole antenna with variable frequency band-notch function," *Progress In Electromagnetics Research C*, vol. 15, pp. 133-144, 2010.

[7] Federal Communications Commission, *First Report and Order, Revision of part 15 of the commission's rule regarding ultra-wideband transmission system FCC 02-48*, Federal Communications Commission, Washington, DC, 2002.

[8] M. Abdollahvand, H. R. Hassani, and G. R. Dadashzadeh, "Novel modified monopole antenna with band-notch characteristic for UWB application," *IEICE Electronics Express (ELEX)*, vol. 7, no. 16, pp. 1207-1213, 2010.

[9] M. Abdollahvand, G. R. Dadashzadeh, and H. Ebrahimian, "Compact band-rejection printed monopole antenna for UWB application," *IEICE Electronic Express (ELEX)*, vol. 8, no. 7, pp. 423-428, 2011.

[10] J. R. Kelly, P. S. Hall, and P. Gardner, "Band-notched UWB antenna incorporating a microstrip open-loop resonator," *Antennas and Propagation, IEEE Transactions on*, vol. 59, pp. 3045-3048, 2011.

[11] Y. Sung, "UWB monopole antenna with two notched bands based on the folded stepped impedance resonator," *Antennas and Wireless Propagation Letters, IEEE*, vol. 11, pp. 500-502, 2012.

[12] L. X. Li, S. S. Zhong, and M. H. Chen, "Compact band notched ultra wide band antenna using defected ground structure," *Microwave and Optical Technology Letters*, vol. 52, pp. 286-289, 2010.

[13] J. Ding, Z. Lin, Z. Ying, and S. He, "A compact ultra-wideband slot antenna with multiple notch frequency bands," *Microw. Opt. Technol. Lett.*, vol. 49, no. 12, pp. 3056-3060, 2007.

[14] L. Luo, Z. Cui, J.-P. Xiong, X.-M. Zhang, and Y.-C. Jiao, "Compact printed ultra-wideband monopole antenna with dual band-notch characteristic," *Electron. Lett.*, vol. 44, no. 19, Sep. 2008.

[15] M. Abdollahvand, G. R. Dadashzadeh, and D. Mostafa, "Compact dual band-notched printed monopole antenna for UWB application," *IEEE Ant. and Wireless Propag. Lett*., vol. 9, pp. 1148-1151, 2010.

[16] R. Azim, M. T. Islam, and A. T. Mobashsher, "Dual band-notch UWB antenna with single tri-arm resonator," *Antennas and Wireless Propagation Letters, IEEE*, vol. 13, pp. 670-673, 2014.

[17] M. Rahimi, R. A. Sadeghzadeh, F. B. Zarrabi, and Z. Mansouri, "Band-notched UWB monopole

antenna design with novel feed for taper rectangular radiating patch," *Progress In Electromagnetics Research C*, vol. 47, pp. 147-155, 2014.

[18] A. Subbarao and S. Raghavan, "A novel ultra-wideband planar antenna with rejection of WLAN and ITU bands," *Applied Computational Electromagnetics Society (ACES) Journal*, vol. 28, no. 9, 2013.

[19] M. Mirmozafari, Ch. Ghobadi, H. Mirhedayati, A. Rezaee, "A planar UWB monopole antenna with on-ground slot band-notch performance," *Applied Computational Electromagnetics Society (ACES) Journal*, vol. 28, no. 8, 2013.

[20] D. Jiang, Y. Xu, R. Xu, "A microstrip printed band-notched UWB antenna using modified CSRR structure,"*Applied Computational Electromagnetics Society (ACES)* Journal, vol. 28, no. 6, 2013.

[21] H.-J. Zhou, Q.-Z. Liu, Y.-Z. Yin, and W. B. Wei, "Study of the band-notch function for swallow-tailed planar monopole antennas," *Progress In Electromagnetics Research*, PIER 77, pp. 55-65, 2007.

# Polarization Angle Independent Metamaterial Absorber in both of C- and X-Bands

**M. Karaaslan and A. O. Demirci**

Department of Electrical and Electronic Engineering
Mustafa Kemal University, Hatay, 31140, Turkey
mkaraaslan@mku.edu.tr, ademirci@mku.edu.tr

***Abstract*** ─ In this study, perfect metamaterial absorbers (MAs) based on circle- and square-shaped configurations that are numerically and experimentally designed and analyzed in both of C- and X-band. The proposed models have very simple designs and present perfect absorption for all polarization angles. A sensor application of the suggested model (for circle-shaped) is also presented to introduce further feature of the structure. Moreover, the suggested models can be easily reconfigured for THz and infrared frequency regimes to enable myriad potential applications such as sensors, defense systems and stealth in the next studies.

***Index Terms*** ─ Absorber, metamaterial, sensor.

## I. INTRODUCTION

Metamaterials have been rapidly a great deal of interest by the electromagnetic community due to present unusual EM properties, such as negative refraction. Also, they have many potential application areas such as sensing [1], cloaking [2], super lens [3], antenna [4], polarization rotator [5], and absorber [6]. These materials are manmade and can be artificially manufactured at the desired frequency regimes of the EM spectrum from MHz [7], GHz [8], sub-THz [9], THz [10], sub-PHz [11], near-IR [12] to the near optical frequency region [13].

Moreover, the concept of MA has great attention during the recent years by the researchers because of having crucial importance applications, especially for military areas. There are many MA studies in literature in order to achieve perfect absorption at a certain frequency range such as ultra-thin [14], extremely broad band [15], tunable [16], based on chiral metamaterial [17], multi-band [18], based on isotropic resonators [19]. Unlike the others, this study focuses on microwave absorber that has very simple design, easy fabrication and introduces wide band perfect absorption for all polarization angles and so on at certain frequency regime. Additionally, electric field and surface current distributions of the proposed model at the resonance frequencies are separately examined to realize its' physical operation mechanism. Obtained numerical and experimental results are realized and compared according to the other MA studies in literature.

## II. NUMERICAL AND EXPERIMENTAL SETUP OF THE PROPOSED MODEL

In order to achieve perfect absorption for all polarization angles, firstly we proposed two different symmetric geometric shaped, and then to have very simple designs and easy fabrication process, we created circle-with gap and square-shaped. After these processes, we optimized the aimed models of circle- with gap and square-shaped to obtain perfect absorption. So, the proposed structures are created with the best dimension values. The proposed resonators are designed of copper with the conductivity of 5.8001 S/m and thickness of 0.035 mm. The substrates are chosen as FR4 (flame resistant); thickness, loss tangent, and relative permittivity of 1.6 mm, 0.02 and 4.2, respectively. Figures 1 (a), 2 (a) and 1 (b), 2 (b) shows dimensions of the optimized resonators and numerical setups picture, in order. It can be seen that the periodic boundary conditions (x,y) with floquet port (z) are used in the simulation study for both of study. The numerical studies are performed with a commercial full-wave EM solver (CST

*Submitted On: March 9, 2014*
*Accepted On: December 6, 2014*

Microwave Studio) based on finite integration technique.

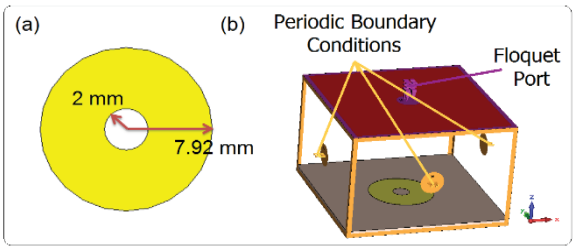


Fig. 1. Proposed perfect circle with gap-shaped MA: (a) dimensions, and (b) numerical setup.

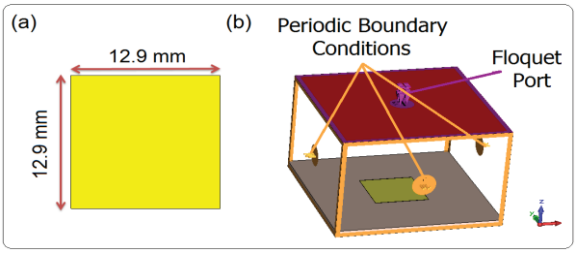


Fig. 2. Proposed perfect square-shaped MA: (a) dimensions, and (b) numerical setup.

The S-parameter (scattering parameter) defines device characteristics using the degree of scattering when an electromagnetic wave is applied. Scattering as a general term means reflection back to the incident direction or transmission to other directions. All linear characteristics of electromagnetic material or electronic device can be defined in terms of the degree of scattering (S-parameter).The input/output ports of a system can be numbered and the S-parameter is defined as Sij; i.e., "Incident at port j→ Obtained at port i." Reflection and transmission cases are valid when i=j and i≠j, respectively. Hence, in an n-port system, $n^2$ times S-parameters can be defined. Besides these S-parameters can be aligned as a matrix and referred as S-matrix (scattering matrix). The absorption behavior of the proposed MA can be calculated by $A(\omega)=1-R(\omega)-T(\omega)$, where $A(\omega),R(\omega)=|S_{11}|^2$ and $T(\omega)= |S_{21}|^2$ are the absorption, reflection, and transmission, in order. Therefore, to achieve perfect absorption, reflection and transmission EM waves must be very close to zero. This provided by impedance matching at the resonance frequency. It is well known that metamaterials can be characterized by a complex frequency dependent electric permittivity $\varepsilon(\omega)=\varepsilon_1(\omega)+i\varepsilon_2(\omega)$ and a complex frequency dependent magnetic permeability $\varepsilon(\omega)=\mu_1(\omega)+i\mu_2(\omega)$. Reflectivity can also be reduced (near-zero) when the effective permittivity $\varepsilon(\omega)$ and permeability $\mu(\omega)$ have minimum values. Therefore, $\varepsilon(\omega)$ and permeability $\mu(\omega)$ can properly be adjusted to absorb both the incident electric and magnetic fields to achieve perfect absorption [14-19].

After numerical results, the fabricated structure is also experimentally tested to verify numerical results. Therefore, the absorption measurement setup is installed. The measurement is carried out by using R&S ZVL6 Vector Network Analyzer (VNA) and two horn antennas with the range of 4 GHz to 6 GHz in C-band. In the measurement, one horn acts as a transmitter and the other one detects the transmitted or reflected wave. Firstly, free space measurement without sample is carried out to obtain calibration data for the VNA. The sample is then inserted into the experimental measurement setup and *S*-parameters measurements are performed. The fabricated sample and devices for measurements setup are shown in Fig. 3.

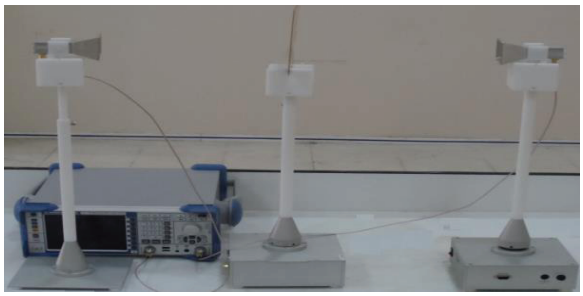

Fig. 3. A picture from the measurement setup.

## III. NUMERICAL AND MEASUREMENT RESULTS

Figures 4 and 5 show numerical and measured results for proposed perfect MA. It can be seen that the simulation maximum absorptions of 99.98% is obtained at the resonance frequency of 4.69 and 4.99 GHz, and the corresponding reflection magnitude is 0.0001 at the resonance frequencies for both of structures, respectively. Also, the measured maximum absorption of 98.67% and 99.78% is observed at the resonance frequency of 4.69 GHz and 5.00 GHz for circle with gap- and square-shaped MAs, in order. The simulation

results are in good agreement with the experimental ones. The suggested structures have potential applications of long-distance radio telecommunications in relation with C-band and it will also be a very good candidate for the applications of satellite communication transmissions, some Wi-Fi devices, some cordless telephones, some weather radar systems and so on.

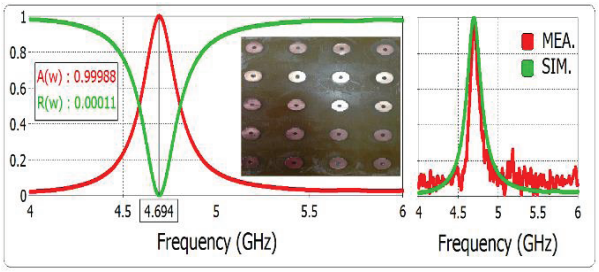


Fig. 4. Simulated reflection and absorption values in C-band Inset: fabricated picture and measured absorption spectrum of the proposed circle with gap-shaped MA at certain frequency regime.

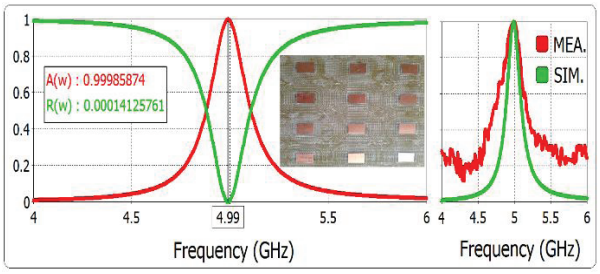


Fig. 5. Simulated reflection and absorption values in C-band Inset: fabricated picture and measured absorption spectrum of the proposed square-shaped MA at certain frequency regime.

Besides, bandwidth calculations are performed to show the performance of the structure in C-band. The fractional bandwidth (FBW) is calculated as FBW=$\Delta f/f_0$, where $\Delta f$ is the half power bandwidth and $f_0$ is the center frequency. These parameters are found as $\Delta f$=0.23-0.25 GHz, $f_0$=4.69-4.99 GHz and FBW≈4.90%-5.01%, for circle with gap- and square-shaped MAs, respectively. This means that the proposed structure has approximately 230-250 MHz bandwidth range referring to 4.90%-5.01-FBW which is very well for many applications. For example, a patch antenna needs around 3% FBW. Therefore, the proposed model would provide enough margins to work with. These computations confirm performance quality of the suggested MA.

Moreover, we performed numeric studies using the suggested structures for X-band frequency regimes. Since the proposed models introduce flexibility to adjust its metamaterial features, the structure is easily rescaled for infrared and visible frequency regions. Maximum absorptions for X-band frequency regime is numerically obtained around 99.68% and 99.99% at the resonance frequency of 10.6 GHz and 8.51 GHz, for circle- and square-shaped, respectively as shown in Figs. 6 and 7.

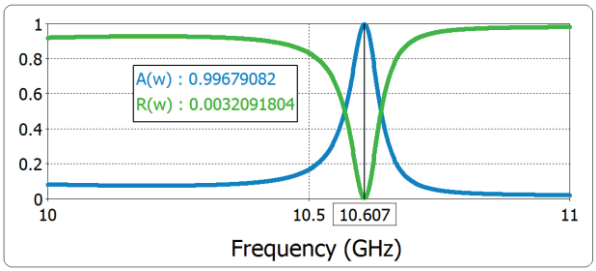


Fig. 6. Simulated reflection and absorption values in X-band for the proposed circle with gap-shaped MA.

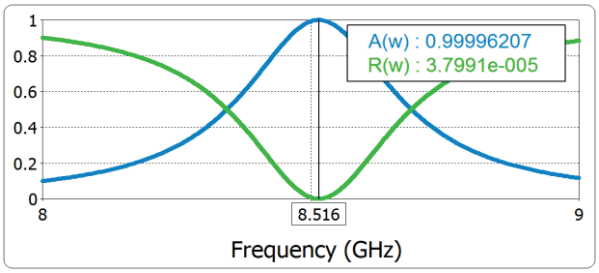


Fig. 7. Simulated reflection and absorption values in X-band for the proposed square-shaped MA.

As next investigation, we examined the effect of the polarization angle on the absorption behavior of the proposed perfect MA in both C-band and X-band as shown in Figs. 8 and 9, respectively. Both of obtained numerical results show that when the polarization angle is increased from $0^o$to $90^o$with 30 degree step and both of absorptions do not change. The suggested MAs perfectly keep polarization angle independency. These features provided by the symmetric-shaped of the proposed models and also the suggested very simple geometry MAs respond the same electric field for all polarization angles at the resonance frequencies.

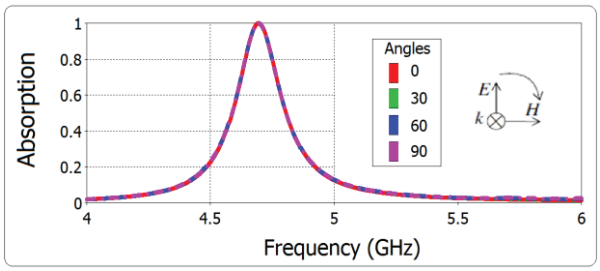


Fig. 8. Simulated absorptions at different polarization angles in C-band.

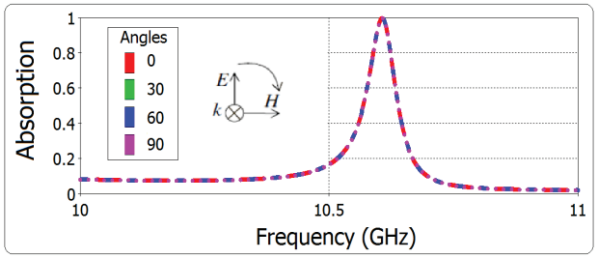


Fig. 9. Simulated absorptions at different polarization angles in X-band.

Additionally, we examined and discussed the electric field and surface current distributions at the resonance frequency of 4.69-4.99 GHz in order to show physical operation mechanism of the proposed circle with gap- and square-shaped perfect MAs, respectively (Figs. 10 and 11). It can be seen that the electric field is concentrated at the right- and left-side of the circle resonator. For square-shaped MA, the electric field is concentrated at the up- and below-side. So, the structure behaves as an electrical dipole for the all applied polarization angles. Also, the current circulation excites magnetic response and as a result an absorption phenomenon increases for surface current distribution.

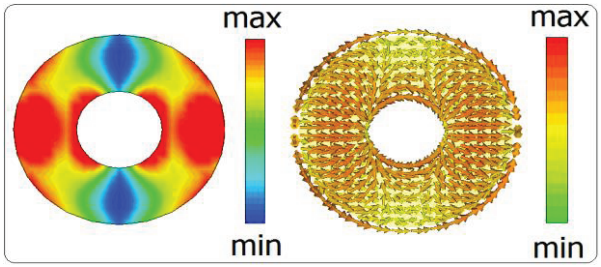


Fig. 10. Electric field and surface current distribution at the resonance frequency of 4.69 GHz of circle with gap-shaped.

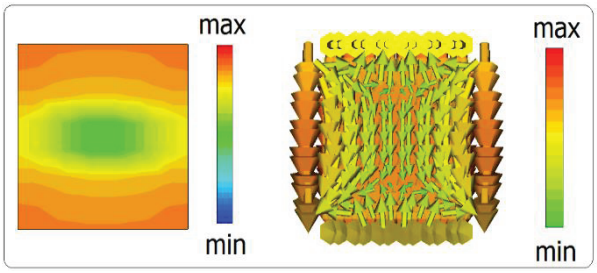


Fig. 11. Electric field and surface current distribution at the resonance frequency of 4.69 GHz of square-shaped.

With this regard, to show performance quality of the suggested MAs according to the current MA studies in literature, proposed models are compared with other MA studies as shown in Table 1. It can be understood that many MA studies show polarization angle independency only in some angles or do not in any [5-8]. Although, some of them provide perfect absorption for all polarization angle, their *FBW* values are low and/or proposed geometry is complex and/or have inflexible geometry design.

Table 1: Performance comparison of MAs

| Absorber | Freq. (GHz) | A(w) | FBW | Indep.*** |
|---|---|---|---|---|
| PropCirc. | 4.69 | 99.98% | 4.9% | Yes |
| PropSqu. | 4.99 | 99.98% | 5.01% | Yes |
| [20] | 11.5 | 96% | 4.0% | No |
| [21] | 10.14 | 97% | 4.7% | S.A.** |
| [22] | 10.45 | 99.9% | 4.2% | No |
| [23] | 10.07 | 98% | N.C.* | Yes |

*N.C.= not calculated **S.A.= some angles
***Indep: independency

However, the suggested MA has many advantages according to the many MA studies in literature such as perfect absorption, polarization independencies, wide band, flexibility and very simplicity are some of the important advantageous of the proposed MA.

## IV. SENSOR APPLICATION OF THE SUGGESTED MODEL

The proposed perfect circle with gap-shaped MA can also be used for sensor applications by located dielectric layer on the front face of the absorber with indicated distance, as shown in Fig.

12. With this regard, the effect of distance between dielectric layer (FR4) and front-face of the proposed MA is investigated and evaluated as detailed, as shown in Fig. 12. The distance (all other parameters of design and simulation are remained constant) is varied from 1.5 mm to 3.5 mm by 0.5 mm step. The reflection results of the simulations for different dielectric thickness are shown in Fig. 12. It can be seen that reflection magnitude values change with the variation of dielectric thickness (for 1.5 mm-dielectric (0.42) and for 3.5 mm-dielectric (0.02), the resonance frequency shifts to lower frequencies when the thickness of the dielectric is increased. The reason of this downward shift can be explained by the variation of the capacitance of the overall structure. The increment of the thickness of dielectric-FR4 leads to increase capacitance, therefore resonance frequency slide downward with increased dielectric thicknesses. Hence, the proposed structure can also be used as a pressure sensor beside absorber applications. One of the most important properties of the proposed MA based sensor is polarization angle independency and its easily obtainable frequency range. These are the superiority of the proposed system.

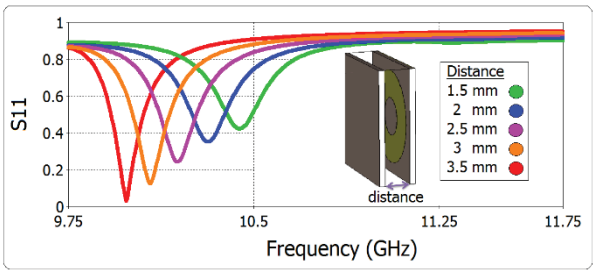


Fig. 12. Reflection values for different distance values of the over-layer in X-band.

## V. CONCLUSION

In this study, very simple designs of perfect MAs numerically and experimentally are designed and investigated as detailed. The proposed models are also realized in X-band, too. Obtained numerical and experimental results show that the structures have many advantages such as perfect absorption, polarization angle independency, wide band, very simple design, and so on according to the current MA studies in literature. Also, they can be tuned the dimensions to achieve perfect absorption in other frequency regimes because of the symmetric-shaped, and realized for different application areas such as stealth and defense systems. Moreover, the suggested structures can be implemented/adopted tunable MA applications to use applications of some Wi-Fi devices, some cordless telephones, and some weather radar systems and so on.

## ACKNOWLEDGMENT

This work is supported by the TUBITAK (113E290-114E295).

## REFERENCES

[1] C. Sabah and H. G. Roskos, "Terahertz sensing application by using planar split-ring-resonator structures," *Microsyst. Technol*., vol. 18, pp. 2071-2076, 2012.

[2] J. B. Pendry, D. Schuriand, and D. R. Smith, "Controlling electromagnetic fields," *Science*, vol. 312, pp. 1780-82, 2006.

[3] N. Fang, H. Lee, C. Sun, and X. Zhang, "Sub-diffraction-limited optical imaging with a silver superlens," *Science*, vol. 308, pp. 534-37, 2005.

[4] D. Li, Z. Szabo, X. Qing, E. P. Li, and Z. N. Chen, "A high gain antenna with an optimized metamaterial inspired superstrate," *IEEE T. Antenn. Propag*., vol. 60, pp. 6018-23, 2012.

[5] C. Sabah and H. G. Roskos, "Design of a terahertz polarization rotator based on a periodic sequence of chiral-metamaterial and dielectric slabs," *PIERs*, vol. 124, pp. 301-314, 2012.

[6] F. Dincer, M. Karaaslan, E. Unal, and C. Sabah, "Dual-band polarization independent metamaterial absorber based on omega resonator and octa-star strip configuration," *PIERs*, vol. 141, pp. 219-231, 2013.

[7] M. C. K. Wiltshire, J. B. Pendry, I. R. Young, D. J. Larkman, D. J. Gilderdale, and J. V. Hajnal, *Science*, vol. 291, pp. 849, 2001.

[8] D. R. Smith, W. J. Padilla, D. C. Vier, S. C. Nemat-Nasser, and S. Schultz, *Physical Review Letters*, vol. 84, pp. 4184, 2000.

[9] M. Gokkavas, K. Guven, I. Bulu, K. Aydin, R. S. Penciu, M. Kafesaki, C. M. Soukoulis, and E. Ozbay, *Physical Review B*, vol. 73 pp. 193103, 2006.

[10] T. J. Yen, W. J. Padilla, N. Fang, D. C. Vier, D. R. Smith, J. B. Pendry, D. N. Basov, and X. Zhang, "Terahertz magnetic response from artificial materials," *Science*, vol. 303, pp.

1494-1496, 2004.
[11]S. Linden, C. Enkrich, M. Wegener, J. Zhou, T. Koschny, and C. M. Soukoulis, "Magnetic response of metamaterials at 100 terahertz," *Science*, vol. 306, pp. 1351-1353, 2004.
[12]S. Zhang, W. Fan, N. C. Panoiu, K. J. Malloy, R. M. Osgood, and S. R. J. Brueck, "Experimental demonstration of near-infrared negative-index metamaterials," *Physical Review Letters*, vol. 95, pp. 137404, 2005.
[13]G. Dolling, M. Wegener, C. M. Soukoulis, and S. Linden, "Negative-index metamaterial at 780nm wavelength," *Optics Letters*, vol. 32, pp. 53-55, 2007.
[14]J. Lee, Y. J. Yoon, and S. Lim, "Ultra-thin polarization independent absorber using hexagonal interdigital metamaterial," *ETRI Journal*, vol. 34, no. 1, pp. 126-129, 2012.
[15]J. Sun, L. Liu, G. Dong, and J. Zhou, "An extremely broadband metamaterial absorber based on destructive interference," *Opt. Express*, vol. 19, pp. 21155-62, 2011.
[16]J. Zhao, Q. Cheng, J. Chen, M. Q. Qi, W. X. Jiang, and T. J. Cui, "A tunable metamaterial absorber using varactor diodes," *New Journal of Physics*, vol. 15, pp. 043049, 2013.
[17]B. Wang, T. Koschny, and C. M. Soukoulis, "Wide-angle and polarization independent chiral metamaterial absorber," *Phys. Rev. B*, vol. 80, pp. 033108-4, 2009.
[18]Q. Ye, Y. Liu, H. Lin, M. Li, and H. Yang, "Multi-band metamaterial absorber made of multi-gap SRRs structure," *Appl. Phys. A*, vol. 107, pp. 155-160, 2012.
[19]F. Dincer, M. Karaaslan, E. Unal, K. Delihacioglu, and C. Sabah, "Design of polarization and incident angle insensitive dual-band metamaterial absorber based on isotropic resonators," *PIERs*, vol. 144, pp. 123-132, 2014.
[20]N. I. Landy, S. Sajuyigbe, J. J. Mock, D. R. Smith, and W. J. Padilla, "A perfect metamaterial absorber," *Phys. Rev. Lett*., vol. 100, pp. 207402, 2008.
[21]B. Zhu, Z. Wang, C. Huang, Y. Feng, J. Zhao, and T. Jiang, "Polarization insensitive metamaterial absorber with wide incident angle," *Prog. Electromagn. Res*., vol. 101, pp. 231-239, 2010.
[22]Y. Cheng and H. Yang, "Design, simulation, and measurement of metamaterial absorber," *J. Appl. Phys*., vol. 108, pp. 034906, 2010.
[23]Y. Cheng, H. Yang, Z. Cheng, and B. Xiao, "A planar polarization-insensitive metamaterial absorber," *Photonic. Nanostruct*., vol. 9, pp. 8-14, 2011.

**Muharrem Karaaslan** received the Ph.D. degree in Physics Department from The University of Cukurova, Adana, Turkey, in 2009. He is the co-author of about 35 scientific contributions published in international journals and peer-reviewed conference proceedings. His research interest includes the applications of metamaterials in the analysis and synthesis of antennas, waveguides and textile.

**Ahmet Oğuzhan Demirci** received the B.S degree in Electrical-Electronics Engineering from Erciyes University in 2001 and he is still studying on the M.S degree at Mustafa Kemal University, Hatay in Electrical-Electronics Engineering.

# Optimization of Frequency Selective Surface with Simple Configuration Based on Comprehensive Formation Method

**N. Fallah Amini [1], M. Karimipour [1], K. Paran [1], and S. Chamani [2]**

[1] Faculty of Electrical and Computer Engineering
Shahid Beheshti University G.C. (SBU), Tehran, +98, Iran
majid.karimipour2000@gmail.com, n.falahamini@gmail.com, k_paran@sbu.ac.ir

[2] Faculty of Electrical and Computer Engineering
K. N. Toosi University of Technology, Tehran, +98, Iran
Chamaani@eetd.kntu.ac.ir

***Abstract*** ─ A new approach to design a frequency selective surface (FSS) is presented based on optimizing the shape of its unit cell geometry. A method based on spline concept has been adopted to specify geometrical features of the elements. In the design process, a hybrid optimization process including genetic algorithm and pattern search method has been used for this purpose. The shape of the structure is improved in each iteration based on specific fitness function. The commercial software CST is used for accurate analysis of structures along the optimization process. A VBA code is developed in order to link Matlab code, which includes optimization tools, and analyzer software CST. This method is used to develop band-pass and band-stop FSSs. Our simulated results show that the transmission and reflection characteristics of the designed FSS are very good in specified frequency band.

***Index Terms*** ─ Frequency Selective Surface (FSS), genetic algorithm, spline.

## I. INTRODUCTION

Frequency selective surfaces are periodic structures in either one or two dimensions (i.e., singly or doubly periodic structures), which, as the name suggests, perform a filter operation. Thus, depending on their physical construction, material and geometry, they are divided into low-pass, high-pass, band-pass, and band-stop filters [1,2]. FSSs are also used as a high-impedance surface, radome, absorber, and so on [3-5]. Nowadays, FSSs find many applications from the microwave to the THz region, for both scientific and commercial purposes, which span from antenna systems for radio astronomy research to the screen doors of the microwave ovens. To meet the requirements of those application purposes, many things should be considered at the design stage of FSSs such as selection of the appropriate unit cell geometry, spacing between unit cells, thickness and electrical properties of substrate [5], etc. Several approaches have been proposed to obtain multiple resonance properties, which include FSSs consisting of unit cells with same geometrical shape but different sizes [6] or unit cells with fractal geometry [7,8].

There are two frequency sensitive processes which are commonly exploited in the design of these surfaces. One is the interference of waves reflected from cascaded partially transmitting, and the other is the resonant interaction of waves with segments of conductor - normally periodic arrays of conducting elements or slots in conducting screens. The cascaded boundaries could simply be the interfaces between stacked dielectric sheets, where the number of boundaries, their spacing and the dielectric permittivity are the quantities influencing the transmission response. Double or multiple layers of the metallic grids described later in these notes or cascaded arrays of elements can be employed, or more often in practice a combination of dielectric interfaces and arrays of elements.

The performance and behavior of the FSS filters depend on the following factors: (I) the conductivity and thickness of the FSS conductor, (II) the geometry of the FSS element, (III) the permittivity and thickness of the FSS substrate, and

*Submitted On: December 13, 2013*
*Accepted On: December 11, 2014*

(IV) the periodic arrangement of FSS elements [1]. Many numerical methods have been proposed in the last decades for the simulation of FSSs, both in the hypothesis of infinitely thin metal screens and by considering metal screens with finite thickness. Among those, the most popular methods are Finite Difference Time Domain (FDTD) technique [9,10], Finite Element Method (FEM) [11], and Method of the Moments (MoM) technique [12,13].

In this paper, at first a new optimization process will be introduced to design a FSS with desired radiation properties. Secondly, some examples including band-pass filter and band-stop filter are presented to verify the proposed method. The proposed design procedure searches for the optimal shape of the FSS elements. The outline of each FSS element is formed symmetrically by 8 splines. The optimal shape of the FSS element can be obtained by tuning the parameters of the main spline through an optimization process. During the optimization process the analysis of structures is carried out by CST software. A VBA code is developed in order to link Matlab code, which includes optimization tools, and analyzer software.

## II. THE PROPOSED METHOD FOR DESIGNING A FREQUENCY SELECTIVE SURFACE

### A. Spline interpolation method

In the mathematical field of numerical analysis, spline interpolation is a form of interpolation where the interpolant is a special type of piecewise polynomial called a spline. Spline interpolation is preferred over polynomial interpolation because the interpolation error can be made small even when low degree polynomials is used for the spline. Moreover, spline interpolation avoids the problem of Rung's phenomenon which occurs when interpolating using high degree polynomials. Splines can be considered as a mathematical model that associates a continuous representation (curve or surface) with a discrete set of points of an affine space. The resulting curve may either approximate the control points or interpolate them [14].

A spline can be generated in several procedures such as interpolation and approximation method. We used the approximated spline to derive the final shape of FSS unit cell. In this method, several points are obtained instead of calculating the formulation of the polygon curves. This leads to simplify the definition of the shape unit cell in the design softwares. As shown in Fig. 1 (a), a spline replaces each edge of a given polygon by a curve with specified expansion and sharpness which are determined respectively by expansion ($e_n$) and sharpness ($s_n$) factors assigned to that edge. Expansion factor represents a part of curve length at a corner which can be replaced with spline. The amount of expansion factor is considered between 0 and 0.5 (when it is equal to 0.5, spline is obtained in form of a straight line from middle of one side to middle of another side of corner). The value of sharpness factor is also considered between 0 and 1 (when it is equal to 1, the sharpness of spline shape is the same as sharpness of corner).

After assigning the values of expansion and sharpness factors, the points A, B, $C_1$, $C_2$ and $U_1$ (middle point of $\overline{C_1C_2}$ segment) are determined (Fig. 1 (b)). Shaping process of spline is done by an iterative method. This method is done by connecting the middle of each adjacent segment to the others which leads to generate the new segment. For example in the first step, the middle of $AC_1$ and $BC_2$ segments are connected to middle of $C_1U_1$ and $U_1C_2$ segments, respectively. This method is repeated to generate a smooth shape from corner.

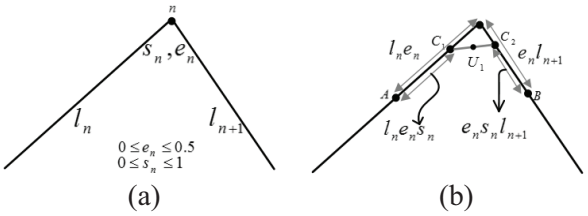


Fig. 1. Expansion and sharpness factors at a corner.

### B. Design of FSS element

To create the shape of the unit cell, we used a spline interpolation method. The proposed method has been recently used for optimization of UWB antennas [15]. One of the main advantages of this method is applying some limitations to the boundaries in order to decrease the complexity of the element shape. It results in less manufacturing difficulties. With the spline concept, discontinuity problem is eliminated at the boundaries of the structures and elements can also be described with low number of parameters without limiting the variety of possible geometries. Figure 2 shows the primitive sketch with its main parameters of the

proposed element based on spline interpolation procedure.

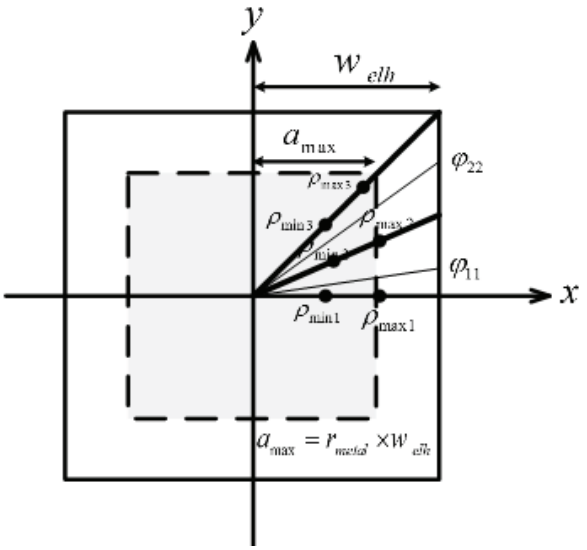


Fig. 2. Primitive design and geometrical parameters of element.

As shown in Fig. 2, desired structure has been considered within the square with dimensions $w_{elh} \times w_{elh}\left(cm^2\right)$. In order to have sensible margin with other neighboring elements, boundaries are embedded in the region with dimensions $a_{max} \times a_{max}$ where $a_{max} = r_{metal} \times w_{elh}$ and $r_{metal} \leq 1$. For simplifying purposes and having the element least sensitivity with respect to the wave polarization, the elements have been considered with one of eighth (1/8) symmetry in the $\varphi$ plane. Therefore we will require to design only 1/8 of element shape in the optimization process. In the first step, three primitive points of the element boundaries is considered at $\varphi_1 = 0°$, $\varphi_2$, and $\varphi_3 = 45°$ planes, where $\varphi_2$ is a polar angle between the specified $\varphi_{11}$ and $\varphi_{22}$ planes according to Fig. 2. For each point a certain boundary is considered for the variation of its polar radius. Parameters $\rho_1, \rho_2$ and $\rho_3$ are the polar radius of the points where $\rho_{min1} < \rho_1 < \rho_{max1}$, $\rho_{min2} < \rho_2 < \rho_{max2}$ and $\rho_{min3} < \rho_3 < \rho_{max3}$. Amounts of $\rho_{min1}$, $\rho_{max1}$, $\rho_{min2}$, $\rho_{max2}$, $\rho_{min3}$ and $\rho_{max3}$ parameters are constant and will be determined at the beginning of the optimization process. Altogether, 10 parameters including the expansion and the sharpness factors corresponding to each point ($s_i$ and $e_i$ $i = 1,\ 2,\ 3$) also $\rho_1, \rho_2, \rho_3$ and $\varphi_2$ are the optimization variables that must be changed during the optimization process. These parameters are tuned according to the desired fitness function to minimize the cost function defined in the optimization algorithm.

The variety of possible geometries raise the possibility of having different optimum designs. On the other hands, the objective function may have multiple local minima in the search domain. Consequently, global optimization methods should be used in order to search for the best design. Moreover, the process of calculating the objective function for each FSS structure is relatively complex and time consuming, including the electromagnetic simulation of antenna and the computation of characteristics which are involved in the definition of objective function. Therefore, the implementation of heuristic strategies is necessary in order to reduce the overall time needed for the completion of the optimization process. On the other hand, the final stages of optimization with heuristic strategies are subjected to stagnation, so it is better to complete the global optimization by implementing a local optimization method. Accordingly, the optimization process includes a combination of local and global optimization algorithm. The traditional electromagnetic software CST is used during the optimization process to calculate the desired characteristic of the FSS (including the reflection and transmission coefficients). It will raise the accuracy of the designed structure. This optimization procedure is much better than CST's inner code optimization. More degree of freedom for designed parameters, capability to determine arbitrary genetic algorithm options, possibility to combine local and global optimization procedures, are some advantages of the proposed method.

While the optimization process was completed, the optimum position of each point is determined. A spline is fitted to these points and the element shape will be constructed by repeating the spline in the whole $\varphi$ plane according to the 1/8 symmetry. Finally, obtained element is simulated with

frequency solver CST microwave studio considering periodic boundaries and excitation. This is important to point that substrate thickness $(t_{sub})$ and dielectric constant $(\varepsilon_r)$ will be remained fix during the optimization process.

### C. Determining the fitness function of the optimization method

Figure 3 shows a sample shape for desired transmission coefficient ($S_{21}$) of a band-pass FSS. Desired reflection coefficient ($S_{11}$) of a band-stop FSS can be determined in a similar manner.

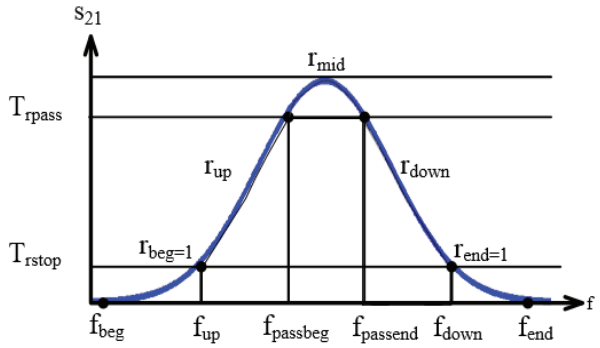


Fig. 3. Desired $S_{21}$ with relative parameters to determine the fitness function.

As shown in Fig. 3, there are many parameters to clarify the fitness function. These parameters have been determined based on desired frequency band and maximum acceptable amount of $S_{21}$ or $S_{11}$ coefficients. It would be desired that $S_{21}$ coefficient should be more than $T_{rpass}$ in the pass-band region and less than $T_{rstop}$ in the stop-band region and behaves as a linear function in the transient bands from $T_{rpass}$ to $T_{rstop}$ and vice versa. Given the importance of different regions in the frequency band, different weights such as $r_{beg}, r_{mid}, r_{up},$ and $r_{end}$ have been assigned to different regions of $S_{21}$ curve. The fitness function has been considered as follows:

$$F = F_{beg} + F_{up} + F_{mid} + F_{down} + F_{end}, \qquad (1)$$

where $F_{beg}$, $F_{up}$, $F_{mid}$, $F_{down}$ and $F_{end}$ are assigned in different frequency regions as follows:

For $f_{beg} < f < f_{up}$ :

$$F_{beg} = \left(r_{beg} / n_{beg}\right) \sum_{n=1}^{n_{beg}} \left[ \begin{array}{l} \left|S_{21}(n)\right| - \\ \min\left(\left|S_{21}\right|, T_{rstop}\right) \end{array} \right], \qquad (2)$$

where $f_{beg}$ and $f_{up}$ are the beginning frequency of the channel and transient region, respectively. Parameter $n_{beg}$ is the number of sample frequency in the first region.

For $f_{up} < f < f_{passbeg}$ :

$$F_{up} = \left(r_{up} / n_{up}\right) \sum_{n=1}^{n_{up}} \left[ \begin{array}{l} \left|S_{21}(n)\right| - \\ \min\left(\left|S_{21}, T_{rm1}\right|\right) \end{array} \right], \qquad (3)$$

where $f_{passbeg}$ is the beginning frequency of the pass band region with high reflection or transmission coefficient. Parameter $n_{up}$ is the number of sample frequency in the transient region and parameter $T_{rm1}$ is obtained as follows:

$$\begin{array}{l} T_{rm1} = T_{rpass} + \left(T_{rpass} - T_{rstop}\right) \times \\ \left(f - f_{up}\right) / f_{passbeg} - f_{up}. \end{array} \qquad (4)$$

For $f_{passbeg} < f < f_{passend}$ :

$$F_{mid} = \left(r_{mid} / n_{mid}\right) \sum_{n=1}^{n_{mid}} \left[ \begin{array}{l} \min\left(\left|S_{21}(n)\right|, T_{rpass}\right) \\ -\left|S_{21}(n)\right| \end{array} \right], \qquad (5)$$

where $f_{passend}$ is the ending frequency of the pass band region with high reflection or transmission coefficient. Parameter $n_{mid}$ is the number of sample frequency in the pass band region.

For $f_{passend} < f < f_{down}$ :

$$\begin{array}{l} F_{down} = \left(r_{down} / n_{down}\right) \times \\ \sum_{n=1}^{n_{down}} \left[ \begin{array}{l} \left|S_{21}(n)\right| - \\ \min\left(\left|S_{21}(n)\right|, T_{rm2}\right) \end{array} \right], \end{array} \qquad (6)$$

where $f_{down}$ is the ending frequency of the second transient region. Parameter $n_{down}$ is the number of sample frequency in the second transient region and parameter $T_{rm2}$ is obtained as follows:

$$\begin{array}{l} T_{rm2} = T_{rpass} + \left(T_{rpass} - T_{rstop}\right) \times \\ \left(f_{down} - f\right) / f_{down} - f_{passend} \end{array}. \qquad (7)$$

And finally for $f_{down} < f < f_{end}$ :

$$F_{end} = \left(r_{end} / n_{end}\right) \times \sum_{n=1}^{n_{end}} \left[ \begin{array}{l} \left|S_{21}(n)\right| - \\ \min\left(\left|S_{21}(n)\right|, T_{rstop}\right) \end{array} \right], \quad (8)$$

where $f_{end}$ is the ending frequency of the channel. Parameter $n_{end}$ is the number of sample frequency in this region.

## III. SIMULATION RESULTS

In this section, two examples are provided to verify the proposed method. At first, we designed a band-pass FSS. It is desired that the designed FSS has a high transmission coefficient and low reflection coefficient around at 1.2 THz. Important parameters of the band-pass FSS and fitness function associated with transmission coefficient ($S_{21}$), are shown in Table 1. Optimization process has been done for normal incidence and both TE and TM polarizations. Schematic of the designed FSS has been shown in Fig. 4. The population size and number of generations of the optimization process have been considered 50 and 6, respectively, which are appropriate to reach good results. There is a tradeoff between the accuracy and the optimization time. Accordingly, the population size and the generation numbers values are selected based on the optimization time and the accuracy of the results. The number of frequency samples are considered 1000 in the whole band. For simplifying, these frequency samples are considered with equal distances. Parameters $r_{beg}$, $r_{mid}$, and $r_{end}$ are valued relative to each other. It means, they represent the importance of different regions in the fitness function, accordingly the final results don't merely depend on their exact values. Almost, the value of parameter $r_{mid}$ is assigned greater than the others. The optimization time takes about 8 hours by a computer with 8 core CPU and 16 GHz of RAM. The transmission coefficient of TE and TM mode of the designed FSS as a function of frequency is shown in Fig. 5.

As shown in Fig. 5, the 3-dB bandwidth of the designed FSS is from 0.72 THz to 1.7 THz which has a good agreement with input parameters $f_{passbeg}$ and $f_{passend}$.

Table 1: Unit cell, substrate, frequency band, and fitness function parameters for band-pass FSS design

| | |
|---|---|
| Unit Cell Parameters | |
| $w_{elh}$ ($\mu$m) | 102 |
| $r_{metal}$ | 0.95 |
| Substrate Parameters | |
| $\varepsilon_r$ (F/m) | 2.89 |
| $tan(\delta)$ | 0.002 |
| T($\mu$m) (thickness) | 12 |
| Frequency Band Parameters | |
| $f_{beg}$ (THz) | 0.2 |
| $f_{end}$ (THz) | 2.3 |
| $f_{passbeg}$ (THz) | 0.7 |
| $f_{passend}$ (THz) | 1.8 |
| Coefficients of Fitness Function | |
| $r_{beg}$ | 20 |
| $r_{mid}$ | 40 |
| $r_{end}$ | 20 |

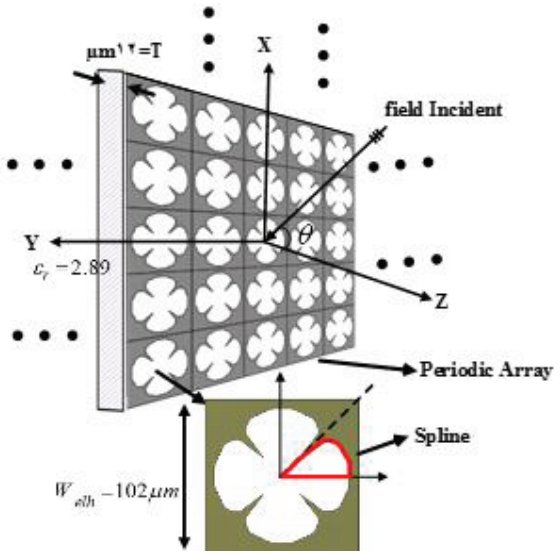


Fig. 4. Designed band-pass FSS with the proposed method around at 1.2 THz.

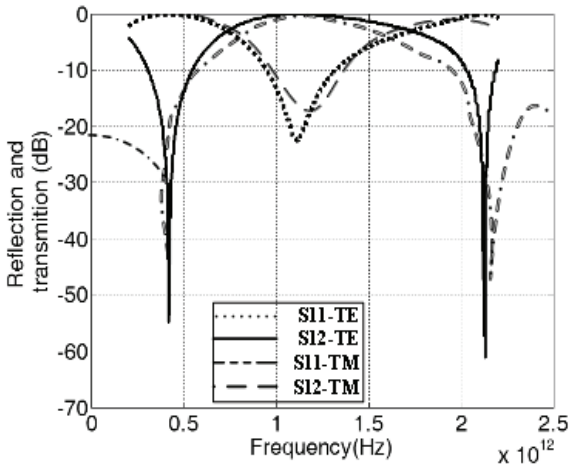


Fig. 5. Reflection and transmission of the designed band-pass FSS obtained by CST software for TE and TM waves.

The deviation of resonance frequency is less than 3% for TE polarization and less than 2% for TM case. The most important feature of the proposed structure is nearly same reflection-transmission behavior under different incident angles. Due to the 1/8 symmetry of the structure, which is applied to reduce optimization parameters and decrease the optimization time, FSS has less sensitivity to the incident angle. In order to investigate this fact, we considered the optimized configuration and calculated reflection and transmission coefficients for $\theta = 30°$. Figure 6 shows that a $30°$ inclination of incident wave has a little effect on reflection-transmission characteristics.

As a second example, we designed an FSS configuration to behave as a band-stop filter around at 9.2 GHz. Therefore, the fitness function has been changed to realize this configuration. Table 2 shows important data associated to FSS and its fitness function. Figure 7 shows the optimized structure. The population size and number of generations in the optimization process have been considered 54 and 6, respectively. These values are selected by testing the algorithm several times to get better results. Other parameters have been considered similar to the previous example. Reflection and transmission of the designed FSS is shown in Fig. 8. As shown in Fig. 8, a band-stop FSS around at 9.2 GHz is realized. There is more than 20 dB difference between amounts of $S_{11}$ and $S_{21}$ coefficients. Furthermore, this structure has low sensitivity with respect to the impinging wave polarization, especially near the central frequency.

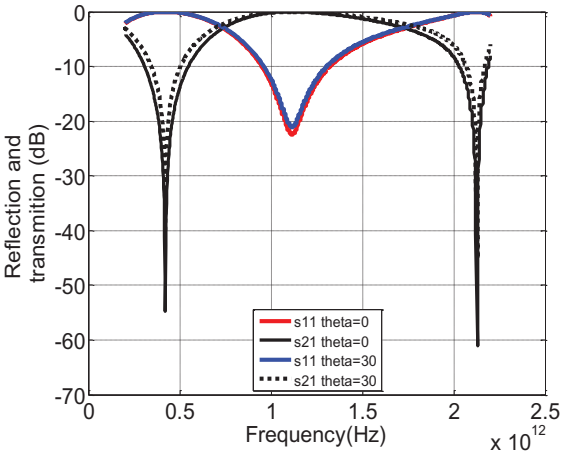


Fig. 6. Reflection and transmission of band-pass FSS for two different incident angles obtained by CST software.

Table 2: Unit cell, substrate, frequency band, and fitness function parameters for band-stop FSS design

| | |
|---|---|
| Unit Cell Parameters | |
| $w_{elh}$ (mm) | 15 |
| $r_{metal}$ | 0.95 |
| Substrate Parameters | |
| $\varepsilon_r$ (F/m) | 2.89 |
| $tan(\delta)$ | 0.02 |
| T($\mu$m) (thickness) | 12 |
| Frequency Band Parameters | |
| $f_{beg}$ (GHz) | 7.5 |
| $f_{end}$ (GHz) | 11.4 |
| $f_{passbeg}$ (GHz) | 8.6 |
| $f_{passend}$ (GHz) | 9.8 |
| Coefficients of Fitness Function | |
| $r_{beg}$ | 5 |
| $r_{mid}$ | 10 |
| $r_{end}$ | 5 |

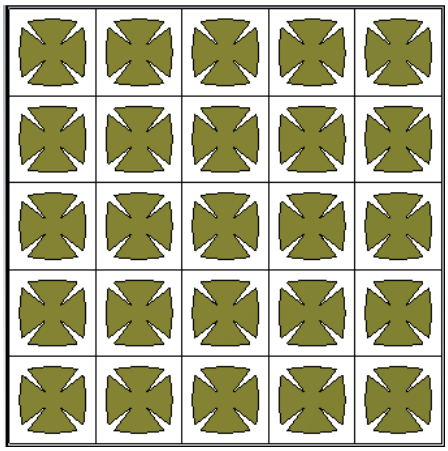

Fig. 7. A part of periodic array designed with the proposed method to have band-stop behavior around at 9.2 GHz.

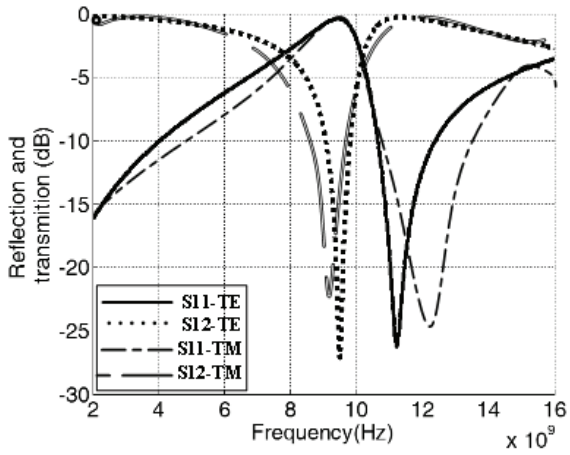


Fig. 8. Reflection and transmission of the resulted band-stop FSS for TE and TM waves obtained by CST software.

Figure 9 and Fig. 10 show the output results of genetic and pattern search algorithm for this example.

In the previous works, the binary parameters were used to describe the shape of the unit cell [16-18]. For example, in the case of the genetic algorithm, all the parameters which require optimization, namely, the kind and the thickness of each dielectric layer, the periodicity of the surface and the shape of the unit cell element are encoded into a binary-encoded chromosome. Disadvantage of the proposed design procedures is high sensitivity of structures to fabrication tolerance.

The advantage of the designed structure in this present is low sensitivity of the designed FSS with respect to the manufacturing tolerance. The use of spline concept in the design procedure is the main reason of this fact. Splice concept cause to generate unit cell with continuous borders and prevents to generate complex unit cell shape. In order to show this advantage, a FSS with +5% variation at the input variables of the optimization algorithm is generated, simulated and compared with original case. Figure 11 shows the result of new structure with 5% tolerance in its shape. As shown in Fig. 11, there is no sensible difference between modified structure and original one. This is an acceptable criterion for designing a FSS.

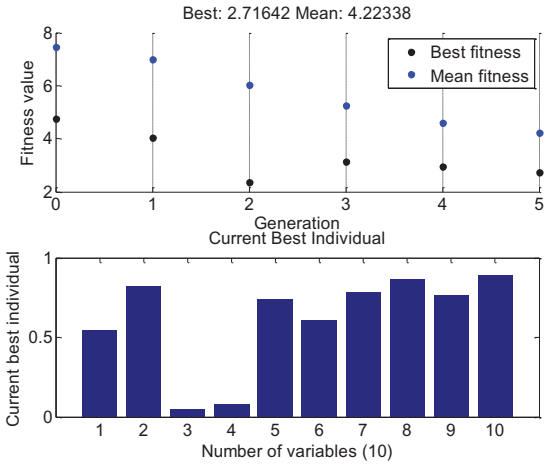


Fig. 9. Fitness value and current best individual in the genetic algorithm.

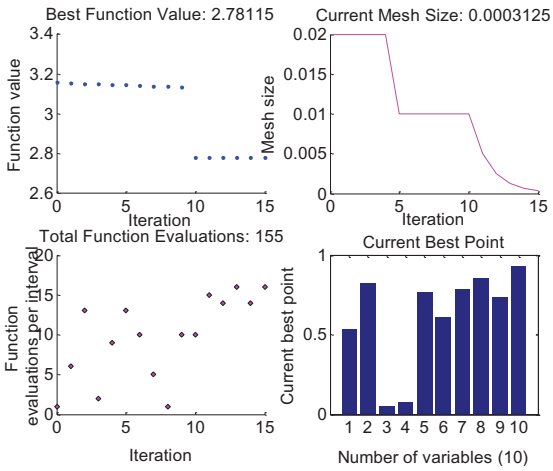


Fig. 10. Results of pattern search method.

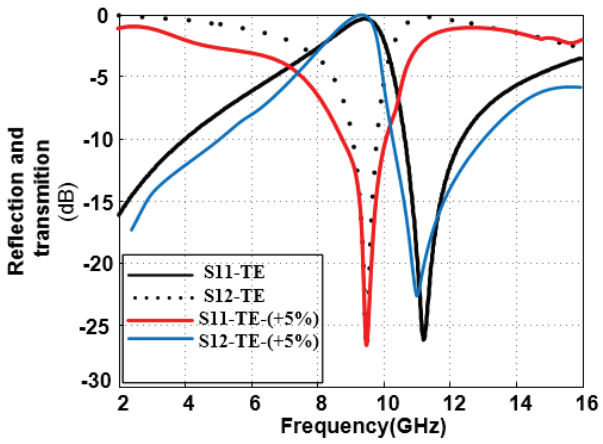


Fig. 11. Comparison between designed FSS and modified case.

## IV. CONCLUSION

A novel method for the optimization of FSS with simple configuration is proposed. The main idea is formation the boundaries of each element symmetrically with 8 splines and then finding the parameters of the main spline through an optimization process to have a desired reflection or transmission characteristics. For the accurate analysis of periodic structure, we used CST software to simulate FSSs during the optimization process. The optimization process is a hybrid procedure including genetic algorithm and pattern search method. A VBA code is developed to link CST software and optimization code. The process resulted in structures with low sensitivity to the polarization and incident angle.

## REFERENCES

[1] B. A. Munk, *Frequency-Selective Surfaces: Theory and Design*, Wiley, New York, pp. 5-6, 2000.

[2] J. C. Vardaxoglou, *Frequency Selective Surfaces*, Wiley, New York, NY, USA, 1997.

[3] F. Costa, S. Genovesi, and A. Monorchio, "On the bandwidth of high-impedance frequency," *IEEE Antennas and Wireless Propagation Letters*, vol. 8, pp. 1341-1344, 2009.

[4] F. Costa and A. Monorchio, "A frequency selective radome with wideband absorbing properties," *IEEE Trans. Antennas Propagat.*, vol. 60, no. 6, pp. 2740-2747, Jun. 2012.

[5] C. Chen, "Scattering by a two-dimensional periodic array of conducting plates," *IEEE Trans. Antennas Propagat*., vol. AP-18, no. 5, pp. 660-665, Sep. 1970.

[6] T. K. Wu, "Four-band frequency selective surface with double-square-loop patch elements," *IEEE Trans. Antennas Propagat.*, vol. 42, no. 12, pp. 1659-1663, Dec. 1994.

[7] J. P. Gianvittorio, J. Romeu, S. Blanch, and Y. Rahmat-Samii, "Self-similar prefractal frequency selective surfaces for multiband and dual-polarized applications," *IEEE Trans. Antennas and Propagat*., vol. 51, no. 11, pp. 3088-3096, Nov. 2003.

[8] D. H. Werner and D. Lee, "Design of dual-polarized multiband frequency selective surfaces using fractal elements," *Electronics Letters*, vol. 36, no. 6, pp. 487-488, Mar. 2000.

[9] P. Harms, R. Mittra, and W. Ko, "Implementation of the periodic boundary condition in the finite difference time domain algorithm for FSS structures," *IEEE Trans. Antennas Propagat.*, vol. AP-49, no. 9, pp. 1317-1324, Sep. 1994.

[10] W. Yu, S. Dey, and R. Mittra, "Modeling of periodic structures using the finite difference time domain (FDTD)," *IEEE APS/URSI Symp.*, pp. 594-597, Jul. 1999.

[11] A. Pellegrini, A. Monorchio, and G. Manara, "Optimization of unconventional inductive frequency selective surfaces based on genetic algorithm and MM/FEM analysis," *Antennas and Propagation Society International Symposium*, pp. 3289-3292, 2006.

[12] N. Don, M. Bozzi, A. Kirilenko, and L. Perregrini, "Analysis of inductive frequency selective surfaces by the method of moments with entire-domain basis functions," *Microwave and Optical Technology Letters*, vol. 49, issue 12, pp. 2929-2932, Dec. 2007.

[13] J. Yeo and R. Mittra, "Numerically efficient analysis of microstrip antennas using the characteristic basis function method (CBFM)," in *Proc. IEEE AP Society Int'l. Symp. 2003*, vol. 4, pp. 85-88, Jun. 2003.

[14] C. Blanc and C. Schlick, "A spline model designed for the end-user," *Computer Graphics and Geometric Modeling*, pp. 377-386, 1995.

[15] L. Lizzi, F. Viani, R. Azaro, and A. Massa, "Optimization of a spline-shaped UWB antenna by PSO," *IEEE Antennas Wireless*

*Propagat. Letter*, vol. 6, pp. 182-185, 2007.

[16] Y. Rahmat-Sami and E. Michielssen, *Electromagnetic Optimization by Genetic Algorithm*, John Wiley and Sons, 1999.

[17] S. Genovesi, R. Mittra, A. Monorchio, and G. Manara, "Particle swarm optimization for the design of frequency selective surfaces," *IEEE Antennas and Wireless Propagation Letters*, vol. 5, 2006.

[18] G. Manara, A. Monorchio, and R. Mittra, "Frequency selective surface design based on genetic algorithm," *Electronic Letter*, vol. 35, pp. 1400-1401, Aug. 1999.

**Majid Karimipour** received his B.S. and M.S. degrees in Electrical Engineering in 2008 and 2011 from Shahrekord University, Shahrekord, Iran and Shahid Beheshti University (SBU), Tehran, Iran, respectively. He is currently working towards the Ph.D. degree in Communication Engineering at Iran University of Science and Technology (ISUT), Tehran, Iran. His major research interests are the development and design of reflectarray antennas, complex EM media, design antennas in THz bands such as reflectarray, numerical methods in EM, and design of microwave devices.

# Rotor Configuration for Cogging Torque Minimization of the Open-Slot Structured Axial Flux Permanent Magnet Synchronous Motors

**E. Aycicek, N. Bekiroglu, I. Senol, and Y. Oner**

Department of Electrical Engineering
Yildiz Technical University, Electrical - Electronic Faculty, 34349 Besiktas, Istanbul, Turkey
eaycicek@yildiz.edu.tr, nbekir@yildiz.edu.tr, senol@yildiz.edu.tr, yoner@yildiz.edu.tr

***Abstract*** ─ In this study, the rotor structure of the double rotor – single stator axial flux permanent magnet synchronous motor (AFPM) is optimized for minimizing the cogging torque without significantly changing the average torque of the motor. Three-dimensional (3-D) finite element analysis (FEA) is used for this optimization. Obtained results are compared with a base line reference axial flux synchronous motor.

***Index Terms*** ─ AFPM motor, FEA, structural analysis, surface permanent magnet motor.

## I. INTRODUCTION

After utilization of high energy density magnets, the AFPMs have been widely used in different industrial applications due to their advantages such as their high efficiency, simple structure, high power and torque densities, and low rotor losses [1]-[4]. AFPM machines can be single- or double-sided, with or without armature slots/core, have internal/external PM rotors, contain a surface-mounted or interior PM, and are single- or multi-stage [5].

AFPM machines have an inherent 3D electromagnetic structure. Indeed, most of authors use 3D finite element analysis (3D FEA) for its study [6-8].

Most of these applications require torque ripple minimization for ensuring the smooth operation of the motors [9]. While torque ripples can be filtered by the system inertia at high speed operations, torque ripples can cause undesired speed variations, vibrations, and acoustic noise at low speed operations [10]. One of the two fundamental reasons of the torque ripples is the harmonic distortions in the voltage and current waveforms and the latter is the cogging torque generated due to the magnetic interactions between the rotor magnets and the stator teeth [11]-[12].

The cogging torque of these motors is known to influence significantly the behavior of this type of machine. In general, techniques of minimizing cogging torque to improve torque quality can be classified into two major categories. The first one includes the technique for modifying motor design so that the pulsating torque component is minimized. Cogging torque can also be significantly reduced by optimal selection of slot and pole combinations [13] and stator tooth width and rotor magnet spacing [13], [14], [15]-[18]. Less common yet ingenious measures, such as stator teeth pairing [18], stator slot pairing [19], teeth notching [13], [17], [20], [21], magnet pairing [13], magnet segmentation [22], and magnet shifting [13], [23], have also been proposed [24].

The second way is based upon control schemes for modifying the stator excitation waveform to obtain smooth torque. There are various techniques for reducing the cogging torque in permanent magnet (PM) machines such as shoe of stator teeth, fractional pitch, change of PM magnetization shape and skewing. Previous research work has been made in order to reduce the cogging torque in PM synchronous machine and it was demonstrated that it is greatly affected by the configuration of the stator, and magnetization distribution. Cogging torque can be calculated accurately using the FEM [25], [26], [27].

In this study, to determine the rotor structure that minimizes the cogging torque in double rotor – single stator AFPM, the cogging torque variations are observed by relatively rotating one rotor with respect to the other rotor at various values of the

*Submitted On: May 24, 2013*
*Accepted On: December 11, 2014*

magnet pole-arc and for different magnet structures. Furthermore, the effects of the applied techniques on the average torque are investigated. The 3-D finite element analysis method is used for this purpose. 3D FEA analysis was performed with Maxwell 3D. Obtained results are compared with a base line reference axial flux synchronous motor and experimental data.

## II. COGGING TORQUE IN AXIAL GAP PM MOTORS

Cogging torque of a full-pole stepping becomes equal to zero when the thread centre and interpolar axes are in the same line, and/or centre of the grooves and interpolar axes are in the same line. However, magnet always tends to be located around the location, where maximum energy is stored. This position comes to a stable balance position when leakage flux path between poles is minimum, and corresponds to unstable balance position when leakage flux paths contain groove apertures. Positive and negative end points of knocking torque in the form of waves, approximately correspond to the position, in which interpolar axes and edges of the grooves are in the same line [17].

In axial flux synchronous motors, rotor discs are made of massive iron. On the surface of the rotor, magnets are glued with a special adhesive material or they are bolted as demonstrated in Fig. 1.

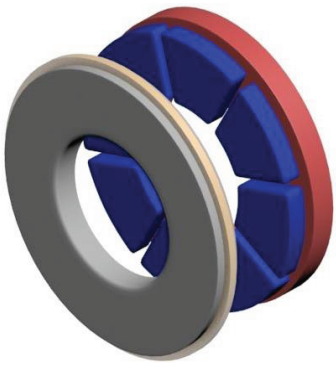

Fig. 1. Rotor with surface mounted magnet and stator.

The stator of the machine is formed by spirally winded laminated iron plaques. Different rotor and stator structures are presented in Fig. 2. Due to the ease of manufacturing and low cost and to provide the highest level of cogging torque minimization, the stator sluts in our study is designed to be totally open and they are winded in laminated structure. The rotor and stator structures are represented in more details for the configurations given in Fig. 2.

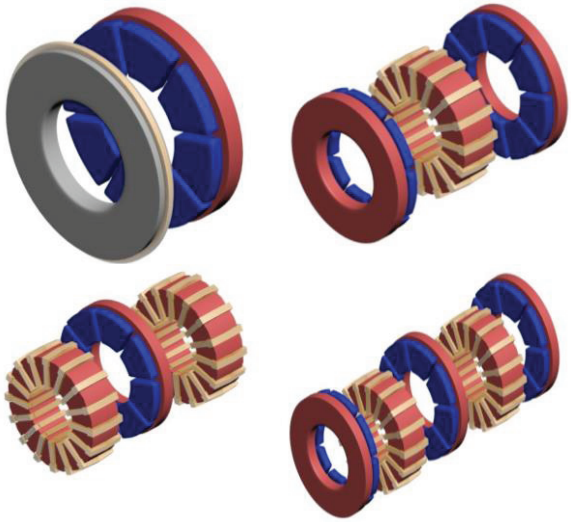

Fig. 2. Axial flux motors in various structures.

In permanent magnet motors, the cogging torque is generated due to the interactions between the magnets mounted within the rotor or rotor surface and the stator slots. Cogging torque has a negative effect on the average output torque and it is generated due to the movement of the rotor magnets because of the change in magnetic field [28].

If the amount of energy stored in the airgap is known, the cogging torque can be computed easily. If the electromagnetic system includes only the linear soft magnetic materials and linear permanent magnets, the system energy is simply the energy obtained from the magnets.

$$T_{cog}(\theta) = -\frac{dW}{d\theta}, \qquad (1)$$

here, θ is the mechanical rotor angle.

In Fig. 3, the curve that connects the permanent magnet motor's operating point and the origin is known as the load curve. Load curve is defined by the airgap reluctance. In SM machines with salient or slotted stator structures, the operating point of the magnet changes as the rotor rotates. For each rotor position, the operating point of the permanent magnet is defined and the total energy stored in the system is obtained. Thereby, the cogging torque is computed, too.

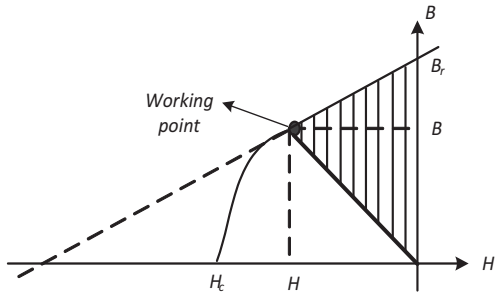


Fig. 3. B-H diagram and the energy density curve [29].

In this study, the cogging torque analysis is performed through the finite element method at the electromagnetic design process. The important advantage of the finite element analysis method is that its ability to calculate the torque ripples and cogging torque as the rotor position changes. In Fig. 4, one example of the mesh structures obtained with the 3-D FEA model is presented that is obtained by rotating one rotor relative to the other one. These analyses are completed with a computer with 3.16 GHz Intel Core 2 Quad processor and 3.49 GB of RAM. The number of total elements is 234745 and the total CPU processing time is 22 minutes.

In Fig. 5, the flux density of the AFPM motor's stator and no-load rotor is shown.

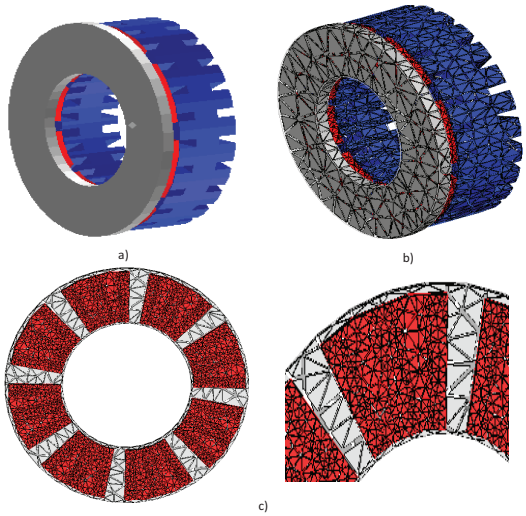


Fig. 4. AFPM motor's: (a) FEA model, (b) 3-D element structure, and (c) magnet element structure.

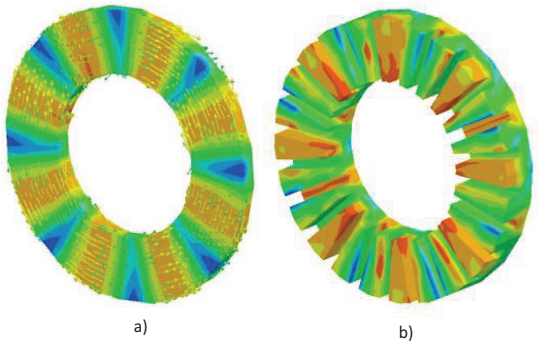


Fig. 5. Stator and no-load condition rotor flux density variations of the AFPM motor.

## III. PROPOSED TORUS NN-TYPE AXIAL FLUX PERMANENT MAGNET SYNCHRONOUS MOTOR STRUCTURE

In the analyses of this study, the permanent magnet motor of which the details are given in reference [30], is used as a base line. The reference motor is an axial flux motor with 24 slots, 8 poles, it has 2 rotors and 1 stator, its stator is siliceous laminated, and its rotor is a disc with surface mounted fan type magnets with 140° degrees of magnet pole-arc. No cogging torque reduction techniques are applied for this motor design. However for this study, differently from reference [30], an open stator slot structure is proposed. When the slot openings increased, the cogging torque increases about 2.5 times as compared to the previous structure as shown in Fig. 6. The reference motor parameters used in this study are given in Table 1.

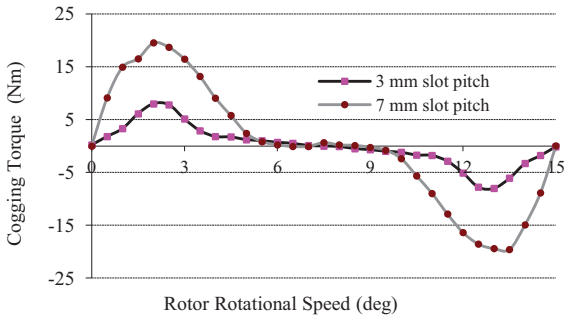


Fig. 6. Cogging moment variations with respect to the slot openness.

Table 1: AFPM reference motor parameters

| Parameter | Value |
|---|---|
| Stator outer radius | 89 mm |
| Stator inner radius | 50 mm |
| Magnet thickness | 7.2 mm |
| Stator axial length | 22 mm |
| Slot/pole/phase | 1 |
| Airgap | 0.8 mm |
| Phase number | 3 |
| Slot number | 24 |
| Slot pitch | 7 mm |

## IV. COGGING TORQUE REDUCTION TECHNIQUES FOR AXIAL FLUX PERMANENT MAGNET MOTORS AND 3-D FINITE ELEMENT ANALYSIS STUDIES

In this study, first, the various values of the magnet pole-arc is investigated for the fan type magnets. Then, according to the best results among these magnet pole-arc (126° degrees), triangle and oval shifting techniques are applied while keeping the magnet surface the same.

Similar to the fan type magnets, the different values of the magnet pole-arc are studied for triangle and oval type magnets.

### A. Varying the magnet pole-arc

One of the most common methods in cogging torque reduction of AFPM motors is changing the magnet pole-arc to an appropriate value. As known, cogging torque occurs due to the interactions between the magnet pole edges and the stator slots. Therefore, both the cogging torque waveform and its magnitude depend on the magnet pole-arc. Magnet leakage flux can be reduced by reducing the magnet pole-arc angle. However, reducing magnet flux reduces the average torque as well. Therefore, and appropriate magnet pole-arc angle should not cause a significant reduction in average torque while reducing the cogging torque.

In this study first of all, models are built in order to determine the most suitable structure of the conventional fan type magnets for reducing the cogging torque. Based on the obtained results, as can be seen in Table 2, 92.51% reduction is achieved in the fan type magnet structure with 126° degrees magnet pole-arc as compared to the 140° degrees magnet pole-arc. At this angle value, the cogging torque is measured as 1.426 Nm in the fan type magnet motor. In Fig. 7, the cogging torque magnitudes are graphically presented for the fan type magnet structures.

Table 2: Comparison of cogging torque values of fan type magnet structures with the reference motor

| Magnet Pole-arc (deg) | Peak Cogging Torque [Nm] | Comparisons with the Reference Motor |
|---|---|---|
| 100 | 24.802 | 27.06% rise |
| 120 | 12.62 | 35.34% decrease |
| 122 | 8,18 | 58,88% decrease |
| 125 | 2,976 | 84,75% decrease |
| 125.5 | 2,28 | 88,31% decrease |
| 126 | 1,462 | 92,51% decrease |
| 126.5 | 2,26 | 88,4% decrease |
| 128 | 5.28 | 73.94% decrease |
| 130 | 9.044 | 53.66% decrease |
| 140 | 19.518 | Reference motor |

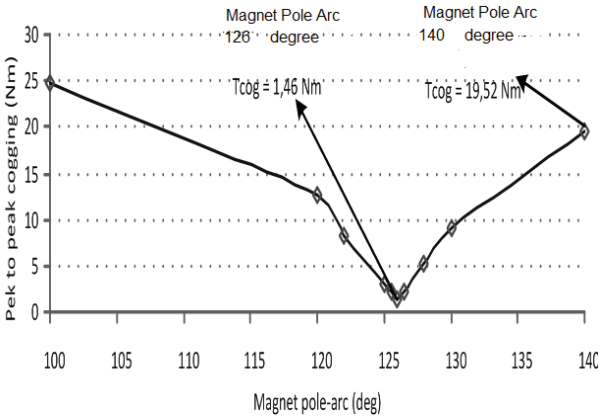


Fig. 7. Cogging torque peak values for the fan type magnet structures.

After obtaining the optimum structure for the fan type magnets, triangle and oval shaped magnet models are also studied while keeping the same magnet surface area.

All the triangle and oval skewed structures have the same magnet surface area with the fan type magnet structure with 126° degrees of magnet pole-arc. In other words, the magnet pole-arc angles are all defined for the same magnet surface areas for the triangle and oval skewed structures such that, $A_{126fan}=A_{triangle\_skew}=A_{oval\_skew}$.

The example drawings are illustrated in Fig. 8

that are used for determining the triangle and oval skew angles.

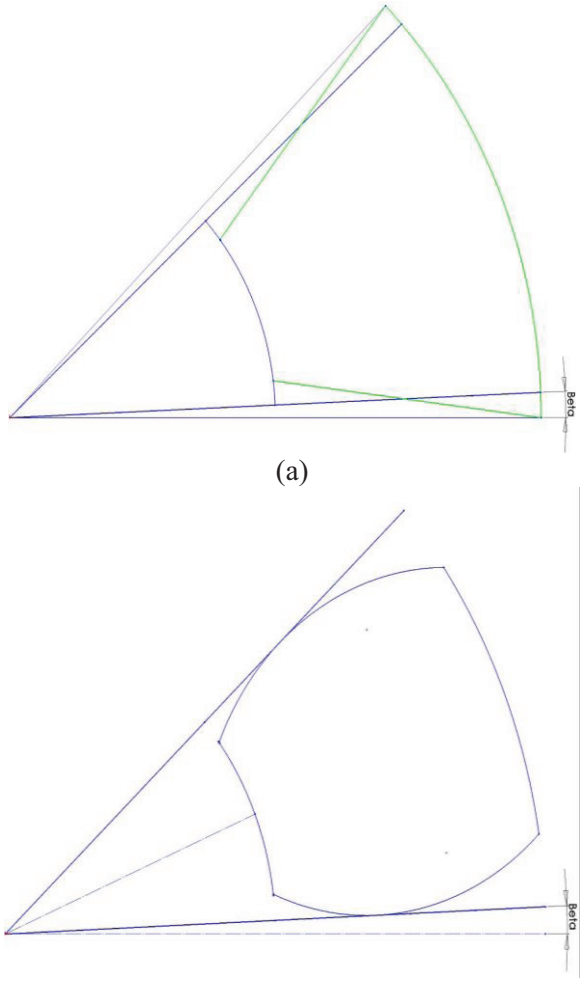


Fig. 8. Definition of the skew angle: (a) oval skew, and (b) triangle skew.

The cogging torque values obtained for these structures are given in Tables 3 and 4. According to the obtained results, the triangle type magnet model with 162° degrees magnet pole-arc has the maximum cogging torque reduction of 85.3% among the other triangle type models. At this magnet pole-arc angle of the triangle skewed type magnet motor, the cogging toque is obtained as 2.868 Nm. In Fig. 9, the cogging torque peak values are graphically represented for the triangle skew magnet structures.

Table 3: Comparison of cogging torque values of the triangle skew magnet structures with the reference motor

| Magnet Pole-arc (deg) | Peak Cogging Torque [Nm] | Comparisons with the Reference Motor |
|---|---|---|
| 152 | 3.622 | 81.44% decrease |
| 156 | 3.056 | 84.34% decrease |
| 160 | 2.934 | 84.96% decrease |
| 162 | 2.868 | 85.3% decrease |
| 164 | 3.104 | 84.09% decrease |
| 168 | 3.32 | 82.99% decrease |
| 170 | 3.514 | 81.99% decrease |
| 172 | 3.964 | 79.69% decrease |
| 176 | 4.576 | 76.55% decrease |
| 180 | 5.206 | 73.32% decrease |

Table 4: Comparison of cogging torque values of the oval type magnet structure with the reference motor

| Magnet Pole-arc (deg) | Peak Cogging Torque [Nm] | Comparisons with the Reference Motor |
|---|---|---|
| 130 | 8.538 | 81.44% decrease |
| 135 | 3.1 | 84.34% decrease |
| 137 | 2.044 | 84.96% decrease |
| 138 | 2.736 | 85.3% decrease |
| 139 | 2.738 | 84.09% decrease |
| 141 | 3.926 | 82.99% decrease |
| 154 | 7.628 | 81.99% decrease |
| 140 | 19.518 | Reference motor |

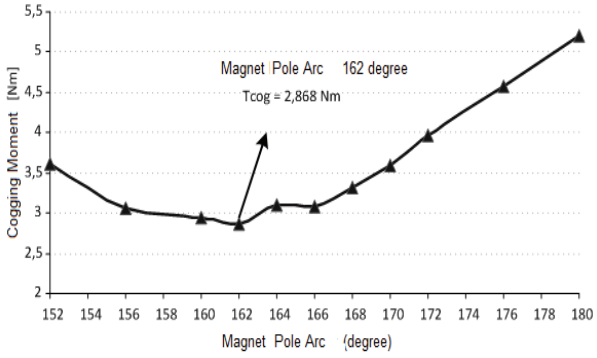


Fig. 9. Cogging torque peak values for the triangle skew magnet structures.

In Fig. 10, cogging torque peak values are graphically represented for the oval skew magnet structures.

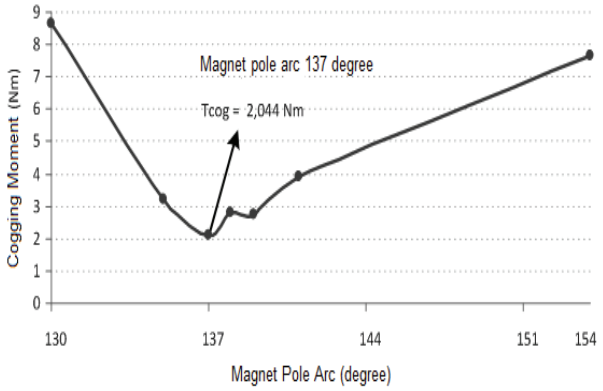


Fig. 10. Cogging torque peak values for the oval skew magnet structures.

According to the obtained results, the oval type magnet model with 137° degrees magnet pole-arc has the maximum cogging torque reduction of 89.527% among the other oval type models. At this magnet pole-arc angle of the oval skewed type magnet motor, the cogging toque is obtained as 2.044 Nm.

According to the analyses performed so far, the rotor with fan type magnets with 126° degrees of magnet pole-arc, the rotor with triangle skew type magnets with 162° degrees of magnet pole-arc, and the rotor with oval type skew magnets with 137° degrees of magnet pole-arc have resulted in the optimal designs among their categories. For all three types of magnet structures, the fan type magnet structure with 126° degrees of magnet pole-arc achieved the minimal cogging torque value.

**B. Rotating one rotor relatively to the other one**

In AFPM motors with two airgaps, the total cogging torque equals to the vector sum of the cogging torque at each airgaps. Therefore, if one of the rotors is rotated relatively to the other one, the vector summation of the cogging torques, hence the total cogging torque can be reduced. With this respect, this technique is applied on the fan, triangle skewed, and the oval skewed magnet structures and the graphs shown in Figs. 11 to 13 are obtained. According to these results, the triangle skew magnet structure with 156° degrees of magnet pole-arc angle achieves the best results in terms of cogging torque reduction when one of the rotors is rotated with 4° degrees with respect to the other rotor. In this case, the peak value of the cogging torque is reduced to 0.475 Nm. When compared to the reference motor, this means 97.56% reduction in cogging torque.

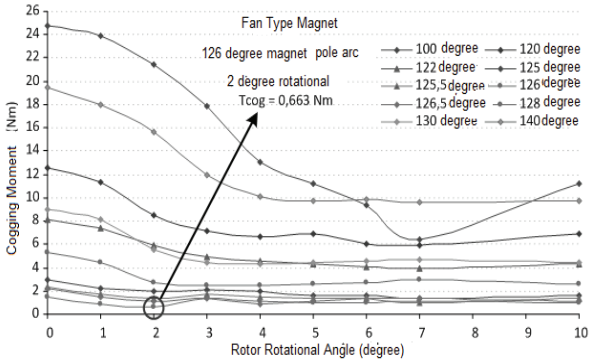


Fig. 11. Rotor rotation technique results for the fan type magnet structures.

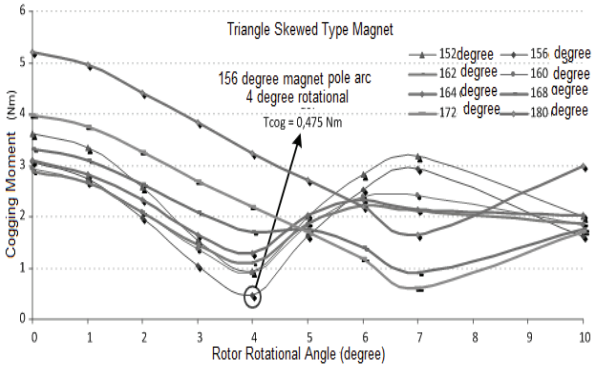


Fig. 12. Rotor rotation technique results for the triangle skewed type magnet structures.

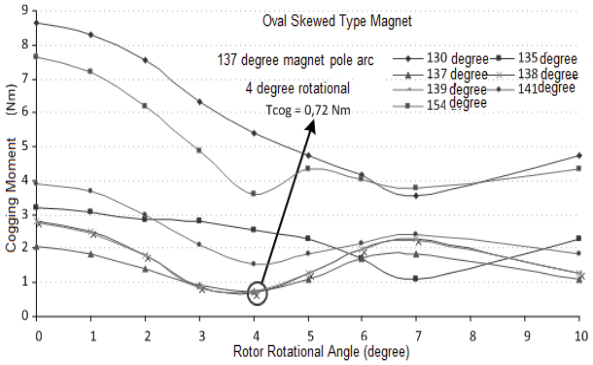


Fig. 13. Rotor rotation technique results for the oval skewed type magnet structures.

According to the analyses performed with the rotor rotation technique, when one rotor is rotated 2° degrees with respect to the other one, 0.663 Nm value is obtained for the fan type magnet structure with 126° degrees of magnet pole-arc angle. Similarly, when one rotor is rotated 4° degrees with respect to the other one, 0.475 Nm value is obtained for the triangle skewed type magnet structure with 156° degrees of magnet pole-arc angle. Consequently, when one rotor is rotated 4° degrees with respect to the other one, 0.72 Nm value is obtained for the oval skewed type magnet structure with 137° degrees of magnet pole-arc angle. The techniques that achieved best results for different motor structures are altogether presented in Table 5.

Table 5: Best results achieved with the applied techniques

| Applied Technique | $T_{cog}$ Peak Value [Nm] | Comparisons with the Reference |
|---|---|---|
| Fan type magnet structure with 126° degrees of magnet pole-arc angle | 1.462 | 92.51% reduction |
| Triangle type skewed magnet structure with 162° degrees of magnet pole-arc angle | 2.868 | 85.3% reduction |
| Oval type skewed magnet structure with 137° degrees of magnet pole-arc angle | 2.044 | 89.527% reduction |
| When one rotor is 4° degrees with respect to the other one, the triangle skewed type magnet structure with 156° degrees of magnet pole-arc angle | 0.475 | 97.56% reduction |
| Fan type magnet structure with 140° degrees of magnet pole-arc angle | 19.518 | Reference structure |

## V. EXPERIMENTAL RESULT

Magnet structures, from which the best results are obtained in terms of cogging torque as a result of the analyses performed, are shown in Table 6.

Table 6: Rotor structure, cogging torques of which will be analysed in laboratory

| Magnet Structure | Magnet Type | Description |
|---|---|---|
| Fan type 140° degrees | NdFeB | Reference structure |
| Fan type 126° degrees | NdFeB | Fan structure with the lowest $T_{cog}$ value |
| Triangular type 156° degrees | NdFeb | Triangular structure with the lowest $T_{cog}$ value |

Drawings of magnet types, FEA analysis of which have been performed, and optimum rotor structures of which are determined in Table 6, and magnet drawings used in production process are shown in Figs. 14, 15 and 16. Rotor disk of EASM motor, a prototype of which has been manufactured, can be made of standard steel and they can be produced as one-piece rotor discs, which will be used in this study, are designed specially for reducing cogging torque. The feature of these discs is that one can be turned in desired angles according to the other. In this way, knocking value of rotors, which are in different positions according to each other, will be analysed easily. In Fig. 17, drawings of rotor structure are given; in Fig. 18, pictures of special design rotor disc of motor and structure of turning gear operation are shown. In Fig. 19, phases of stator production are shown.

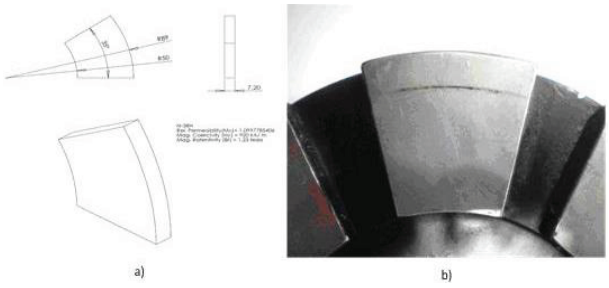


Fig. 14. Fan type 140° degree magnet.

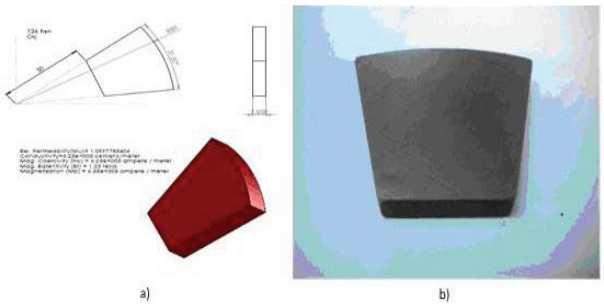


Fig. 15. Fan type 126° degree magnet.

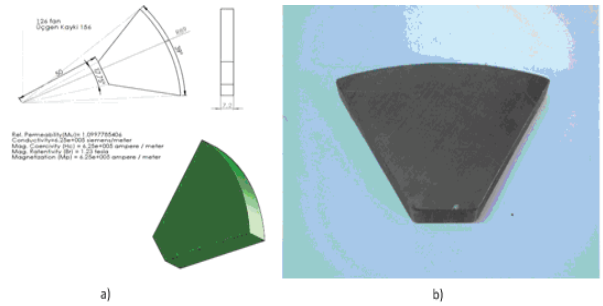


Fig. 16. Triangular skew 156° degree magnet.

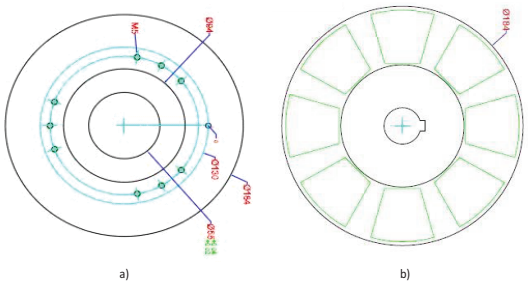


Fig. 17. (a) Moving disc, and (b) rotor drawings of EASM motor.

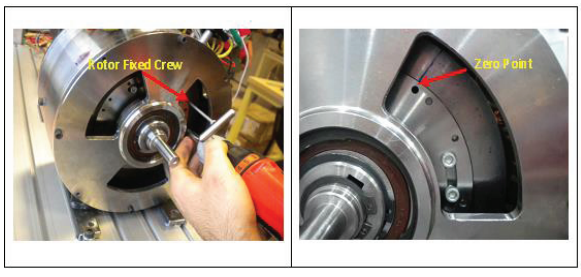


Fig. 18. (a) Rotation of rotor for EASM motors, and (b) specially designed rotor disc.

Fig. 19. Production phases of EASM disc motor stator.

Test system, which is designed for measuring the cogging torque after production process is completed, is shown in Fig. 20. In the measuring system, there are excitation oriented step motor and its driver and a torque sensor in order to retrieve data related to torque values. Motor was rotated at a low speed (1 rpm) in order to obtain more accurate results in knocking torque measurement.

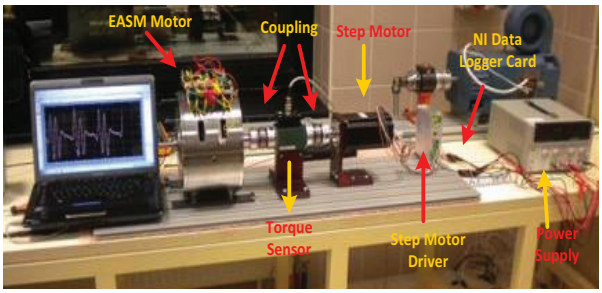


Fig. 20. Test system of EASM motor.

Experimental studies were conducted for axial flux machines with fan and triangular skew type rotor, and results of comparing each rotor structure with 3D FEA analysis were obtained as shown in Figs. 21 and 22. As shown in the results, FEA analyses of cogging torque and experimental results are compatible with each other.

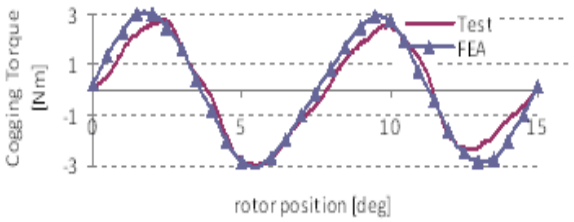


Fig. 21. A graphical comparison of FEA simulation of triangular skew (156° degree with magnet stepping) structure and cogging torque of experimental study.

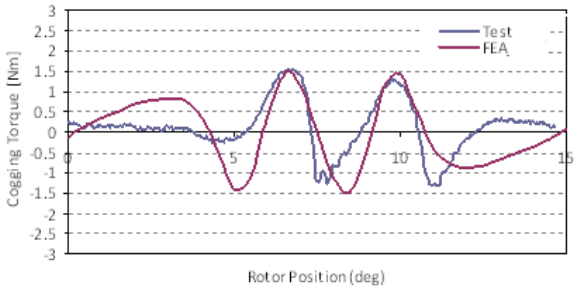


Fig. 22. A graphical comparison of FEA simulation of fan type (126° degree with magnet stepping) structure and cogging torque of experimental study.

## VI. RESULTS OF THE TORQUE ANALYSIS

In this section, the techniques achieved the better results for cogging torque reduction for the fan, triangle skewed, and oval skewed magnet structures are compared in terms of average torque analyses and the torque ripples. It is observed from the obtained results that that the methods proposed for the cogging torque reduction did not cause any significant reduction in the average torque (Fig. 23).

Furthermore, it is seen that the proposed structures and dimensions for the fan, triangle skewed and oval skewed magnets that achieved the best results in cogging torque reductions also significantly reduced the torque ripples as compared to the reference motor, according to Fig. 24. Since the reference motor is designed to have the maximum cogging torque, its torque ripples are also the maximum.

Among the fan type magnet structures, at 126° degrees of magnet pole-arc angle, the lowest cogging torque value and the smallest torque ripples are obtained. Similarly, among the triangle skewed type structures, at 156° degrees of magnet pole-arc angle, lowest cogging torque and lowest torque ripples are obtained when the rotor rotation technique is applied.

Thus, when the rotor rotations are applied too, the triangle skewed type magnet structure with 156° degrees of magnet pole-arc angle becomes the most optimal structure in terms of both the average torque and the torque ripples.

In this article, cogging torque reduction methodologies are discusses for the AFPM motors and a double rotor – single stator AFPM with open slot structure is designed in order to have a reference motor with the maximum cogging torque. Then, several techniques are applied to the motor to reduce the cogging torque and the motor is analyzed with the 3-D finite element analysis method in order to test the effectiveness of the proposed methods.

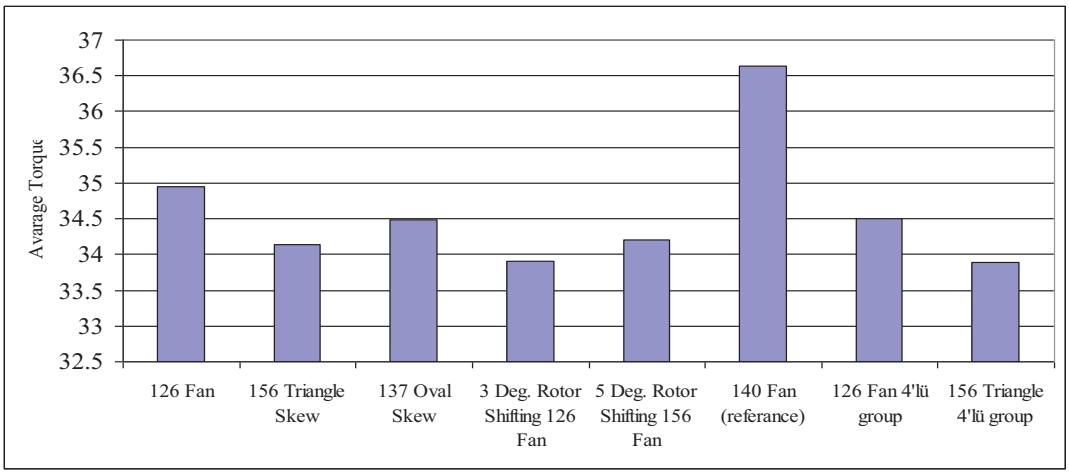


Fig. 23. Average torque comparisons.

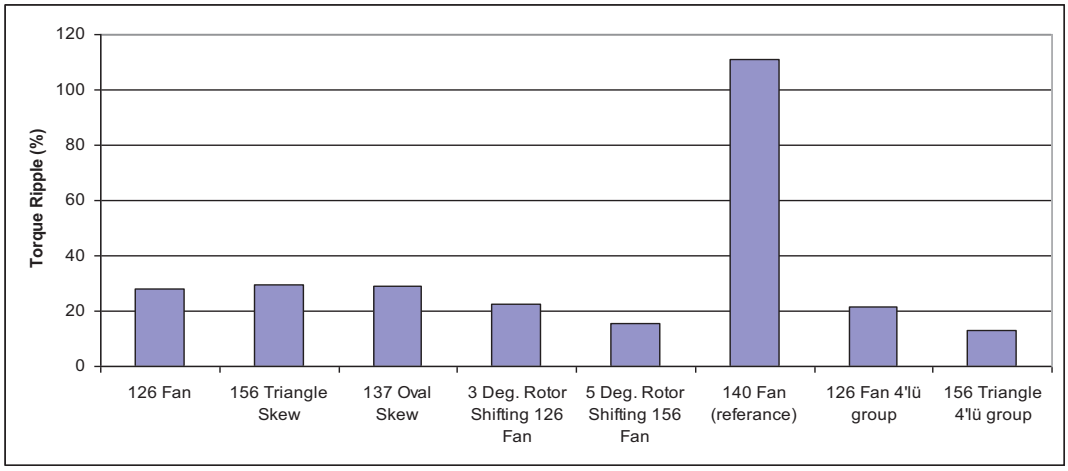


Fig. 24. Torque ripple comparisons.

The magnet skew method applied on the rotor site is a very functional method due to the manufacturing advantages introduced for the disc motors. Therefore, rotor side configuration adjustments are discussed in the proceeding sections of the article. Varying the magnet pole-arc angle on the rotor side and rotating one rotor relatively to the other rotor techniques are used.

According to the first studies performed to reduce the cogging torque, the maximum cogging torque reduction is observed at the fan type magnet structure with 126° degrees of magnet pole-arc angle as compared to the reference motor with 140° degrees of magnet pole-arc angle. At this angle value, the cogging torque is obtained as 1.462 Nm.

Once the optimal structure is obtained for the fan type magnet structure, magnet models with triangle skewed and oval skewed structures with the same surface area are studied. Accordingly, the motor with the triangle skewed magnet structure with 162° degrees of magnet pole-arc angle resulted in 58.3% maximum reduction as compared to the reference motor and the cogging torque value is obtained as 2.868 Nm. Similarly, the motor with the oval skewed magnet structure with 137° degrees of magnet pole-arc angle resulted in 89.527% maximum reduction as compared to the reference motor and the cogging torque value is obtained as 2.044 Nm.

The other technique used for the cogging toque reduction is that rotating one rotor relatively to the other one. According to the obtained results, the best cogging torque reduction is achieved when one rotor is 4° degrees rotated with respect to the other rotor in the triangle skewed structure with 156° degrees of magnet pole-arc angle. The peak value of the cogging torque is reduced to 0.475 Nm in this structure. Thus, 97.56% reduction is accomplished as compared to the reference motor.

In the last section of our study, the cogging torque reduction techniques applied on the rotor side are compared in terms of their effects on the average torque and the torque ripples. According to the analyses results, it is observed that the techniques that significantly reduce the cogging torque do not considerably reduce the average torque and they quite successfully reduce the torque ripples as compared to the reference motor.

## VII. CONCLUSION

In this study, analyses were performed on different magnet structures of rotor in order to decrease the cogging torque of axial flux permanent magnet synchronous machines and a prototype motor was produced by using magnet models in optimal structures, which were obtained as a result of FEM analyses. Experimental measurements were made by using the apparatus of the performed experiment, and relevant data were authenticated by comparison with simulation results. As a result of the experimental study for AFPM's, it was observed that in fan type structure with 126° degree magnet stepping, torque ripple decreased by

74.9% according to the reference structure, and in triangular skew structure with 156° degree magnet stepping, torque rippled decreased by according to the reference structure.

## REFERENCES


[1] N. Chaker, I. B. Salah, S. Tounsi, and R. Neji, "Design of axial-flux motor for traction application," *Journal of Electromagnetic Analysis and Applications*, vol. 1, no. 2, pp. 73-84, 2009.

[2] F. Caricchi, F. Crescimbini, F. Mezzetti, and E. Santini, "Multistage axial flux PM machine for wheel direct drive," *IEEE Transactions on Industry Applications*, vol. 32, no. 4, pp. 882-887, July/Aug. 1996.

[3] A. B. Letelier, D. A. González, J. A. Tapia, R. Wallace, and M. A. Valenzuela, "Cogging torque reduction in an axial flux PM machine via stator slot displacement and skewing," *IEEE Transactions on Industrial Applications*, vol. 43, no. 3, pp. 685-693, May/June 2007.

[4] M. Aydin, S. Huang, and T. A. Lipo, "New axial flux surface mounted permanent magnet machine capable of field control," *Industry Applications Conference, 37th IAS Annual Meeting*, pp. 1250-1257, Oct. 13-18, 2002.

[5] F. G. Capponi, G. De Donato, and F. Caricchi, "Recent advances in axial-flux permanent-magnet machine technology," *IEEE Transactions on Industry Applications*, vol. 48, no. 6, pp. 2190-2205, Nov.-Dec. 2012.

[6] H. Tiegna, Y. Amara, and G. Barakat, "Study of cogging torque in axial flux permanent-magnet machines using an analytical model," *Compumag 2013*, June 30-July 4, 2013.

[7] M. R Barzegaran, A. Sarikhani, and O. A. Mohammed, "Equivalent current loop model for the study of radiated electromagnetic field interference in multi-machine electric drives," *ACES 2011*, VA, USA, Mar. 27-31, 2011.

[8] M. R. Barzegaran, A. Sarikhani, and O. A. Mohammed, "An optimized equivalent source modeling for the evaluation of time harmonic radiated fields from electrical machines and drives," *Applied Computational Electromagnetics Society (ACES) Journal*, vol. 28, no. 4, pp. 273-283, Apr. 2013.

[9] R. Islam, I. Husain, A. Fardoun, and K. Mclaughlin, "Permanent-magnet synchronous motor magnet designs with skewing for torque ripple and cogging torque reduction," *IEEE Transactıons on Industry Applıcatıons*, vol. 45, no. 1, pp. 152-160, 2009.

[10] M. Aydin, Z. Q. Zhu, T. A. Lipo, and D. Howe, "Minimization of cogging torque in axial-flux permanent-magnet machines: design concepts," *IEEE Transactıons on Magnetıcs*, vol. 43, no. 9, pp. 3614-3622, 2007.

[11] C. Studer, A. Keyhani, T. Sebastian, and S. K. Murthy, "Study of cogging torque in permanent magnet machines," *IEEE Industry Applications Society Annual Meeting*, pp. 42-49, Oct. 5-9, 1997.

[12] D. A. González, J. A. Tapia, and A. Letelier, "Design consideration to reduce cogging torque in axial flux permanent-magnet machines," *IEEE Transactions on Magnetics*, vol. 43, no. 8, pp. 3435-3440, 2007.

[13] L. Zhu, S. Z. Jiang, Z. Q. Zhu, and C. C. Chan, "Analytical methods for minimizing cogging torque in permanent-magnet machines," *IEEE Transactions on Magnetics*, vol. 45, no. 4, pp. 2023-2031, Apr. 2009.

[14] N. Bianchi and S. Bolognani, "Design techniques for reducing the cogging torque in surface-mounted PM motors," *IEEE Transactions on Industry Applications*, vol. 38, no. 5, pp. 1259-1265, Sep./Oct. 2002.

[15] T. Li and G. Slemon, "Reduction of cogging torque in permanent magnet motors," *IEEE Transactions on Magnetics*, vol. 24, no. 6, pp. 2901-2903, Nov. 1988.

[16] B. Ackermann, J. H. H. Janssen, R. Sotteck, and R. I. van Steen, "New technique for reducing cogging torque in a class of brushless DC motors," *Proc. Inst. Elect. Eng.-Electr. Power Appl*., vol. 139, no. 4, pp. 315-320, July 1992.

[17] Z. Q. Zhu and D. Howe, "Influence of design parameters on cogging torque in permanent magnet machines," *IEEE Transaction on Energy Conversion*, vol. 15, no. 4, pp. 407-412, Dec. 2000.

[18]Y. Yang, X. Wang, R. Zhang, T. Ding, and R. Tang, "The optimization of pole-arc coefficient to reduce cogging torque in surface-mounted permanent magnet motors," *Transactions on Magnetics*, vol. 42, no. 4, pp. 1135-1138, Apr. 2006.

[19]Y. Yang, X. Wang, R. Zhang, C. Zhu, and T. Ding, "Research of cogging torque reduction by different slot width pairing permanent magnet motors," *In Proc. 8th Int. Electr. Mach. Syst. Conf.*, vol. 1, pp. 367-370, Sep. 2005.

[20]C. S. Koh and J.-S. Seol, "New cogging torque reduction method for brushless permanent-magnet motors," *Transactions on Magnetics*, vol. 39, no. 6, pp. 3503-3506, Nov. 2003.

[21]Y. Yang, X. Wang, X. Leng, D. Wang, and S. Liu, "Reducing cogging torque in surface-mounted permanent magnet motors by teeth notching," *In Proc. 2nd IEEE Ind. Eletron. Appl. Conf.*, pp. 265-268, May 2007.

[22]R. Lateb, N. Takorabet, and F. Meibody-Tabat, "Effect of magnet segmentation on the cogging torque in surface-mounted permanent-magnet motors," *Transactions on Magnetics*, vol. 42, no. 3, pp. 442-445, Mar. 2006.

[23]L. Dosiek and P. Pillay, "Cogging torque reduction in permanent magnet machines," *IEEE Transactions on Industry Applications*, vol. 43, no. 6, pp. 1565-1571, Nov./Dec. 2007.

[24]W. Fei and P. Luk, "A new technique of cogging torque suppression in direct-drive permanent-magnet brushless machines," *IEEE Transactions on Industry Applications*, vol. 46, no. 4, pp. 1332-1340, July/Aug. 2010.

[25]J. H. Choi, J. H. Kim, D. H. Kim, and Y. S. Baek, "Design and parametric analysis of axial flux PM motors with minimized cogging torque," *IEEE Transactions on Magnetics*, vol. 45, no. 6, pp. 2855-2858, 2009.

[26]Y. D. Chun, D. H. Koo, Y. H. Cho, and Y. W. Won-Young Cho, "Cogging torque reduction in a novel axial flux PM motor," *SPEEDAM 2006, International Symposium on Power Electronics, Electrical Drives, Automation and Motion*, pp. 1020-1023, May 23-26, 2006.

[27]L. Dong-Kuk, W. Dong-Kyun, K. Il-Woo, R. Jong-Suk, and J. Hyun-Kyo, "Cogging torque minimization of a dual-type axial-flux permanent magnet motor using a novel optimization algorithm," *IEEE Transactions on Magnetics*, vol. 49, no. 9, pp. 5106-5111, 2013.

[28]S. G. Asghar and A. Yousefi, "Power density comparison for three phase non-slotted double-sided AFPM motors," *Australian Journal of Basic and Applied Sciences*, vol. 4, pp. 5947-5955, 2010.

[29]K. Lu, P. O. Rasmussen, and E. Ritchie, "An analytical equation for cogging torque calculation in permanent magnet motors," *17th International Conference on Electrical Machines*, pp. 382-386, Oct. 5-8, 2006.

[30]E. Yolacan, E. Ozyurt, O. Ocak, and M. Aydin, "Coggıng torque minimization and torque qualıty of radıal and axıal flux permanent magnet servomotors," *11th International Workshop on Research and Education in Mechatronics*, Sept. 9-10, 2010.

**E. Aycicek** received his B.S., M.S. and Ph.D. degrees in Electrical Engineering from Yildiz Technical University, in 2001, 2005, and 2012, respectively. He is currently a Research Assistant at Yildiz Technical University. His current research interests include design and analysis of electrical machinery.

**N. Bekiroğlu** received her Ph.D. degree in Electrical Engineering from Yildiz Technical University, Turkey, in 1998. From 2000 to 2013, she worked as an Assistant Professor in the Electrical Engineering Department at the Yildiz Technical University. She is currently an Associate Professor in the Electrical Engineering Department at the same University. Her current

research interests include analysis and design of electrical machines and drives.

**I. Senol** received his Ph.D. degree in Electrical Engineering from Yildiz Technical University, Turkey, in 1992. During 1993-1999, he was an Assistant (Associate) Professor of Electrical Engineering at the Yildiz Technical University. He is currently a Professor in the Electrical Engineering Department at Yildiz Technical University. His current research interests include analysis and design of electrical machines and drives.

**Y. Oner** received her B.S., M.S. and Ph.D. degrees in Electrical Engineering from Yildiz Technical University, in 2007, 2009, and 2013 respectively. She is currently a Research Assistant in the Department of Electrical Engineering, Yildiz Technical University. Her current research interests include design and analysis of electrical machinery.

# Extended Bandwidth Monopole Antenna with Frequency Band-Stop Operation for Wireless Applications

**M. Akbari*[1], N. Rojhani [3], M. Saberi [3], S. Zarbakhsh [1], and A. Sebak [2]**

[1] Young Researchers and Elite Club, Central Tehran Branch
Islamic Azad University, Tehran, Iran
*akbari.telecom@gmail.com

[2] Electrical and Computer Department
Concordia University, Quebec, Canada, H3G 1M8

[3] Young Researchers and Elite Club, South Tehran Branch
Islamic Azad University, Tehran, Iran

***Abstract*** ― This letter proposes a new monopole antenna for wireless applications, in particular ultra wideband (UWB) with 3.5/5.5 GHz dual notched bands. The antenna includes square patch, 50 Ω microstrip feed-line, and a partial ground plane using a new structure provides a broad impedance bandwidth. In order to achieve dual notched bands at 3.5 GHz and 5.5 GHz, two radiating strips and a T-shaped slot on the radiating patch are applied, respectively. The antenna is simple in geometry and has a small size of 19×14 mm$^2$. The measured results show a desirable agreement with the simulated results. The antenna approximately produces omnidirectional radiation patterns in H-plane, and flat gain over the whole UWB frequency excluding the two notched bands (WiMAX and WLAN bands).

***Index Terms*** ― Antennas, notched band, UWB (Ultra Wideband), WiMAX, WLAN.

## I. INTRODUCTION

The advancement in ultra wideband (UWB) communication systems are developing at an unbelievable rate. Ultra wideband wireless systems are renowned and popular due to its advantages including high degree of reliability, robustness against jamming, low power consumption, and high data rate transmissions. Meanwhile, Federal Communications Commission (FCC) have defined UWB systems from the frequency band of 3.1 to 10.6 GHz in 2002 [1]. The design of the set of antennas in a compact dimension while providing wideband properties on all desirable frequency band is one of key issues in UWB communication. Thus, many antennas in different geometries with capabilities of super and ultra wideband have been presented [2-4]. However, there are some of the interference frequency bands into UWB such as the IEEE 802.16 standard for the Worldwide Interoperability for Microwave Access (WiMAX) system at 3.5 GHz (3.3-3.69 GHz), and the IEEE 802.11a standard for the Wireless Local Area Network (WLAN) system at 5.5 GHz (5.15-5.825 GHz). To address these drawbacks, there needs to be designed a special antenna with property of filtering interference bands. Recently, multiband stopped UWB antennas based on various techniques have been proposed [5-14]. The most common technique for a band-stopping is inserting slots. Diverse slots have been proposed by many researchers, to be inserted in the radiating element, ground plane, feeding line and vicinity of the radiating element [5-8]. The fractal structure is used to obtain both size reduction and frequency band notched characteristic in UWB antennas [12-13]. Because these structures are electronically small resonators with very high Qs, they can be considered as filters providing sharp notches or pass of certain frequency bands. Also, Electromagnetic Band Gap (EBG) structures are used to improve UWB antenna performance, such

*Submitted On: November 6, 2013*
*Accepted On: October 4, 2014*

as increasing the antenna's gain as well as producing a frequency stop-band characteristic [14]. These aforementioned methods can obtain a good single or dual stop-band property, but some of them are with large size or complicated design procedure which makes them unsuitable for the UWB antenna candidates. In this paper, a new dual stop-band antenna with compact size of 19×14 mm$^2$ is suggested. To obtain two stopped bands, two strip lines as radiating patch and a T-shaped slot which is etched off the radiating patch are used. The antenna was successfully fabricated and measured, and the experimental results depict an acceptable agreement with simulations. Section II describes the antenna design, discussions on results is presented in Section III followed by conclusive comments in Section IV.

## II. ANTENNA DESIGN

The proposed monopole antenna fed by a microstrip line is shown in Fig. 1, which is printed on an FR4 substrate of thickness of 1 mm, and relative permittivity of 4.4. The antenna has a compact size of 19×14 mm$^2$ or approximately 0.27λ×0.20λ at 4.2 GHz (the first resonant frequency). The antenna is excited using a 50 Ω microstrip line, with width 2.0 mm and length 7.0 mm. The basic antenna structure consists of a square radiating patch, a feed line, and a partial ground plane. By etching two inverted T-shaped slots on the ground plane, another resonant frequency is excited, which results in an extended impedance bandwidth of 13.7 GHz. Furthermore, by deforming square radiating patch to two radiating strip lines, a notched band at 3.5 GHz can be achieved whilst by etching a T-shaped slot off the patch and feed line, another notched band at centre frequency 5.5 GHz is obtained.

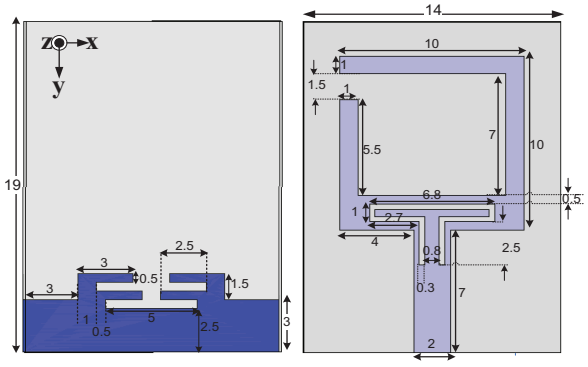


Fig. 1. Geometry of the proposed antenna.

## III. ANTENNA PERFORMANCE AND DISCUSSION

In this section, the effects of the different parameters on the antenna performance are investigated. The parameters of the antenna are studied by varying one or two parameters at a time and fixing the others. The simulated results are achieved using the Ansoft simulation software High-Frequency Structure Simulator (HFSSTM) [15] and CST software [16].

As mentioned before, to earn broad impedance bandwidth, the set of slots are utilized on the ground plane. Figure 2 shows reflection coefficient for different structures of antenna indicating tangible resonant frequencies and wide impedance bandwidth. As shown in Fig. 2, by etching two inverted T-shaped slots on the ground plane, the antenna will have a good impedance matching from 3.3 GHz by 13.5 GHz.

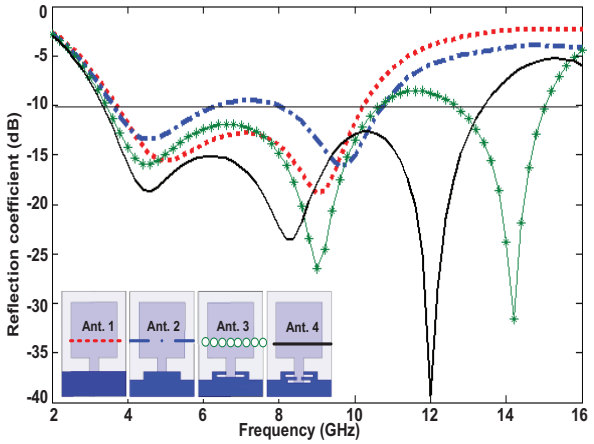


Fig. 2. Reflection coefficient characteristics for different structures of antenna indicating impedance bandwidth.

In other words, in Ant. 3, the third resonant frequency is excited by an inverted slot in 14.2 GHz, although impedance bandwidth from 10.8 GHz to 12.6 GHz is ruined, it means that it is more than -10 dB; therefore, by etching the second inverted T-shaped slot on the ground (Ant. 4), the third resonant frequency is replaced from 14.2 to 12 GHz. Consequently, the antenna will see a wide bandwidth from 3.3 to 13.5 GHz.

To study the effect of various parameters on the ground, Figs. 3 and 4 are presented. Regarding to Fig. 3, it is obvious that dx1 has important effect in producing the third resonant frequency. The best

value dx1 is 3.0 mm.

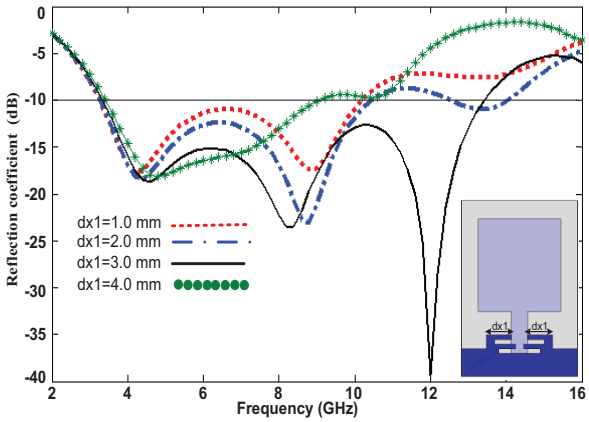


Fig. 3. Reflection coefficient characteristics for the antenna with different values dx1.

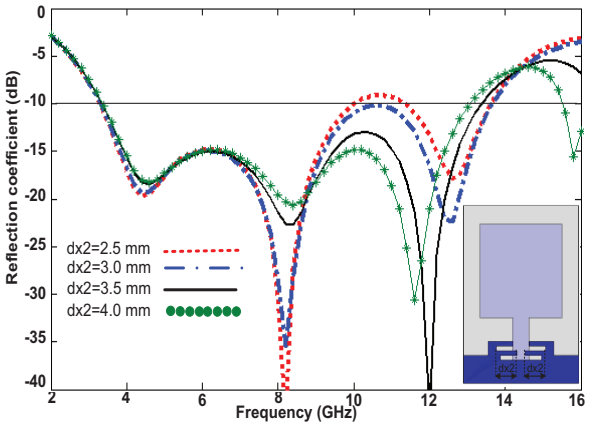


Fig. 4. Reflection coefficient characteristics for the antenna with different values dx2.

As exhibited in Fig. 4, parameters dx2 play an important role in shifting the third resonant frequency. Thus, among values of dx2 presented in Fig. 4, 3.5 mm is the best. As illustrated in Fig. 5, VSWR characteristics for different radiating patches of antenna including (1) square, (2) ring, (3) two strips, (4) two strips with T-shaped slot are compared to each other. As far as Fig. 5 is concerned, in order to generate single notched band at centre frequency 3.5 GHz, two radiating strips are utilized while by etching a T-shaped slot off the patch and feed line, another notched band at centre frequency 5.5 GHz is achieved. To exhibit being independent and controllable of both notched bands are applied Figs. 6 to 7. As depicted in Fig. 6, parameter dy1 has a markedly influence on frequency shifting for lower band stop. According to it, with increasing length dy1, the center frequency is decreased regularly in a way that by rising 1 mm in its length centre frequency of the notched band is reduced about 0.2 GHz. The best value dy1 for covering 3.3 to 3.69 corresponds to 10.0 mm. As mentioned before, in this study to generate the stop-band performance on upper band with center frequency 5.5 GHz, is used an T-shaped slot on the patch. The simulated VSWR curves with different values dy2 are plotted in Fig. 7. Related to it, when the length dy2 increases gradually, center frequency of the notched band is decreased steadily. Thus, the optimized dy2 is 2.8 mm.

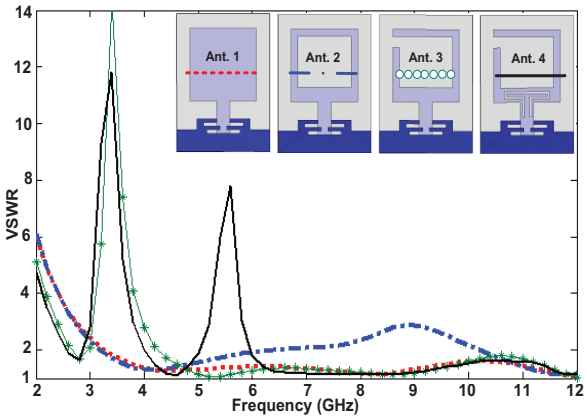


Fig. 5. VSWR characteristics for various structures of antenna indicating notched bands.

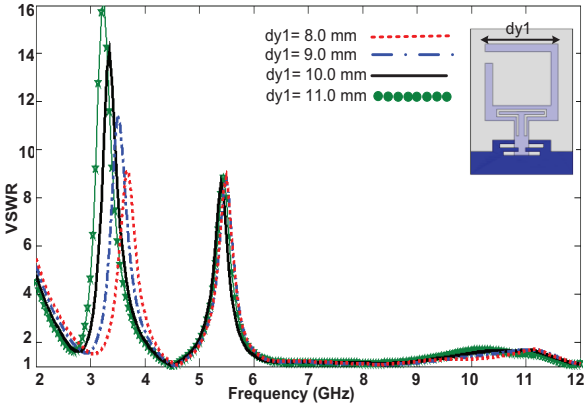


Fig. 6. VSWR characteristics for the antenna with different values dy1.

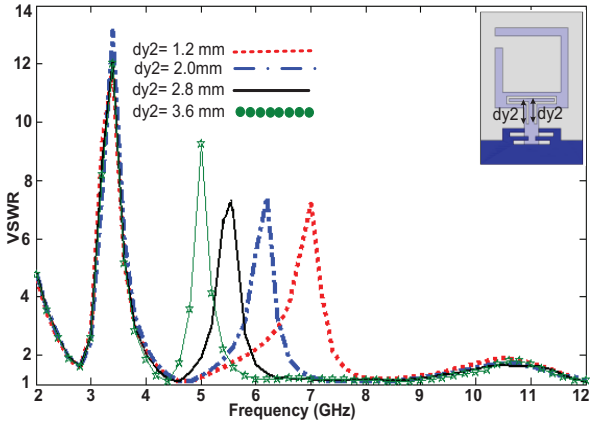


Fig. 7. VSWR characteristics for the antenna with different values dy2.

From these results, it can be found that the notched frequencies are controllable by changing the lengths dy1 and dy2. The proposed antenna with optimal design was fabricated and tested in the Antenna Measurement Laboratory at Iran Telecommunication Research Center. The numerical and experimental results of the input impedance and radiation characteristics are presented and discussed. Figure 8 shows the measured and simulated VSWR characteristics and photo of the fabricated antenna. The fabricated antenna is able to cover the frequency band from 2.6 GHz to more than 14.0 GHz for VSWR≤2, except the notched bands around 3.0 GHz to 4.05 GHz and 4.95 GHz to 5.9 GHz. The antenna has been simulated by both HFSS [15] and CST [16].

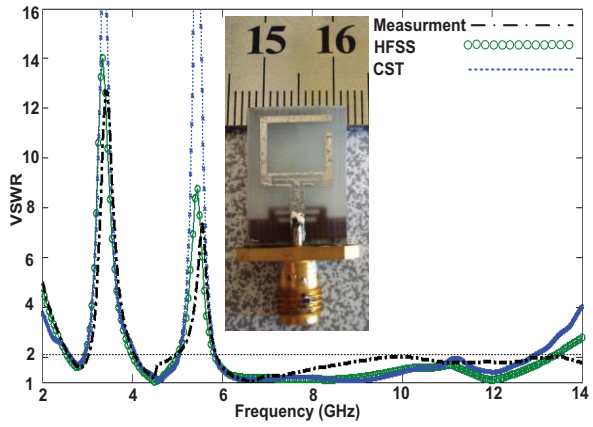


Fig. 8. Measured and simulated VSWR for the proposed antenna and photograph of the fabricated antenna.

Good agreement between simulated and measured results is observed and negligible difference between them is attributed to factors such as SMA connector effects, fabrication imperfections, and inappropriate quality of the microwave substrate. Figure 9 depicts measured gain of the antenna without and with notched bands. As shown in Fig. 9, two sharp decrease of maximum gain on notched bands at 3.5 GHz and 5.3 GHz are apparent. For other frequencies outside notched bands, the antenna nearly has a flat gain. Figure 10 exhibits the normalized far-field radiation patterns in both H-plane (x-z plane) and E-plane (y-z plane) at frequencies 6.5 and 8.5 GHz. It can be observed that the radiation patterns in x-z plane are approximately omnidirectional for the two frequencies, while radiation pattern in y-z plane are nearly bidirectional.

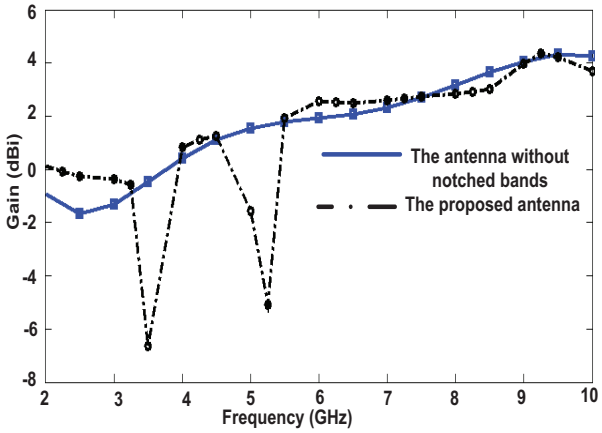


Fig. 9. Measured gain of the proposed antenna without and with notched bands.

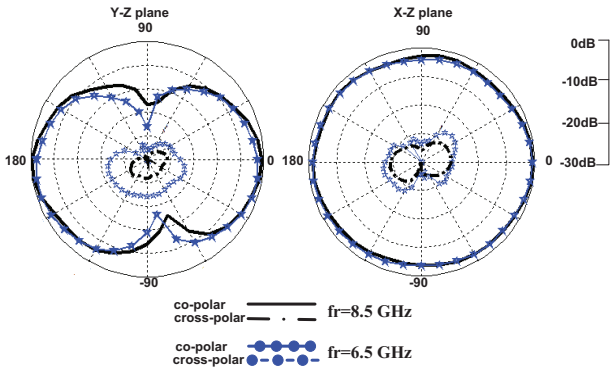


Fig. 10. Radiation patterns of the antenna at: (a) 6.5, and (b) 8.5 GHz.

## IV. CONCLUSION

In this letter, a new monopole antenna with frequency band-stop operation for wireless, in particular UWB, has been suggested. The fabricated antenna can cover an extended impedance bandwidth of 2.6 GHz to 14.0 GHz with two notched bands around 3.0 GHz to 4.05 GHz and 4.95 GHz to 5.9 GHz. The antenna has a simple configuration with a small size 19×14 $mm^2$ which is easy to fabricate. Generally speaking, novel techniques utilized in geometry and configuration to obtain extended bandwidth, two notched bands, compact size, and inexpensive substrate for fabrication are important factors indicating the antenna could be a good candidate for UWB applications.

## REFERENCES


[1] *Federal Communications Commission*, "First report and order on ultra-wideband technology," FCC 02-48, Washington, DC, April 22, 2002.

[2] M. Mighani, M. Akbari, and N. Felegari, "A novel SWB small rhombic microstrip antenna with parasitic rectangle into slot of the feed line," *Applied Computational Electromagnetics Society (ACES) Journal*, vol. 27, no. 1, pp. 74-79, January 2012.

[3] M. Akbari, M. Koohestani, C. H. Ghobadi, and J. Nourinia, "A new compact planar UWB monopole antenna," *International Journal of RF and Microwave Computer-Aided Engineering*, vol. 21, no. 2, pp. 216-220, March 2011.

[4] M. Akbari, M. Koohestani, C. Ghobadi, and J. Nourinia, "Compact CPW-fed printed monopole antenna with super wideband performance," *Microwave and Optical Technology Letters*, vol. 53, no. 7, pp. 1481-1483, July 2011.

[5] M. Akbari, S. Zarbakhsh, and M. Marbouti, "A new slot antenna with triple stop-band performance for UWB applications," *Microwave Opt Technol Lett*., vol. 55, no. 10, 2350-2354, 2013.

[6] M. Akbari, M. Khodaee, S. Zarbakhsh, and R. Gholami, "A simple UWB antenna with dual stop-band performance using rectangular slot and strip line ended up shorting pin," *Progress In Electromagnetics Research C*, vol. 42, 83-94, 2013.

[7] C. M. Li and L. H. Ye, "Improved dual band-notched UWB slot antenna with controllable notched bandwidths," *Progress In Electromagnetics Research*, vol. 115, 477-493, 2011.

[8] M. M. Abdollahi, H. R. Dalili Oskouei, M. Akbari, and M. Mighani, "A novel compact UWB antenna with triple band-notches for WiMAX/WLAN/ITU bands," *The Applied Computational Electromagnetic Society*, vol. 27, no. 12, 1014-1021, 2012.

[9] M. Akbari, S. Zarbakhsh, and M. Marbouti, "A novel UWB antenna with dual stop-band characteristics," *Microwave Opt Technol Lett*., vol. 55, no. 11, 2741-2745, 2013.

[10] M. Mighani, M. Akbari, and N. Felegari, "A CPW dual band notched UWB antenna," *Applied Computational Electromagnetics Society*, vol. 27, no. 4, 352-359, 2012.

[11] S. K. Mishra and J. Mukherjee, "Compact printed dual band-notched U-shape UWB antenna," *Progress In Electromagnetics Research C*, vol. 27, 169-181, 2012.

[12] J. K. Ali, A. J. Salim, A. I. Hammoodi, and H. Alsaedi, "An ultra-wideband printed monopole antenna with a fractal based reduced ground plane," *PIERS Proceedings*, 613-617, Moscow, Russia, August 2012.

[13] A. Karmakar, S. Verma, M. Pal, and R. Ghatak, "An ultra wideband monopole antenna with multiple fractal slots with dual band rejection characteristics," *Progress In Electromagnetics Research C*, vol. 31, 185-197, 2012.

[14] F. Xu, Z. X. Wang, X. Chen, and X. A. Wang, "Dual band- notched UWB antenna based on spiral electromagnetic-band gap structure," *Progress In Electromagnetics Research B*, vol. 39, 393-409, 2012.

[15] "Ansoft high frequency structure simulation (HFSSTM), ver. 13, *Ansoft Corporation*, 2010.

[16] "CST reference manual," Darmstadt, Germany, *Computer Simulation Technology*, 2008.


**Mohammad Akbari** was born on February 3, 1983 in Tehran, Iran; he received his B.Sc. degree in Engineering - Telecommunication from The University of Shahid Bahonar, Kerman, Iran, in 2007 and M.Sc. degrees in Electrical Engineering - Telecommunication from The University of Urmia, Urmia, Iran, in 2011. He has taught courses in microwave engineering, antenna theory, and Fields & Waves, and electromagnetic at Aeronautical University, Tehran, Iran. He is currently pursuing the Ph.D. degree jointly at Concordia University, Montreal, Canada. His main field of research contains analysis and design of microstrip antennas, modeling of microwave structures, radar systems, electromagnetic theory and analysis of UWB antennas for WBAN applications, antenna interactions with human body, computational electromagnetics (time- and frequency-domain methods), and microwave circuits and components. He is the author or co-author of

approximately 40 peer-reviewed scientific journals and international conference papers. Akbari was awarded the Graduate Concordia Merit Scholarship.

**Neda Rojhani** was born on September 21, 1987 in Zahedan, Iran; she received her B.Sc. degree in Electrical Engineering at The University of Sistan and Baluchestan, Zahedan, Iran, in 2010; she is studying her M.Sc. degree in Electrical Engineering at Islamic Azad University of South Tehran, Tehran, Iran. Her research interests include design of various antennas, antenna miniaturization, and antenna theory.

**Mehdi Saberi** was born in Iran; he is currently studying his M.Sc. degree in Electrical Engineering at Semnan University, Semnan, Iran. His research interests include antenna design antenna, miniaturization, microstrip antennas, filters and electromagnetic theory.

**Saman Zarbakhsh** was born on January 7, 1984 in Tehran, Iran; he received his B.Sc. degree in Electrical Engineering at Azad University of South Tehran, Tehran, Iran, in 2007 and his M.Sc. degree in Electrical Engineering from Urmia University, Urmia, Iran, in 2010. His research interests contain antenna design, antenna miniaturization and broadband circular polarized antennas.

**Abdel Razik Sebak** (F'10) received the B.Sc. degree (with honors) in Electrical Engineering from Cairo University, in 1976 and the B.Sc. degree in Applied Mathematics from Ein Shams University, in 1978. He received the M.Eng. and Ph.D. degrees from the University of Manitoba, in 1982 and 1984, respectively, both in Electrical Engineering. From 1984 to 1986, he was with the Canadian Marconi Company, working on the design of microstrip phased array antennas. From 1987 to 2002, he was a Professor in the Electrical and Computer Engineering Department, University of Manitoba. He is a Professor of Electrical and Computer Engineering, Concordia University. His current research interests include phased array antennas, computational electromagnetics, integrated antennas, electromagnetic theory, interaction of EM waves with new materials and bioelectromagnetics. Sebak received the 2000 and 1992 University of Manitoba Merit Award for outstanding Teaching and Research, the 1994 Rh Award for Outstanding Contributions to Scholarship and Research, and the 1996 Faculty of Engineering Superior Academic Performance. He is a Fellow of IEEE. He has served as Chair for the IEEE Canada Awards and Recognition Committee (2002-2004) and the Technical Program Chair of the 2002 IEEE-CCECE and 2006 ANTEM conferences.

# The Parallel Ray Propagation Fast Multipole Algorithm with Curve Asymptotic Phase Basis Function for Large-Scale EM Scatterings

**Z. H. Fan, Z. He, D. Z. Ding, and R. S. Chen**

Department of Communication Engineering
Nanjing University of Science and Technology, Nanjing, 210094, China
eerschen@njust.edu.cn

***Abstract*** ─ The curve asymptotic phase basis functions (AP-CRWG) are introduced to reduce the number of unknowns. Moreover, the parallel ray-propagation fast multipole algorithm (RPFMA) is used to accelerate the far-interaction calculation. The translation between any two groups in the multilevel fast multipole algorithm (MLFMA) is expensive and the translator is defined on an Ewald sphere with many $\hat{k}$ directions. When two groups are well separated, the translation can be simplified by using RPFMA, where only a few sampling $\hat{k}$ directions are required within a cone zone on the Ewald sphere. As a result, both the memory requirement and the CPU time can be saved significantly. Numerical examples are given to demonstrate that the proposed method is more efficient than both the conventional MLFMA and the RPFMA-MLFMA.

***Index Terms*** ─ Curve asymptotic phase basis function, electromagnetic scattering, method of moments (MoM), multilevel fast multipole algorithm (MLFMA), parallization, ray-propagation fast multipole algorithm (RPFMA).

## I. INTRODUCTION

The method of moments (MoM) [1-4] has been widely applied in a variety of electromagnetic (EM) radiation and scattering problems. The multilevel fast multipole algorithm (MLFMA) which is one of the most efficient approaches to solve large scale scattering problems can reduce both the memory requirement and the computational complexity. However, MLFMA is still expensive in solving the EM scattering problems for very large objects. The translation process is time consuming even though the interpolation and anterpolation are used. For very large-scale problems, the exact translation is used when two groups are close to each other. When groups are well separated, however, the translation can be simplified using a ray-propagation fast multipole algorithm (RPFMA) [5]-[7], where only a few sampling $\hat{k}$ directions are required within a cone zone on the Ewald sphere. Combining AP-CRWG and RPFMA with MLFMA, the algorithm AP-RPFMA-MLFMA is developed in this paper. It can be seen from the numerical results that the proposed AP-RPFMA-MLFMA is more efficient than both the conventional MLFMA and the RPFMA-MLFMA in 3-D electromagnetic scattering and radiation for very large structures.

In this paper, an efficient approach to accelerating the parallel curve asymptotic phase basis function (AP-CRWG) with the RPFMA is proposed for large scale scattering problems. The remainder of this paper was organized as follows. The introduction of the AP-CRWG, the RPFMA and the parallization are given in the Section II. Section III presents the numerical results to demonstrate the accuracy and efficiency of the proposed method. Finally, some conclusions are given in section IV.

## II. THEORY

### A. Curve asymptotic phase basis function

According to the Maxwell's equations, the surface equivalence principle and the constitutive relation, we can get:

$$\nabla \times \vec{E} = j\omega\mu\vec{H}, \tag{1}$$

$$\vec{J} = \hat{n} \times \vec{H}, \tag{2}$$

*Submitted On: May 20, 2013*
*Accepted On: April 15, 2015*

$$\vec{D} = \varepsilon \vec{E}, \tag{3}$$

where $\vec{E}$ stands for the electric field, $\vec{H}$ is the magnetic field, $\vec{J}$ is the electric current and $\vec{D}$ denotes the electric flux.

Therefore, the relationship between $\vec{J}$ and $\vec{D}$ can be written as:

$$\vec{J} = \frac{1}{j\omega\mu\varepsilon} \hat{n} \times \nabla \times \vec{D}, \tag{4}$$

where $\mu, \varepsilon$ are permittivity and permeability respectively. The curl of $\vec{D}$ can be written as:

$$\begin{aligned} \nabla \times \vec{D} &= (\nabla_t + \hat{n}\frac{\partial}{\partial n}) \times (\vec{D}_t + \hat{n} D_n) \\ &= \nabla_t \times \vec{D}_t + \nabla_t \times \hat{n} D_n + \hat{n} \times \frac{\partial \vec{D}_t}{\partial n}, \end{aligned} \tag{5}$$

where $\hat{n}$ stands for the normal unit vector, $D_n$ is the normal component of $\vec{D}$, $\vec{D}_t$ is the tangential component of $\vec{D}$. From (4) and (5), we can get:

$$\vec{J} = \frac{1}{j\omega\mu\varepsilon} (\nabla D_n - \frac{\partial D_t}{\partial n}). \tag{6}$$

In addition to the boundary conditions and the current continuity:

$$D_n = \rho_s, \tag{7}$$

$$\nabla_t \cdot \vec{J} = j\omega\rho_s. \tag{8}$$

From (6), (7) and (8), we can get:

$$\nabla_t^2 \rho_s + k^2 \rho_s = \nabla_t \bullet \frac{\partial D_t}{\partial n}. \tag{9}$$

The solution of (9) can be written as:

$$\rho_s(\vec{r}) = \sum_{m=1}^{M} C_m e^{-j\vec{k}^i \bullet \vec{r}} + D(\vec{r}) e^{-j\vec{k}^i \bullet \vec{r}}, \tag{10}$$

where $\vec{k}^i$ is the incident direction of propagation.

From the above analysis, the relationship is formed as:

$$\vec{J}(\vec{r}) \sim e^{-j\vec{k}^i \bullet \vec{r}}. \tag{11}$$

The current on ideal conductive surfaces has the phase characteristic, so the basis function which is used to approximate surface current also has amplitude and phase. Curved triangles are used to subdivide the surface of the target. Surface current can be expressed as follows:

$$\vec{J}(\vec{r}) = \sum_{n=1}^{N} a_n \vec{F}_n(\vec{r}) = \sum_{n=1}^{N} a_n \vec{f}_n(\vec{r}) e^{-j\vec{k}^i \cdot \vec{r}}, \tag{12}$$

where $\vec{f}_n(\vec{r})$ is CRWG basis function.

By using this basic function, the number of unknowns can be reduced greatly with encouraging accurate results when compared with the RWG basis functions.

### B. Ray propagation fast multipole algorithm (RPFMA)

The scalar Green's function for 3-D problems can be expanded:

$$\frac{e^{ik\left|\vec{r}_i - \vec{r}_j\right|}}{\left|\vec{r}_i - \vec{r}_j\right|} = \frac{ik}{4\pi} \int d^2\hat{k} e^{i\vec{k} \cdot (\vec{r}_{im} + \vec{r}_{nj})} \alpha_{mn}\left(\hat{k} \cdot \hat{r}_{mn}\right), \tag{13}$$

where the integral is defined on a unit sphere $S_E$, the Ewald sphere, and $\vec{r}_i, \vec{r}_j$ are the observation point vector and the source point vector respectively, and $\vec{r}_{im}, \vec{r}_{nj}$ are the spatial vector from the center of the observation group to the observation point and the spatial vector from the center of the source group to the source point respectively, and $\alpha_{mn}$ is called a translator between the two groups which is defined as:

$$\alpha_{mn}\left(\hat{k} \cdot \hat{r}_{mn}\right) = \sum_{j=0}^{L} i^j (2j+1) h_j^{(1)}(kr_{mn}) P_j(\hat{k} \cdot \hat{r}_{mn}), \tag{14}$$

where L is the truncation number of an infinite series, and related to the group size.

In the conventional MLFMA based on (14), all $\hat{k}$ directions on the Ewald sphere are involved in the translation. Hence, a large number of sampling $\hat{k}$ directions have to be used in the numerical implementation for large-scale problems [8]. As a result, it is very time consuming to perform the exact translation. It should be noted that the truncation of an infinite summation is required for the translator. Such truncation is equivalent to the use of a square window. However, it is equally valid to use another window function which makes a smooth transition from one to zero. (14) can be rewritten as:

$$\alpha_{mn}\left(\hat{k} \cdot \hat{r}_{mn}\right) = \sum_{j=0}^{L} i^j (2j+1) h_j^{(1)}(kr_{mn}) P_j(\hat{k} \cdot \hat{r}_{mn}) w_j, \tag{15}$$

where $w_l = \begin{cases} 1 & l \le J \\ \frac{1}{2}\left[1 + \cos(\frac{l-J}{L-J}\pi)\right] & l > J \end{cases}$ is the window function. The advantage of such window function in (15) is to make the main beam of the translator pattern sharper and sidelobes lower. This

is the main idea of RPFMA. Physically speaking, as shown in Fig. 1, the effective beamwidth forms a cone region around the ray direction $\hat{r}_{mn}$ on the Ewald sphere, whose solid angle is $\hat{\theta}_e$. Hence, only the $\hat{k}$ directions within the cone region have strong contribution to the translator, and all the $\hat{k}$ directions outside the region will be discarded. In this case, only a small number of $\hat{k}$ directions on the Ewald sphere are used, which makes RPFMA much more efficient.

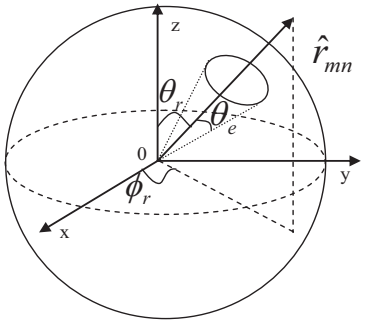


Fig. 1. Ewald sphere.

### C. Parallization

Although the MLFMA reduces the complexity of MoM from $O(N^2)$ to $O(N\log N)$, allowing for the solution of large problems with limited computational resources. However, accurate solutions of large problems require discretization's with millions of unknowns, which cannot be solved with sequential implementations of MLFMA running on a single processor easily. To solve such large problems, it is helpful to increase computational resource by assembling parallel computing platforms and, at the same time, by paralleling MLFMA [9-13]. There are many studies that have been done to improve the efficiency of the parallel MLFMA [14-15] Thanks to these studies, problems with millions of unknowns have been solved on relatively inexpensive platforms.

Series of implementation techniques have been developed for efficiently parallelizing the MLFMA. These techniques are different, but the most important thing in those techniques in parallelizing MLFMA is load-balancing and minimizes the communications between the processors. This is achieved by using different partitioning strategies for the lower and higher levels of the tree structure. In the lower levels of the tree structure, there are many clusters with small number of samples for the radiated and incoming fields. The number of cubes is much larger than the number of processors. Therefore, it is natural to distribute the cubes equally among processors. However, it is difficult to achieve good load-balancing in higher levels with this parallel approach, since the number of cubes in the coarse levels is small and the electric size of the cube is large, the far-field patterns is large. Therefore, in the coarse level, we adopt another parallel approach in the coarse levels; we partition the far-field patterns equally among all processors and send the needed messages to each processor. Using this approach for the parallel MLFMA in the far-field, good load balancing can be achieved.

## III. NUMERICAL RESULTS

In this section, three examples are presented to demonstrate the benefits of the proposed method. In our experiments, the restarted version of GMRES [16] algorithm is used to solve the linear systems. All cases are tested on HP server with Intel Xeon CPU X5550 (2.67 GHz). The operating system is Red Hat Enterprise Linux Server release 5.3. The environment of compiling is Intel Visual Fortran 9. Additional details and comments on the implementation are given as follows:

- The terminating tolerances of the RPFMA are set as 0.001.
- The resulting linear systems are solved iteratively by the GMRES (30) solver with a relative residual of $10^{-3}$.
- Zero vector is taken as initial approximate solution for all examples.
- The maximum number of iterations is limited to be 5000.
- The second and third examples are performed on 10-node cluster connected with an Infiniband network. Each node includes 8 cores and 48 GB of RAM. One node is used in the first examples with 8 cores.
- The mesh size for both the conventional MLFMA and the RPFMA-MLFMA is $0.15\lambda$, while the mesh size for the proposed AP-RPFMA-MLFMA is $1.0\lambda$.

We first consider the scattering from a strip of $9m\times 3m$ at the frequency of 3 GHz. When the incident plane wave is fixed at $\theta_{inc}=60^\circ$ $\phi_{inc}=0^\circ$,

the bistatic RCS results for VV polarization computed by the conventional MLFMA, AP-RPFMA-MLFMA are shown in Fig. 2. Four-level algorithms have been used in the AP-RPFMA-MLFMA algorithm while seven-level algorithms have been used in the conventional MLFMA. Figure 2 illustrates the validation of numerical results from the AP-RPFMA-MLFMA against the conventional MLFMA. The comparison of the translator numbers between the MLFMA and the RPFMA is listed in Table 1. The comparisons of the number of unknowns, the iteration number, the translator pattern memory and the total time of the conventional MLFMA, RPFMA-MLFMA and the AP-RPFMA-MLFMA are shown in Table 2.

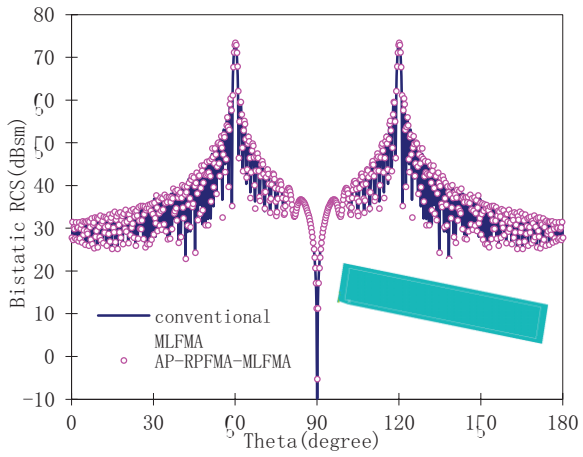


Fig. 2. Bistatic RCS of a strip of $90\lambda \times 30\lambda$ (V-V polarization).

Table 1: Comparison of the translator numbers between the MLFMA and the RPFMA for the strip

| Nlevel | $\hat{\theta}_e$ | Number of Translator for MLFMA | Number of Translator for RPFMA |
|---|---|---|---|
| 1 | $1.0\pi$ | 2738 | 2738 |
| 2 | $0.6\pi$ | 9522 | 6881 |
| 3 | $0.3\pi$ | 34848 | 10296 |
| 4 | $0.2\pi$ | 130050 | 50090 |

Next, we consider the scattering from a PEC sphere with the radius of 80 m at the frequency of 0.6 GHz. The incident plane wave is fixed at $\theta_{inc} = 0^\circ \quad \phi_{inc} = 0^\circ$, the scattering angle is fixed at $\theta_s = 0^\circ \sim 180^\circ \quad \phi_s = 0^\circ$. As shown in Fig. 3, there is a good agreement between the AP-RPFMA-MLFMA and the conventional MLFMA. Six-level algorithms have been used in the AP-RPFMA-MLFMA while nine-level algorithms have been used in the conventional MLFMA. The comparison of the translator numbers between the MLFMA and the RPFMA is listed in Table 3. The comparisons of the number of unknowns, the iteration number, the translator pattern memory and the total time of the conventional MLFMA, RPFMA-MLFMA and the AP-RPFMA-MLFMA are illustrated in Table 4. Clearly, both the memory requirement and the total CPU time in AP-RPFMA-MLFMA have been reduced.

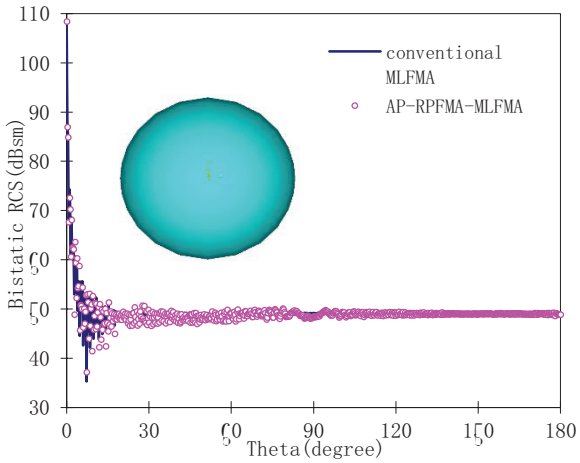


Fig. 3. Bistatic RCS of a PEC sphere of radius 80 m at 0.6 GHz (V-V polarization).

Table 3: Comparison of the translator numbers between the MLFMA and the RPFMA for the PEC sphere

| Nlevel | $\hat{\theta}_e$ | Number of Translator for MLFMA | Number of Translator for RPFMA |
|---|---|---|---|
| 1 | $1.0\pi$ | 2312 | 2312 |
| 2 | $0.6\pi$ | 7688 | 5550 |
| 3 | $0.3\pi$ | 27848 | 8260 |
| 4 | $0.2\pi$ | 103968 | 41195 |
| 5 | $0.15\pi$ | 399618 | 117785 |
| 6 | $0.1\pi$ | 1562912 | 303751 |

At last, the proposed method is used to analysis scattering from a satellite with longest length of 22 m at 13 GHz. Seven-level algorithms have been used in the AP-RPFMA-MLFMA while eleven-level algorithms have been used in the conventional

MLFMA. The incident plane wave direction is fixed at $\theta_{inc} = 0^\circ \quad \phi_{inc} = 0^\circ$, the scattering angle is fixed at $\theta_s = 0^\circ \sim 180^\circ \quad \phi_s = 0^\circ$. Figure 4 shows the bistatic RCS results for VV polarization computed by the conventional MLFMA and the AP-RPFMA-MLFMA. The comparison of the translator numbers between the MLFMA and the RPFMA is listed in Table 5. The comparisons of the number of unknowns, the iteration number, the translator pattern memory and the total time of the conventional MLFMA, RPFMA-MLFMA and the AP-RPFMA-MLFMA are shown in Table 6.

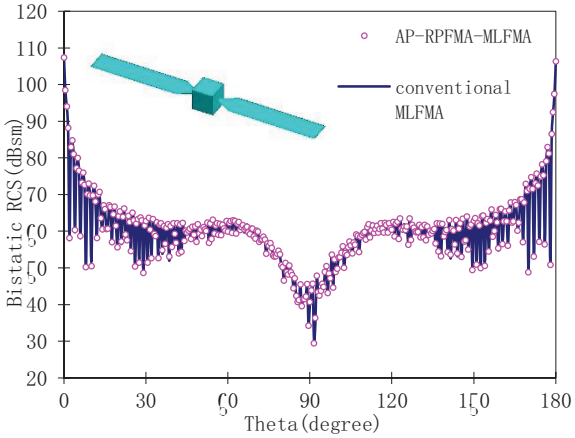


Fig. 4. Bistatic RCS of a satellite at 13 GHz (V-V polarization).

From the above figures, we clearly see that the numerical results from the AP-RPFMA-MLFMA are very accurate in both cases while the tolerance is set as 0.001. This is because the near neighbor groups have been treated using MLFMA exactly. $\hat{\theta}_e$ is an experiential number, which is related to the distance between the observation group and the source group. The corresponding $\hat{\theta}_e$ can be chosen smaller when the observation group is far away from the observation group.

Table 5: Comparison of the number of translator between the MLFMA and the RPFMA algorithm for the satellite

| Nlevel | $\hat{\theta}_e$ | Number of Translator for MLFMA | Number of Translator for RPFMA |
|---|---|---|---|
| 1 | $1.0\pi$ | 4418 | 4418 |
| 2 | $0.6\pi$ | 15488 | 11190 |
| 3 | $0.3\pi$ | 57800 | 17340 |
| 4 | $0.2\pi$ | 219122 | 87691 |
| 5 | $0.15\pi$ | 852818 | 254895 |
| 6 | $0.1\pi$ | 3348872 | 665146 |
| 7 | $0.08\pi$ | 13271552 | 2099288 |

Table 2: Comparisons of the number of unknowns, the iteration number, the translator pattern memory and the total time of the conventional MLFMA, RPFMA-MLFMA and the AP-RPFMA-MLFMA for the strip

| Method | Unknowns | Iteration Number | Translator Pattern Memory (MB) | Total Time (s) | Saving in Memory (%) |
|---|---|---|---|---|---|
| Conventional MLFMA | 415,692 | 1788 | 415.91 | 13919 | * |
| RPFMA-MLFMA | 415,692 | 1790 | 276.34 | 9561 | 33.56 |
| AP-RPFMA-MLFMA | 12,750 | 278 | 34.18 | 785 | 91.78 |

Table 4: Comparisons of the number of unknowns, the iteration number, the translator pattern memory and the total time of the conventional MLFMA, RPFMA-MLFMA and the AP-RPFMA-MLFMA for the PEC sphere

| Method | Unknowns | Iteration Number | Translator Pattern Memory (MB) | Total Time (s) | Saving in Memory (%) |
|---|---|---|---|---|---|
| Conventional MLFMA | 12,275,926 | 168 | 6519.06 | 19370 | * |
| RPFMA-MLFMA | 12,275,926 | 169 | 1741.97 | 12291 | 73.27 |
| AP-RPFMA-MLFMA | 478,776 | 30 | 223.29 | 3984 | 96.57 |

Table 6: Comparisons of the number of unknowns, the iteration number, the translator pattern memory and the total time of the conventional MLFMA, RPFMA-MLFMA and the AP-RPFMA-MLFMA for the satellite

| Method | Unknowns | Iteration Number | Translator Pattern Memory (MB) | Total Time (s) | Saving in Memory (%) |
|---|---|---|---|---|---|
| Conventional MLFMA | 18,502,579 | 5000 | 94080.48 | 57156 | * |
| RPFMA-MLFMA | 18,502,579 | 5000 | 8941.63 | 34209 | 90.49 |
| AP-RPFMA-MLFMA | 596,696 | 1534 | 1533.31 | 23652 | 98.37 |

## IV. CONCLUSION

This paper presents the parallel ray propagation fast multipole algorithm with curve asymptotic phase basis function for large scale scattering problems. Numerical results show the efficiency of the presented technique for analyzing large-scale EM scattering problems. AP-CRWG is more efficient in reducing the number of unknowns, memory requirement and calculation time than the conventional RWG. Based on the conventional MLFMA, we introduce RPFMA to accelerate far interactions. Compared with both the conventional MLFMA and the RPFMA-MLFMA, both the memory requirement and the CPU time can be reduced by using the proposed algorithms while assuring the precision.

## ACKNOWLEDGMENT

We would like to thank the support of Natural Science Foundation of 61431006, 61271076, 61171041, 61371037, Jiangsu Natural Science Foundation of BK2012034, Ph.D. Programs Foundation of Ministry of Education of China of 20123219110018; the Fundamental Research Funds for the Central Universities of No. 30920140111003, No. 30920140121004.

## REFERENCES

[1] S. Rao, D. Wilton, and A. Glisson, "Electromagnetic scattering by surfaces of arbitrary shape," *IEEE Trans. Antennas and Propag*., vol. 30, no. 3, pp. 409-418, May 1982.

[2] L. P. Zha, Y. Q. Hu, and T. Su "Surface integral equation using hierarchical vector bases for complex EM scattering problems," *IEEE Trans. Antennas and Propag*., vol. 60, no. 2, pp. 952-957, Feb. 2012.

[3] K. A. Michalski and D. L. Zheng, "Electromagnetic scattering and radiation by surfaces of arbitrary shape in layered media, part II: implementation and results for contiguous half-spaces," *IEEE Trans. Antennas and Propag*., vol. 38, no. 3, pp. 345-352, 1990.

[4] D. Ding, J. Ge, and R. Chen, "Well-conditioned CFIE for scattering from dielectric coated conducting bodies above a half-space," *ACES Journal*, vol. 25, no. 11, pp. 936-946, Nov. 2010.

[5] R. Coifman, V. Rokhlin, and S. M. Wandzura, "Fast single-stage multipole method for the wave equation," in *Proc. 10th Annu. Rev. Progress Appl. Computat. Electromagn*., Monterey, CA, pp. 19-24, Mar. 1994.

[6] R. L. Wagner and W. C. Chew, "A ray-propagation fast multipole algorithm," *Microwave Opt. Tech. Lett*., vol. 7, no. 10, pp. 435-438, 1994.

[7] C. C. Lu and W. C. Chew, "Fast far-field approximation for calculating the RCS of large objects," *Microwave Opt. Tech. Lett*., vol. 8, no. 5, pp. 238-241, 1995.

[8] T. J. Cui, W. C. Chew, G. Chen, and J. Song, "Efficient MLFMA, RPFMA, and FAFFA algorithms for EM scattering by very large structures," *IEEE Trans. Antennas and Propag*., vol. 52, no. 3, Mar. 2004.

[9] H. Zhao, J. Hu, and Z. Nie, "Parallelization of MLFMA with composite load partition criteria and asynchronous communication," *ACES Journal*, vol. 25, no. 2, pp. 167-173, Feb. 2010.

[10] H. Fangjing, N. Zaiping, and H. Jun, "An efficient parallel multilevel fast multipole algorithm for large-scale scattering problems," *ACES Journal*, vol. 25, no. 4, pp. 381-387, Apr. 2010.

[11] K. C. Donepudi, J. M. Jin, et al., "A higher order parallelized multilevel fast multipole algorithm for 3-D scattering," *IEEE Trans.*

*Antennas and Propag*., vol. 49, no. 7, pp. 1069-1078, July 2001.

[12]W. Rankin and J. Board, "A potable distributed implementation of the parallel multipole tree algorithm," *Proceedings of IEEE Symposium on High Performance Distributed Computing*, 17-22, 1995.

[13]X. M. Pan and X. Q. Sheng, "A sophisticated parallel MLFMM for scattering by extremely large targets," *IEEE Trans. Antennas and Propag*., vol. 50, no. 3, pp. 129-138, June 2008.

[14]M. Chen, R. S. Chen, X. Q. Hu, Z. H. Fan, and D. Z. Ding, "Augmented MLFMM for solving the electromagnetic scattering from multi-scale objects," *ACES Journal*, vol. 26, no. 5, pp. 418-428, May 2011.

[15]M. Chen, R. S. Chen, D. Z. Ding, and Z. H. Fan, "Accelerating the multilevel fast multipole method with parallel preconditioner for large-scale scattering problems," *ACES Journal*, vol. 26, no. 10, pp. 815, Oct. 2011.

[16]Y. Saad and M. Schultz, "GMRES: a generalized minimal residual algorithm for solving nonsymmetric linear systems," *SIAM Journal on Scientific and Statistical Computing*, vol. 7, pp. 856-869, 1986.

**Zhenhong Fan** was born in Jiangsu, China, in 1978. He received the M.Sc. and Ph.D. degrees in Electromagnetic Field and Microwave Technique from Nanjing University of Science and Technology (NJUST), Nanjing, China, in 2003 and 2007, respectively.

During 2006, he was with the Center of Wireless Communication in the City University of Hong Kong, Kowloon, as a Research Assistant. He is currently an Associate Professor with the Electronic Engineering of NJUST. He is the author or co-author of over 20 technical papers. His current research interests include computational electromagnetics, electromagnetic scattering and radiation.

**Zi He** received the B.Sc. degree in Electronic Information Engineering from the School of Electrical Engineering and Optical Technique, Nanjing University of Science and Technology, Nanjing, China, in 2011.

She is currently working towards the Ph.D. degree in Electromagnetic Fields and Microwave Technology at the School of Electrical Engineering and Optical Technique, Nanjing University of Science and Technology. Her research interests include antenna, RF-integrated circuits, and computational electromagnetics.

**Dazhi Ding** was born in Jiangsu, China, in 1979. He received the B.S. and Ph.D. degrees in Electromagnetic Field and Microwave Technique from Nanjing University of Science and Technology (NUST), Nanjing, China, in 2002 and 2007, respectively.

During 2005, he was with the Center of Wireless Communication in the City University of Hong Kong, Kowloon, as a Research Assistant. He is currently an Associate Professor with the Electronic Engineering of NJUST. He is the author or co-author of over 30 technical papers. His current research interests include computational electromagnetics, electromagnetic scattering, and radiation.

**Rushan Chen** (M'01) was born in Jiangsu, China. He received the B.Sc. and M.Sc. degrees from the Department of Radio Engineering, Southeast University, China, in 1987 and 1990, respectively, and the Ph.D. degree from the Department of Electronic Engineering, City University of Hong Kong, in 2001.

He joined the Department of Electrical Engineering, Nanjing University of Science and Technology (NJUST), China, where he became a Teaching Assistant in 1990 and a Lecturer in 1992. Since September 1996, he has been a Visiting Scholar with the Department of Electronic Engineering, City University of Hong Kong, first as

Research Associate, then as a Senior Research Associate in July 1997, a Research Fellow in April 1998, and a Senior Research Fellow in 1999. From June to September 1999, he was also a Visiting Scholar at Montreal University, Canada. In September 1999, he was promoted to Full Professor and Associate Director of the Microwave and Communication Research Center in NJUST, and in 2007, he was appointed Head of the Department of Communication Engineering, NJUST. He was appointed as the Dean in the School of Communication and Information Engineering, Nanjing Post and Communications University in 2009. And in 2011 he was appointed as Vice Dean of the School of Electrical Engineering and Optical Technique, Nanjing University of Science and Technology. His research interests mainly include microwave/millimeter-wave systems, measurements, antenna, RF-integrated circuits, and computational electromagnetics. He has authored or co-authored more than 200 papers, including over 140 papers in international journals.

Chen received the 1992 third-class science and technology advance prize given by the National Military Industry Department of China, the 1993 third-class science and technology advance prize given by the National Education Committee of China, the 1996 second-class science and technology advance prize given by the National Education Committee of China, and the 1999 first-class science and technology advance prize given by Jiangsu Province, as well as the 2001 second-class science and technology advance prize. He is the recipient of the Foundation for China Distinguished Young Investigators presented by the National Science Foundation (NSF) of China in 2003. In 2008, he became a Chang-Jiang Professor under the Cheung Kong Scholar Program awarded by the Ministry of Education, China. Besides, he was selected as a member of Electronic Science and Technology Group by Academic Degree Commission of the State Council in 2009. Chen is a Senior Member of the Chinese Institute of Electronics (CIE), Vice-Presidents of Microwave Society of CIE and IEEE MTT/APS/EMC Nanjing Chapter. He serves as the Reviewer for many technical journals such as IEEE Trans. on AP and MTT, Chinese Physics, etc., and now serves as an Associate Editor for the International Journal of Electronics.

# Compact Band-Stop Filter for X-Band Transceiver in Radar Applications

**Mohammad Pourbagher [1], Nasser Ojaroudi [2], Changiz Ghobadi [1], and Javad Nourinia [1]**

[1] Department of Electrical Engineering
Urmia University, Urmia, Iran
armanpurbaqer@yahoo.com, ch.ghobadi@urmia.ac.ir, j.nourinia@urmia.ac.ir

[2] Young Researchers and Elite Club
Ardabil Branch, Islamic Azad University, Ardabil, Iran
n.ojaroudi@yahoo.com

***Abstract*** ─ In this paper, we introduce a compact microstrip band-stop filter (BSF) at X-band communication and this shall be used in local oscillator chain for X-band transceiver due to its simple structure, compact size, and excellent performance. Presented microstrip filter consists of a transmission line with a square ring stub and four arrow-shaped strips protruded inside the ring, and a ground plane. Operation frequencies of the filter can be easily controlled by changing four protruded arrow-shaped strips in the square-ring stub. The proposed band-stop filter has wide bandwidth from 8 to 12 GHz for X-band communication that can be used in radar applications. Experimental results show good agreement between simulation results and measurements that excellent stop-band performance could be obtained through the proposed band-stop filter. The proposed microstrip filter is fabricated on a Rogers RT/Duroid 5880 substrate with a relative dielectric constant of 2.2 and has a very small size of 10×15 mm$^2$.

***Index Terms*** ─ Band-stop filter, radar application, X-band communications.

## I. INTRODUCTION

RF/microwave filter is one of the indispensable components in wireless communication systems. As the complexity of the communication systems increases, the demand for RF components operating in multiple bands becomes critically important. There have been numerous publications in the area of the filter technology. The development of microwave filter technology from an application perspective is given in detail in [1]. In modern communications, one of the important parameters is isolation between channels in a given bandwidth. Filters with different configurations are essential components in communication systems and these are generally used as signal rejection for unwanted signals and simultaneously allow the wanted signals in required bands [2].

Conventionally the microwave band-stop filter (BSF) is implemented either by all shunt stubs or by series connected high-low stepped-impedance microstrip line sections. However, generally these are not easily available in microwave band due to the high impedance microstrip line and the spurious pass-bands. Lately, to generate the frequency band-stop function, several modified planar microstrip filters have been reported [3-5]. In [3] and [4], different shapes of ground structures (i.e., slotted ground) are used to obtain the desired band-stop characteristics at X-band frequency range. In [5], band-stop function is achieved by using modified self-complementary structure. The desired resonant frequencies are obtained by adjusting the number of L-shaped teeth.

This paper work deals with design and development of a micro strip filter for X-band applications. In this structure, the resonant behaviors of the square-ring stub are used here introduces transmission zeroes to the filter response and consequently improves its stop-band performance. The reason for the choice of the protruded arrow-shaped strips is that they provide

*Submitted On: January 22, 2014*
*Accepted On: November 14, 2014*

an almost constant tight coupling, which is important to generate a good frequency response. The designed filter has a small dimension of 10×15×0.635 mm$^3$.

## II. MICROSTRIP FILTER DESIGN

The proposed microstrip filter configuration is shown in Fig. 1. Petal-shaped stub connected with the input and output ports at the top layer as revealed in Fig. 1. This added circuit behaves as a low pass filter, which improves the high stop band characteristics of the entire filter without the need to add more sections.

In general, the cut-off frequency of the microwave band-stop filter can be adjusted by setting proper values of the arrow-shaped structures of the filter stub [3]. To realize the desired capacitive and inductive values of the filter elements by the stub of the high/low impedance transmission lines, the characteristic impedance and effective dielectric constant of these transmission lines have to be determined. This band-stop filter was designed on a Rogers RT/Duroid 5880 substrate with 0.635 mm in thickness and with a relative dielectric constant of 2.2.

Theoretically, the loaded Q can be found using the 3 dB bandwidth of the insertion loss which is given by $Q_L = \omega_0 / \Delta\omega$. The arrow-shaped resonators were protruded on a 50 Ω microstrip-line 0.9 mm wide ($L_f$). There is an obvious band gap at the resonant frequency of 9 GHz. In addition, the arrow-shaped resonators provide a higher insertion loss and a narrow bandwidth. Basically, in order to obtain a deeper rejection and a wider band stop of the open-stub filter, more arrow-shaped should be employed. However, it would also increase the insertion loss [9]. On the other hand, two arrow-shaped filters are suitable only for moderate rejection bandwidth applications. The four types of resonator filters were designed with the center frequency of 10 GHz. The wave length, L= ($\lambda_g$/4) in microstrip filter is given by:

$$\lambda_g = \frac{\lambda}{\sqrt{\varepsilon_{eff}}} = \frac{c}{f_{bs}\sqrt{\varepsilon_{eff}}}, \qquad (1)$$

where L is the length of the arrow-shaped strips; C is the light speed (3×10$^8$ m/s), $f_{bs}$ the band stop and (i. e., the desired rejected frequency) frequency, and $\varepsilon_{eff}$ the substrate effective permittivity [5]. The electrical length can be calculated from equation (2):

$$\phi = \beta.l = \frac{2\pi}{\lambda_g}.l, \qquad (2)$$

where $\phi$ is the phase, $\beta$. the phase constant, and $l$ the equivalent electrical length of the spurline.

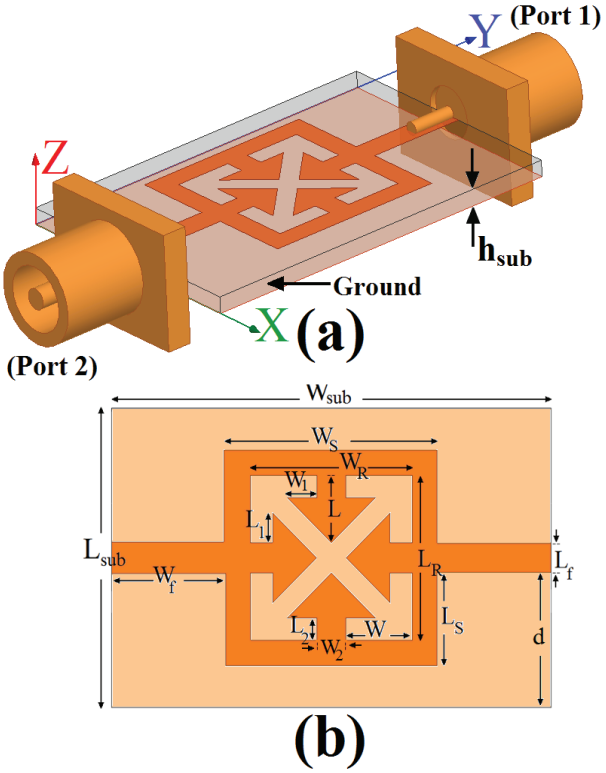


Fig. 1. Geometry of proposed microstrip band-stop filter: (a) side view, and (b) top view.

Final values of the presented band-stop filter design parameters are specified in Table 1.

Table 1: Final parameter values of the filter

| $W_{Sub}$ | $L_{Sub}$ | $h_{Sub}$ | $W_S$ |
|---|---|---|---|
| 15 mm | 10 mm | 0.635 mm | 7.2 mm |
| $L_S$ | $W_f$ | $L_f$ | $W_R$ |
| 3.15 mm | 3.9 mm | 0.9 mm | 5.5 mm |
| $L_R$ | $W$ | $L$ | $W_1$ |
| 5.5 mm | 2.3 mm | 2.25 mm | 1.05 mm |
| $L_1$ | $W_2$ | $L_2$ | $d$ |
| 1.05 mm | 0.9 mm | 0.75 mm | 4.55 mm |

## III. RESULTS AND DISCUSSIONS

The microstrip band-stop filter was designed on both substrate sides by opening apertures in the ground metallization under the high-impedance

transmission line. Replacing of the square-ring stub with four protruded arrow-shaped strips introduces transmission zeroes. For the input/output connections 50-Ohm microstrip lines are used.

The simulated results are obtained using the Ansoft simulation software high-frequency structure simulator (HFSS) [6].

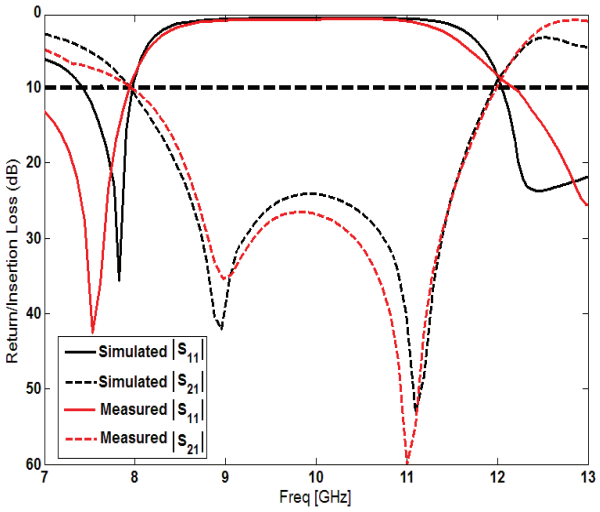


Fig. 2. Measured and simulated return/insertion loss characteristics for the proposed band-stop filter.

Figure 2 shows the simulated and measured insertion and return loss of the filter. As shown in Fig. 2, a flat insertion and return losses are introduced to the filter response at about 8.22 to 11.82 GHz. Consequently, a wide stop-band was achieved.

There exists a discrepancy between measured data and the simulated results. Additionally, the proposed band-stop filter also has characteristics of wider and deeper stop-band than those of conventional band-stop filters [7-8]. This discrepancy is mostly due to a number of parameters such as the fabricated filter dimensions as well as the thickness and dielectric constant of the substrate on which the filter is fabricated, the wide range of simulation frequencies and also the effect of SMA. In order to confirm the accurate return loss/insertion characteristics for the designed filter, it is recommended that the manufacturing and measurement process needs to be performed carefully, besides, SMA soldering accuracy and RT/Duroid substrate quality needs to be taken into consideration.

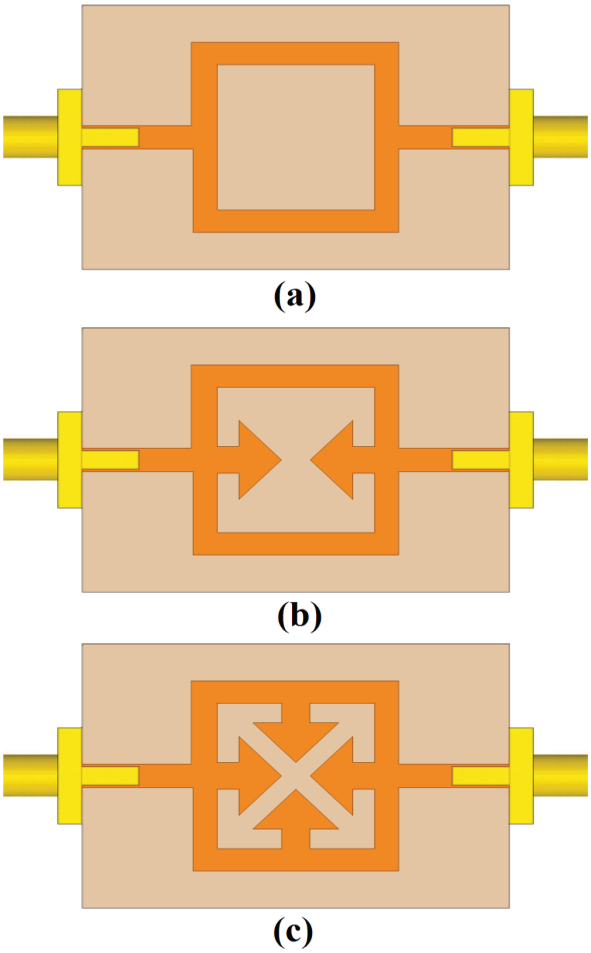


Fig. 3. (a) Ordinary microstrip filter with a circular-disk stub, (b) microstrip filter with a pair of C-shaped strips as a stub, and (c) the proposed microstrip filter structure.

The configuration of the various structures used for simulation studies were shown in Fig. 3. S-parameter characteristics for the microstrip filter with a square-ring stub (Fig. 3 (a)), the filter with a pair of arrow-shaped strips protruded inside the square-ring (Fig. 3 (b)), and the proposed filter structure (Fig. 3 (c)) are compared in Fig. 4. As illustrated in Fig. 4, by using pairs of protruded arrow-shaped strips inside the square-ring stub, two transmission zeroes at the lower and upper frequencies can be achieved, which provide an UWB frequency range. Good impedance matching for insertion/return loss ($S_{11}/S_{21}$) characteristics is generated [9-10].

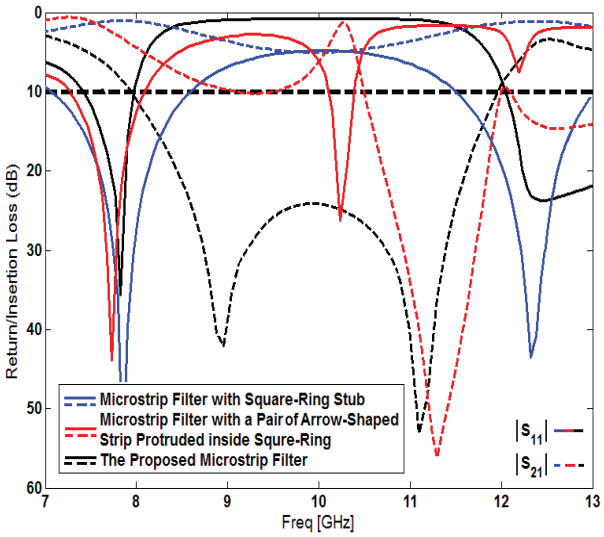


Fig. 4. Simulated return/insertion loss characteristics for various structures shown in Fig. 3.

From the simulated results in Fig. 4, the rejection bandwidth of four arrow-shaped strips is very wide compared to that of two arrow-shaped strips. Also, the rejection level of final configuration is very deep compared to that of two arrow strips.

With the compact circuit size of protruded strips, it is very suitable to apply pairs of arrow strips as a compact band stop filter. Both types of strips can be modeled as one parallel LCR resonator. The resonant frequencies are modeled by one LC resonator, and the radiation effect and transmission loss are considered as a resistor (R). Based on the transmission line theory and the spectral domain approach [1], the circuit elements can be extracted using the follow equations:

$$R = 2Z_0\left(\frac{1}{S_{21}} - 1\right), \tag{3}$$

$$C = \frac{\sqrt{0.5(R + 2Z_0)^2 - 4Z_0^2}}{2.83\pi Z_0 R \Delta f}, \tag{4}$$

$$L = \frac{1}{4(\pi f_0)^2 C}, \tag{5}$$

where $Z_0$ is the 50 Ω characteristic impedance of the microstrip line, $f_0$ is the resonant frequency, $S_{21}$ is the transmission coefficient at $f_0$, and Δf is -3 dB bandwidth of $S_{21}$.

From the simulated results in Fig. 4, the extracted circuit elements are the following. For two arrow-shaped strips are: L= 0.867 nH, C=1.852 pF, and R=17.05 *k*Ω. For the proposed structure with pairs of arrow-shaped strips are: L= 4.021 nH, C= 0.601 pF, and R= 71.33 *k*Ω.

The proposed filter with final design, as shown in Fig. 5, was fabricated and tested that has a good insertion and return losses are introduced to the filter response from 8 to 12 GHz.

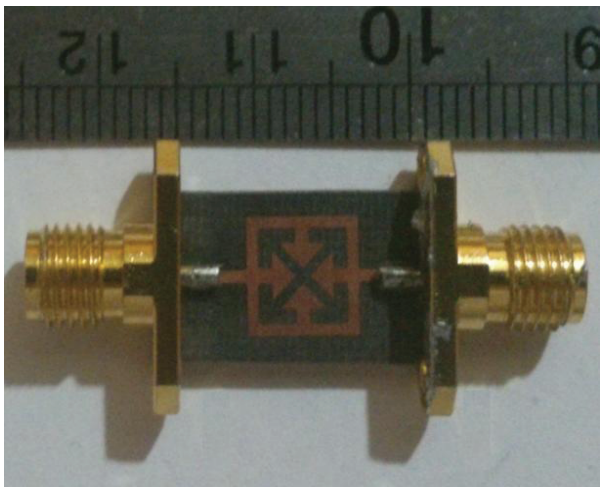

Fig. 5. Photograph of the realized printed band stop filter.

Figure 6 shows the current distribution of the proposed filter at the transmission zeroes. It can be seen that using the protruded arrow-shaped strips inside square-ring stub have effect on the overall performance of the filter. As shown in Fig. 6 (a), at 9 GHz (first zero transmission resonance) the current flows are more dominant around the arrow-shaped strips which are used at top/bottom sides of the square-ring stub and first zero transmission resonance of insertion loss response is affected from them. Figure 6 (b) clearly shows at the second zero transmission resonance in 11 GHz, the pair of arrow-shaped strips embedded at right/left sides acts as a half-wave resonant structure [7].

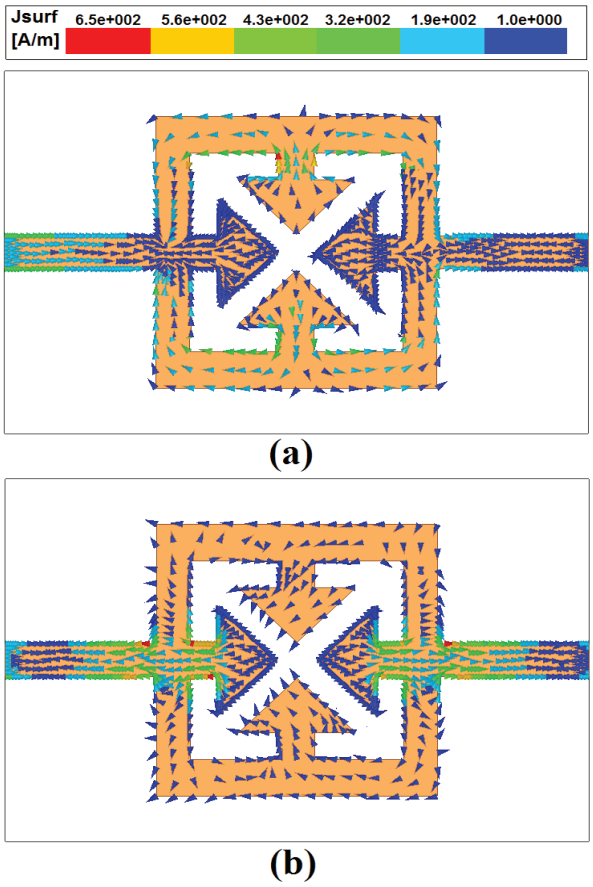


Fig. 6. Simulated surface current distributions for the proposed microstrip filter on the microstrip transmission line at: (a) 9 GHz, and (b) 11 GHz.

## IV. CONCLUSION

In this paper, a novel design of band-stop microstrip filter that covers all frequency range of X-band has been presented. Configuration of the presented filter consists of a transmission line with a square-ring stub, two pairs of arrow-shaped strips protruded inside square-ring stub and a ground plane. Operation frequencies of the filter can be easily controlled by changing the size of arrow-shaped strips. Controlling the transmission zeroes at the creating stop band, can be used to increase or decrease the stop-band generated by conventional filter. The measured results have shown that the fabricated filter has a band-stop that extends from 8.02 to 12.05 GHz. An excellent agreement between measured and simulated was obtained. Therefore, the proposed filters are promising for use in radar wireless technologies for X-band communications.

## ACKNOWLEDGMENT

The authors are thankful to MWT Company staff for their help (www.microwave-technology.com).

## REFERENCES

[1] J. A. Kong, *Electromagnetic Wave Theory*, EMW Publishing, Cambridge, 2000.

[2] X.-H. Wang, B.-Z. Wang, H. Zhang, and K. J. Chen, "A tunable band-stop resonator based on a compact slotted ground structure," *IEEE Trans. Microwave Theory Tech.*, vol. 55, pp. 1912-1918, 2007.

[3] D. S. La, Y. H. Lu, S. Y. Sun, N. Liu, and J. L. Zhang, "A novel compact band stop filter using defected microstrip structure," *Microw. Opt. Technol. Lett.*, vol. 53, pp. 433-435, 2011.

[4] W. D. Yan and R. R. Mansour, "Compact tunable band stop filter integrated with large deflected actuators," *IEEE MTT-S International Microwave Symposium*, Honolulu, HI, pp. 1611-1614, 2007.

[5] R. Habibi, Ch. Ghobadi, M. Ojaroudi, and N. Ojaroudi, "Very compact broad band-stop filter using periodic L-shaped stubs based on self-complementary structure for X-band application," *Electronic Letters*, vol. 48, 2012.

[6] *Ansoft High Frequency Structure Simulator (HFSS)*, ver. 13, Ansoft Corporation, Pittsburgh, PA, 2010.

[7] N. Ojaroudi, M. Ojaroudi, and Sh. Amiri, "Compact UWB microstrip antenna with satellite down-link frequency rejection in X-band communications by etching an E-shaped step-impedance resonator slot," *Microw. Opt. Technol. Lett.*, 55: 922-926, 2013.

[8] N. Ojaroudi, M. Ojaroudi, and R. Habibi, "Design and implementation of very compact band-stop filter with petal-shaped stub for radar applications," *Microw. Opt. Technol. Lett.*, vol. 55, pp. 1130-1132, 2013.

[9] N. Ojaroudi, "Novel design of low-profile microstrip band-stop filter (BSF) with koch fractal RSLRs," *22nd Telecommunications Forum, TELFOR 2014*, Belgrade, Serbia, November 25-27, 2014.

[10] N. Ojaroudi, H. Ojaroudi, and Y. Ojaroudi, "Very low profile ultra-wideband microstrip band-stop filter," *Microw. Opt. Technol. Lett.*, vol. 56, pp. 709-711, 2014.

# Implementation of Two Different Moving Window FDTD Methods to Simulate the Electromagnetic Propagation in Tunnel with Parallel Computing

**Yun-Fei Mao, Jia-Hong Chen, Liang Pan, and Xiao-Ming Wang**

China Satellite Maritime Tracking and Control Department
Jiangyin, 2144000, China
myf4494@163.com, stone_cjh@sina.com, panliang@163.com, wangxiaoming@163.com

***Abstract*** ─ Tunnel engineering is electrically large compared with the GHz electromagnetic pulse (EMP), it is difficult to simulate the EMP propagation in large-scale and long-distances vaulted tunnel by using the conventional finite-difference time-domain (FDTD) method. In this work, based on the parallel computing, two kinds of moving window FDTD (MW-FDTD) methods are presented to simulate the EMP propagation in tunnel, the results are validated by comparing with the results of the conventional parallel FDTD method. The convolution PML (CPML) is adopted to truncate the computation domain, which reduces the reflection error greatly. The accuracy and the efficiency of the proposed method are proposed by comparing with the conventional method. Results show that the relative errors for the Alternate MW-FDTD (AMW-FDTD) and the Chain MW-FDTD (CMW-FDTD) are 0.11% and 0.43%, respectively. The CPU time for the AMW-FDTD method can be reduced to about 45% of the conventional FDTD method, while the CMW-FDTD method can be reduced to about 35%.

***Index Terms*** ─ EMP, Finite-Difference Time-Domain (FDTD), moving window, parallel computing, tunnel.

## I. INTRODUCTION

Modeling the radio wave propagating over long distance in tunnel is significant for the tunnel-communication system design and the electromagnetic pulse (EMP) interference protection [1]-[6]. Recently, a new radio wave propagation model based on the finite difference time domain (FDTD) method is prevailing. However, being subject to the restriction of the stability condition and Courant criterion, the FDTD method faces severe difficulties in modeling some long distance or large-scale propagation problems for great computing requirements [7]-[8]. However, as the pulse propagates only over confined domain, large amount of computational power is wasted to update the domain that the pulse has propagated over and the domain that the pulse has not arrived.

It allows us to make the best use of the limited memory to design the FDTD mesh to move with the pulse, so as to insure the limited mesh long enough to overcast the pulse. According to this, many papers have designed the moving-window finite-difference time-domain FDTD (MW-FDTD) or the segmented (SFDTD) method [9]-[19] to solve the similar problems, but none of them are applicable for all. Of course we also could take the advantage of parallel computing using the message passing interface, but huge numbers of PCs and long computational time will be required as the modeling domain increases. Apparently, it is not a good solution to the problem.

In this paper, based on the parallel computing, two kinds of moving window FDTD (MW-FDTD) methods are presented to simulate the EMP propagation in tunnel, the results are validated by comparing with the results of the conventional parallel FDTD method. The convolution PML (CPML) is adopted to truncate the computation domain, which reduces the reflection error greatly. For the tunnel's vaulting boundary is a piece of curved dielectric surface which cannot be simulated with the conventional FDTD algorithm,

*Submitted On: October 6, 2014*
*Accepted On: December 12, 2014*

here we take the technique of conformal FDTD (CFDTD) [20] to deal with it. The accuracy and the efficiency of the proposed method are proposed by comparing with the conventional parallel FDTD method. Results show that the relative errors for the AMW-FDTD 0.11%and the CMW-FDTD are $e_{rA}=0.11\%$ and $e_{rC}=0.43\%$, respectively. The CPU time for the AMW-FDTD method can be reduced to about 45% of the conventional FDTD method, while the CMW-FDTD method can be reduced to about 35%.

## II. THEORY

### A. The calculation model

The tunnel engineering always has long distance, its computational model can be seen in Fig. 1.

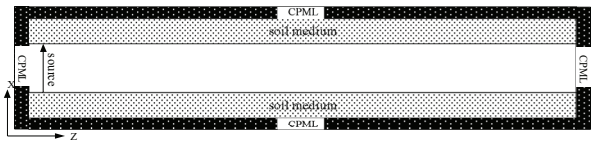


Fig. 1. The computational model of the tunnel.

Its section can be seen in Fig. 2 on the left side. The sizes of the hemline and the height are 4 m. The vault can be approximately regarded as hemi-cycle, its semi-diameter is 2 m. The relative permittivity is $\varepsilon_{rs}=10.0$. The conductivity is $\delta=1.0E-3$. Both ends of the tunnel and the soil domain around the tunnel are terminated by the CPML. For the tunnel's vaulting boundary is a piece of curved dielectric surface which cannot be simulated with the conventional FDTD algorithm, here we take the technique of CFDTD to deal with it, the results can be seen on the right hand of Fig. 2.

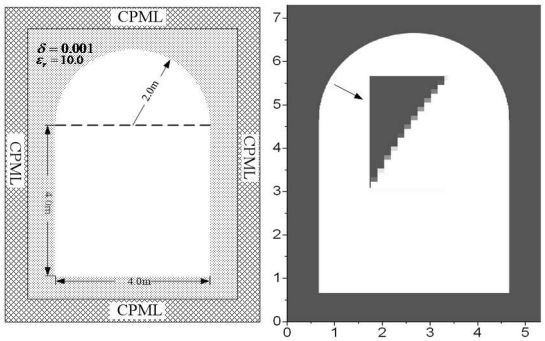


Fig. 2. The section of the tunnel.

### B. Modeling of the source

In the wave-guide system, we usually use hard source to introduce the incident wave. Because the soil around the tunnel is not ideal conductor and the section is not typical wave-guide section such as cycle or rectangle, we can't obtain the field expression easily. To solve this problem, we can suppose the section as rectangle approximately, then use the mode distribution to introduce the source. Note that the mode of the pulse propagating in tunnel is not the same as the mode in wave-guide, we could assume that there are many modes at beginning, but as the wave propagating only those standing wave patterns which satisfy the boundary conditions at certain frequency will exist. Take typical mode TE10 and TM11 as example, the sizes of the rectangle are $a$, $b$.

(1) TM11 mode:

It has five field components, the field equations are as follows:

$$\begin{cases} E_x=-\dfrac{j\beta_{11}}{k_c^{\,2}}\dfrac{\pi}{a}A\cos(\dfrac{\pi}{a}x)\sin(\dfrac{\pi}{b}y)\,e^{-j\beta_{11}z} \\ E_y=-\dfrac{j\beta_{11}}{k_c^{\,2}}\dfrac{\pi}{b}A\sin(\dfrac{\pi}{a}x)\cos(\dfrac{\pi}{b}y)\,e^{-j\beta_{11}z} \\ E_z=A\sin(\dfrac{\pi}{a}x)\sin(\dfrac{\pi}{b}y)\,e^{-j\beta_{11}z} \\ H_x=\dfrac{j\omega\varepsilon}{k_c^{\,2}}\dfrac{\pi}{b}A\sin(\dfrac{\pi}{a}x)\cos(\dfrac{\pi}{b}y)\,e^{-j\beta_{11}z} \\ H_y=-\dfrac{j\omega\varepsilon}{k_c^{\,2}}\dfrac{\pi}{a}A\cos(\dfrac{\pi}{a}x)\sin(\dfrac{\pi}{b}y)\,e^{-j\beta_{11}z} \\ H_z=0 \end{cases} . \quad (1)$$

(2) TE10 mode:

It has three field components, the field equations are as follows:

$$\begin{cases} E_y=-\dfrac{j\omega\mu a}{\pi}A\sin(\dfrac{\pi}{a}x)\,e^{-j\beta_{10}z} \\ H_x=\dfrac{\beta_{10}a}{\pi}A\sin(\dfrac{\pi}{a}x)\,e^{-j\beta_{10}z} \\ H_z=A\cos(\dfrac{\pi}{a}x)\,e^{-j\beta_{10}z} \\ E_x=E_z=H_y=0 \end{cases} . \quad (2)$$

Suppose the source is located at $z=k_s\Delta z$, the field distribution functions $f(x,y,z)$ are shown in (1) and (2), the time function is $g(t)$, so the source can be set as:

$$E^{n+1}(i,j,k_s) = E^n(i,j,k_s) + f(x,y,z)g(t). \quad (3)$$

Usually, the time function $g(t)$ is set as high power microwave (HPM) or ultra wide-band (UWB).

HPM can be expressed as:

$$E_i(t) = \begin{cases} E_0 \dfrac{t}{t_1}\sin(2\pi f_0 t) & 0 < t < t_1 \\ E_0 \sin(2\pi f_0 t) & t_1 < t < t_1 + \tau \\ E_0\left(\dfrac{\tau + 2t_1}{t_1} - \dfrac{t}{t_1}\right)\sin(2\pi f_0 t) & t_1 + \tau < t < 2t_1 + \tau \end{cases}, \quad (4)$$

where, $\tau$ is the width of the pulse, $t_1$ is the ascending time, $f_0$ is the frequency of the carrier wave.

UWB can be expressed as:

$$E_i(t) = E_0 k (t - t_0) e^{-\frac{4\pi(t-t_0)^2}{\tau^2}}, \quad (5)$$

where $k = e^{0.5}\sqrt{8\pi}/\tau$ . Its waveform is shown in Fig. 3.

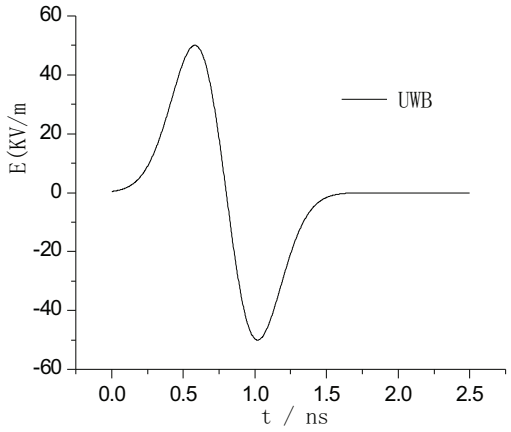


Fig. 3. The waveform for the UWB.

## C. Introduction of the parallel implementation

Parallel FDTD is a kind of algorithm that the computational domain is divided into several sub-domains and each node only handle for the corresponding sub-domain calculation. As we can see from Fig. 1, that the tunnel is elongated in one direction. For simplicity, the one-dimensional parallel FDTD division is used in this paper. Along the z direction, the whole domain can be divided into several sub-domains, which can be seen in Fig. 4.

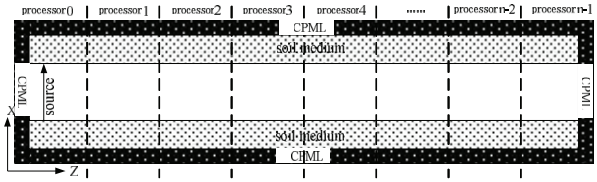


Fig. 4. The parallel model of the tunnel.

The Message Passing Interface (MPI) is a standard specification of a set of libraries call for passing messages between computers interconnected via a data communication network. According to the domain decomposition, each sub-domain can be treated as a process, and MPI connects these processes together.

By using this method, only the first and the last process need to be disposed specially, because of the CPML. Other processes can be implemented all the same. In one iterative only needs to exchange the magnetic field in the nearby processes. The data exchanging can be seen in Fig. 5.

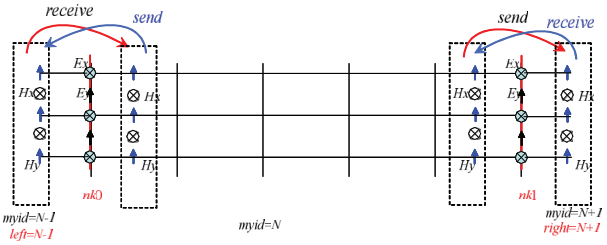


Fig. 5. The data exchanging between two nearby processes.

## D. Calculation results

Take TE10 mode as the source, the field components are shown in equation (2) $a = 6.0\text{m}$ . We choose UWB as the time function. $\tau = 3.0\text{ns}$ , $t_0 = 2\tau$. $\Delta x = \Delta y = \Delta z = 0.01333\text{m}$, $\Delta t = \Delta z/(2v_p)$, $v_p$ is the velocity of the pulse in tunnel.

The length of the tunnel is 40 m. The results are shown in Fig. 6. On the left side it is the distribution of $E_y$ , on the right side the waveforms for different distances are given. It can be seen in Fig. 6 (a) that the energy is concentrated in a small region. From Fig. 6 (b), we can find when the distance is increasing the waveform broadened.

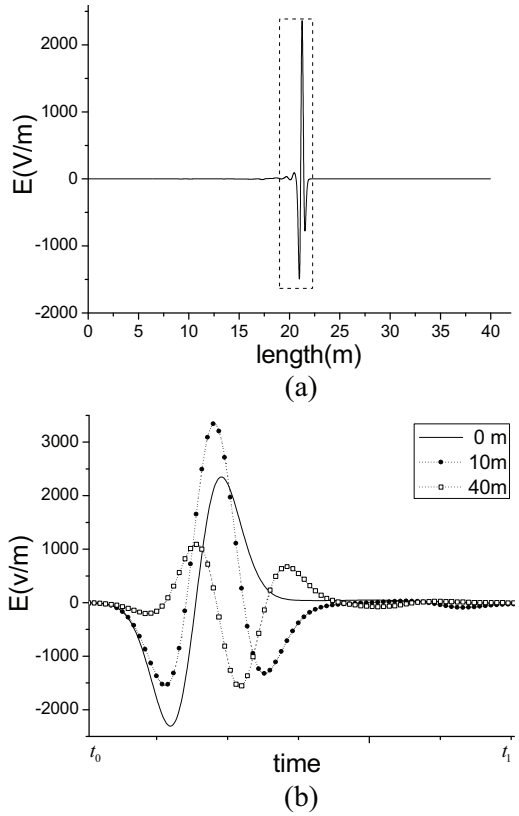


Fig. 6. The waveform of the calculation results.

## III. IMPLEMENTATION OF THE MW-FDTD METHOD

From the forgoing section we know that the energy is concentrated in a small region when the wave is propagating in 40 m tunnel, in the other region we can nearly set as zero. However, we calculate the whole region including the zero region, so large amount of computational resources are wasted to update the domain that the pulse has propagated over and the domain that the pulse has not arrived. It allows us to make the best use of the limited memory to design the FDTD mesh to move with the pulse, so long as to insure the limited mesh long enough to overcast the pulse. In this section two different MW-FDTD methods are introduced to solve this problem.

### A The alternate MW-FDTD method

The calculation model for the Alternate MW-FDTD (AMW-FDTD) method is shown in Fig. 7. Compare with the conventional parallel FDTD method, the AMW-FDTD has four CPMLs, CPML1 and CPML4 are the same with the conventional method, CPML2 and CPML3 are in the middle of the tunnel, by using the alternate of the four CPMLs the iterative can be implemented.

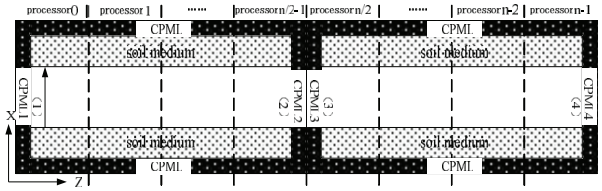


Fig. 7. The calculation model for the AMW-FDTD method.

The procedures of the AMW-FDTD method are list as follows.

First step, join interface 2 to interface 3, CPML2 and CPML3 are out of work, see in Fig. 8. Run the conventional FDTD updating with the source of the pulse added at the source interface.

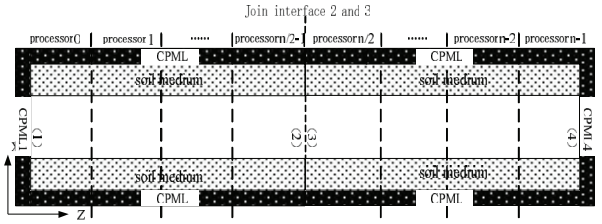


Fig. 8. The first step for the AMW-FDTD method.

Second step, when the pulse move to interface 4, set the domain including CPML between interface 1 and interface 2 to be zeros, join interface 4 to interface 1 conducting the pulse propagate to interface 2, take the CPML2 and CPML3 into function, set CPML4 and CPML1 out of work and stop the source adding at the source interface, see in Fig. 9.

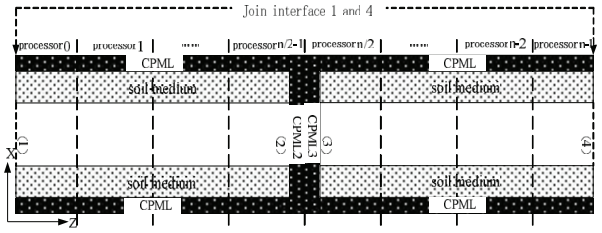


Fig. 9. The second step for the AMW-FDTD method.

Third step, when the pulse arrives at interface 2, set the field between interface 3 and interface 4

to be zeros, join interface 2 to interface 3 to conduct the pulse move to interface 4, and take CPML1 and CPML4 into function, see in Fig. 8.

Fourth step, follow the second step when the pulse arrives at interface 4. And the around-CPML of the tunnel is in function through the procedures.

To verify the efficiency and accuracy of the AMW-FDTD method, the calculation results are compared with the conventional parallel FDTD method. For the constraint of the computational resources, the conventional method can only calculate limited distances. For the AMW-FDTD method, the reflection error of the CPML and the cut error of the window are the main error. So when we expand the window the error can be reduced. First, we run the code with 500 grids. Figure 10 (a) shows the waveform for the AMW-FDTD method and the conventional method at 40 m, results show they agree well with each other. When we change the window to 1000 grids, the results in Fig. 10 (b) show good agreement with each other. So we can conclude that the reflection error and the cut error are negligible.

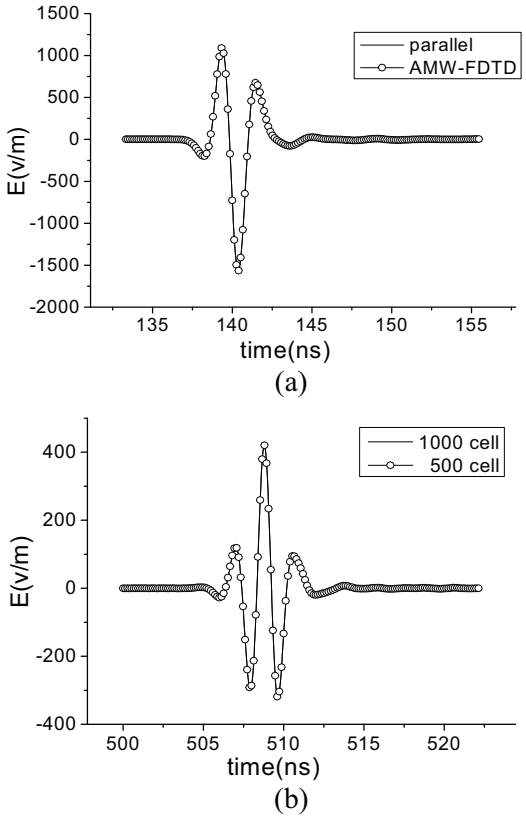


Fig. 10. The waveform for AMW-FDTD method at 40 m and 150 m.

Figure 11 shows the field attenuation at 40 m and 150 m. Results show the high frequency part attenuates slowly than the low frequency, which is consistent with the physical process.

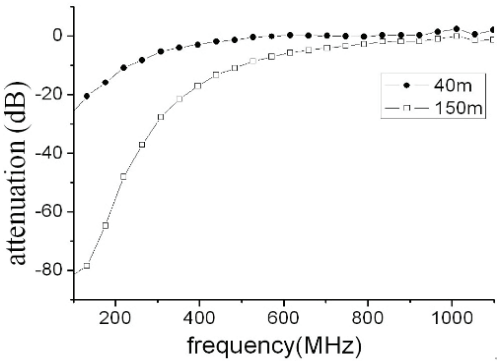


Fig. 11. The field attenuation at 40 m and 150 m.

**B. The chain MW-FDTD method**

The calculation model for the Chain MW-FDTD (CMW-FDTD) method is shown in Fig. 12. Instead of the right CPML in the conventional parallel FDTD method, it has a moving reset area, which is used to set the tail of the pulse to be zero, so that we can reduce the error.

The procedures of the CMW-FDTD method are list as follows.

First step, run the conventional FDTD method, the moving reset area moves along with time step.

Second step, when the left propagating pulse is totally absorbed by the CPML, join interface 1 and interface 2, form an annular iterative domain, which can be seen in Fig. 13.

To verify the efficiency and accuracy of the CMW-FDTD method, the calculation results are also compared with the conventional parallel FDTD method. Figure 14 (a) shows the waveform for the CMW-FDTD method and the conventional method at 40 m, results show they agree well with each other. The results for 150 m in Fig. 14 (b) show good agreement with the AMW-FDTD method.

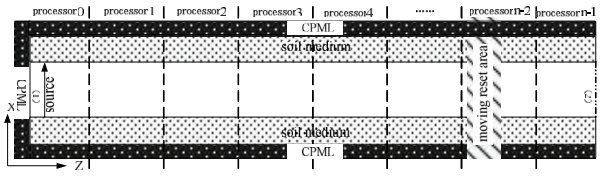


Fig. 12. The calculation model for the CMW-FDTD method.

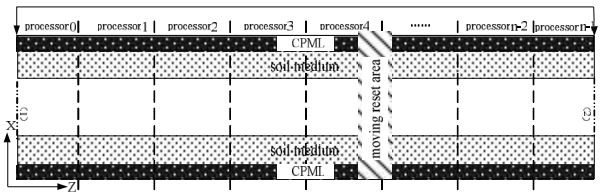


Fig. 13. The second step for the CMW-FDTD method.

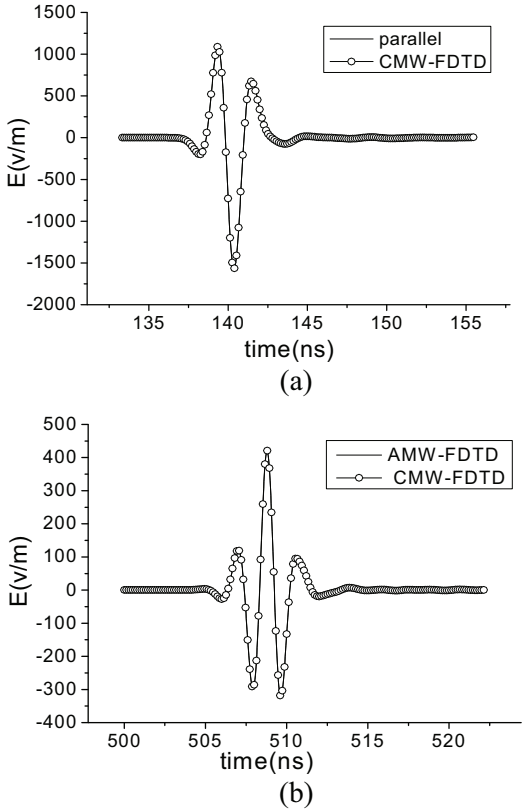


Fig. 14. The waveform for CMW-FDTD method at 40 m and 150 m.

## IV. ANALYSIS OF THE ACCURACY AND THE EFFICIENCY

### A. The calculation error for two different methods

To compare the calculation error of the two different MW-FDTD methods, we choose the conventional FDTD method as the reference. The relative error can be given as:

$$e_r = \frac{\left|E^*(t) - E(t)\right|_{\max}}{\left|E(t)\right|_{\max}}, \qquad (6)$$

where $E(t)$ is the reference results, $E^*(t)$ is the MW-FDTD results.

Figure 15 shows the absolute error for two different MW-FDTD method. Substitute the results into equation (5), we can obtain the relative error for 40 m are $e_{rA} = 0.0415\%$ and $e_{rC} = 0.42\%$, respectively. And the relative error for 150 m are $e_{rA} = 0.11\%$ and $e_{rC} = 0.43\%$, respectively. So we can conclude that the calculation error for the AMW-FDTD method is smaller than the CMW-FDTD method. The relative error for the CMW-FDTD method is about 0.4%.

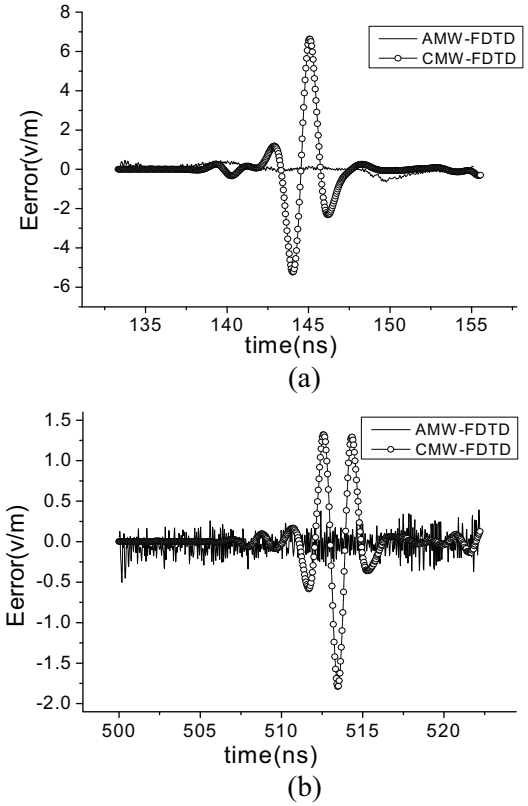


Fig. 15. The absolute error for two different CMW-FDTD methods at 40 m and 150 m.

### B. The calculation efficiency for two different methods

In this section, the calculation efficiency is proposed. Table 1 shows the calculation resources and time for the AMW-FDTD, the CMW-FDTD and the conventional method at 40 m. From Table 1 we can see that the relative error for the AMW-FDTD method is less than 0.12%, for the CMW-FDTD method is about 0.43%, which means both the two proposed MW-FDTD methods have high accuracy. On a core2 2.4-GHz machine, it took the FDTD method 27.3h and the AMW-FDTD method

12.4h, which is 9.8h in the CMW-FDTD method. So compare with the conventional FDTD method the CMW-FDTD method has the highest efficiency. When the propagating distance is 200 m the calculation resources and efficiency for the two different MW-FDTD methods are shown in Table 2. For the limited of the computational resource this time the conventional method can't run. The memory for the AMW-FDTD and the CMW-FDTD method is 295 MB and 161.5 MB, respectively. The running time is 24.5h for the AMW-FDTD method and 14.0h for the CMW-FDTD method.

Table 1: The resource and efficiency for different methods at 40 m

| | FDTD | AMW-FDTD | CMW-FDTD |
|---|---|---|---|
| Memory (MB) | 1145 | 483 | 348 |
| Time (hour) | 27.3 | 12.4 | 9.8 |
| Relative error | — | 0.12% | 0.43% |

Table 2: The resource and efficiency for different methods at 200 m

| | AMW-FDTD | CMW-FDTD |
|---|---|---|
| Memory (MB) | 295 | 161.5 |
| Time (hour) | 24.5 | 14.0 |

## V. CONCLUSION

In this paper, we present two different MW-FDTD methods to simulate the electromagnetic propagating in tunnel. Numerical results indicate that the proposed methods are accurate and efficient. The CPU time for the AMW-FDTD method can be reduced to about 45% of the conventional FDTD method, while the CMW-FDTD method can be reduced to about 35%. The relative error for the AMW-FDTD method is less than 0.12%, for the CMW-FDTD method is about 0.43%, which means both the two proposed MW-FDTD methods have high accuracy.

## ACKNOWLEDGMENT

This work was supported by Chinese National Science Foundation under Grant No. 60971063.

## REFERENCES

[1] D. G. Dudley, M. Lienar, S. F. Mahmud, and P. Degauque, "Wireless propagation in tunnels," *IEEE Antennas Propag. Magazine*, vol. 49, 11-26, 2007.

[2] Y. P. Zhang, "Novel model for propagation loss prediction in tunnels," *IEEE Trans. Veh. Technol.*, vol. 52, 1308-1314, 2003.

[3] E. Heyman, R. Kastner, and R. W. Ziolkowski, "Hybrid Ray-FDTD moving window approach to pulse propagation," *Journal of Computational Physics*, vol. 138, 480-500, 1997.

[4] J. F. Liu, X. L. Xi, G. B. Wan, and L. L. Wang, "Simulation of electromagnetic wave propagation through plasma sheath using the moving window finite-difference time-domain method," *IEEE Trans. on Plasma Science*, vol. 39, 852-855, 2011.

[5] G. S. Ching, M. Ghoraishi, M. Landmann, and H. Sakamoto, "Wideband polarimetric directional propagation channel analysis inside an arched tunnel," *IEEE Trans. Antennas Propagat.*, vol. 57, 760-767, 2009.

[6] K. Guan, Z. Zhong, B. Ai, and C. Briso-Rodriguez, "Complete propagation model in tunnels," *IEEE Antennas and Wireless Propagation Letters*, vol. 12, 741-743, 2013.

[7] K. S. Yee, "Numerical solution of initial boundary value problems involving Maxwell's equations in isotropic media," *IEEE Trans. Antennas Propagat.*, vol. 14, 302-307, 1966.

[8] A. Taflove and S. C. Hagness, *Computational Electrodynamics: The Finite-Difference Time-Domain Method*, 2nd ed., Boston, MA: Artech House, 2000.

[9] J. W. Schuster, K. C. Wu, R. R. Ohs, and R. J. Luebbers, "Application of moving window FDTD to predicting path loss over forest covered irregular terrain," *Antennas and Propagation Society International Symposium*, 1607-1610, 2004.

[10] Y. Wu and Ian Wassell, "Introduction to the segmented finite-difference time-domain method," *IEEE Trans. on Magnetics*, vol. 45, 1364-1367, 2009.

[11] M. Masud Rana and A. Sanagavarapu Mohan, "Segmented locally one dimensional FDTD method for EM propagation inside large complex tunnel environments," *IEEE Trans. on Magnetics*, vol. 48, 223-226, 2012.

[12] F. Akleman and L. Sevgi, "Realistic surface modeling for a finite difference time domain

wave propagator," *IEEE Trans. Antennas Propagat.*, vol. 51, no. 7, July 2003.
[13]F. Akleman and L. Sevgi, "A novel finite difference time domain wave propagator," *IEEE Antennas and Propagat*., vol. 48, no. 5, 839-841, 2000.
[14]S. A. Torrico, H. L. Bertoni, and R. H. Lang, "Modeling tree effects on path loss in a residential environment," *IEEE Trans. Antennas Propagat*., vol. 46, 1998.
[15]K. Wu and J. Schuster, "Application of moving window FDTD to modeling the effects of atmospheric variations and foliage on radio wave propagation over terrain," *IEEE Military Communications Conference*, 2004.
[16]B. Fidel and E. Heyman, "Hybrid Ray-FDTD moving window approach to pulse propagation," *Journal of Computational Physics*, vol. 138, 480-500, 1997.
[17]M. O. Ozyalcin, F. Akleman, and L. Sevgi, "A novel TLM-based time-domain wave propagator," *IEEE Trans. Antennas Propagat.*, vol. 51, no. 7, 2003.
[18]Z. Kang, et al., "An efficient 2-D compact precise integration time domain method for longitudinally invariant waveguiding structures," *IEEE Trans. Microwave Theory and Techniques*, 2013.
[19]M. Hadi and S. Mahmoud, "A high order compact-FDTD algorithm for electrically large waveguide analysis," *IEEE Trans. Antennas and Propagation*, 2008.
[20]K. K. Mei, A. C. Cangellaris, and D. J. Angelakos, "Conformal time domain finite differentce method," *Radio Science*, 1145-1147, 1984.

**Yun-Fei Mao** was born in Zhejiang Province, China, in 1984. He received the B.S. degrees, the M.S. degree and the Ph.D. degree in Electric Systems from Nanjing Engineering Institute, Nanjing, China, in 2006, 2009 and 2013 respectively. He is currently working with China Satellite Maritime Tracking and Control Department, Yuan Wang Ⅲ, Jiangyin 214400, China. His research interests include computational electromagnetic and electromagnetic tracking.

**Jia-Hong Chen** was born in Jiangsu, China, in 1969. He received the B.S. and M.S. degrees from National University of Defense Technology, Changsha, China, in 1982 and 1987, respectively, and the Ph.D. degree in Control Engineering from Xi'an Jiao Tong University, Xi'an, China. His research interests include electromagnetics and electromagnetic tracking.

**Liang Pan** was born in Zhejiang Province, China, in 1967. He received the B.S. degrees from Zhejiang University, Zhejiang, China, in 1988. He received the M.S. degrees from Nanjing University of Science and Technology, Nanjing, China, in 2007. He is currently working with China Satellite Maritime Tracking and Control Department, Jiangyin 214400, China. His research interests include inertial navigation and electromagnetic tracking.

**Xiao-Ming Wang** was born in Jiangsu Province, China, in 1980. He received He received the B.S. in Industrial Automation from Jiangsu University, Zhenjiang, China, in 2002, and the M.S. degree in Control Theory and Control Engineering from Southeast University, Nanjing, China, in 2005. He is currently working with China Satellite Maritime Tracking and Control Department, Jiangyin 214400, China. His research interests include electromagnetics and electromagnetic tracking.

# Modified Ground Circle Like-Slot Antenna with Dual Band-Notched Characteristics for Super UWB Applications

**Seyed Ramin Emadian and Javad Ahmadi-Shokouh**

Department of Telecommunication Engineering
University of Sistan and Baluchestan, Zahedan, Iran
ramin.emadian@gmail.com, jahmadis@ieee.org

***Abstract*** ─ In this paper, a compact modified ground slot antenna is proposed. This antenna is designed for super ultra-wideband (UWB) applications. To reduce the interference effect on the WLAN and WiMAX systems, it comes up with dual band notched characteristics. In the antenna geometry, a pair of L-shaped stubs connected to the fork-shaped patch is employed to introduce single band-notched characteristics in 5.15-5.825 GHz for WLAN system. This feature also causes that the middle frequency of the band is highly improved. Moreover, a T-shaped stub is added to the center of the fork-shaped patch to generate the frequency band stop performance in 3.3-3.8 GHz for WiMAX system. Furthermore, we propose a modified ground plane including a pair of inverted T-shaped slits, cut from the ground plane, to improve the bandwidth to 164%. The simulation and measurement results indicate a very wide impedance bandwidth from 2.5 up to 23 GHz, with pre-designed dual band notched properties, for the proposed antenna. This slot antenna with above-mentioned frequency bandwidth has a compact size of 24×25 $mm^2$, and therefore is suitable for many UWB applications.

***Index Terms*** ─ Circle-like slot, dual band-notched characteristics, L-shaped and T-shaped stubs, modified ground plane, T-shaped slits.

## I. INTRODUCTION

In recent years, a great interest is focused on slot antennas for the use in broad bandwidth communication systems due to their benefits of low weight, low cost and easy fabrication [1,2]. These types of antennas have also shown several benefits, including broader impedance bandwidth, less dispersion and better radiation efficiency, over conventional microstrip antennas. Recently, many campaigns have been reported to enhance the frequency bandwidth of these structures. For instance, using a pair of L-shaped stubs [3], a fork-like radiating patch [4] and a capacitively probe-fed microstrip patch [5]. A big challenge in using such UWB antennas arises when they have to simultaneously work with the other wireless systems. The available wireless networks such as WLAN and WiMAX may cause interference with the UWB spectrum. A traditional solution to avoid frequency conflict is applying a band notched characteristics to the frequency spectrum of the UWB antenna. There exist many schemes in the literature about the UWB antenna with the band notched specifications. These schemes apply different kinds of slits, slots and parasitic stubs in the patch and ground plane to generate needed band notched properties [6-11]. In this paper, a simple and novel structure is proposed which improves the impedance bandwidth and creates dual band-notched characteristics. In the proposed design, a CPW feed line is used to excite the fork-shaped patch. The CPW feeding mechanism has also many advantages over microstrip type feed lines, such as their low dispersion and low radiation leakage which leads to a better radiation efficiency characteristic [12,13]. In this antenna, we combine the fork-shape patch approach with a pair of L-shaped and a T-shaped stubs to introduce the aforementioned band notched frequency spectrum. Moreover, a modified ground plane with a pair of inverted T-shaped slits is employed to achieve a fractional bandwidth of more than 164%. Compared to the similar reported UWB antennas in [1-16], the proposed antenna has a broader

*Submitted On: October 5, 2014*
*Accepted On: December 11, 2014*

impedance bandwidth.

In ultra-wideband antennas, the mismatch of the reflected power can be the most considerable loss term in the antenna radiation efficiency. Hence, a good impedance matching over the desired frequency range can reduce the mismatch reflected power, resulting in a better radiation efficiency of the antenna.

A Modified Ground Structure (MGS), including T-shaped slits in the ground plane, is used in the antenna designing to further improve the impedance matching and radiation characteristics. In MGS structures, there are some slots with different shapes and dimensions that will be cut from the ground plane. These added slots will disturb the shielded current corresponding to the figure and size of the modifying slots [14]. Recently, several UWB monopole antennas printed on low-cost FR4 substrate with high radiation efficiency have been reported. In these designs, different techniques are employed to improve radiation characteristics [15,16].

The proposed antenna presents a very broad frequency bandwidth from 2.5 to 23 GHz with dual band notched properties covering all the 5-6 GHz WLAN and 3.5-5.5 GHz WiMAX bands, while it is compact as small as 24×25 $mm^2$ in size. The results show a good agreement between simulation and measurement.

The rest of the paper is organized as follows. In Section II, the design of the antenna structure is explained. The effect of each part of the antenna is described in Section III. In the next section, we discuss the experimental results. Finally, Section V concludes the paper.

## II. ANTENNA DESIGN

The base antenna geometry which is applied in this paper uses a fork-shaped patch to excite the circle-like slot on the ground plane [6]. Figure 1 demonstrates the structure of the proposed UWB slot antenna. As the figure shows, the antenna contains a fork-shaped patch, a circle-like slot, two L-shaped stubs, a T-shaped stub connected to the fork-shaped patch, and a pair of T-shaped slits etched in the ground plane. Figure 2 shows the image of the fabricated antenna. Varying the feed shape or slot shape will change the coupling property between the feed and slot, and thus the operating bandwidth is confined by matching between the feed shape and the wide slot on the ground plane [13]. The optimized radius of the circle-like slot is 11.5 mm. The proposed fork-shaped patch consists of two vertical and one horizontal arms. The width of this patch is fixed at 0.6 mm. The antenna is built on an FR4-epoxy substrate with $\varepsilon_r = 4.4$ and a substrate thickness of 1.6 mm. In order to have 50 Ω characteristic impedance, a coplanar waveguide (CPW) feed line with a fixed 2.6 mm width and 0.3 mm ground gap is used. By employing CPW transmission line, misalignment between the fork-shaped patch and ground plane can be removed. For the given values of constant dielectric and characteristic impedance of CPW line and using closed-form expressions shown in [18], the CPW dimensions can be calculated. In the simulation process, a wave port which is renormalized to a 50-ohm full port impedance, is located just behind the CPW feed line to excite the Fork-shaped patch. We add a pair of L-shaped stubs, which are connected to the fork-shaped patch, to obtain the single band-notched function. These stubs have a vertical arm of length $L_l$ and a horizontal arm of length $W_l$, where their width is fixed at 0.5 mm. Moreover, by employing these stubs the impedance matching at the middle frequencies of the band can be highly improved. Furthermore, a T-shaped stub with a horizontal arm of length $W_t$ and a vertical arm of length $L_t$, are added to the antenna structure to generate dual band notched characteristics. The width of the T-shaped stub is set to 0.4 mm. To enhance the bandwidth of the proposed antenna, we add a pair of T-shaped slits with the given values in the ground as shown in Fig. 1. These T-shaped slits width is fixed at 0.3 mm.

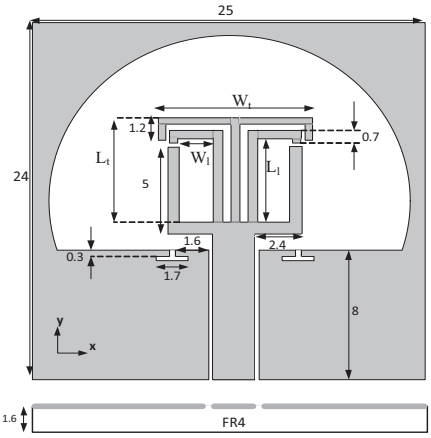


Fig. 1. Geometry of the proposed single-layer slot antenna with dual band notched function (mm).

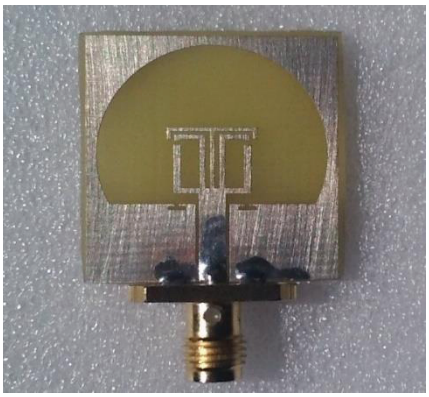

Fig. 2. Photograph of the proposed dual band-notched antenna.

## III. SIMULATION RESULTS AND DISCUSSION

In this section, a simulation study is performed to investigate the effect of different design parameters in the proposed antenna. In this study, the simulated results of the impedance bandwidth characteristics and electrical current distributions are presented and discussed. Ansoft HFSS (High Frequency Simulation Structure) tool, which is based on the finite element method, is employed to obtain the simulated results. In this design, a fork-shaped patch and circle like slot with proper dimension are employed to create the proposed UWB antenna. In UWB slot antennas, the geometrical shape and size of the patch and wide slot etched in the ground plane play an important role in creating consecutive resonances and providing a wide impedance bandwidth. Proper changes in the patch and ground structure will cause a better distribution of the surface currents on the antenna. Hence, the impedance matching and radiation characteristics can be improved for the frequency range of interest. At the first step, a pair of L-shaped stubs is connected to the fork-shaped patch to improve the antenna design with single band-notched properties. The simulated return loss for the antenna with and without L-shaped stubs are depicted in Fig. 3. As seen from Fig. 3, by employing two L-shaped stubs not only single band notched properties can be achieved but also the impedance matching of the antenna is remarkably improved, especially at the middle frequencies of the band. In fact, these stubs are placed to create extra resonant path for the electrical current, which produce an extra resonance around 15.6 GHz, and therefore improve the impedance bandwidth. To show the frequency performance of the L-shaped stubs in the fork-shaped patch, electrical current distributions of the antenna with and without L-shaped stubs at the new resonance frequency of 15.6 GHz are presented in Fig. 4. At this frequency, the directions of the surface currents on the fork-shaped patch and L-shaped stubs are the same. It can be clearly seen that the bandwidth improvement is because of the vertical current arrangement in the modified patch via the L-shaped stubs. At the notch frequency, i.e., 5.6 GHz, the electrical current flows are more concentrated around the L-shaped elements and they are reversely directed between these elements and the radiating fork-shaped patch. Hence, the radiation fields neutralize each other, as demonstrated in Fig. 7 (b). The L-shaped stubs act as a quarter-wavelength resonator. Hence, their total length should be equal to quarter-wavelength at desired notch frequency (5.6 GHz). The L-shaped stub parameters can be determined using the following equations and the simulation results obtained from HFSS software:

$$L_{total\,(l)} \approx L_l + W_l + 0.7 \approx \frac{c}{4f_{notch1}} \approx \frac{\lambda_g}{4} \approx \frac{\lambda_0}{4\sqrt{\varepsilon_{reff}}}, \quad (1)$$

where $L_{total\,(l)}$ is the total length of the L-shaped stub, $L_l$ and $W_l$ are vertical and horizontal arm of the L-shaped stub, respectively. $f_{notch1}$ and $c$ are respectively the desired notch frequency of 5.6 GHZ and the speed of light in free space. Moreover, $\lambda_0$ is the wavelength of free space, $\lambda_g$ is the guided wavelength and $\varepsilon_{reff} \approx \frac{1+\varepsilon_r}{2}$.

To obtain dual band notched feature, we add a T-shaped stub, which is connected to the center of the fork-shaped patch, to the antenna geometry. Similarly, for the 3-4 GHz band (first notched band), the electrical current is more dominant around T-shaped stub. This stub acts also as a quarter wavelength resonator at the desired notch frequency (3.6 GHz), and its total length can be as follows:

$$L_{total\,(t)} \approx L_t + \frac{1}{2} W_t + 1.2 \approx \frac{c}{4f_{notch2}} \approx \frac{\lambda_g}{4}. \quad (2)$$

In (2), $L_{total\,(t)}$ is the total length of the L-shaped stub, $L_t$ and $W_t$ are respectively the vertical and horizontal arm of the T-shaped stub. Moreover, $f_{notch2}$ is the desired notch frequency of 3.6 GHz.

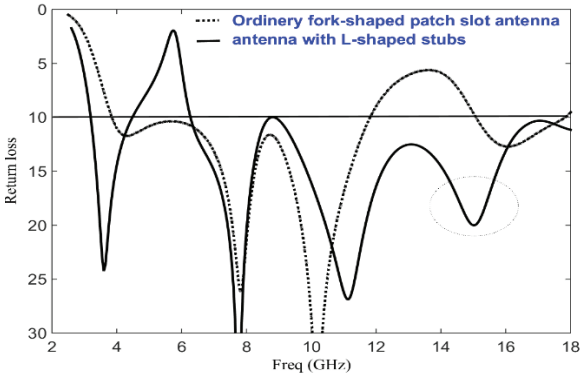


Fig. 3. Simulated VSWR of the basic antenna with and without L-shaped stubs.

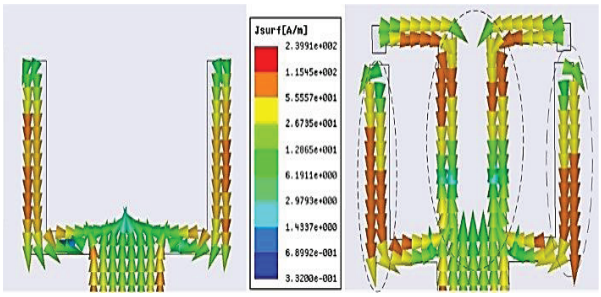


Fig. 4. Surface current distributions of the antenna without *(left)* L-shaped stubs and with *(right)* L-shaped stubs at 15.6 GHz.

By appropriately adjusting the parameters of the L-shaped and T-shaped stubs, the position of the rejected bands are tuned. Figure 5 shows the VSWR of the antenna with different values of $L_t$ and $L_l$ when $W_t$ and $W_l$ are fixed at 8.6 and 2.9 mm, respectively. Figure 6 illustrates the VSWR of the antenna with different values of $W_t$ and $W_l$ when $L_t$ and $L_l$ are set at 6.1 and 5.4 mm respectively. The results illustrate that by controlling the total lengths of the L-shaped and T-shaped stubs to be nearly quarter-wavelength of the desired notched frequency, a reduced interference effect can be seen. To study the dual band-notched properties of the proposed antenna, the simulated electrical current distribution is displayed in Fig. 7. As this figure shows, the current concentration mainly happens on the T-shaped stub at 3.6 GHz, i.e., the center frequency of the first notched band. Moreover, as mentioned earlier, the highest electrical current centralizes over the L-shaped stubs at 5.6 GHz, i.e., the center frequency of the second notched band.

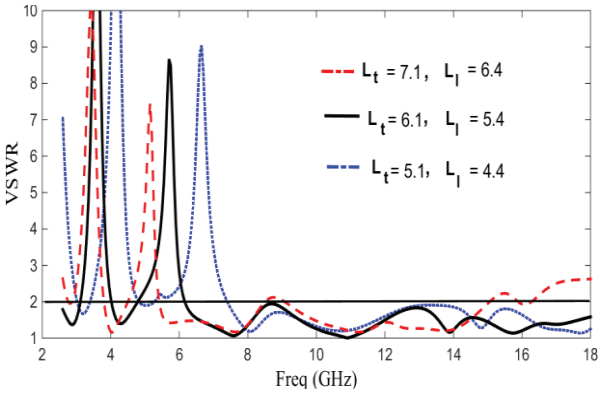


Fig. 5. Simulated VSWR for proposed dual band-notched antenna with different values of $L_t$ and $L_l$ when $W_t = 8.6$ and $W_l = 2.9$ mm.

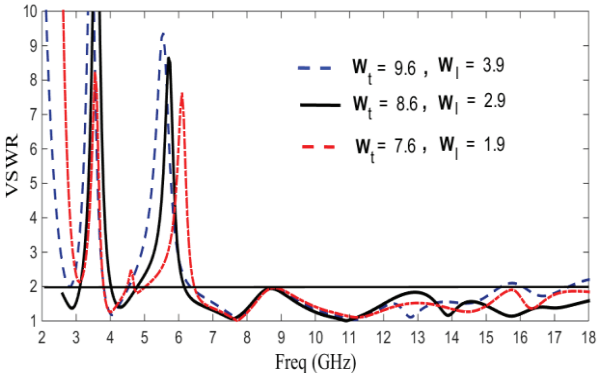


Fig. 6. Simulated VSWR for proposed dual band-notched antenna with different values of $W_t$ and $W_l$ when $L_t = 6.1$ and $L_l = 5.4$ mm.

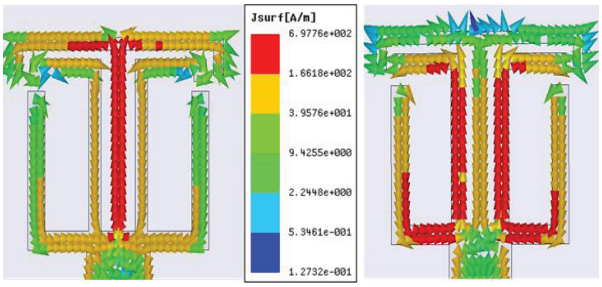


(a) (b)

Fig. 7. Simulated electrical current distributions of the proposed antenna: (a) at 3.6, and (b) at 5.6 GHz.

Two T-shaped slits are cut in both sides of the CPW feed line on the ground plane to increase the impedance bandwidth of the proposed antenna as depicted in Fig. 1. By cutting two T-shaped slits with proper size from the ground plane, surface

currents can be effectively distributed at the edges of the ground below the fork-shaped patch. Figure 8 illustrates the return loss of the base antenna with and without T-shaped slits on the ground plane. According to Modified Ground Structures (MGS), by etching the slits in the ground plane and attentively tuning their components, extra resonances around 16.2 GHz can be excited, and therefore, much increased impedance bandwidth can be earned [9]. Figure 9 depicts the electrical current distribution on the ground plane of the proposed antenna with and without T-shaped slits. As seen in this figure, the electrical current distribution on the modified ground plane alters the impedance properties of the antenna and so it leads to modify the bandwidth.

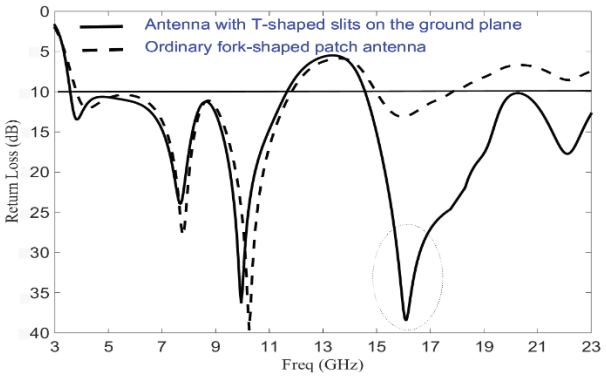


Fig. 8. Simulated VSWR of the basic antenna with and without T-shaped slits on the ground plane.

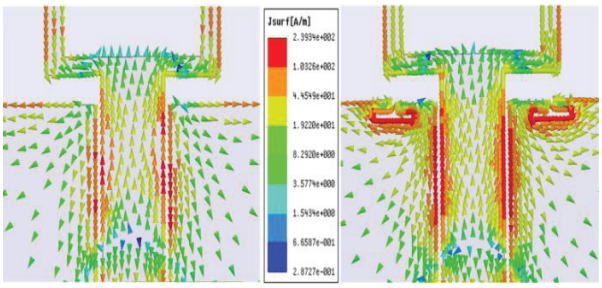


Fig. 9. Electrical current distributions of the antenna without T-shaped slits and with T-shaped slits at 16.2 GHz.

Figure 10 presents the structure of the different antennas used for simulation studies. The VSWR characteristics for the basic fork-shaped patch antenna (Fig. 10 (a)), with a pair of L shaped stubs (Fig. 10 (b)), with the L-shaped and T-shaped stubs (Fig. 10 (c)), and proposed antenna (Fig. 10 (d)) are compared in Fig. 11.

As shown in Fig. 11, it is observed that by using these L-shaped and T-shaped stubs and inserting the T-shaped slits in the ground plane, dual band notched characteristics and bandwidth enhancement can be achieved.

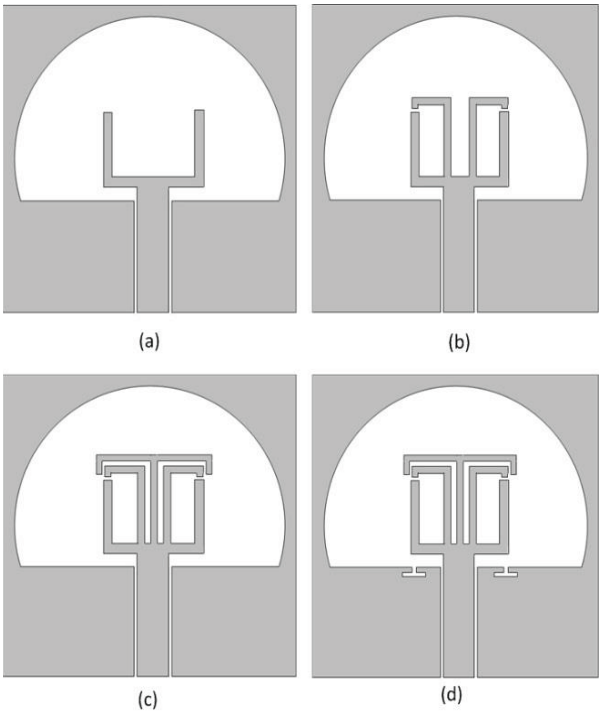


Fig. 10. (a) Basic structure (ordinary fork-shaped patch antenna), (b) basic structure with a pair of L-shaped stubs, (c) basic structure with a pair of L-shaped and a T-shaped stubs, and (d) proposed antenna.

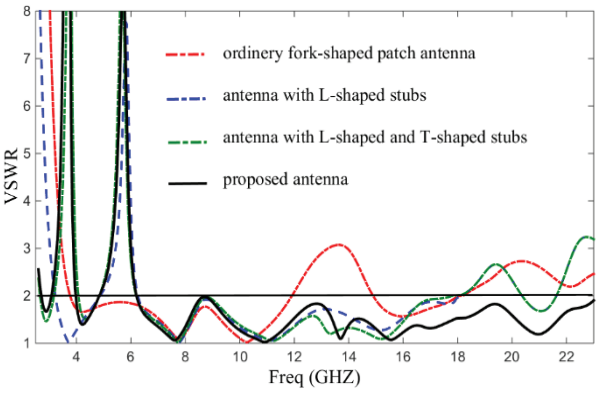


Fig. 11. Simulated VSWR characteristics for the antennas shown in Fig. 10.

## IV. EXPERIMENTAL RESULTS

### A. VSWR measurement

The electrical performance of the proposed antenna such as VSWR, has been measured by using an Agilent 8722ES vector network analyzer with 801 test points over the frequency range. Figure 12 illustrates the simulated and measured VSWR of the proposed antenna. It can be observed that the measured VSWR agrees with the simulated results obtained by using HFSS and CST (Computer Simulation Structure) tool, which is based on the finite integral technique as shown in Fig. 12. A small difference between measured values and the simulated results exists, which could be because of the SMA connector and construction tolerance effects. The proposed antenna provides a very wideband performance of 2.5-23 GHz for VSWR<2, with dual band notched characteristics of 3.2-4 and 5-6.2 GHz.

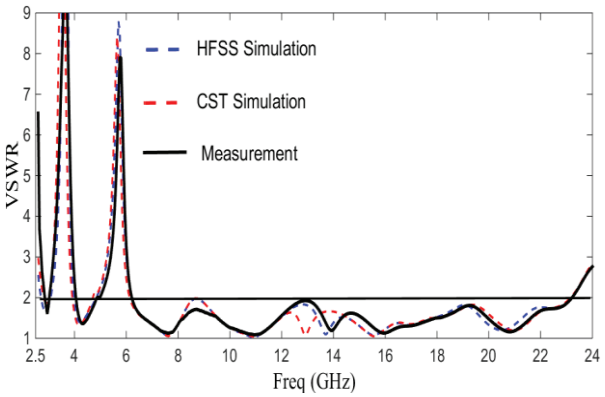


Fig. 12. Measured and simulated VSWR results of the presented dual band notched antenna.

### B. Radiation efficiency measurement

The Wheeler Cap (WC) method [17] is employed to measure the radiation efficiency of the proposed antenna. This method evaluates the return loss of an antenna in free space with the return loss of the antenna in WC. The measured radiation efficiency characteristic of the proposed antenna is obtained by employing an 8-cm radius wideband WC. An important parameter which degrades the radiation characteristics of the antenna such as gain and radiation efficiency is the excitation of surface waves on the substrates. During the measurements, a foil of absorber material beneath the proposed antenna feed is used to reduce the surface waves in the measurement process. Figure 13 shows the measured radiation efficiency and gain of the proposed antenna. As depicted in this figure, two keen gain and radiation efficiency nulls happen in the 3-4 and 5-6 GHz bands.

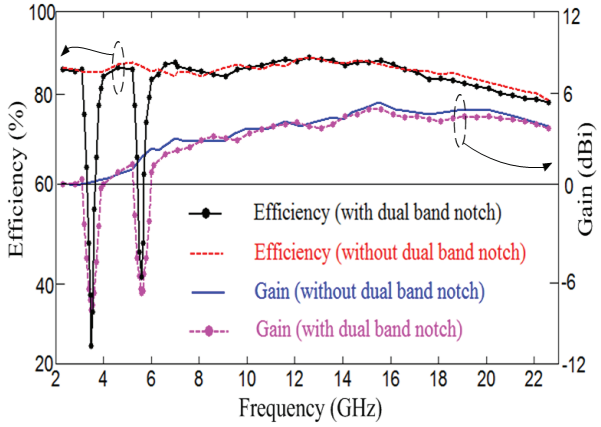


Fig. 13. Measured gain and radiation efficiency of the proposed antenna.

### C. Radiation pattern and gain measurement

A 6×6×12 $m^3$ anechoic chamber along with a Performance Network Analyzer (PNA) 10 MHz - 67 GHz (Agilent E8361C) and far-field measurement software are employed to measure the gain and radiation pattern of the antenna. The absorbers placed in the anechoic chamber absorb electromagnetic waves up to a frequency of 40 GHz. A double-ridged horn antenna is also used as a reference antenna in measurement process.

Figure 14 shows the measured radiation patterns in the two principal planes, H- and E-planes at the resonance frequencies of 2.8, 4.3, 7.6, and 16 GHz. As seen, the radiation patterns in the H-plane, i.e., x-z plane, are nearly omnidirectional for the four frequencies and the antenna exhibits dipole-like radiation patterns in the E-plane. The distortion of the radiation patterns at the higher frequency is caused by the seriously unequal phase distribution of electrical fields on the slot and increased magnitudes of higher order modes.

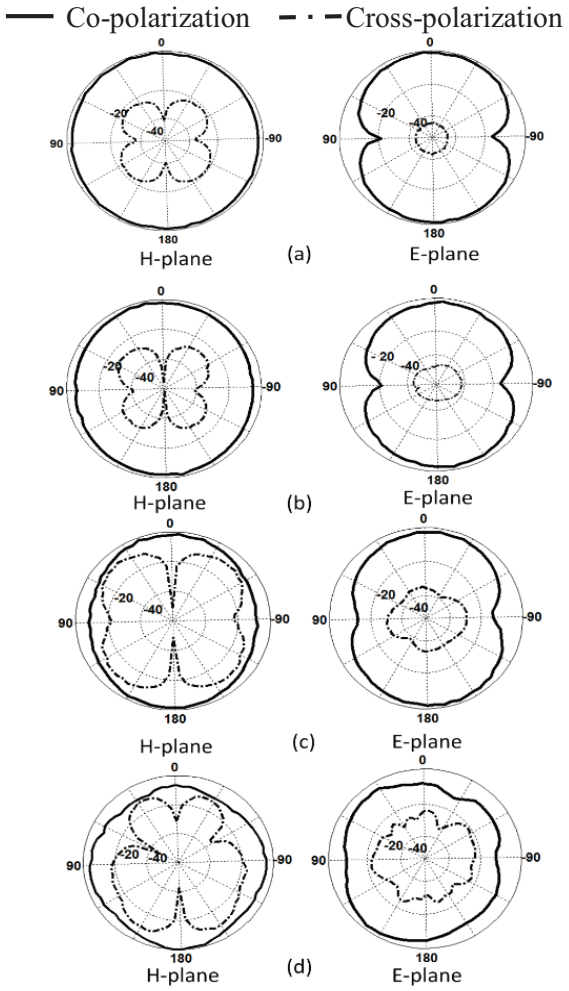


Fig. 14. Radiation pattern for various resonance frequency for the proposed antenna at: (a) 3, (b) 4.3, (c) 7.6, and (d) 16 GHz.

## V. CONCLUSION

In this paper, a novel compact circle-like slot antenna with dual band-notched function for super wideband applications has been reported. Results show that by using a pair of L-shaped stubs connected to the fork-shaped patch, single band notch characteristic and bandwidth improvement at the middle frequencies of the band can be achieved. Then a T-shaped stub connected to the center of the fork-shaped patch is employed to create dual band-notched characteristics. At last, we indicated by using two T-shaped slits etched in the ground plane a wide impedance bandwidth (164%) from 2.5 to 23 GHz can be obtained. The good impedance matching and radiation patterns characteristics over the entire band show that the proposed antenna could be a good applicant for UWB application.

## REFERENCES

[1] C.-C. Yu and X.-C. Lin, "A wideband single chip inductor-loaded CPW-fed inductive slot antenna," *IEEE Trans. Antennas Propag.*, vol. 56, no. 5, pp. 1498-1501, May 2008.

[2] Y. W. Jang, "Experimental study of large bandwidth three-offset microstrip line-fed slot antenna," *IEEE Microw. Wireless Comp. Lett.*, vol. 11, pp. 425-426, 2001.

[3] S. R. Emadian, M. Mirmozafari, C. Ghobadi, and J. Nourinia, "Bandwidth enhancement of dual band-notched circle-like slot antenna," *Electronics Letters*, vol. 48, no. 7, pp. 356-357, Mar. 2012.

[4] S. R. Emadian, C. Ghobadi, J. Nourinia, M. Mirmozafari, and J. Pourahmadazar, "Bandwidth enhancement of CPW-fed circle-like slot antenna with dual band-notched characteristic," *IEEE Antennas Wireless Propag. Lett.*, vol. 11, pp. 543-546, 2012.

[5] M. A. Gonzalez de Aza, J. Zapata, and J. A. Encinar, "Broadband cavity backed and capacitively probe-fed microstrip patch arrays," *IEEE Trans. Antennas Propag*., vol. 48, pp. 784-789, 2001.

[6] V. Sadeghi, C. Ghobadi, and J. Nourinia, "Design of a UWB semi-circle like slot antenna with controllable band-notch function," *Electron. Lett.*, vol. 45, pp. 1282-1283, 2009.

[7] R. Zaker, C. Ghobadi, and J. Nourinia, "Bandwidth enhancement of novel compact single and dual band-notched printed monopole antenna with a pair of L-shaped slots," *IEEE Trans. Antennas Propag.*, vol. 57, no. 12, pp. 3978-3983, Dec. 2009.

[8] R. Zaker, C. Ghobadi, and J. Nourinia, "Novel modified UWB planar monopole antenna with variable frequency band-notch function," *IEEE Antenna Wireless Propag. Lett*., vol. 7, pp. 112-114, 2008.

[9] Y. Lin and K. Hung, "Compact ultra-wideband rectangular aperture antenna and band-notched design," *IEEE Trans. Antennas Propag.*, vol. 54, no. 11, pp. 3075-3081, Nov. 2006.

[10] S. R. Emadian, C. Ghobadi, and J. Nourinia, "A novel compact dual band-notched slot antenna for ultra-wideband applications," *Microw. Opt. Technol. Lett.*, pp. 1365-1368, 2012.

[11] M. Ojaroudi, S. Yzdanifard, N. Ojaroudi, and R. A. Sadeghzadeh, "Band-notched small square-ring antenna with a pair of T-shaped strips protruded inside the square ring for UWB applications," *IEEE Antennas Wireless Propag. Lett.*, vol. 10, pp. 227-230, 2011.

[12] D. Mitra, D. Das, and S. R. Chaudhuri, "Bandwidth enhancement of microstrip line and CPW-fed asymmetrical slot antennas," *Progress In Electromagnetics Research Letters*, vol. 32, 2012.
[13] A. Dastranj and H. Abiri, "Bandwidth enhancement of printed E-shaped slot antennas fed by CPW and microstrip line," *IEEE Trans. Antennas Propag.*, vol. 58, no. 4, pp. 1402-1407, 2009.
[14] P. Kaur, R. Nehra, M. Kadian, A. De, and S. K Aggarwal, "Design of improved performance rectangular microstrip patch antenna using peacock and star shaped DGS," *International Journal of Electronics Signals and Systems*, vol. 3, 2013.
[15] N. Ojaroudi and M. Ojaroudi, "Novel design of dual band-notched monopole antenna with bandwidth enhancement for UWB applications," *IEEE Antenna Wireless Propag. Lett*., vol. 9, pp. 1076-1079, 2010.
[16] R. Shi, X. Xu, J. Dong, and Q. Luo, "Design and analysis of a novel dual band-notched UWB antenna," *International Journal of Antennas and Propagation*, vol. 2014, 2014.
[17] H. G. Schantz, "Radiation efficiency of UWB antennas," in *IEEE Conf. Ultra Wideband Syst. Technol. Dig.*, pp. 21-23, May 2002.
[18] B. C. Wadell, *Transmission Line Design Handbook*, Boston, MA: Artech House, pp. 73-76, 1991.

**Seyed Ramin Emadian** was born in Tehran, Iran in 1985. He received the B.Sc. degree in Electrical Engineering from The University of Mashad, Mashad, Iran in 2008, and the M.Sc. degree in Electrical Engineering from The University of Urmie, Urmie, Iran in 2011. He is currently working towards the Ph.D. degree at The University of Sistan and Baluchestan, Zahedan, Iran. From 2013, he has been with the Department of Electrical Engineering, University of Sistan and Baluchestan. His research concerns include millimeter wave and ultra-wideband systems, analysis and design of multi band microstrip antennas, circular polarization patch antennas, multiple input and multiple output antennas and multi band notched UWB antennas.

**Javad Ahmadi-Shokouh** received the B.Sc. degree in Electrical Engineering from Ferdowsi University of Mashhad, Mashhad, Iran in 1993, the M.Sc. degree in Electrical Engineering from The University of Tehran, Tehran, Iran in 1995, and the Ph.D. degree in Electrical Engineering from The University of Waterloo, Waterloo, ON, Canada in 2008. From 1998 to 2003, he was with the Department of Electrical Engineering, University of Sistan and Baluchestan, Zahedan, Iran as a Lecturer, where he is currently an Assistant Professor. He was also with the Department of Electrical Engineering, University of Manitoba, Winnipeg, MB, Canada (2008-2009) as a Postdoctoral Fellow. His research interests are antenna and microwave systems for all applications, millimeter wave and ultra-wideband systems, smart antennas, optimal and adaptive MIMO systems.

# Numerical Analysis and Design of a New Simple Compact Ultra-Wideband Dielectric Resonator Antenna with Enhanced Bandwidth and Improved Radiation Pattern

**Seyyed Hadi Seyyedhatami [1] and Ramazan Ali Sadeghzadeh [2]**

[1] Department of Electrical Engineering, Science and Research Branch
Islamic Azad University, Tehran, Iran
h.seyyedhatami@srbiau.ac.ir

[2] Faculty of Electrical Engineering
K. N. Toosi University of Technology, Tehran, Iran
sadeghz@eetd.kntu.ac.ir

***Abstract*** ─ A new simple compact ultra-wideband (UWB) dielectric resonator antenna (DRA) is presented. The finite-difference time-domain (FDTD) method is used to the full-wave analysis of this structure. The antenna consists of a modified stepped microstrip fed monopole printed antenna loaded with a rectangular dielectric resonator, truncated ground plane and a parasitic strip underneath the dielectric resonator (DR). By using an optimized truncated ground plane and a combination of stepped feed line with dielectric resonator, an ultra-wide impedance bandwidth of 153% for ($S_{11} \leq$ -10 dB), covering the frequency range of (3.7–28 GHz) is achieved. The added parasitic strip can improve the radiation pattern, especially at high frequencies. The proposed antenna covers almost the entire UWB (3.1–10.6 GHz), Ku (12.4–18 GHz) and K (18–26.6 GHz) frequency bands. Also, this antenna has an omnidirectional and stable radiation pattern over the whole operating frequency range and a compact size of ($15\times20\times5.8$ mm$^3$) that make it suitable for wideband wireless system applications. This structure is light weight and can be easily fabricated. A prototype is built and measured. The simulated and measured results are in good agreement with the computed FDTD result.

***Index Terms*** ─ Dielectric resonator antenna (DRA), finite difference time domain (FDTD), omnidirectional pattern, ultra-wideband (UWB) antenna.

## I. INTRODUCTION

Recently, the demand for ultra-wideband (UWB) communication systems has rapidly increased due to their many advantages including the high data rate, high speed, low cost, high accuracy in localization systems or high resolution in radar applications. Hence, in most of the applications it is necessary that these systems have a wideband antenna with low profile, omnidirectional and stable radiation pattern, constant gain and constant group delay. The dielectric resonator antenna (DRA) has been recently proposed to be one of the attractive candidate antennas for UWB applications due to striking characteristics such as high radiation efficiency, light weight, small size, different feeding mechanisms, wide bandwidth, absence of ohmic losses and no excitation of surface waves. In the last two decades many techniques have been reported to broaden the impedance bandwidth of DRAs, such as stacked DRs [1-3], special feeding mechanisms [4,5] and conformal patch feeding [6,7]. Although these techniques have enhanced the DRA's bandwidth, however, most of these antennas have a large size and common deficiencies such as asymmetric and unstable radiation pattern and complicated structure.

In this article, a new compact ultra-wideband dielectric resonator antenna with enhanced bandwidth and improved radiation pattern is proposed. The proposed antenna covers uwb frequency band, and entire Ku and K-band (12.4–

*Submitted On: April 27, 2014*
*Accepted On: April 8, 2015*

26.5 GHz). Lately, this frequency range receives some particular research interest due to the development of high frequency communication systems. By using the combination of a stepped monopole antenna with truncated ground plane and a rectangular dielectric resonator with proper position respect to the feeding structure, the considerable electromagnetic coupling between the feeding patch and DR can be obtained. As a result, the proposed DRA can provide an ultra-wide impendence bandwidth with symmetrical and stable radiation patterns. The rectangular dielectric resonator (RDR) is chosen because it provides some more advantages compared to cylindrical and hemispherical ones. The three dimensions of a RDR provide one degree of freedom more than cylindrical dielectric resonator, which can be used to control the impedance bandwidth of the antenna [8]. Moreover, a RDR gives more flexibility to the manufacturer making it more versatile in achieving a wide impedance bandwidth. In order to improve the radiation pattern at high frequencies, a parasitic strip underneath the DR is utilized. This strip eliminates some of the higher order modes that would cause a consistent omnidirectional pattern in H-plane across the whole operating frequency band (3.7–28 GHz). This DRA is simulated using a High Frequency Structure Simulator (HFSS) [9]. In addition to the Simulated and measured results, the FDTD calculated result is presented to validate the usefulness of the proposed antenna structure for UWB applications.

## II. ANTENNA DESGIN

Figure 1 shows the configuration of the proposed antenna, which consists of a rectangular dielectric resonator and a stepped microstrip fed monopole antenna printed on an FR4 microwave substrate with size of 15×20 mm$^2$, thickness of 0.8 mm and dielectric constant of 4.4.

In theory, a DRA with a dielectric constant of one for the DR, would have the lowest Q-factor and therefore the widest bandwidth. In practice, however, there is a lower limit on the value of the dielectric constant required to contain the fields within the DRA in order to resonate. As a result, a relative permittivity around 10, which is normally used in related designs, is chosen for our DRA design [8]. The size of the DR has 7.5 mm length, 6 mm width, and 5 mm thickness, which is fabricated on Rogers RT/Duroid 6010 microwave dielectric material with a dielectric constant of 10.2. The feeding structure comprised of a 50 Ω microstrip transformer with $W_f$ =1.6 mm width and $L_f$ = 5.3 mm length and a stepped monopole antenna with lengths of $L_1$ = 4.3 mm, $L_2$ = 2.5 mm and widths of $W_1$ = 1 mm, $W_2$ = 4.3 mm. By applying this step-shaped feeding and adjusting its position underneath the DR ($L_4$), a significant coupling and a good impedance matching can be achieved. The truncated ground plane is printed on the bottom side of the substrate with size of 8.5×15 mm$^2$.

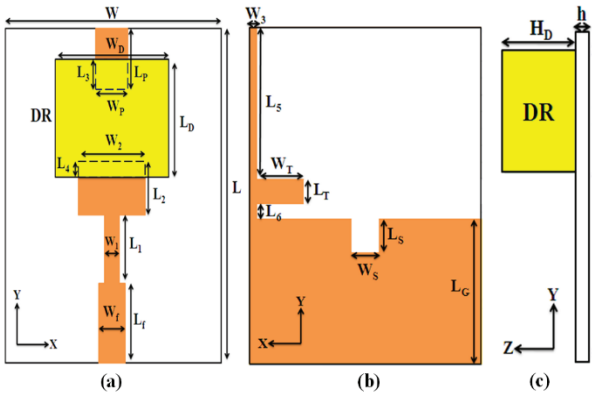


Fig. 1. Configuration of the proposed DRA: (a) top view, (b) bottom view, and (c) side view.

Figure 2 shows the design procedure of the proposed DRA. Also, the simulated reflection coefficients for the various antenna structures shown in Fig. 2, are compared in Fig. 3.

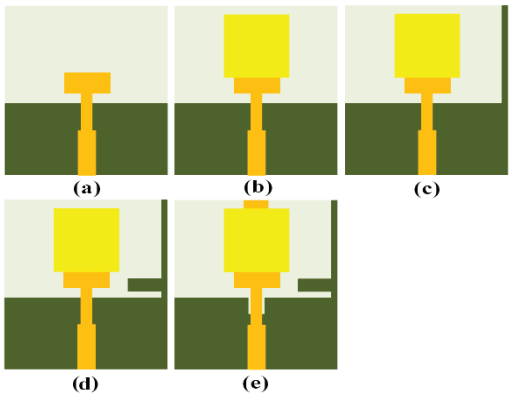


Fig. 2. Design procedure of the proposed DRA: (a) monopole antenna, (b) monopole antenna loaded with the DR, (c) monopole antenna loaded with the DR and the added tuning stub, (d) monopole antenna loaded with the DR and two added tuning stubs, and (e) proposed DRA.

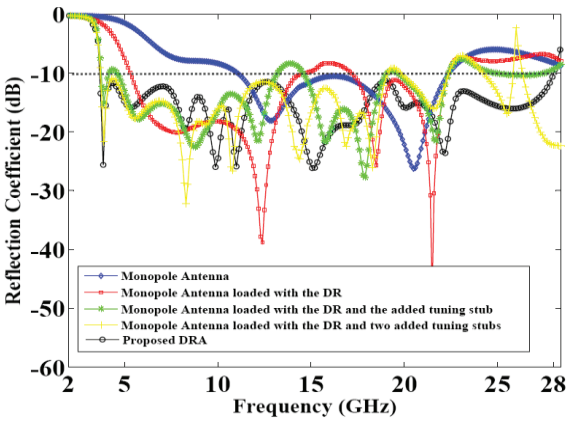


Fig. 3. Simulated reflection coefficients for the various antenna structures shown in Fig. 2.

The basic monopole antenna structure is shown in Fig. 2 (a). From Fig. 3, it can be seen that this monopole has two resonant frequencies and a wide impedance bandwidth from 11 to 22 GHz. In order to increase the bandwidth and shift the lower band towards lower frequencies, the DR is loaded on the monopole structure as shown in Fig. 2 (b). The initial dimensions of these structures are chosen in a manner that the resonant modes of the monopole and the DR can be excited with adjacent resonant frequencies to achieve a wideband operation. Since the DR is fed by a monopole structure in the xy-plane, the transverse electric modes $TE^{x}_{\delta mn}$, $(0 < \delta < 1)$ can be excited in it. By using the dielectric waveguide model (DWM) [10], the resonant frequencies of the DR can be given as follows:

$$f_0 = \frac{c}{2\pi\sqrt{\varepsilon_r}}\sqrt{k_x^2 + k_y^2 + k_z^2}\ , \qquad (1)$$

where

$$k_y = \frac{m\pi}{L_D}\ ,\ k_Z = \frac{n\pi}{H_D}\ , \qquad (2)$$

$$k_x^2 + k_y^2 + k_z^2 = \varepsilon_r k_0^2\ , \qquad (3)$$

$$k_x \tan(k_x W_D/2) = \sqrt{(\varepsilon_r - 1)k_0^2 - k_x^2}\ , \qquad (4)$$

in which $k_0$ is free-space wavenumber, $c$ is the speed of light in vacuum, and $k_x$, $k_y$ and $k_z$ are wavenumbers inside the DR in the three directions. The subscripts $m$, $n$ denote the number of extremes in the $y$ and $z$ directions, respectively. However, since these resonant frequencies are determined for isolated DR and do not account for the coupling mechanisms between the DR and feeding structure, which may introduce new resonant frequencies, to further investigate the properties of DRA, simulations and optimization of the structures are performed using HFSS software. As illustrated in Fig. 3, the monopole antenna loaded with the DR achieves better impedance matching than the basic monopole antenna structure. However, there are some mismatches at the low frequency band (less than 5 GHz), the middle frequency band (around 16 GHz), and the high frequency band (more than 22 GHz). As shown in Fig. 2 (c), in order to obtain a better impedance matching at the low frequency band, a tuning stub is added to the truncated ground plane [11]. As it is observed from Fig. 3, although the added tuning stub can improve the impedance matching and reveal the resonant modes that occur due to the coupling effect between the DR and monopole structure, however, there is still a little mismatch at the low frequency band and the frequency band around 14 GHz. Therefore, to further improve these mismatches, another tuning stub is added to the modified truncated ground plane, as shown in Fig. 2 (d). It can be seen from Fig. 3 that, the monopole antenna loaded with the DR and two added tuning stubs can achieve better impedance matching than the previous structures, but there are still some mismatches at the high frequency bands. Thus, to improve these mismatches, a rectangular slot is etched on the modified truncated ground plane below the feed line, as illustrated in Fig. 2 (e). It is clearly observed from Fig. 3 that, the proposed DRA with the etched slot on the ground plane can achieve a wide impedance matching, even at the high frequency bands; because the rectangular slot creates a capacitive load that neutralizes the inductive nature of the feeding patch, especially at high frequency bands. It can be seen in Fig. 2 (e) that, a parasitic strip is added underneath the DR. This strip can eliminate some of the higher order modes and change the field distribution inside the DR, to achieve a stable omnidirectional radiation pattern in H-plane, especially at high frequency bands.

Design, simulation and optimization of the proposed DRA are carried out using HFSS, leading to the following optimal dimensions: L = 20 mm, W = 15 mm, $L_f$ = 5.3 mm, $W_f$ = 1.6 mm, $L_1$ = 4.3 mm, $W_1$ = 1 mm, $L_2$ = 2.5 mm, $L_D$ = 7.5 mm, $W_D$ = 6 mm, $H_D$ = 5 mm, $L_P$ = 3 mm, $W_P$ = 2 mm, $L_3$ = 2 mm, $L_4$ = 0.6 mm, $L_T$ = 1.5 mm, $W_T$ = 3 mm, $L_S$ = 1.9 mm, $W_S$ = 1.4 mm, $L_G$ = 8.5 mm, $W_3$ = 0.5 mm and h =

0.8 mm.

In order to further investigate the characteristics of the proposed DRA and achieve the optimum antenna performance, a parametric study was carried out. The Ansoft HFSS software, which is based on the finite element method, is used for the parametric analysis of reflection coefficient. The key parameters of the proposed antenna are studied by changing one parameter at a time and fixing the others.

Figure 4 shows the effect of the truncated ground plane length ($L_G$) on the reflection coefficient of the proposed DRA. It can be seen that the best matching and impedance bandwidth is achieved at $L_G = 8.5$ mm.

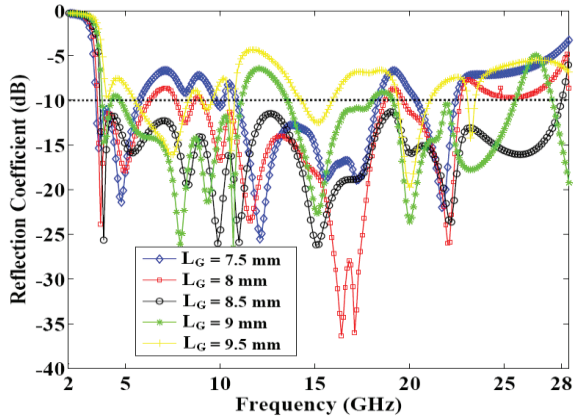


Fig. 4. Simulated reflection coefficient for various length of $L_G$.

The effect of the first tuning stub length ($L_5$) is shown in Fig. 5. It is observed that the impedance matching is degraded by increasing the length of $L_5$, at the low frequency band. Therefore, the optimized value of $L_5$ is equal to 9 mm. Another parametric study is done on various values of $L_6$, which it indicate the distance between the second tuning stub and the truncated ground plane, as shown in Fig. 6. It is observed that the impedance matching is degraded by increasing the length of $L_6$, at the low frequency band. So the best impedance matching is achieved at $L_6 = 1$ mm. Figure 7 shows the effect of the $W_2$ parameter. It can be seen that for the lower value of $W_2$, the impedance matching is poor, because of the weak coupling between the feeding structure and the DR. On the other hand, for the higher value, there are some mismatches. Therefore, the best impedance matching is achieved at $W_2 = 4.3$ mm.

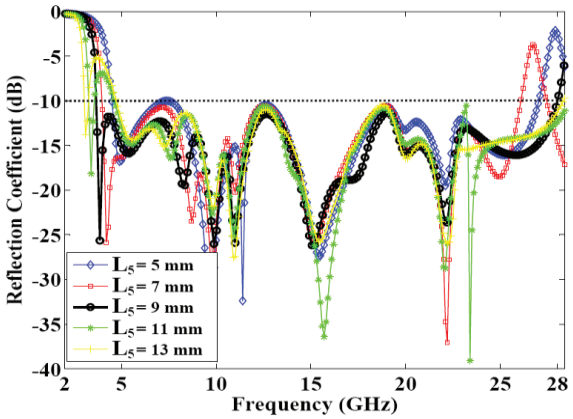


Fig. 5. Simulated reflection coefficient for various length of $L_5$.

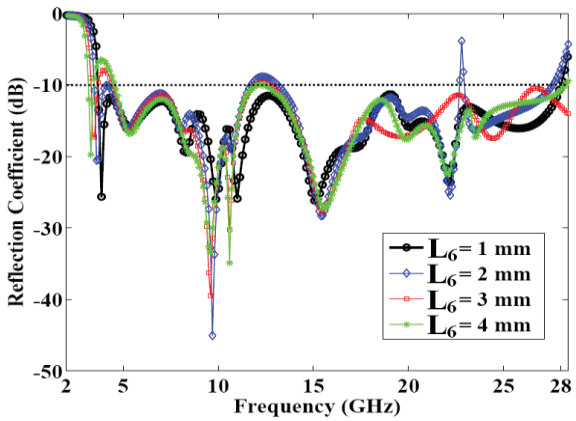


Fig. 6. Simulated reflection coefficient for various length of $L_6$.

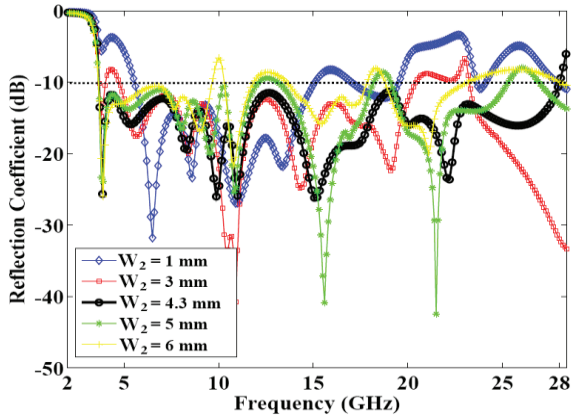


Fig. 7. Simulated reflection coefficient for various length of $W_2$.

## III. FDTD ANALYSIS

FDTD methods are widely used to characterize and simulate electromagnetic wave propagation

and antenna structures [12]. In this work, the FDTD algorithm with uniform Cartesian grid is applied to analyze the proposed DRA [13,14]. The space steps used in the FDTD analysis are $\Delta x$, $\Delta y$, and $\Delta z$. All of them should be smaller than $\lambda_{min}/20$, where $\lambda_{min}$ is the minimum operating wavelength of the antenna structure. In order to correctly model the dimensions of the antenna, the space steps have been chosen so that an integral number of nodes will exactly fit the rectangular dielectric resonator. Unfortunately, this means the stepped monopole structure lengths, widths, and placement will be offset by a fraction of the space step. The sizes of the space steps are carefully chosen to minimize the effect of this error. To model the thickness of the substrate (h) correctly, $\Delta z$ is chosen so that four nodes exactly match the thickness. An additional 14 nodes in the $z$ and $-z$ directions are used to model the free-space above the DR and under the substrate, respectively. The space steps used are $\Delta x = 0.2$ mm, $\Delta y = 0.395$, and $\Delta z = 0.2$ mm.

As in [14], Mur's first order absorbing boundary conditions (ABC) are used to terminate the computational domain. Hence, the tangential electric filed components on the six outer boundaries will obey the one-dimensional wave equation in the direction normal to the mesh wall. Since the reflections from the antenna structure will be reflected again by the source wall, to eliminate this, the microstrip line feeding structure is extended with additional 30 nodes in the $-y$ direction, and in order to reduce the source distortion, a changeable source plane is assumed following Sheen, et al. [14]. This plane is a magnetic wall all over the source plane and when the excitation pulse has been fully launched, it is substituted by Mur's first order ABC. Thus, the length of the microstrip line from the source plane to the reference plane is $30\Delta y$. The total size of the computational domain is $76\Delta x \times 81\Delta y \times 57\Delta z$.

A simple voltage source approximation is used to model the feed of the microstrip line. A baseband Gaussian pulse of half-width $T = 10$ ps is applied at the source plane to suit the frequency range of interest (0–30 GHz). The time delay $t_0$ is set to be $3T$ so the Gaussian will start at approximately 0. The time step used, according to the Courant stability condition [12], is $\Delta t = 0.2$ ps. The iterations are performed for 8000 time steps to allow the input response to vanish.

## IV. RESULTS AND DISCUSSION

To validate the proposed design, an optimized DRA was fabricated and measured, which is shown in Fig. 8. The optimized DRA parameters are as follows: $L = 20$ mm, $W = 15$ mm, $L_f = 5.3$ mm, $W_f = 1.6$ mm, $L_1 = 4.3$ mm, $W_1 = 1$ mm, $L_2 = 2.5$ mm, $W_2 = 4.3$ mm, $L_D = 7.5$ mm, $W_D = 6$ mm, $H_D = 5$ mm, $L_P = 3$ mm, $W_P = 2$ mm, $L_3 = 2$ mm, $L_4 = 0.6$ mm, $L_T = 1.5$ mm, $W_T = 3$ mm, $L_S = 1.9$ mm, $W_S = 1.4$ mm, $L_G = 8.5$ mm, $L_5 = 9$ mm, $W_3 = 0.5$ mm, $L_6 = 1$ mm and $h = 0.8$ mm. The impedance bandwidth was measured by using an Agilent 8722ES vector network analyzer. In addition to the measured and simulated reflection coefficients of the proposed antenna, Fig. 9 shows the calculated result by the FDTD method. A good agreement between the results is observed.

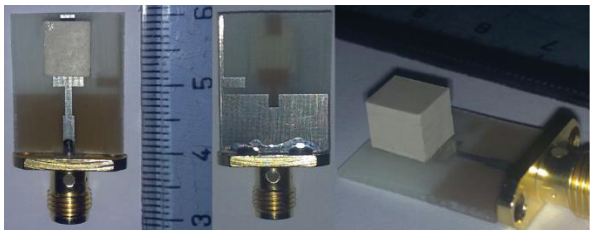

Fig. 8. Photograph of the fabricated DRA.

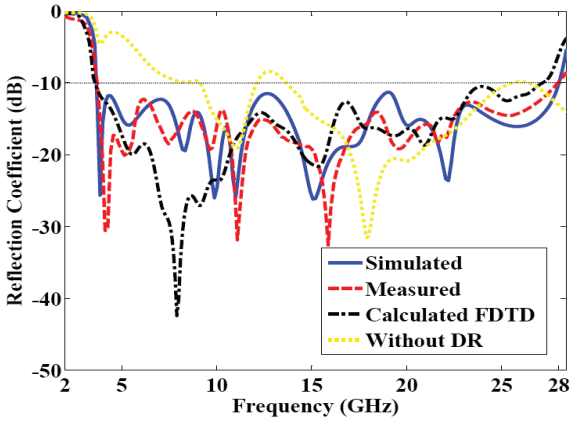


Fig. 9. Reflection coefficients of the proposed DRA.

The measured impedance bandwidth covers the frequency range (3.7–28 GHz), which is equivalent to 153% for ($S_{11} \leq -10$ dB). The discrepancy between the simulated and measured results can be due to the tolerance in manufacturing, imperfect soldering effect of the SMA connector, and also the accuracy of the simulation due to the wide range of

simulation frequencies. The errors in the FDTD calculated result may be due to the modeling error that occurs primarily in the inability to match all of the circuit dimensions, and the imperfect absorbing condition of outer boundaries. Moreover, the simulated reflection coefficient of the proposed antenna without the dielectric resonator is also shown in Fig. 9. It is observed from these results, when the antenna is with the DR a better impedance matching due to the loading effect, with some excited resonant modes in the DR can be achieved. As a result, an ultra-wide bandwidth is obtained by using a dielectric resonator.

The proposed DRA is also measured in far field anechoic chamber. Figure 10 shows the measured and simulated radiation patterns in the H (xz)-plane and E (yz)-plane at five different frequencies (4, 8, 11, 16 and 22 GHz). In the H-plane, it can be seen that the radiation patterns are almost symmetrical and stably omnidirectional across the operating frequency range. However, the radiation patterns in the E-plane are not as symmetrical as in the H-plane and have some deformations at higher frequencies due to the effects of higher order modes.

Figure 11 plots the measured and simulated peak gain of the proposed antenna. It is seen that the peak gain is almost stable in the entire operating frequency range, and slightly increases with frequency due to the higher order modes excitation. The estimated radiation efficiency of the proposed antenna is more than 90% across the operating frequency range.

Group delay is an important parameter in UWB antenna design because it represents the degree of distortion of the transmitted pulses in the UWB communication. The group delay should be almost constant for a good pulse transmission. The measured and simulated group delay of the proposed antenna is shown in Fig. 12. As it can be seen, the group delay variation is less than 2 ns in the whole frequency band. This confirms that the proposed DRA is suitable for UWB communication.

As mentioned in the introduction section, different shapes of DRAs are investigated for wideband application. To determine the validity of the proposed UWB DRA, a comparison with the some existing designs in the literature is presented in Table 1. The comparison shows that the proposed antenna achieves wider bandwidth and smaller volume than other DRAs.

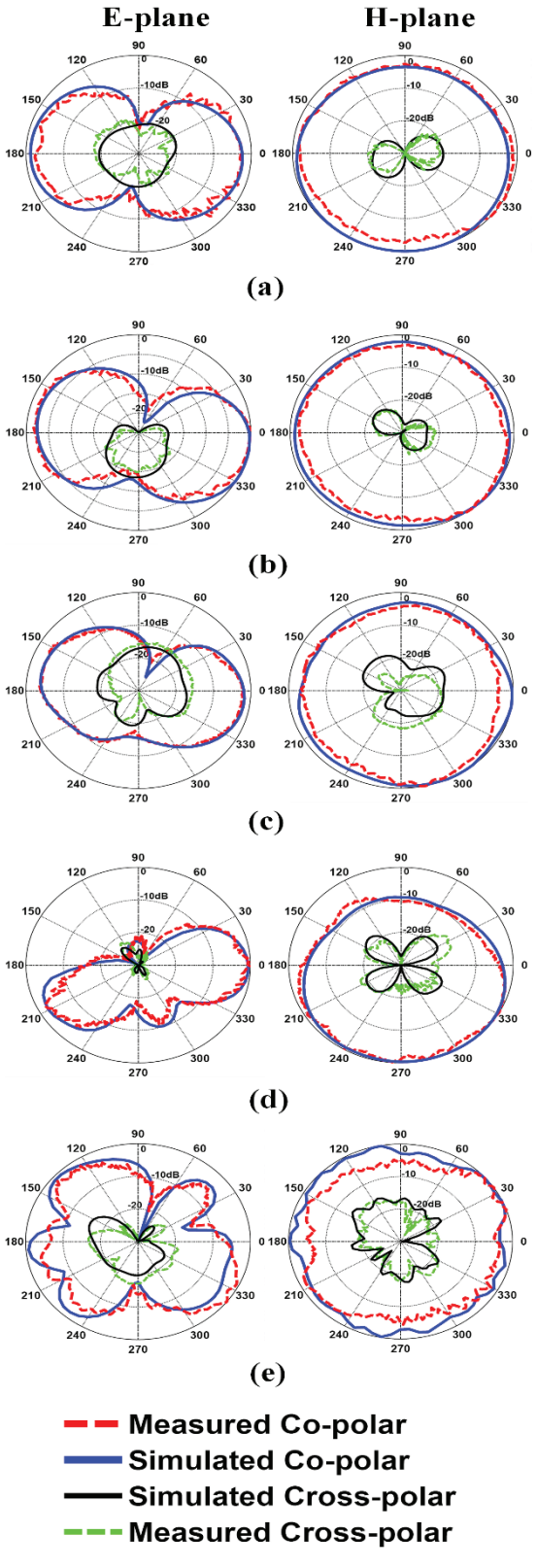


Fig. 10. Measured and simulated radiation patterns at frequencies: (a) 4, (b) 8, (c) 11, (d) 16, and (e) 22 GHz.

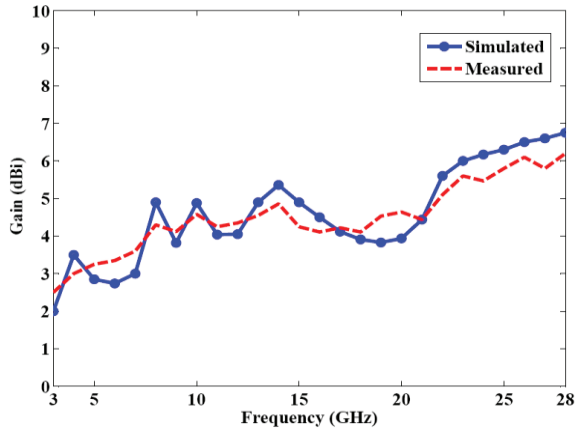


Fig. 11. Measured and simulated peak gain of the proposed DRA.

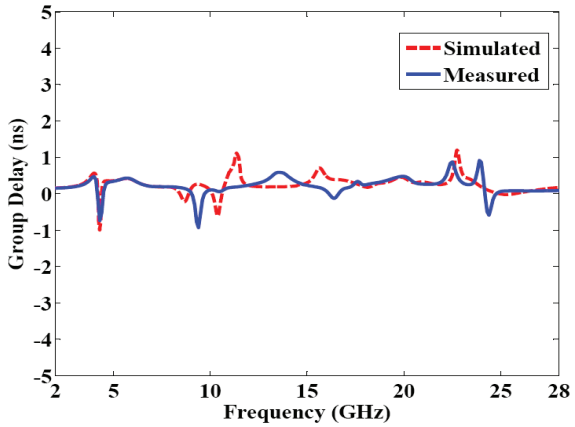


Fig. 12. Measured and simulated group delay of the proposed DRA.

Table 1: Comparison between the proposed antenna and other designs

| Parameters | Volume (mm3) | Height (mm) | Bandwidth | Gain (dBi) |
|---|---|---|---|---|
| L-shaped DRA [3] | 44732 | 24 | 1.71-2.51 GHz (80%) | 6.1-8.7 |
| Hybrid DRA [5] | 15280 | 7.64 | 3.1-10.6 GHz (109.5%) | 2-5 |
| U-shaped DRA [6] | 61572 | 20.5 | 3.115-7.635 GHz (84.09%) | 3-8.5 |
| Asymmetrical T-shaped DRA [7] | 48240 | 13.4 | 3.81-8.39 GHz (75%) | 3.24-7.35 |
| Proposed antenna | 1740 | 5.8 | 3.7-28 GHz (153%) | 2.5-6.75 |

## V. CONCLUSION

A new simple compact UWB dielectric resonator antenna with enhanced bandwidth and improved radiation pattern has been proposed. The uniform grid FDTD method has been used to analyze the scattering characteristic of the proposed DRA. By using a stepped monopole antenna loaded with a rectangular dielectric resonator and an optimized truncated ground plane, an ultra-wideband DRA with increased bandwidth is achieved and the parasitic strip is added underneath the DR to improve the radiation pattern at high frequencies. The measured results demonstrate that the proposed DRA achieves an ultra-wide impedance bandwidth about 153%, covering the frequency range of (3.7–28 GHz). Also, this antenna provides almost stable omnidirectional radiation patterns, stable gain and nearly constant group delay over the entire operating frequency range. In addition to the above characteristics, this DRA has a simple structure, compact size and easy fabrication that make it a good candidate for UWB applications and systems.

## REFERENCES

[1] S. M. Shum and K. M. Luk, "Stacked annular-ring dielectric resonator antenna excited by axi-symmetric coaxial probe," *IEEE Trans. Antennas Propag.*, vol. 43, pp. 889-892, Aug. 1995.

[2] A. G. Wlash, S. D. Young, and S. A. Long, "An investigation of stacked and embedded cylindrical dielectric resonator antenna," *IEEE Antennas Wireless Propag. Lett.*, vol. 5, pp. 130-133, 2006.

[3] T. A. Denidni, Q. J. Rao, and A. R. Sebak, "Broadband L-shaped dielectric resonator antenna," *IEEE Antennas Wireless Propag. Lett.*, vol. 4, pp. 453-454, 2005.

[4] W. Chang and Z. Feng, "Investigation of a novel wideband feeding technique for dielectric ring resonator antennas," *IEEE Antennas Wireless Propag. Lett.*, vol. 8, pp. 348-351, 2009.

[5] T. Denidni and Z. Weng, "Hybrid ultrawideband dielectric resonator antenna and band-notched designs," *Microwaves, Antennas Propagation IET*, vol. 5, no. 4, pp. 450-458, Mar. 2011.

[6] L. N. Zhang, S. S. Zhong, and X. L. Liang, "Wideband U-shaped dielectric resonator

antenna fed by triangle patch," *Microw. Opt. Technol. Lett*., vol. 52, no. 11, pp. 2435-2438, Nov. 2010.

[7] Y. Gao, Z. Feng, and L. Zhang, "Compact asymmetrical T-shaped dielectric resonator antenna for broadband applications," *IEEE Trans. Antennas Propag*., vol. 60, no. 3, pp. 1611-1615, Mar. 2012.

[8] K. M. Luk and K. W. Leung, *Dielectric Resonator Antennas*, Research Studies Press, Hertfordshire, 2003.

[9] Ansoft Corporation, Ansoft High Frequency Structure Simulation (HFSS), Version 11, Ansoft Corporation Pittsburg, PA, 2007.

[10] R. K. Mongia and A. Ittipiboon, "Theoretical and experimental investigations on rectangular dielectric resonator antennas," *IEEE Trans. Antennas Propag*., vol. 45, pp. 1348-1356, 1997.

[11] O. M. H. Ahmed, A. R. Sebak, and T. A. Denidni, "Compact UWB printed monopole loaded with dielectric resonator antenna," *IET Electronics Letters*, vol. 47, no. 1, pp. 7-8, 2011.

[12] A. Taflove and S. Hagness, *Computational Electrodynamics*: *The Finite Difference Time Domain Method*, Artech House, Boston, 2000.

[13] K. S. Yee, "Numerical solution of initial boundary value problems involving Maxwell's equations in isotropic media," *IEEE Trans. Antennas Propag*., vol. 14, pp. 302-307, 1966.

[14] D. M. Sheen, S. M. Ali, M. D. Abouzahra, and J. A. Kong, "Application of the three-dimensional finite-difference time-domain method to the analysis of planar microstrip circuits," *IEEE Trans. Microw. Theory Tech*., vol. 38, no. 7, pp. 849-857, 1990.

**Seyyed Hadi Seyyedhatami** was born in Ardabil, Iran in 1986. He received the B.Sc. degree from Iran University of Science and Technology (IUST), Tehran, in 2008 and the M.Sc. degree from Tabriz University, Tabriz, in 2010, both in Communication Engineering. He is currently working towards the Ph.D. degree at Science and Research Branch, Islamic Azad University, Tehran. His research interests include microstrip antenna, dielectric resonator antenna, microwave passive components and RF circuit design.

**Ramazan Ali Sadeghzadeh** received the B.Sc. degree in Telecommunication Engineering from K. N. Toosi University of Technology, Tehran, Iran, in 1984, the M.Sc. in Digital Communication Engineering from the University of Bradford, Bradford, U.K., and University of Manchester Institute of Science and Technology (UMIST), Manchester, U.K., as a joint program in 1987, and the Ph.D. degree in Electromagnetic and Antenna from the University of Bradford in 1991. During 1992 to 1997, he worked as a Postdoctoral Research Assistant in the field of propagation, electromagnetic, antenna, biomedical, and wireless communication with the University of Bradford. From 1984 to 1985, he was with Iran Telecommunication Company, Tehran, Iran, working on networking. Since 1997, he has been with the Faculty of Electrical and Computer Engineering, K. N. Toosi University of Technology. He has published more than 120 referable papers in international journals and conferences. His research interests include numerical techniques in electromagnetics, antenna, propagation, radio networks, wireless communications, nano antennas, and radar systems.

# An Exact Solution for the Generalized Spherical Orthogonality Integral of the Legendre Functions of the First and Second Kind

**Amir Jafargholi**

Institute of Space Science and Technology
Amirkabir University of Technology, 424 Hafez Ave., P.O. Box: 15875-4413, Tehran, Iran
jafargholi@ieee.org

***Abstract*** ─ An exact formulation of a generalized orthogonality integral for the spherical boundary condition is proposed. This integral usually appears in the problems contained in conical and biconical antennas. The analytical results are successfully validated through a comparison with the numerical results.

***Index Terms*** ─ Orthogonality integral, spherical boundary condition.

## I. INTRODUCTION

In the analysis of electromagnetic boundary-value problems, any solution for the time-harmonic electric and magnetic fields must satisfy Maxwell's/vector wave equations as well as the appropriate boundary conditions [1]. The vector wave equations usually reduce to a number of scalar Helmholtz equations, and the general solutions can be founded in three-dimensional orthogonal coordinate systems.

Many researchers are interested in the formulation of full-wave spherical boundary value problems previously [1-9]. In order to find out unknown coefficients and to drive an exact solution for these structures, it is usually preferred to use the orthogonality properties of spherical functions to reduce the integrals to simple exact solutions. Although most of the orthogonality integrals are solved before, which may be found in the reference [10], there are some integrals which haven't been addressed yet in the mathematical or physical literatures. However, it is worth noting that the numerical solutions to these integrals are the main time consuming part of the electromagnetic boundary-value problems. The importance of the exact solutions is clearer in the problems contained to high degrees of complexity of the boundary condition, as well as mode-matching problems. In such problems, due to complexity and iterative nature of numerical solutions, it is critical to reduce all numerical integrals to their simple exact solutions.

In this paper, an exact formulation for the generalized spherical orthogonality integral of the legend functions of the first and second kind, which usually appears in the problems contained in conical and biconical antennas is proposed. The obtained analytical formulas confirm the general conclusions recently presented in [3-5]. It is demonstrated that the analytical results have been successfully validated through a comparison with the numerical results. The extracted formula is very easy to implement, essentially general and applicable to any problem, without the need to know where the singularities will take place.

## II. FIELD ANALYSIS

Figure 1 (a) illustrates a slotted hollow conducting sphere of radius $a$, containing a Hertzian dipole $\bar{J} = \hat{z}J\delta(\bar{r})$, placed at the center $(\bar{r}=0)$; here $(r,\theta,\varphi)$ are the spherical coordinates and $\delta$ is a delta function. The time convention is $e^{-j\omega t}$ suppressed throughout. Due to azimuthally symmetry, the fields depend on $(r,\theta)$, and the fields are then TM waves, which can be expressed in terms of magnetic vector potentials. The total magnetic vector potential for the un-slotted sphere (first region, I) is a sum of the primary and secondary magnetic vector potentials, [3]:

$$A^i(r,\theta) = \hat{z}A_z^p(r,\theta) + \hat{r}A_r^s(r,\theta), \qquad (1)$$

while the primary magnetic vector potential is a free-space Green's function as:

*Submitted On: August 2, 2013*
*Accepted On: December 10, 2014*

$$A_z^p(r,\theta)=\frac{\mu_1 J}{4\pi}\frac{e^{ikR}}{R}, \tag{2}$$

$\hat{z}$ and $\hat{r}$ are the unit vectors and $R=\sqrt{r^2+r'^2-2rr'\cos\theta}$. And the secondary magnetic vector potential is:

$$A_r^s(r,\theta)=\sum_{n=0}^{\infty}a_n\hat{J}_n(k_1 r)P_n(\cos\theta), \tag{3}$$

where $\hat{J}_n(.)$ and $P_n(.)$ are the spherical Bessel and Legendre functions, respectively, and [3]:

$$a_n=\frac{\mu_1 aJ}{8\pi k_1\hat{J}_n'(k_1 a)}\frac{2n+1}{n(n+1)}\int_0^{\pi}\Omega\frac{\partial P_n(\cos\theta)}{\partial\theta}\sin^2\theta d\theta$$

$$\Omega=\left\{\left(a^2-2r'^2+ar'\cos\theta\right)\left(ik_1\tilde{R}-1\right)+k_1^2\tilde{R}^2\left(a^2-ar'\cos\theta\right)\right\}\frac{e^{ik\tilde{R}}}{\tilde{R}^5}. \tag{4}$$

Now consider a slotted conducting sphere, as shown in Fig. 1 (a). The total magnetic vector potential in region (I) consists of the incident $A^i$ and scattered $A_r^I$ potentials as:

$$A_r^I(r,\theta)=\sum_{n=0}^{\infty}C_n\hat{J}_n(k_I r)P_n(\cos\theta). \tag{5}$$

Here, $C_n$ is an unknown modal coefficient.

The *r*-component of the magnetic vector potential in region (II) of the *l*-th slot is:

$$A_r^{II}(r,\theta)=\sum_{v=0}^{\infty}R_v^l(\cos\theta)\left[D_v^l\hat{J}_\xi(k_{II}r)+E_v^l\hat{N}_\xi(k_{II}r)\right], \tag{6}$$

where

$$R_v^l(\cos\theta)=\begin{cases}Q_\xi(\cos\theta) & v=0\\ Q_\xi(\cos\alpha_2^l)P_\xi(\cos\theta) & v\geq 1\\ -P_\xi(\cos\alpha_2^l)Q_\xi(\cos\theta)\end{cases}, \tag{7}$$

where $Q_n(.)$ is the Legendre function of the second kind and $D_v^l$ and $E_v^l$ are unknown coefficients. Here $\xi_0^l=0$ and $\xi_v^l$ satisfies $R_v^l(\cos\alpha_1^l)=0\ \ (v>1)$.

The *r*-component of the magnetic vector potential in region (III) is:

$$A_r^{III}(r,\theta)=\sum_{v=0}^{\infty}F_n\hat{H}_n^{(2)}(k_{III}r)P_n(\cos\theta), \tag{8}$$

where $F_n$ is an unknown modal coefficient and $\hat{H}_n^{(2)}(.)$ is the spherical Hankel function of the second kind. To determine the modal coefficients, we enforced the field continuities, as described in details in [4-5].

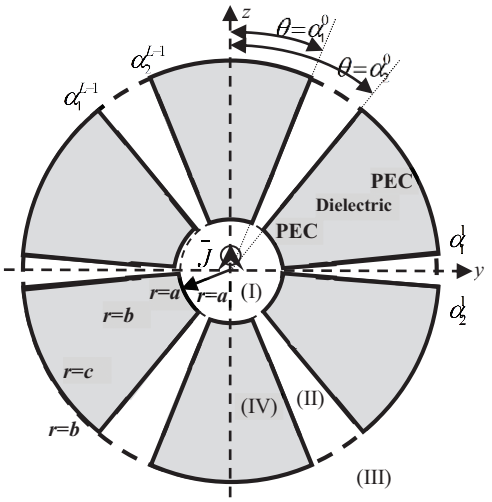


(a)

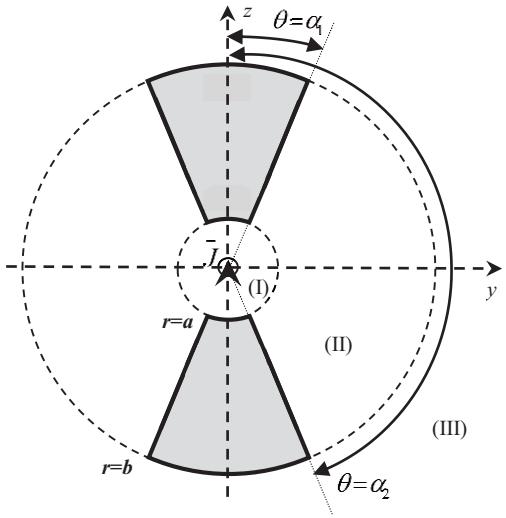


(b)

Fig. 1. (a) Multiply- and (b) single slotted conducting hollow sphere, $k_I\left(=\omega\sqrt{\mu_I\varepsilon_I}\right)$, $k_{II}\left(=\omega\sqrt{\mu_{II}\varepsilon_{II}}\right)$, and $k_{III}\left(=\omega\sqrt{\mu_{III}\varepsilon_{III}}\right)$: wave numbers of region (I) $r\leq a$, (II) $a\leq r\leq b$, and (III) $r\geq b$.

## III. FINDING EXACT SOLUTION

Based on tangential electric field continuity at $r = a$, while we have:

$$E_\theta^{II}=E_\theta^I \quad \alpha_1^l<\theta<\alpha_2^l.$$

Applying Legendre function orthogonality integral, $\int_0^{\pi}(.)\left(dP_{n'}(\cos\theta)\right)/\left(d\theta\right)\sin\theta d\theta$, to this boundary condition, according to [3], $-I_{vn}$ is defined as below:

$$-I_{vn}^{l}=\int_{\alpha_1^l}^{\alpha_2^l}\frac{\partial}{\partial\theta}R_v^l(\cos\theta)\frac{\partial}{\partial\theta}P_n(\cos\theta)\sin\theta d\theta, \quad (9)$$

all required definitions are illustrated in [3-5].

The main goal of this paper is to drive an exact solution for $I_{vn}$ integral. To start calculating the integral, first we assume that there is only a single slot configuration, so the problem is reduced to a simple biconical antenna (Fig. 1 (b)).

Integrating by part, and using Legendre function properties, some may rewrite (9) as:

$$-I_{vn}^{l}=R_v^l(\cos\theta)\frac{\partial}{\partial\theta}P_n(\cos\theta)\sin\theta\Big|_{\alpha_1^l}^{\alpha_2^l} + n(n+1)\int_{\alpha_1^l}^{\alpha_2^l}R_v^l(\cos\theta)P_n(\cos\theta)\sin\theta d\theta = I_1+I_2, \quad (10)$$

where

$$I_1=\frac{R_v^l(\cos\theta)(n+1)\cdot}{\left[P_{n+1}(\cos\theta)-\cos\theta\cdot P_n(\cos\theta)\right]}\Big|_{\alpha_1^l}^{\alpha_2^l}=(n+1)T_vT_p, \quad (11)$$

$$I_2=M_{vn}\sin\theta\left\{\begin{array}{l}\left[R_v^l(\cos\theta)\frac{\partial}{\partial\theta}P_n(\cos\theta)\right]\Big|_{\alpha_1^l}^{\alpha_2^l}\\ -\left[P_n(\cos\theta)\frac{\partial}{\partial\theta}R_v^l(\cos\theta)\right]\Big|_{\alpha_1^l}^{\alpha_2^l}\end{array}\right\}=T_1-T_2, \quad (12)$$

and

$$T_p=\left[P_{n+1}(\cos\alpha_1^l)-\cos\alpha_1^l\cdot P_n(\cos\alpha_1^l)\right], \quad (13)$$

$$T_v=P_\xi(\cos\alpha_2^l)\cdot Q_\xi(\cos\alpha_1^l) -Q_\xi(\cos\alpha_2^l)\cdot P_\xi(\cos\alpha_1^l), \quad (14)$$

$$M_{vn}=\frac{n(n+1)}{\xi_v^l(\xi_v^l+1)-n(n+1)}. \quad (15)$$

Simplification of (12) may result:

$$T_1=(n+1)M_{vn}T_vT_p, \quad (16)$$

$$T_2=M_{vn}\left[P_n(\cos\alpha_2^l)-P_n(\cos\alpha_1^l)\Phi_v\right], \quad (17)$$

where

$$\Phi_v=(\xi_v^l+1)\left[\cos\alpha_1^lT_v-T_{vv}\right], \quad (18)$$

$$T_v=P_\xi(\cos\alpha_2^l)\cdot Q_\xi(\cos\alpha_1^l) -Q_\xi(\cos\alpha_2^l)\cdot P_\xi(\cos\alpha_1^l), \quad (19)$$

$$T_{vv}=P_\xi(\cos\alpha_2^l)\cdot Q_{\xi+1}(\cos\alpha_1^l) -Q_\xi(\cos\alpha_2^l)\cdot P_{\xi+1}(\cos\alpha_1^l). \quad (20)$$

Substitution (16-20) to (12) yields:

$$I_2=M_{vn}\left\{\begin{array}{l}(n+1)T_vT_p-\\ \left[P_n(\cos\alpha_2^l)-P_n(\cos\alpha_1^l)\Phi_v\right]\end{array}\right\} =M_{vn}\left\{\begin{array}{l}T_v\left[\begin{array}{l}(n+1)P_{n+1}(\cos\alpha_1^l)\\ +(\xi_v^l-n)\cos\alpha_1^l\cdot P_n(\cos\alpha_1^l)\end{array}\right]\\ -\left[P_n(\cos\alpha_2^l)+P_n(\cos\alpha_1^l)(\xi_v^l+1)T_{vv}\right]\end{array}\right\}. \quad (21)$$

Using (11) and (21) one obtains:

$$-I_{vn}=(n+1)(M_{vn}+1)T_vT_p -M_{vn}\left[P_n(\cos\alpha_2^l)-P_n(\cos\alpha_1^l)\Phi_v\right]. \quad (22)$$

To verify the extracted formula, a numerical evaluation of the $I_{vn}$ integral, (9), is compared with the results of exact equation (22) in Table 1 and 2. It seems clear that the numerical estimations are in good agreement with exact formula. The commercial software Mathematica is adopted for the numerical integrations.

Table 1: Calculation comparison, for $\alpha_1=\pi/3$, $\alpha_2=2\pi/3$

| Number of Modes | Eq. 22 | Numerical Integration |
|---|---|---|
| $n$=2, $\xi_v^l$=1 | 0.237011470359071 | 0.237011470359071 |
| $n$=3, $\xi_v^l$=1 | 0.612011470359070 | 0.612011470359070 |
| $n$=4, $\xi_v^l$=1 | -0.387356331794832 | -0.387356331794832 |
| $n$=1, $\xi_v^l$=2 | -0.190747132410232 | -0.190747132410232 |
| $n$=1, $\xi_v^l$=3 | 0.167614963435814 | 0.167614963435814 |
| $n$=1, $\xi_v^l$=4 | 0.265859967903335 | 0.265859967903335 |

Table 2: Calculation comparison, for $n$=11, $\xi_v^l$=3, $\alpha_2$=π- $\alpha_1$

| Cone Angle | Eq. 22 | Numerical Integration |
|---|---|---|
| $\alpha_1$=π/3 | 0.034245642954503 | 0.034245642954479 |
| $\alpha_1$=π/6 | -0.366169292285009 | -0.366169292456850 |
| $\alpha_1$=π/12 | 0.013319388336234 | 0.013319365546954 |
| $\alpha_1$=π/24 | -0.037508615096376 | -0.037508811221276 |
| $\alpha_1$=π/48 | -0.005357753392885 | -0.005358297043497 |

## IV. CONCLUSION

An exact formulation of a generalized orthogonality integral for the spherical boundary condition which is usually calculated numerically in the problems contained in conical and biconical antennas has been proposed. The analytical results have been successfully validated through a comparison with the numerical results.

## REFERENCES


[1] R. E. Collin and F. J. Zucker, *Antenna Theory*, McGraw-Hill, New York, 1969.

[2] K. W. Leung, "Analysis of zonal and rectangular slots on a conducting spherical cavity," *IEEE Trans. Antennas Propag*., vol. 49, no. 12, pp. 1739-1745, Dec. 2001.

[3] J. S. Ock and H. J. Eom, "Radiation of a hertzian dipole in a slotted conducting sphere," *IEEE Trans. Antennas Propag*., vol. 57, no. 12, pp. 3847-3851, 2009.

[4] A. Jafargholi and M. Kamyab, *Metamaterials in Antenna Engineering, Theory and Applications*, LAP Lambert Academic Publishing, Berlin, Germany, 2011.

[5] A. Jafargholi and M. Kamyab, "Full-wave analysis of double positive/double negative loaded dipole antennas," *Electromagnetics*, 32:2, 103-116, 2012.

[6] A. Jafargholi and M. Kamyab, "Full-wave analysis of loaded dipole antennas using mode-matching theory," *Applied Computational Electromagnetics Society, ACES Journal*, vol. 26, no. 11, pp. 915-921, Nov. 2011.

[7] S. Saoudy and M. Hamid, "Input admittance of a biconical antenna with wide feed gap," *IEEE Trans. Antennas Propag*., vol. 38, no. 11, pp. 1784-1790, 1990.

[8] C. Polk, "Resonance and supergain effects in small ferromagnetically or dielectrically loaded biconical antennas," *IRE Trans. Antennas Propag*., 414-423, 1959.

[9] C. T. Tai, "On the theory of biconical antennas," *J. of Appl. Phys*., vol. 19, 1155-1160, 1958.

[10] M. Abramowitz and I. A. Stegun, *Handbook of Mathematical Functions*, Dover, New York, 1965.


**Amir Jafargholi** received the Ph.D. degree in Electrical Engineering from K. N. Toosi University of Technology, Tehran, Iran, in 2011. During the first half of 2012 he was a Research Associate, and in the same year he was appointed as an Assistant Professor in the Institute of Space Science and Technology, Amirkabir University of Technology, Iran.

His research is generally in applied electromagnetics - and particularly in antennas, array and phased array antennas for applications in wireless and satellite communications. At present, his interests focus on the applications of metamaterials in the analysis and synthesis of antennas and phased array antennas. He is the author of Metamaterials in Antenna Engineering, Theory and Applications (LAP Academic Publishing, Germany, 2011). He also has authored or co-authored over 30 journal papers, 3 book chapters and 40 refereed conference papers. He has supervised or co-supervised over 15 Ph.D. and M.Sc. theses.

Jafargholi was a recipient of the Student's Best Thesis National Festival award for his BS thesis, on

May 2006. He was a recipient of the 22nd Khawarizmi International and 13th Khawarizmi Youth Award in Jan. 2009 and Oct. 2011, respectively. He was also the recipient of the Research Grant Awarded in Metamaterial 2010. Jafargholi has been a member of the IEEE Antennas and Propagation Society since 2011. He is also a member of Iranian National Elite Foundation since 2011. Currently he is the Scientific Editor of the Journal of Electrical Industries.

# Compact Planar Microstrip-Fed Printed Antenna with Double Band-Filtering for UWB Application

**S. Ojaroudi [1], Y. Ojaroudi [1], and N. Ojaroudi [2]**

[1] Young Researchers and Elite Club
Germi Branch, Islamic Azad University, Germi, Iran

[2] Young Researchers and Elite Club
Ardabil Branch, Islamic Azad University, Ardabil, Iran
n.ojaroudi@yahoo.com

***Abstract*** ─ In this paper, a new design of dual band-notch printed monopole antenna for UWB applications is proposed. The antenna consists of a circular disc radiating patch with a protruded anchor-shaped strip, a feed line with an inverted U-ring slot and a ground plane structure, which provides a wide usable fractional bandwidth of more than 125% (2.69-12.53 GHz) with dual band-stop performance around of 3.3-4.2 GHz and 5-6 GHz. In the proposed structure, by using a protruded anchor-shaped strip in the radiating patch, a single frequency band-stop performance can be achieved. Also, in order to create the second notched frequency, an inverted U-ring slot was cut at the feed line. Simulated and measured results obtained for this antenna show that the proposed monopole antenna offers two notched bands, covering all the 5.2/5.8 GHz WLAN, 3.5/5.5 GHz WiMAX and 4-GHz C-band range. The proposed antenna has a small dimension of 12×18×1.6 $mm^3$.

***Index Terms*** ─ Anchor-shaped strip, inverted U-ring structure, UWB applications.

## I. INTRODUCTION

There has been more and more attention in ultra-wideband (UWB) antennas ever since the Federal Communications Commission (FCC)'s allocation of the frequency band 3.1-10.6 GHz for commercial use [1-2]. In UWB communication systems, one of key issues is the design of a compact antenna while providing wideband characteristic over the whole operating band. Consequently, a number of microstrip antennas with different geometries have been experimentally characterized [3-4].

There are many narrowband communication systems which severely interfere with the UWB communication system, such as the wireless local area network (WLAN) operating at 5.15-5.35 and 5.725-5.825 GHz, international telecommunication union operating from 8.025 to 8.4 GHz, and etc. Therefore, UWB antennas with band-notched characteristics to filter the potential interference are desirable. Nowadays, to mitigate this effect many UWB antennas with various band-notched properties have developed [5-6].

All of the above methods are used for rejecting a single band of frequencies. To effectively utilize the UWB spectrum and to improve the performance of the UWB system, it is desirable to design the UWB antenna with dual band rejection. It will help to minimize the interference between the narrow band systems with the UWB system. Some methods are used to obtain the dual band rejection in the literature [7-8]. In this paper, a new dual band-notched monopole antenna is presented. In the proposed structure, single band-notched function is provided by using a rectangular slit with a protruded anchor-shaped strip in top of the circular disc radiating patch, and dual band-notched characteristic is obtained by cutting an inverted U-ring slot inside the feed line. Simulated and measured results are presented to validate the usefulness of the proposed antenna structure for UWB applications.

*Submitted On: August 16, 2013*
*Accepted On: September 28, 2014*

## II. ANTENNA DESIGN

The presented small monopole antenna fed by a microstrip line is shown in Fig. 1, which is printed on an *FR4* substrate of thickness of 1.6 mm, permittivity of 4.4, and loss tangent of 0.018.

Microstrip feed line is one of the easier methods to fabricate as it is just a conducting strip connecting to the patch and therefore can be considered as an extension of radiating patch. It is simple to model and easy to match by controlling the inset position. In the microstrip-fed technique, a conducting strip is made contact directly to the edge of the radiating patch or microstrip patch. The conducting strip is having minimum in width as compared to the radiating patch.

The proposed antenna is connected to a 50-Ω SMA connector for signal transmission. The circular disc patch has a radial of *R*. The radiating patch is connected to a feed line with width of $W_f$ and length of $L_f$ .The width of the microstrip feed line is $W_f$=*2mm*. On the other side of the substrate, a conducting ground plane of is placed.

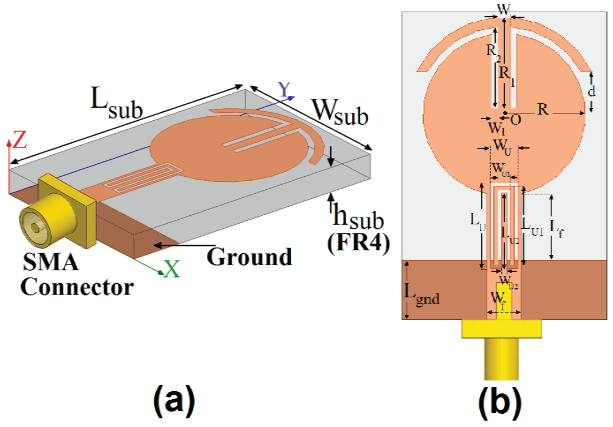


Fig. 1. Geometry of proposed monopole antenna: (a) side view, and (b) top view.

In this work, we start by choosing the dimensions of the designed antenna. These parameters including the substrate is $W_{sub}\times L_{sub}$=12×18 mm$^2$ or about 0.15λ×0.25λ at 4.8 GHz (the first resonance frequency of the ordinary monopole antenna). We have a lot of flexibility in choosing the radios of the radiating patch. This parameter mostly affects the antenna bandwidth. As R decreases, so does the antenna bandwidth, and vice versa. This parameter is approximately $\lambda_{lower}/4$, where $\lambda_{lower}$ is the lower bandwidth frequency wavelength. $\lambda_{lower}$ depends on a number of parameters such as the monopole width as well as the thickness and dielectric constant of the substrate on which the antenna is fabricated.

The last and final step in the design is to choose the length of the band-stop filter elements. In this design, the optimized length $L_{notch}$ is set to band-stop resonate at $0.5\lambda_{notch}$, where $L_{notch1}=R_1+0.5R_2+0.5$ for 3.9 GHz notched frequency and $L_{notch2}=L_{U1}+0.5W_{U1}+0.25L_{U2}$ for 5.5 GHz notched frequency. $\lambda_{notch1}$ and $\lambda_{notch2}$ corresponds to first band-notch frequency (3.9 GHz) and second band-notch frequency (5.5 GHz), respectively.

In this study, the protruded anchor-shaped strip in the radiating patch perturbs the resonant response and also acts as a half-wave resonant structure [4]. At the notched frequency, the current concentrated on the edges of the interior and exterior of this structure [7]. Additionally, the inverted U-ring slot inside the feed line act as a filtering element to generate another notched frequency, because it can create additional surface current path. As a result, the desired attenuation near the notched frequencies can be produced. Final values of the designed antenna parameters are indicated in Table 1.

Table 1: The final dimensions of the antenna

| Param. | mm. | Param. | mm. | Param. | mm. |
|---|---|---|---|---|---|
| $W_{sub}$ | 12 | $L_{sub}$ | 18 | $H_{sub}$ | 1.6 |
| $L_f$ | 7 | $W_f$ | 2 | W | 7 |
| R | 4.75 | $W_1$ | 0.4 | $R_1$ | 5.5 |
| $R_2$ | 5 | $W_U$ | 1.1 | $L_U$ | 5 |
| $W_{U1}$ | 0.5 | $L_{U1}$ | 4.6 | $W_{U2}$ | 0.2 |
| $L_{U2}$ | 4.4 | d | 2.25 | $L_{gnd}$ | 3.5 |

## III. RESULTS AND DISCUSSIONS

In this Section, the microstrip monopole antenna with various design parameters were constructed. The simulated results are obtained using the Ansoft simulation software high-frequency structure simulator (HFSS) [9].

### A. UWB monopole antenna

In the proposed structure, in order to increase the upper frequency bandwidth, we use a modified circular disc structure instead of square structure in radiating patch of the antenna [7]. By properly tuning the length of R in the radiating patch, the antenna can actually radiate over a very wide

frequency band based on a coupling condition.

Figure 2 shows the effects of circular disc radiating patch with different values of radial sizes on the impedance. It is found that by applying a circular disc structure of suitable dimensions at the radiating patch much wider impedance bandwidth can be produced, especially at the higher band [3-6].

The simulated current distributions for the ordinary monopole antenna with a circular-disc radiating patch at the resonance frequencies are presented in Fig. 3. It can be observed in Figs. 3 (a) and 3 (b) that the directions of surface currents at the circular-disc radiating patch are reversed in compared to each other, which cause the antenna impedance changes at 4.8 and 11 GHz due to the resonant properties of the top layer structure.

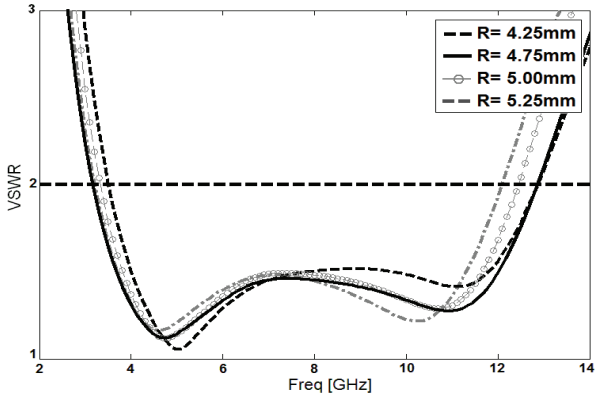


Fig. 2. Simulated VSWR characteristic with different values of $R$.

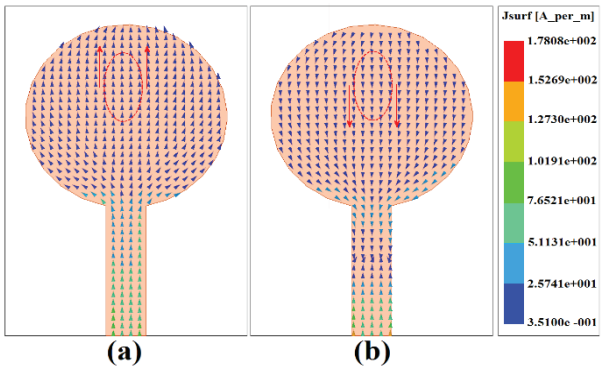


Fig. 3. Simulated surface current distributions for the circular antenna at: (a) 4.8 GHz, and (b) 11 GHz.

**B. Dual band-notched UWB antenna**

The structure of the various antennas used for simulation studies are shown in Fig. 4. VSWR characteristics for the ordinary circular disc monopole antenna [Fig. 4 (a)], circular disc monopole antenna with a Protruded anchor-shaped strip in the rectangular slit at radiating patch [Fig. 4 (b)], and the proposed antenna structure [Fig. 4 (c)] are compared in Fig. 5.

As shown in Fig. 5, to generate a single frequency band notch function (3.3-4.2 GHz), we insert a rectangular slot with an anchor-shaped strip protruded inside the rectangular slot in the radiating patch of the ordinary circular disc monopole antenna, and also by using an inverted U-ring slot at feed line, the dual band-notched function can be achieved.

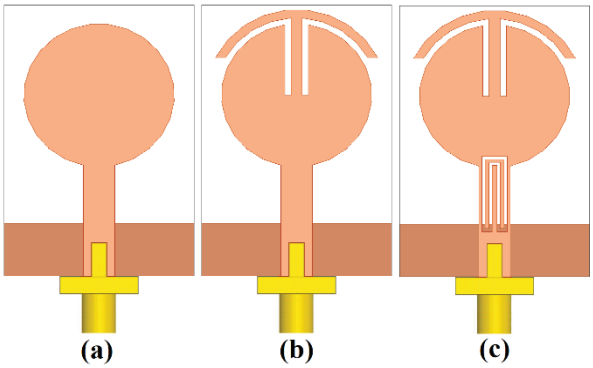


Fig. 4. (a) Basic structure, (b) antenna with a protruded anchor-shaped strip inside rectangular slot, and (c) the proposed antenna.

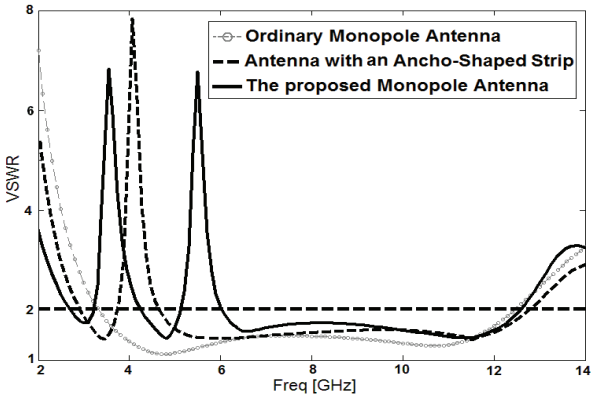


Fig. 5. Simulated VSWR characteristics for the antennas shown in Fig. 2.

In order to know the phenomenon behind the dual band-notched performance, the simulated current distributions on the circular disc radiating patch for the proposed antenna at 3.8 GHz are presented in Fig. 6 (a). It can be observed in Fig. 5 (a), that the current concentrated on the edges of the interior and exterior of the protruded anchor-shaped strip at 3.8 GHz.

Other important design parameter of this structure is the inverted U-ring slot use in the feed line. Figure 6 (b) presents the simulated current distributions on the feed line at the second notched frequency (5.5 GHz). As shown in Fig. 6 (b), at the second notched frequency the current flows are more dominant around of the inverted U-ring shaped slot. As a result, the desired high attenuation near the second notched frequency can be produced [10].

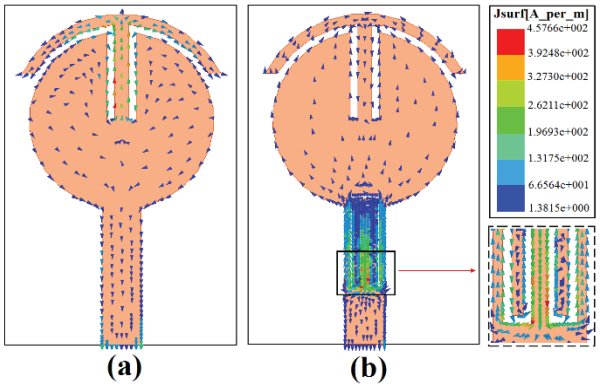


Fig. 6. Simulated surface current distributions on the radiating patch for: (a) the circular disc antenna with a protruded anchor-shaped stub at 3.9 GHz (first notched frequency), and (b) the proposed antenna at 5.5 GHz (second notched frequency).

The simulated VSWR curves with different values of $d\&L_U$ are plotted in Fig. 7. As illustrated, when the interior width of the anchor-shaped strip and the length of the inverted U-ring slot increase from 3.5 to 5.3 mm and 2 to 2.5 mm respectively, the center of notched frequencies decrease from 6.2 and 4.2 GHz to 5 and 3.5 GHz. From these results, we can conclude that the notched frequencies are controllable by changing the length of the embedded structure.

Another main effect of the anchor-shaped and inverted U-ring structures occurs on the filter bandwidth. In the proposed structure, the lengths of $R_1\&W_{U1}$ are the critical parameter to control the filter bandwidth. Figure 8 illustrates the simulated VSWR characteristics with various lengths of $R_1\&W_{U1}$. As the interior width of the $R_1\&W_{U1}$ increases from 5.3 to 5.7 mm and 0.4 to 0.6 mm respectively, the filter bandwidth is varied from 0.7 to 1.5 GHz. Therefore the bandwidth of notched frequencies is controllable by changing the length of $R_1\&W_{U1}$.

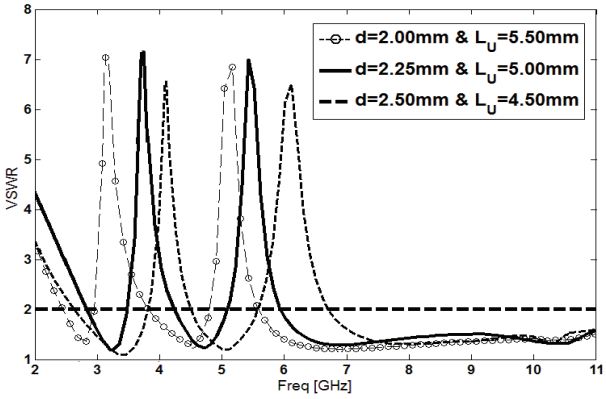


Fig. 7. Simulated VSWR characteristic with different values of $d\&L_U$.

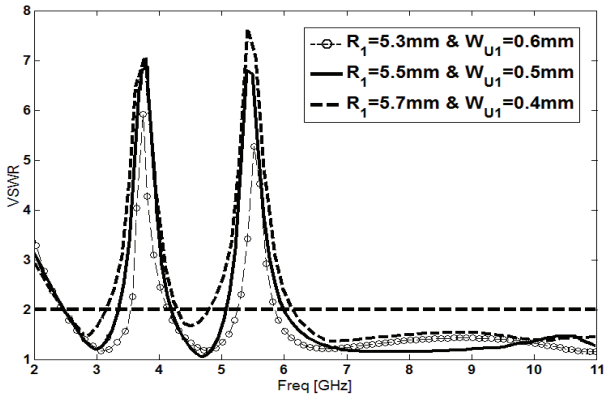


Fig. 8. Simulated VSWR characteristics for the proposed antenna with different values of $R_1\&W_{U1}$.

The proposed microstrip monopole antenna with final design as shown in Fig. 9 was built and tested, and the VSWR and return loss characteristics were measured using a network analyzer in an anechoic chamber. The radiation patterns have been measured inside an anechoic chamber using a double-ridged horn antenna as a reference antenna placed at a distance of 2 m. Also, a two-antenna technique using a spectrum analyzer

and a double-ridged horn antenna as a reference antenna placed at a distance of 2 m, is used to measure the radiation gain in the z axis direction (x-z plane).

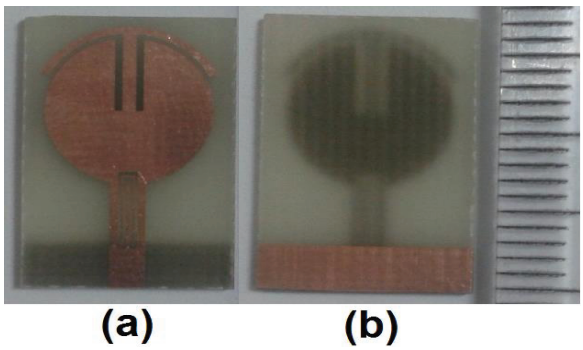


Fig. 9. Photograph of the realized antenna: (a) top view, and (b) bottom view.

Figures 10 and 11 show the measured and simulated VSWR and return loss characteristics of the proposed antenna, respectively. As illustrated, the fabricated antenna has the frequency band of 2.69 to over 12.53 GHz. However, as seen, there exists a discrepancy between measured data and the simulated results. This discrepancy is mostly due to a number of parameters such as the fabricated antenna dimensions as well as the thickness and dielectric constant of the substrate on which the antenna is fabricated, the wide range of simulation frequencies.

In a physical network analyzer measurement, the feeding mechanism of the proposed antenna is composed of a SMA connector and a microstrip line (the microstrip feed-line is excited by a SMA connector), whereas the simulated results are obtained using the Ansoft simulation software (HFSS), that in HFSS by default, the antenna is excited by a wave port that it is renormalized to a 50-Ohm full port impedance at all frequencies. In order to confirm the accurate return loss characteristics for the designed antenna, it is recommended that the manufacturing and measurement processes need to be performed carefully.

Measured maximum gain of the proposed antenna in compared with ordinary structure is shown in Fig. 12. As illustrated, two sharp decreases of the maximum gain in the notched frequencies (3.9 and 5.5 GHz) are shown. For other frequencies outside the notched frequency band, the antenna gain with the filters is similar to this without them. As seen, the proposed antenna has sufficient and acceptable gain level in the operation bands [5-6].

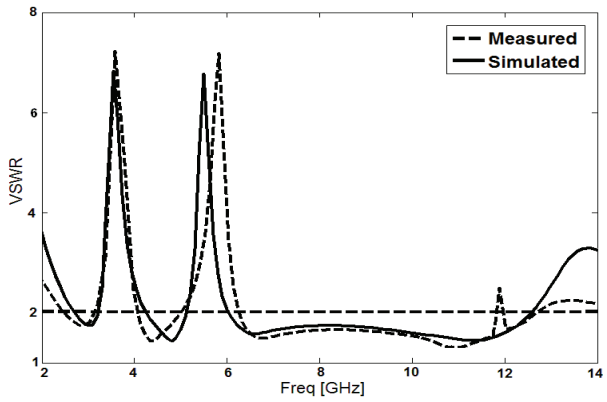


Fig. 10. Measured and simulated VSWR for the proposed antenna.

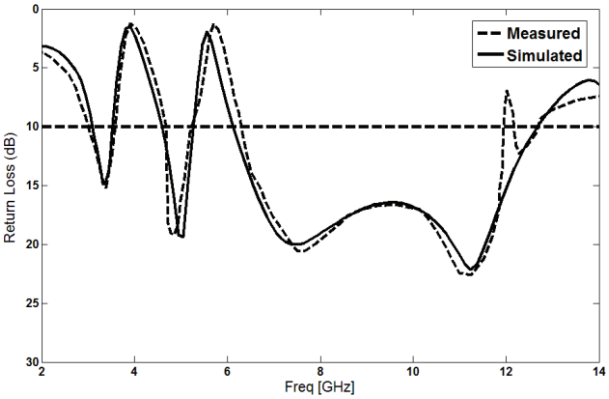


Fig. 11. Measured and simulated return loss characteristics for the proposed antenna.

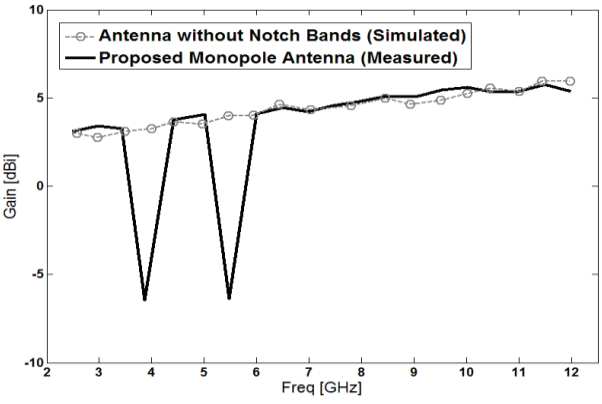


Fig. 12. Measured and simulated maximum gain characteristics for the proposed antenna.

Figures 13 and 14 depict the measured radiation patterns including the co-polarization and cross-polarization in the H-plane (x-z plane) and E-plane (y-z plane) at the resonance and notched frequencies, respectively. It can be seen that nearly omnidirectional radiation pattern can be observed on x-z plane over the whole UWB frequency range, especially at the low frequencies. The radiation patterns on the y-z plane are like a small electric dipole leading to bidirectional patterns in a very wide frequency band [7-8], [10].

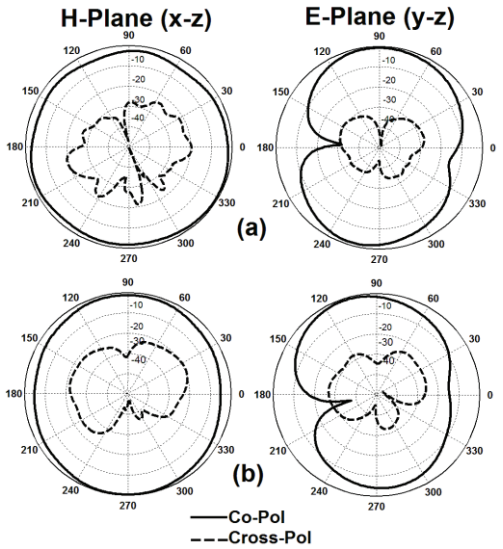


Fig. 13. Measured radiation patterns at resonance frequencies: (a) 4.8 GHz, and (b) 11 GHz.

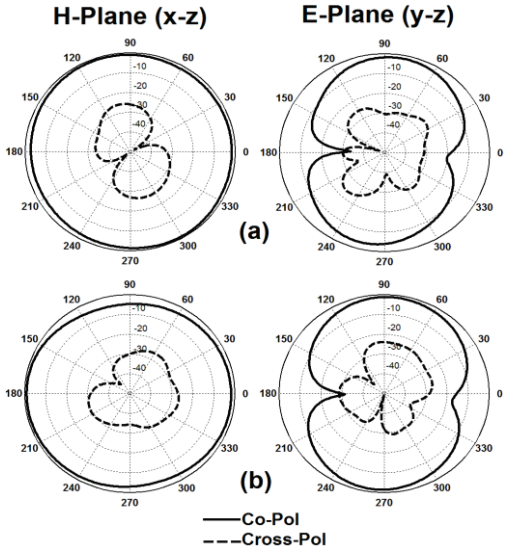


Fig. 14. Measured radiation patterns at notched frequencies: (a) 3.9 GHz, and (b) 5.5 GHz.

## IV. CONCLUSION

In this paper, a compact planar monopole antenna (PMA) with single and dual band-notched characteristics has been proposed for various UWB applications. The fabricated antenna has the frequency band of 2.69 to over 12.53 GHz with two rejection bands around 3.3-4.23 and 5.07-5.96 GHz. By cutting a rectangular slit with a protruded anchor-shaped stub in the circular disc radiating patch, single band-notched characteristic is generated, and also by inserting an inverted U-ring slot inside the feed line, a good dual band-notched characteristic can be achieved. The proposed antenna has a simple configuration and small size.

## REFERENCES

[1] *FCC*, "First report and order on ultra-wideband technology," Tech. Rep., 2002.

[2] H. Schantz, *The Art and Science of Ultra-Wideband Antennas*, Artech House, Norwood, MA, 2005.

[3] N. Ojaroudi, "A new design of Koch fractal slot antenna for ultra-wideband applications," *21st Telecommunications Forum, TELFOR 2013*, Belgrade, Serbia, pp. 1051-1054, November 27-28, 2013.

[4] N. Ojaroudi, "Small microstrip-fed slot antenna with frequency band-stop function," *21st Telecommunications Forum*, *TELFOR 2013*, Belgrade, Serbia, pp. 1047-1050, November 27-28, 2013.

[5] N. Ojaroudi, "Design of small reconfigurable microstrip antenna for UWB-CR applications," *19th International Symposium on Antenna and propagation, ISAP2014,* Kaohsiung, Taiwan, December 2-5, 2012.

[6] N. Ojaroudi and M. Ojaroudi, "Ultra-wideband slot antenna with band-stop notch," *IET Microw. Antennas Propag.*, vol. 10, pp. 831-835, 2013.

[7] L. H. Ye and Q. X. Chu, "3.5/5.5 GHz dual band notch ultra-wideband slot antenna with compact size," *Electronics Letters*, vol. 46, no. 5, pp. 325-327, 2010.

[8] M. Mighani, M. Akbari, and N. Felegari, "A CPW dual band notched UWB antenna," *Applied Computational Electromagnetics Society (ACES Journal)*, vol. 27, no. 4, pp. 352-359, April 2012.

[9] Ansoft Corporation, *Ansoft high frequency structure simulator (HFSS)*, ver. 13, Ansoft Corporation, Pittsburgh, PA, 2010.

[10] N. Ojaroudi, "Circular microstrip antenna with dual band-stop performance for ultra-wideband systems," *Microw. Opt. Technol. Lett.*, vol. 56, pp. 2095-2098, 2014.

# Ultra-Wideband Antenna with Variable Notch Band Function by Defected Ground Structure and Shorting Pin

**Mohammad Akbari*[1], Saman Zarbakhsh[1], Reza Movahedinia[2], and Abdelrazik Sebak[2]**

[1] Young Researchers and Elite Club
Central Tehran Branch, Islamic Azad University, Tehran, Iran
*akbari.telecom@gmail.com, mo_akba@encs.concordia.ca

[2] Electrical and Computer Department
Concordia University, Quebec, Canada, H3G 1M8

***Abstract*** ─ In this paper, a simple miniaturized printed antenna for ultra-wideband applications with variable band-notch function is proposed. The presented antenna consists of a square radiating patch and a ground plane with inverted T-shaped slot which increases the bandwidth of 2.3–11 GHz. Frequency band-stop performance is created by two techniques: Defected Ground Structure (DGS) and shorting pins. The designed antenna has a small size of 17×21×1 mm$^3$ while showing the band rejection performance in the frequency bands of 3.2 to 3.8 and 5.1 to 5.85 GHz, respectively.

***Index Terms*** ─ Antenna, DGS (Defected Ground Structure), notch band, shorting pin.

## I. INTRODUCTION

Commercial ultra-wideband (UWB) systems require compact, cheap antennas with omnidirectional radiation patterns and extended bandwidth [1]. It is a renowned fact that monopole antennas present really appealing physical features, such as simple structure, small size and low cost. Due to all these fascinating characteristics, planar monopoles are quite appealing to be used in emerging UWB applications, and growing research activity is being focused on them. In UWB communication systems, one of major subjects is the design of a small antenna while providing wideband characteristic over the total operating frequency band. Consequently, a big number of microstrip antennas with various structure have been experimentally characterized [2-4]. The frequency range for UWB systems between 3.1 and 10.6 GHz will cause interference to the existing wireless communication systems; as an example, the wireless local area network (WLAN) for IEEE 802.11a operating in 5.15–5.35 GHz and 5.725–5.825 GHz bands, so the UWB antenna with a band-stop performance is needed. To create frequency band-notch function, modified planar monopoles have recently been proposed [5-7]. In [5], novel shape of the slot (folded trapezoid) is used to obtain the appropriated band notched characteristics. Single and multiple half-wavelength U-shaped slots are embedded in the radiation patch to generate single and multiple band-notched [6] functions. In [7], a band-notch function is achieved by using a T-shaped coupled-parasitic element in the ground plane. In this paper, a novel band-notched printed monopole antenna is proposed. The notched bands, covering the 3.2 to 3.8 and 5.1 to 5.85 GHz, is provided by using two techniques: Defected Ground Structure (DGS) and shorting pins. Also by inserting an inverted T-shaped slot on the ground plane, wider impedance bandwidth can be obtained. Measured and simulated results of the constructed miniaturized prototype are presented and discussed.

## II. ANTENNA DESIGN

The square monopole antenna is exhibited in Fig. 1, which is printed on a 1 mm thick FR4 substrate with relative permittivity of 4.4. The width Wf of the microstrip feedline is fixed at 1.9 mm. The basic antenna structure consists of a square patch, a feedline, and a ground plane. The square patch has a width Wp. As illustrated in Fig.

*Submitted On: June 10, 2013*
*Accepted On: July 14, 2014*

1, the patch is connected to a feed line of width Wf and length Lf. On the other side of the substrate, a conducting ground plane of width Wsub and length Lgnd is placed. The proposed antenna is connected to a 50-Ω SMA connector for signal transmission. The ground plane with an inverted T shape is playing an important role in the broadband characteristics of this antenna, because they can adjust the electromagnetic coupling effects between the patch and the ground plane, and improves its impedance bandwidth without any cost of size or expense [2]. To obtain two notched bands has been used two different techniques, the former DGS (Defected Ground Structure) and the latter shorting pin that will more be examined below.

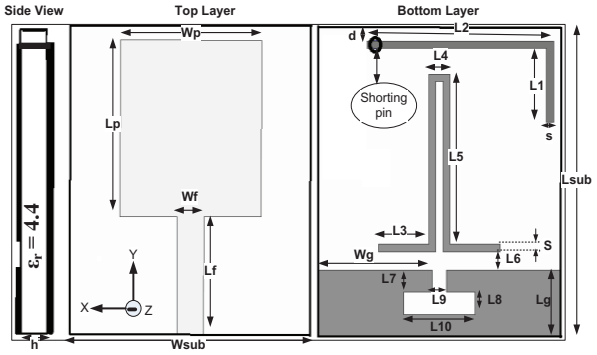


Fig. 1. Geometry of proposed antenna: Wsub=17, Lsub=21, Lp=12, Wp=10, Wf=1.9, Lf=8, Wg=8, Lg=4.5, d=1, L1=3, L2=13, L3=3.5, L4=1.5, L5=11.5, L6=1.25, L7=1.5, L8=1.5, L9=1, L10=5, S=0.5, h=1, and εr=4.4.

## III. ANTENNA PERFORMANCE AND DISCUSSION

The performance analysis of the proposed antenna is carried out in both frequency- and time-domain.

### A. Frequency-domain analysis

In this part, the square monopole antenna with different design parameters were constructed, and the numerical and experimental results of the input impedance and radiation characteristics are presented and discussed. The parameters of this proposed antenna are studied by changing one parameter at a time and fixing the others. Figure 2 depicts the structure of the different square antennas. As illustrated in Fig. 3, bandwidth is increased dramatically and the third resonance has been excited by cutting an inverted T-shaped notch on the ground. The upper frequency limit of the bandwidth is affected by using a pair of L-shaped arms on the back in a way that the L-shaped arms causes to create a resonance at 11 GHz that extends the bandwidth. However, the main purpose form using a pair of L-shaped arms was to obtain a notch.

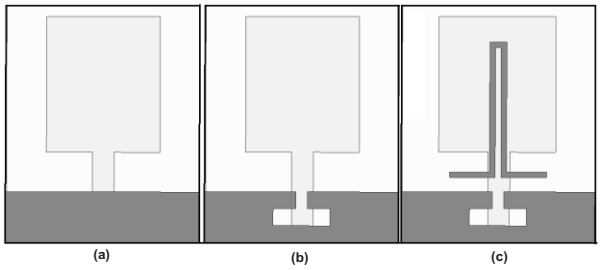


Fig. 2. (a) The ordinary square antenna, (b) the antenna with an inverted T-shape notch on the ground plane, and (c) the antenna with a pair of L-shaped arms on the back (DGS technique).

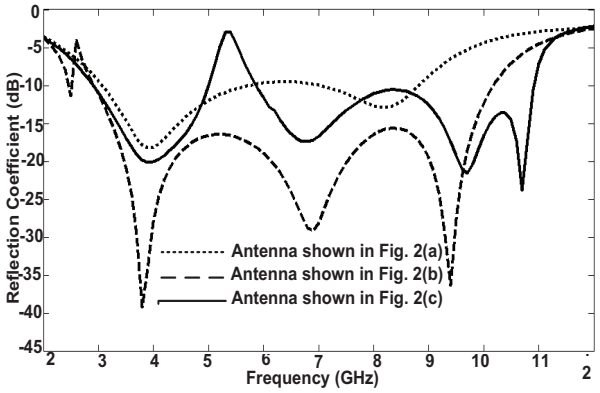


Fig. 3. Simulated reflection coefficient characteristics for the various square monopole antenna structures, as shown in Fig. 2.

In this work, through new technique of DGS and by a pair of L-shaped arms, a band-stop performance at frequency 5.5 GHz is produced that has an acceptable bandwidth. The central frequency of notch can easily be shifted by some key parameters like L1. Figure 4 exhibits the different structures of the antenna showing major elements of generating a stop-band, namely a pair of L-shaped arms and shorting pin. Figure 5 demonstrates the voltage standing wave ratio (VSWR) for the three cases shown in Fig. 4. It is quite apparent that the pair of L-shaped arms have effect on notched band at center frequency 5.5 GHz, while shorting pin produces a stop band at center

frequency 3.5 GHz to filter WLAN and WiMAX bands, respectively. Meanwhile, it is found out that both notches are autonomous; i.e., they have no effect on each other. As illustrated in Fig. 6, parameter L5 has a considerable influence on frequency shifting. Increasing the length of L5 results in decreasing the center frequency while the rejection magnitude is nearly constant. A best value L5 for covering 5.15 to 5.825 GHz band corresponds to 11.5 mm. In this study, to generate the band-stop performance on WiMAX band with center frequency 3.5 GHz, we used an arm with length L1+L2 that has been connected to a shorting pin.

The simulated VSWR curves with different values of L1 are plotted in Fig. 7. As shown in Fig. 7, when L1 increases from 1 to 7 mm, the center frequency of the notched band is fallen from 3.8 to 2.8 GHz. Therefore, the optimized L1 is 3 mm. From these results, we can conclude that the notch frequencies are controllable by changing L1 and L5. To understand the behavior of the proposed antenna, Fig. 8 shows simulated current distributions on the radiating patch and a pair of L-shaped arms on the back. It can be observed from Fig. 8 (a), that the current is concentrated on the arms and patch using an arm ended up with shorting pin. It can be noticed that the current direction on the patch is opposed (180 degree phase difference) with the current on arm. On the other hand, Fig. 8 (b) depicts the current distribution at 3.5 GHz. It is clear that most of the current is seen on the pair of L-shaped arms with the current directions on the arms are in opposite direction with the current on patch.

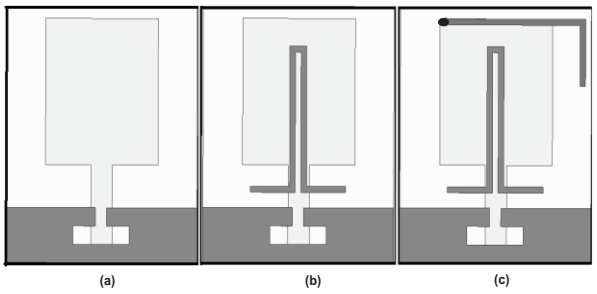


Fig. 4. (a) The square antenna with an inverted T-shaped slot, (b) the square antenna with a pair of L-shaped arms, and (c) proposed antenna.

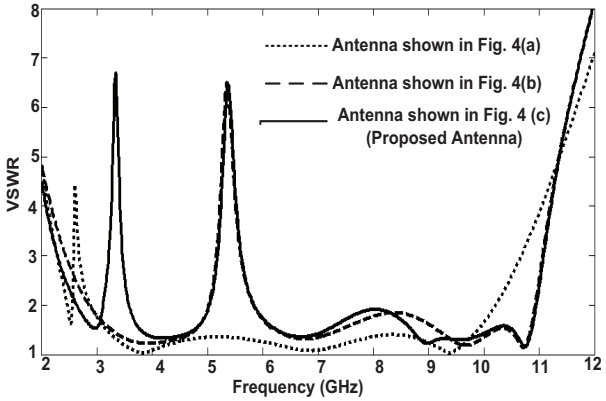


Fig. 5. Simulated VSWR characteristics for antennas shown in Fig. 4.

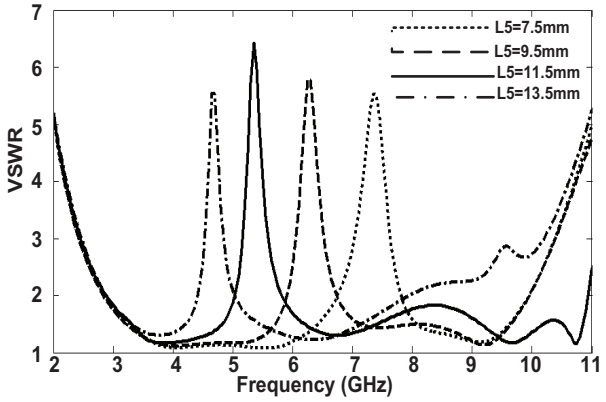


Fig. 6. Simulated VSWR characteristics of the antenna with a pair of L-shaped arms with different values of L5.

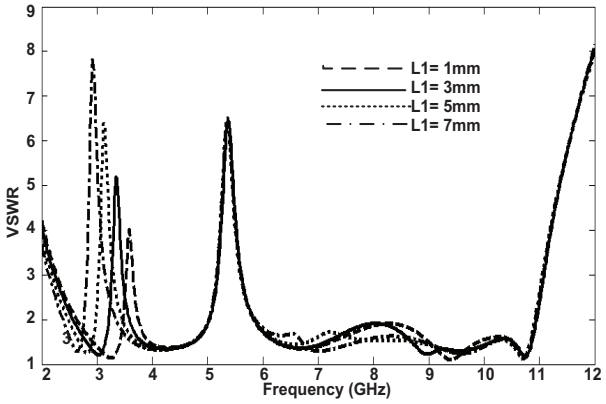


Fig. 7. Simulated VSWR characteristics of the antenna with an arm ended up shorting pin with different values of L1.

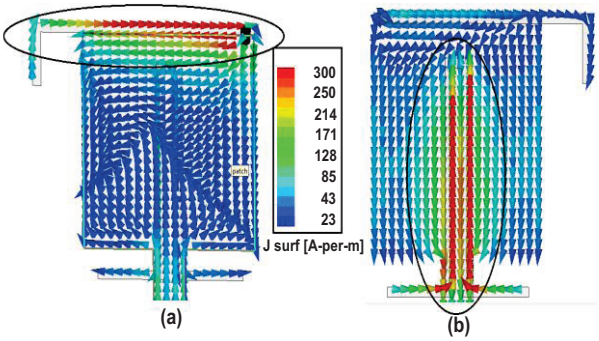


Fig. 8. Simulated surface current distributions on radiating patch: (a) on L-shaped arm ended up shorting pin at 5.5 GHz (bottom view), and (b) on a pair of L-shaped arms at 3.5 GHz (top view).

The proposed antenna with optimal design, as shown in Fig. 9, was fabricated and tested in the Antenna Measurement Laboratory at Iran Telecommunication Research Center. Figure 10 exhibits the measured and simulated VSWR characteristics of the proposed antenna. The fabricated antenna has the frequency band of 2.3 to over 11 GHz. The designed antenna has a small size of 21×17 mm$^2$ while showing the band rejection performance in the frequency bands of 3.2 to 3.8 and 5.1 to 5.85 GHz, respectively. The measured and simulated VSWR by both software HFSS [8] and CST [9] are shown in Fig. 10. As shown in Fig. 10, there exists a discrepancy between measured data and the simulated results, and this could be due to the effect of the SMA port.

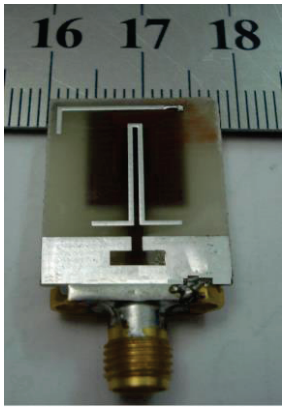


Fig. 9. Photograph of the realized antenna.

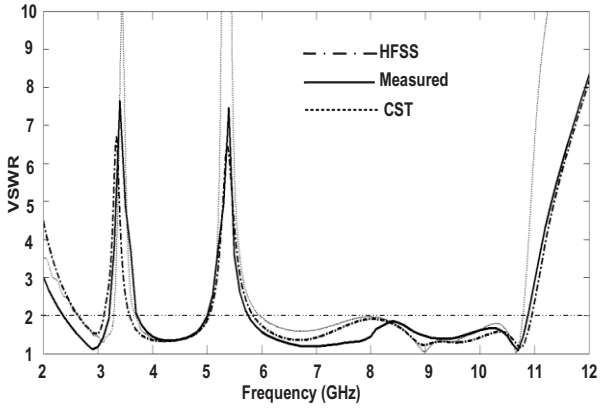


Fig. 10. Measured and simulated VSWR characteristics for the antenna.

Figure 11 illustrates the measured maximum gain of the proposed antenna with and without stop band. A sharp decrease of maximum gain in the notched frequencies band at 3.5 and 5.5 GHz is shown.

For other frequencies outside the notched frequency band, the antenna gain with the slot is similar to those without it. Figure 12 shows the measured radiation patterns including the co-polarization and cross-polarization in the H-plane (x-z plane) and E-plane (y-z plane). It can be seen that the radiation patterns in x-z plane are nearly omnidirectional for the two frequencies while radiation pattern in y-z plane are approximately directional.

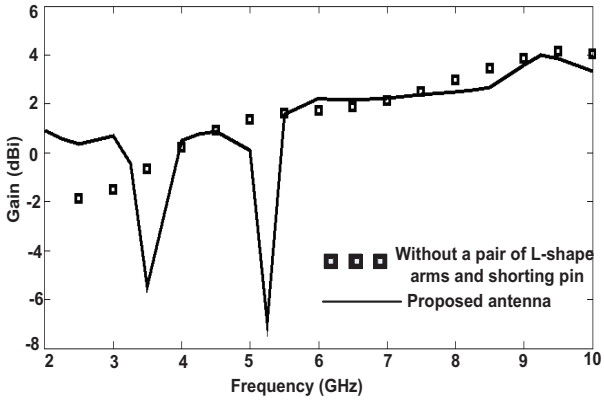


Fig. 11. Measured gain of the antenna without and with stop bands.

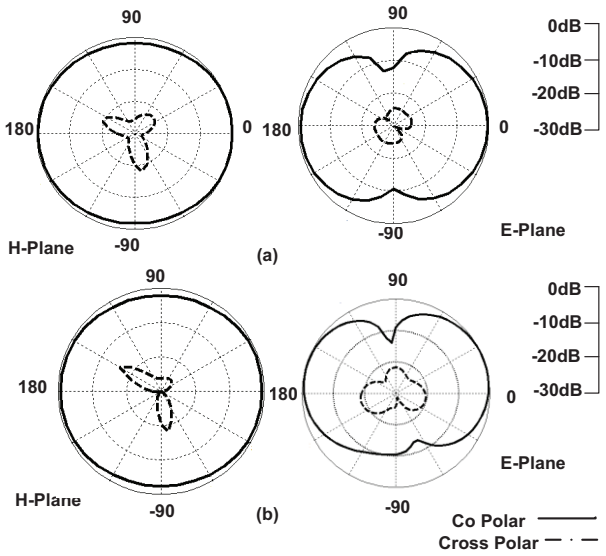


Fig. 12. Measured radiation patterns of the antenna at: (a) 4 and (b) 8 GHz.

### B. Time-domain analysis

Computation of the dispersion that happens when the antenna radiates a pulse signal is an important issue in UWB systems. The transmit transfer functions of the antennas were utilized to calculate the radiated pulse in various directions when a reference signal was used at the antenna input. The signal should present an UWB spectrum masking the antenna bandwidth and specially the FCC mask (3.1 up to 10.6 GHz). A pulse of Gaussian seventh derivative is shown in Fig. 13 that is an acceptable approximation to a FCC mask compliant pulse. This pulse is represented in the time domain by:

$$G(t) = A.\exp\left(\frac{-t^2}{2\delta^2}\right), \quad (1)$$

$$G^n(t) = \frac{d^n G}{dt^n} = (-1)^n \frac{1}{\left(\sqrt{2}\delta\right)^2}.H_n\left(\frac{t}{\sqrt{2}\delta}\right).G(t), \quad (2)$$

where, for n=7,

$$H_7(t) = 128t^7 - 1344t^5 + 3360t^3 - 1680t. \quad (3)$$

Both signal and spectrum are depicted in Fig. 13. The pulse bandwidth fits very well into the desired mask. Fortunately, after drawing various Gaussian pulses from the first to eighth derivative, it was found that the best pulse to cover the FCC mask is the seventh derivative. Furthermore, with a few tolerances, the sixth and eighth derivative can be acceptable. The correlation between the transmitted (TX) and received (RX) signals in telecommunications systems, is evaluated using the fidelity factor (4):

$$F = \max_\tau \left| \frac{\int_{-\infty}^{+\infty} S(t)r(t-\tau)dt}{\sqrt{\int_{-\infty}^{+\infty} S(t)^2 . \int_{-\infty}^{+\infty} r(t)^2 dt}} \right|. \quad (4)$$

In which S(t) and r(t) are the TX and RX signals, respectively. For impulse radio in UWB communications, it is needful to have a high degree of correlation between the TX and RX signals to avoid losing the modulated information. Although, for most other telecommunication systems, the fidelity parameter is not that relevant. In order to evaluate the pulse transmission characteristics of the antenna without notch, two configurations (side-by-side and face-to-face orientations) were chosen. The transmitting and receiving antennas were placed in a d=25 cm distance from each other [10]. As shown in Fig. 14, the received pulses in each of the two orientations are broadened, a relatively good similarity exists between the RX and TX pulses. Using (4), the fidelity factor for the face-to-face and side-by-side configurations was earned equal to 0.95 and 0.96, respectively. These values for the fidelity factor demonstrate which the antenna imposes negligible effects on the transmitted pulses. The pulse transmission results are obtained using CST [9].

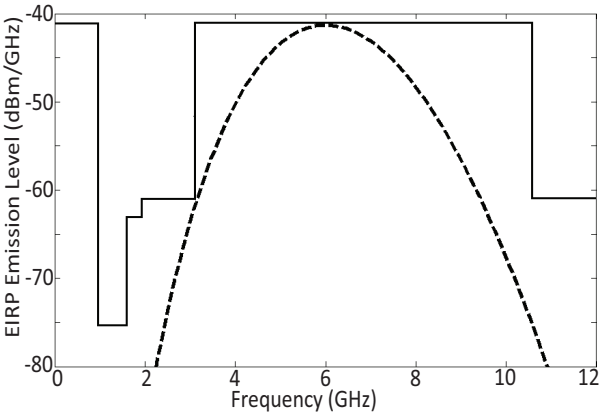


Fig. 13. Power spectrum density compared to FCC mask.

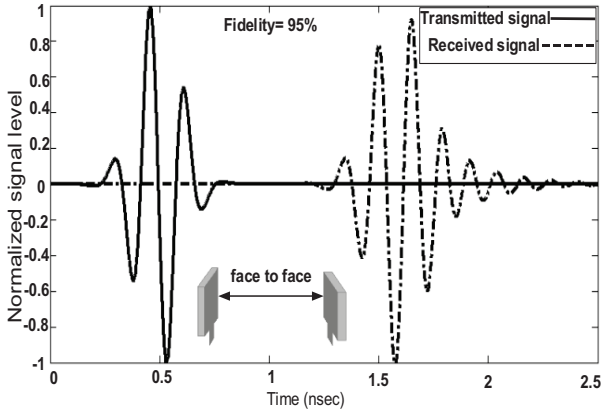


(a)

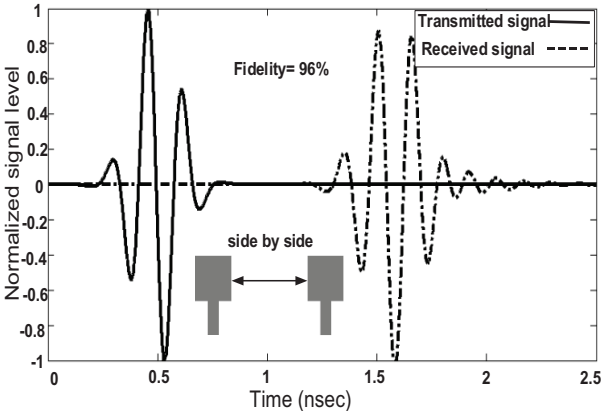


(b)

Fig. 14. Transmitted and received pulses in time domain for a UWB link with identical antennas without notches in: (a) face-to-face and (b) side by side orientations.

## IV. CONCLUSION

In this paper, a novel microstrip antenna with extended bandwidth capability for UWB applications was presented. In this design, the proposed antenna can operate from 2.3 to 11 GHz with VSWR<2,and displays a good omnidirectional radiation pattern even at higher frequencies. The designed antenna has a small size of 17×21 mm$^2$ while showing a band rejection performance in the frequency bands of 3.2 to 3.8 and 5.1 to 5.85 GHz, respectively. Good reflection coefficient and radiation pattern characteristics are obtained in the frequency band of interest. Simulated and experimental results exhibit that the antenna could be a good candidate for UWB application.

## REFERENCES

[1] H. Schantz, *The Art and Science of Ultra Wideband Antennas*, Artech House, Norwood, MA, 2005.

[2] M. Akbari, M. Koohestani, Ch. Ghobadi, and J. Nourinia, "Compact CPW-fed printed monopole antenna with super wideband performance," *Microwave Opt. Technol. Lett*., 53, pp. 1481-1483, July 2011.

[3] M. Akbari, M. Koohestani, Ch. Ghobadi, and J. Nourinia, "A new compact planar UWB monopole antenna," *International Journal of RF and Microwave Computer-Aided Engineering*, 21, pp. 216-220, 2011.

[4] M. Mighani, M. Akbari, and N. Felegari, "Design of a small rhombic monopole antenna with parasitic rectangle into slot of the feed line for SWB application," *The Applied Computational Electromagnetics Society*, 27, pp. 74-79, 2012.

[5] M. Ojaroudi, "Printed monopole antenna with a novel band-notched folded trapezoid ultra-wideband," *J. Electromagn. Waves. Appl*., 23, pp. 2513-2522, 2009.

[6] M. Ojaroudi, Gh. Ghanbari, N. Ojaroudi, and Ch. Ghobadi, "Small square monopole antenna for UWB applications with variable frequency band-notch function," *IEEE Antennas Wirel. Propag. Lett*., 8, pp. 1061-1064, 2009.

[7] R. Rouhi, Ch. Ghobadi, J. Nourinia, and M. Ojaroudi, "Ultra-wideband small square monopole antenna with band notched function," *Microwave Opt. Technol. Lett*., 52, pp. 2065-2069, 2010.

[8] Ansoft High Frequency Structure Simulation (HFSS), ver. 10, Ansoft Corporation, Pittsburgh, PA, 2005.

[9] CST Microwave Studio, ver. 2008, Computer Simulation Technology, Framingham, MA, 2008.

[10] C. R. Medeiros, J. R. Costa, and C. A. Fernandes, "Compact tapered slot UWB antenna with WLAN band rejection," IEEE Antennas and Wireless Propagation Letters, vol. 8, pp. 661-664, 2009.